

**Modeling of the Stress-Strain-Resistance
Behaviour of Ni-Ti and Ni-Ti-Cu Shape Memory
Alloys for use in Sensorless Actuator Position
Control**

by

Brian Lynch

A Thesis submitted to
the Faculty of Graduate Studies and Research
in partial fulfilment of
the requirements for the degree of
Doctor of Philosophy
in

Aerospace Engineering

Department of Mechanical & Aerospace Engineering
Carleton University
Ottawa, Ontario, Canada
February 2013



Library and Archives
Canada

Published Heritage
Branch

395 Wellington Street
Ottawa ON K1A 0N4
Canada

Bibliothèque et
Archives Canada

Direction du
Patrimoine de l'édition

395, rue Wellington
Ottawa ON K1A 0N4
Canada

Your file Votre référence

ISBN: 978-0-494-94552-0

Our file Notre référence

ISBN: 978-0-494-94552-0

NOTICE:

The author has granted a non-exclusive license allowing Library and Archives Canada to reproduce, publish, archive, preserve, conserve, communicate to the public by telecommunication or on the Internet, loan, distribute and sell theses worldwide, for commercial or non-commercial purposes, in microform, paper, electronic and/or any other formats.

The author retains copyright ownership and moral rights in this thesis. Neither the thesis nor substantial extracts from it may be printed or otherwise reproduced without the author's permission.

AVIS:

L'auteur a accordé une licence non exclusive permettant à la Bibliothèque et Archives Canada de reproduire, publier, archiver, sauvegarder, conserver, transmettre au public par télécommunication ou par l'Internet, prêter, distribuer et vendre des thèses partout dans le monde, à des fins commerciales ou autres, sur support microforme, papier, électronique et/ou autres formats.

L'auteur conserve la propriété du droit d'auteur et des droits moraux qui protègent cette thèse. Ni la thèse ni des extraits substantiels de celle-ci ne doivent être imprimés ou autrement reproduits sans son autorisation.

In compliance with the Canadian Privacy Act some supporting forms may have been removed from this thesis.

While these forms may be included in the document page count, their removal does not represent any loss of content from the thesis.

Conformément à la loi canadienne sur la protection de la vie privée, quelques formulaires secondaires ont été enlevés de cette thèse.

Bien que ces formulaires aient inclus dans la pagination, il n'y aura aucun contenu manquant.

Canada

Copyright ©
2013 - Brian Lynch

Abstract

Shape memory alloys have become increasingly popular for use in many engineering fields, including aerospace, robotics, and biomechanics. A major research focus is the application of Nitinol shape memory alloy wire as an actuator. While position and force control of shape memory alloy actuator wires has been successfully demonstrated in the past, most control algorithms have been developed using position feedback. Recently, it has been shown that there exists a significant correlation between the electrical resistance and strain of the material. This correlation has been used to model the strain as a function of the electrical resistance for use in predicting the actuator position for control purposes. However, the influence of applied stress as well as the presence of a third microstructure phase (R-phase) make modeling of the resistance-strain correlation difficult since hysteretic effects become more substantial. This thesis presents new models of the resistance-stress-strain behaviour of shape memory alloy for use in actuator position control. Characterization of the material behaviour was performed through experimental analysis, and used to develop the models based on empirical curve fitting. The models were then validated through simulation as well as application in a simple PID position control algorithm. Furthermore, two different alloys were investigated: a Ni-Ti alloy called Flexinol which exhibits significant hysteresis due to the presence of R-phase, as well as a Ni-Ti-Cu alloy which shows negligible hysteresis.

For my parents, who always point me in the right direction...
For my grandparents, who inspire me to reach for greatness...
...and for my brother, who strengthens the best in me.

Acknowledgments

Many thanks to my thesis supervisors Alex Ellery and Fred Nietzsche, as well as my former supervisor Daniel Feszty, who have supported and encouraged me throughout my time as a graduate student.

I would also like to thank those who have fostered my growth as an engineer, scientist, and researcher throughout my education, including Mehrdaad Ghorashi, Bruce Burlton, Tarik Kaya, Joshua Marhsall, Mojtaba Ahmadi, Fred Afagh, John Hayes, Choon-Lai Tan, Metin Yaras, and Jonathan Beddoes.

Thank you as well to the supporting staff who helped hone my laboratory and hands-on skills, including Gary Clements, Steve Truttman, Stefan Biljan, Alex Proctor, Kevin Sangster, Fred Barrett, Graham Beard, and Steve Tremblay, as well as administrative staff Nancy Powell, Christie Egbert, Marlene Groves, and Irene Helder.

Finally, many thanks to the Canadian Space Agency, who made this research possible under the guidance of Xin-Xiang Jiang and with the support of Darius Nikanpour, Guanghan Wang, Yan-Ru Hu, Rémy Grenier, Philippe Vincent, Ralph Nolting, Pierre Lortie and Maxime Pepin-Thivierge.

Table of Contents

Abstract	iii
Acknowledgments	v
Table of Contents	vi
List of Tables	x
List of Figures	xi
1 Introduction	1
1.1 History of Shape Memory Alloy	2
1.2 Nitinol	4
1.2.1 Phase Composition	5
1.2.2 Shape Memory Effect	6
1.2.3 Superelasticity	9
1.3 Applications	10
1.3.1 Commercial & Consumer Products	11
1.3.2 Biomedical Devices	14
1.3.3 Robotics	18
1.3.4 Aerospace	21
1.4 Design Considerations	24

1.4.1	Stroke	24
1.4.2	Load	25
1.4.3	Activation	27
1.4.4	Boundary Conditions	27
1.4.5	Fatigue	28
1.5	Electrical Resistance	29
1.6	Research Summary	33
2	Literature Review	36
2.1	Modeling	37
2.2	Position-Feedback Control	41
2.2.1	PID Controllers	42
2.2.2	Linearization	43
2.2.3	Optimal & Robust Control	44
2.2.4	Model-Based Control	45
2.2.5	Learning-Based Control	47
2.3	Resistance-Feedback Control	48
2.3.1	Linear Models	50
2.3.2	Polynomial Models	51
2.3.3	Hysteresis Compensation	53
2.3.4	Neural Network Control	53
2.4	Research Contributions	54
3	Experimental Setup	58
3.1	Test Stand	59
3.2	Wire Mounting	59
3.3	Displacement Transducer	61
3.4	Load Cell	63

3.5	Electrical Resistance Feedback	65
3.6	Data Acquisition	67
3.7	Power Supply	69
4	Material Characterization	71
4.1	Flexinol	72
4.1.1	Resistance-Displacement Behaviour	72
4.1.2	Influence of Applied Stress	76
4.1.3	Minor Hysteresis Loops	79
4.1.4	Training & Fatigue	81
4.2	Furukawa	84
4.2.1	Resistance-Displacement Behaviour	84
4.2.2	Influence of Applied Stress	86
4.2.3	Minor Hysteresis Loops	89
4.2.4	Training & Fatigue	91
5	Modeling	94
5.1	Flexinol	96
5.1.1	Heating & Cooling Curves	97
5.1.2	Influence of Applied Stress	99
5.1.3	Hysteresis Loops	103
5.1.4	Simulation	107
5.1.5	Normalization	116
5.1.6	Model Correlations	120
5.2	Furukawa	126
5.2.1	Heating & Cooling Curves	127
5.2.2	Influence of Applied Stress	129
5.2.3	Hysteresis Loops	132

5.2.4	Simulation	137
5.2.5	Normalization	147
5.2.6	Model Correlations	153
6	Control	156
6.1	Flexinol	158
6.1.1	Exclusive Model	159
6.1.2	Normalized Model	162
6.2	Furukawa	165
6.2.1	Exclusive Model	166
6.2.2	Normalized Model	169
7	Conclusions	172
A	Load Cell Calibration	175
B	LVDT Calibration	177
C	Flexinol Model Asymptote Slope & Offset Determination	179
	List of References	182

List of Tables

1	Expected and calibrated coefficients for LVDT position output.	63
2	Mean absolute error for simulations under each load condition with stress influence effects included as well as assuming a constant load condition.	116
3	Mean absolute error for simulations under each load condition using the averaged model, direct switching model, transition curve model, and average model without stress influence.	146
4	Summary of Flexinol model, control, and output errors in terms of total actuator stroke.	159
5	Summary of mean model, control, and output errors using the exclusive Flexinol model.	162
6	Summary of mean model, control, and output errors using the normalized Flexinol model.	164
7	Summary of Furukawa model, control, and output errors in terms of actuator stroke.	165
8	Summary of mean model, control, and output errors using the exclusive Furukawa model.	169
9	Summary of mean model, control, and output errors using the normalized Furukawa model.	171

List of Figures

1	Raychem Cryofit coupling	3
2	Austenite and martensite crystal structures for a Ni-Ti alloy.	5
3	Transformation sequence of shape memory alloy.	6
4	Temperature-strain hysteresis during phase transformation of shape memory alloy.	8
5	Influence of applied stress upon phase transformation temperatures. .	9
6	Stress-strain response during superelastic loading and unloading. . . .	11
7	Superelastic Nitinol eyeglass frames (left) and cellphone antennae (right).	12
8	Miga Motors MigaOne actuator (left) and TiNi Aerospace Frangibolt mechanism (right).	14
9	Various Nitinol stents.	15
10	Nitinol surgical staple (left) and proximal humerus connector (right).	16
11	Active endoscope actuated by SMA coil springs.	17
12	Robotic manipulator actuated by SMA wires.	19
13	Biomimetic Jellybot design (top) and swimming cycle (bottom). . . .	21
14	Hybrid SMA composite rotor blade (left) and rotor blade tab actuated by SMA wires (right).	22
15	SMA actuators used on the Sojourner rover (left) and Rosetta lander (right).	23
16	Actuation strain as a function of applied stress.	25

17	Strain-resistance curves of Nitinol at various stress levels.	30
18	Earthquake monitoring using an SMA transducer.	31
19	Results of modeling the electrical resistance of Nitinol.	33
20	Results of PID control investigated by Singh et. al..	44
21	Results of position control using LQR linearized control law investi- gated by Lee and Marvoidis.	45
22	Comparison of position control by Lee and Lee using PID control with Ziegler-Nichols tuning, time delay control, PID control based on time delay control, and relay control.	46
23	Comparison of PID control (left) and model based control (right) stud- ied by Majima et. al..	47
24	Performance of the neural network based controller developed by Song et. al..	49
25	Hysteresis gap for Ni-Ti alloys with various quantities of copper addition.	50
26	Control performance using the linear model studied by Neugebauer et. al..	51
27	Control performance using the polynomial model studied by Lan and Fan.	52
28	Comparison of control with and without compensation of the hysteresis effects as studied by Liu et. al..	54
29	Results of position control using a neural network model developed by Ma et. al..	55
30	Test stand with load cell mounting (A), LVDT mounting (B), and bias spring mounting (C).	60
31	Actuator wire mounting.	61
32	Solartron LVDT displacement transducer mounted on test stand. . .	62
33	Futek LRF300 load cell mounted on test stand.	64

34	Ectron 563H conditioner-amplifier.	64
35	Resistance measurement circuit diagram.	66
36	National Instruments PXI-1033 chassis with PXI-4110, PXI-6220, and PXI-4070 modules.	67
37	National Instruments SCXI-1000 chassis with SCXI-1102B and SCXI- 1122 modules.	68
38	Data acquisition, signal conditioning, and power supply system. . . .	69
39	Diagram of the experimental setup.	70
40	Major hysteresis loop resistance-displacement behaviour of Flexinol ac- tuator wire.	73
41	Major hysteresis loop resistivity-strain behaviour of Flexinol actuator wire.	74
42	Simplified resistance-displacement response including lines of constant resistivity for martensite at M_f (dark blue), martensite at A_s (light blue), austenite at A_f (red), austenite at R_s (orange), and R-phase at M_s (purple).	76
43	Influence of stress upon the resistance-displacement behaviour of Flex- inol actuator wire.	77
44	Influence of stress upon the heating and cooling curves of Flexinol actuator wire.	78
45	Minor hysteresis loop behaviour of Flexinol actuator wire.	80
46	Minor hysteresis loop behaviour of Flexinol actuator wire (reduced). .	81
47	Fatigue behaviour of Flexinol actuator wire.	82
48	Minimum and maximum resistance and displacement during cycling including logarithmic curve fitting.	83
49	Overall resistance-displacement behaviour of Furukawa actuator wire.	85
50	Overall resistivity-displacement behaviour of Furukawa actuator wire.	86

51	Influence of stress upon the resistance-displacement behaviour of Furukawa actuator wire.	87
52	Influence of stress upon heating and cooling curves of the Furukawa actuator wire.	88
53	Minor hysteresis loop behaviour of Furukawa actuator wire (incomplete heating).	90
54	Minor hysteresis loop behaviour of Furukawa actuator wire (incomplete cooling).	90
55	Minor hysteresis loop behaviour of Furukawa actuator wire (incomplete heating and cooling).	91
56	Fatigue behaviour of Furukawa actuator wire.	92
57	Minimum and maximum resistance and displacement during cycling including logarithmic curve fitting.	93
58	Heating and cooling asymptotes for major hysteresis loop of Flexinol wire.	99
59	Families of heating and cooling asymptotes for Flexinol wire.	100
60	Slope and intercept coefficients of heating and cooling asymptotes for Flexinol wire.	101
61	Polynomial fitting of relationships between applied stress and asymptote coefficients.	102
62	RMS error of model coefficients as a function of polynomial order.	103
63	Exponential transition curves for Flexinol wire.	106
64	Simulation results for the Flexinol model under constant load of 0.49 N.110	
65	Simulated resistance-displacement curves for the Flexinol model (0.49 N).	111
66	Simulation results for the Flexinol model under constant load of 0.98 N.111	

67	Simulated resistance-displacement curves for the Flexinol model (0.98 N).	112
68	Simulation results for the Flexinol model under constant load of 1.96 N.112	
69	Simulated resistance-displacement curves for the Flexinol model (1.96 N).	113
70	Simulation results for the Flexinol model under spring constraint loading.113	
71	Simulated resistance-displacement curves for the Flexinol model (spring constraint).	114
72	Simulation results for the Flexinol model under spring constraint loading while assuming constant applied load.	114
73	Simulated resistance-displacement curves for the Flexinol model (spring constraint with assumption of constant applied load).	115
74	Resistance-strain responses of Flexinol actuator wires with various lengths.	117
75	Initial resistance of Flexinol actuator wires with various lengths.	118
76	Normalized actuation curves of Flexinol actuator wires with various lengths.	119
77	Simulated actuation curves of Ni-Ti actuator wire using the extended model by Brammajyosula under various constant applied loads.	121
78	Relationship between phase transformation temperatures and applied stress.	123
79	Comparison of slope and offset coefficients determined experimentally and fitted for Flexinol wire as well as determined analytically for the Ni-Ti alloy model by Brammajyosula.	126
80	Heating and cooling resistance-displacement curves of Furukawa alloy with polynomial fitting functions.	128
81	Heating and cooling asymptote families for Flexinol wire.	130

82	Slope and intercept coefficients of heating and cooling asymptotes for Furukawa wire.	131
83	Polynomial fitting of the heating and cooling curve coefficients.	132
84	Error of the Furukawa model as a function of polynomial order.	133
85	Comparison of transition curves and direct switching in the Furukawa model.	135
86	Comparison of transition curves and averaged activation curve in the Furukawa model.	136
87	Simulation results for the averaged Furukawa model under constant load of 0.49 N.	140
88	Simulated resistance-displacement curves for the averaged Furukawa model (0.49 N).	140
89	Simulation results for the averaged Furukawa model under constant load of 0.98 N.	141
90	Simulated resistance-displacement curves for the averaged Furukawa model (0.98 N).	141
91	Simulation results for the averaged Furukawa model under constant load of 1.96 N.	142
92	Simulated resistance-displacement curves for the averaged Furukawa model (1.96 N).	142
93	Simulation results for the averaged Furukawa model under spring constraint loading.	143
94	Simulated resistance-displacement curves for the averaged Furukawa model (spring constraint).	143
95	Simulation results for the averaged Furukawa model under spring constraint loading while assuming constant applied load.	144

96	Simulated resistance-displacement curves for the averaged Furukawa model under spring constraint loading while assuming constant applied load.	144
97	Comparison of simulation results using the direct switching, smooth transition curves, and averaged Furukawa models.	145
98	Comparison of simulated resistance-displacement curves using the direct switching, smooth transition curves, and averaged Furukawa models.	145
99	Normalized resistance-displacement activation curves for the Furukawa alloy.	148
100	Normalized resistance-displacement activation curves for the Furukawa alloy with polynomial fit.	149
101	Upper and lower limits of resistance and displacement for normalized activation curves.	150
102	Polynomial curves approximating mechanical displacement, actuation stroke, and maximum resistance.	151
103	Resistance-length relationships for Furukawa actuator wires of various lengths.	151
104	Simulated actuation curves of Ni-Ti-Cu actuator wire using the Liang & Rogers model.	154
105	Simulated actuation curves of Ni-Ti-Cu actuator wire including stress-dependent actuator stroke.	155
106	Block diagram of PID position control algorithm based on model feedback.	157
107	Step-wise tracking response of the control system under a constant applied load using the exclusive Flexinol model.	160
108	Step-wise tracking response of the control system under a spring constraint applied load using the exclusive Flexinol model.	161

109	Step-wise tracking response of the control system under varying applied load using the exclusive Flexinol model.	161
110	Step-wise tracking response of the control system under varying applied load using the normalized Flexinol model.	163
111	Sine tracking response of the control system under varying applied load using the normalized Flexinol model.	164
112	Step tracking response of the control system under constant applied load using the exclusive Furukawa model with direct switching between heating and cooling curves.	167
113	Step tracking response of the control system under constant applied load using the averaged exclusive Furukawa model.	167
114	Step tracking response of the control system under spring constraint loading using the averaged exclusive Furukawa model.	168
115	Step tracking response of the control system under varying applied load using the averaged exclusive Furukawa model.	168
116	Step-wise tracking response of the control system under varying applied load using the normalized Furukawa model.	170
117	Triangle wave tracking response of the control system under constant load using the normalized Furukawa model.	171
118	Linear fit of experimental data for load cell calibration.	176
119	Linear fit of experimental data for LVDT calibration.	178

Chapter 1

Introduction

Smart materials have become increasingly popular for use in many engineering applications due to their ability to change physical properties in a controlled and predictable manner [1]. Each type of smart material exhibits a phenomenal response to stimuli such as electricity, light, or heat. Examples of smart materials include electrochromic materials, which change colour when excited by an electric potential; magnetorheological fluids, which experience a change in viscosity when exposed to a magnetic field; and piezoelectrics, which develop an electric potential due to temperature changes. Two well studied types of smart materials are piezoelectric materials and shape memory alloys, which are popular due to their ability to perform as an actuator. Piezoelectric materials demonstrate a coupling between electrical and mechanical properties. Applying mechanical stress causes electric potential to develop along the material, while applying an electric field causes mechanical strain [2]. Shape memory alloys, on the other hand, have the ability to restore a previous geometry upon application of heat. This restoration is accomplished by transformations in the crystal structure which are dependent upon both temperature and mechanical stress [3].

The phenomena associated with each smart material may be exploited and controlled in order to create discrete devices such as actuators, dampers, sensors, etc.

[4] [5] [6] [7] [8]. Furthermore, smart materials may be integrated into structures to achieve distributed control, sensing, or energy harvesting [9] [10] [11] [12]. Much research is now focusing on the development of actuation systems employing smart materials. Actuator designs have been primarily based upon piezoelectric materials and shape memory alloys [13]. These smart material actuators demonstrate a significant reduction in mass and complexity when compared to typical actuators based upon electric motors, solenoids, hydraulics, or pneumatics [14] [15].

Both piezoelectric materials and shape memory alloys are suitable for use in actuator technologies due to their ability to generate force and displacement. Piezoelectric materials are preferred for applications where small displacements are required on the order of micrometres or nanometres. They are able to operate at a wide range of frequencies, but require very high voltage. Shape memory alloys, on the other hand, produce much higher strains and carry high loads. For example, a Ni-Ti shape memory alloy wire with a diameter of 0.5 mm and length of 100 mm can achieve a stroke of approximately 5 mm while carrying over 30 N. Since the shape change phenomenon is dependent upon temperature, thermal inertia limits shape memory alloys to low frequency applications. However, the temperature dependency also allows the alloy to be activated simply through resistive heating at reasonable voltage and current levels. High force and displacement capabilities, combined with simplicity and low cost, make shape memory alloy a superior choice for actuator design [16].

1.1 History of Shape Memory Alloy

The shape memory phenomenon was first observed in gold-cadmium alloys by Olander in 1932, who discovered the alloy's pseudoelasticity. Similar behaviour was also observed in copper-zinc, indium-thallium, and copper-aluminum-nickel alloys throughout the 1940's and 1950's. Kurdjumov and Khandros determined that the source of

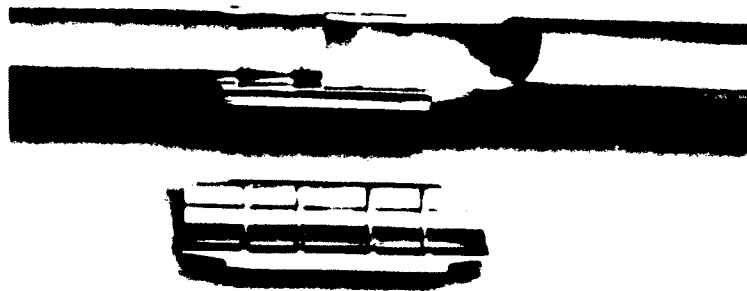


Figure 1: Raychem Cryofit coupling [19].

this behaviour was reversible martensitic phase transformations which were dependent upon temperature [17]. In 1962, researchers at the Naval Ordnance Laboratory in the United States discovered that nickel-titanium alloys also exhibit the shape memory phenomenon. This alloy was then named Nitinol in reference to its composition (Ni-Ti) and the laboratory (NOL) at which it was discovered. Extensive metallurgical testing and analysis of Nitinol was carried out in the following years and the thermomechanical properties of the alloy were well established. After characterizing the material properties and driving mechanism behind the martensitic phase transformations, Nitinol was considered for various applications. The first commercial application was the Cryofit coupling ring developed by Raychem and used to connect hydraulic pipelines in the Grumman F-14 Tomcat aircraft [18], as shown in Figure 1. Nitinol has since received enormous attention from researchers in many engineering disciplines, with significant developments in biomedical, robotic, and aerospace applications.

1.2 Nitinol

The nickel-titanium alloy Nitinol has high durability and strength properties, which make it favourable over other shape memory alloys despite the fact that it is also difficult to machine and process. Nitinol is also highly resistant to corrosion and exhibits good fatigue life. Furthermore, the alloy is biocompatible, and therefore a suitable choice for many biomedical applications [20]. Typical Nitinol alloys are composed of approximately 55% titanium by weight. Altering the composition results in changes to the transformation temperatures which define the onset and completion of the shape memory phenomenon. These transformation temperatures may also be changed through the appropriate selection of heat treatments as well as the addition of tertiary alloying elements such as iron, chromium, or cobalt [21] [22]. Furthermore, the addition of copper has been shown to significantly improve the fatigue life and reduce the hysteresis effects [23]. Other elements such as oxygen and carbon must be removed otherwise the properties of the alloy are degraded [24].

While the alloy may be produced in many shapes, it is typically drawn into strips or wires. Sputtering is also used for fabricating micro- and nano-scale elements in many MEMS applications. However, Nitinol in its wire form is most commonly used in actuator design since it has many advantages. The high ratio of surface area to volume allows the wire to cool quickly, which is desirable for fast actuation and return. Nitinol wire is also flexible enough to be wound around pulleys in order to gain mechanical advantage. Furthermore, modeling of the wire mechanically and thermodynamically may be treated as a one-dimensional problem, thus reducing the complexity of the model.

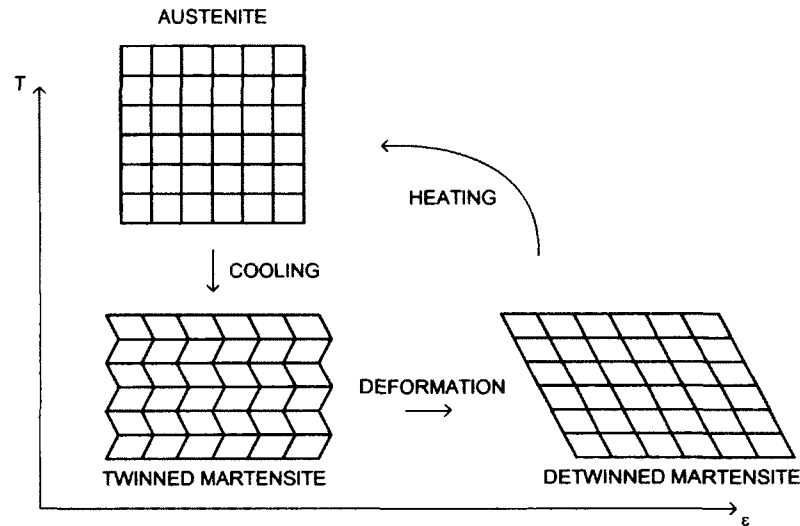


Figure 3: Transformation sequence of shape memory alloy.

In addition to austenite and martensite, a third phase has been discovered in Nitinol. Labeled R-phase due to its rhombohedral crystal structure, this phase has been observed intermediately during both heating and cooling [27]. The appearance of R-phase during transformation from martensite to austenite and vice-versa depends upon the manufacturing processes used while producing the alloy [28]. Various thermomechanical treatments such as cold working, annealing, and aging may result in the occurrence of R-phase, and through careful selection of appropriate treatments it is possible to minimize the amount of R-phase that appears during transformation.

1.2.2 Shape Memory Effect

Shape memory alloys are so named due to the shape memory effect which they exhibit. This phenomenon is driven by the phase transformations described earlier. When the material is stressed, detwinning occurs within the martensite phase which appears as plastic deformation at a macroscopic scale. After removing the stress, heating then

causes the martensite phase to transform into austenite, which causes the material to recover its original geometry. Upon cooling, the austenite transforms back into twinned martensite and the material retains the original geometry [29]. During these transformations, the fraction of martensite is determined by the material's temperature and applied mechanical stress. The transformation strain is a function of the martensite fraction, therefore the strain is dependent upon both applied stress and temperature.

The phase transformation process begins and ends at critical transformation temperatures, which depend upon the applied mechanical stress. However, the phase transformation temperatures for the forward transformation process (martensite to austenite) are different from those for the reverse process (austenite to martensite). This gap therefore causes hysteretic behaviour in Nitinol, which is apparent when observing the relationships of various material properties such as martensite fraction, strain, and electrical resistance [30].

Figure 4 shows a typical strain-temperature curve for a Nitinol wire under a tensile bias load. Due to the applied stress, the wire is elongated at the start of the curve. Heating the wire causes the temperature to rise until reaching the start of the martensite-to-austenite phase transformation, which is defined by the austenite start critical temperature, A_s . Phase transformation from martensite to austenite then occurs while the wire temperature continues to rise. The end of the martensite-to-austenite phase transformation is defined by the austenite finish critical temperature, A_f . Once the wire has reached this temperature, the forward phase transformation process is complete and the alloy is composed entirely of austenite (any further increase in temperature causes no significant response in the material). The wire is then cooled and the temperature decreases until reaching the start of the austenite-to-martensite phase transformation, which is defined by the martensite start critical

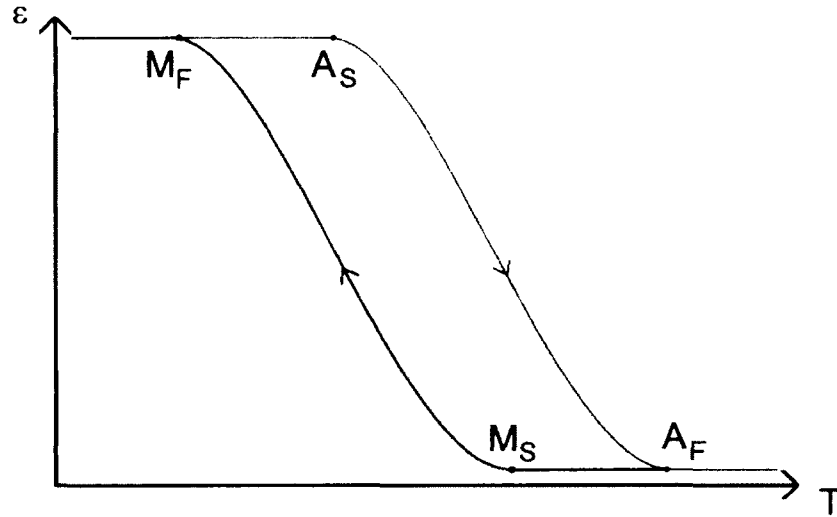


Figure 4: Temperature-strain hysteresis during phase transformation of shape memory alloy.

temperature, M_s . As the temperature continues to decrease, the phase transformation from austenite to martensite occurs until reaching completion at the martensite finish critical temperature, M_f .

Without any bias load, the wire would retain the original undeformed geometry, however, with the bias load still applied the wire returns to a deformed state. Applying a bias load therefore allows the material to be used as an actuator. At low temperature, the bias load causes a deformation as the martensite undergoes detwinning, while at high temperature the deformation is recovered due to the phase transformation to austenite. Under the presence of boundary constraints, the alloy will develop stress and therefore can be used to generate displacement and force.

Another important aspect of the phase transformation properties of Nitinol is the relationship between applied stress and the critical transformation temperatures. Figure 5 shows the critical transformation temperatures as a function of applied stress. The relationship is linear, with the critical transformation temperatures rising with increased applied stress. Therefore, as the applied stress is increased, the material

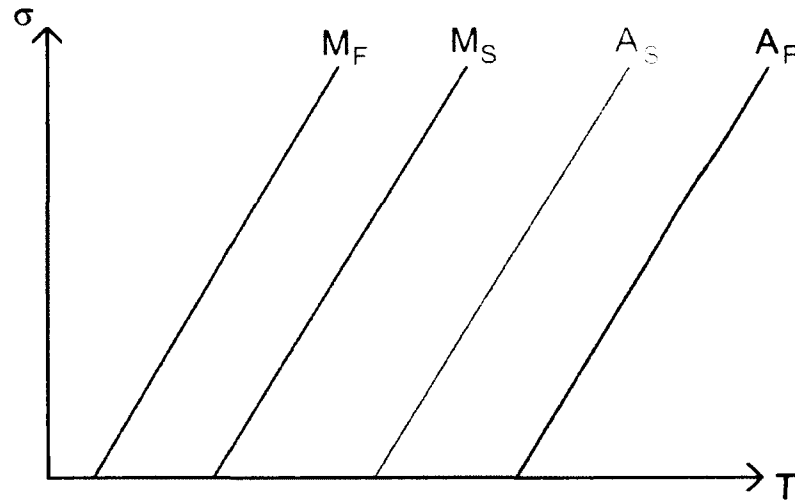


Figure 5: Influence of applied stress upon phase transformation temperatures.

must be heated to higher temperatures in order to undergo phase transformation. Furthermore, it is possible to cause phase transformation at a constant temperature by varying the amount of applied stress. For example, if the material is held at a constant state of low stress and high temperature such that it is entirely austenite, a reverse phase transformation to the martensite phase will take place upon increasing the applied stress. Similarly, if the stress is then decreased the material will transform back to the austenite phase. This effect is called superelasticity and is described in the next section.

1.2.3 Superelasticity

Another phenomenon exhibited by shape memory alloy is superelasticity, which manifests as the material's ability to recover large strains with seemingly elastic behaviour. Although this phenomenon is distinguished as being separate from the shape memory effect, both are in fact driven by the same fundamental phase transformation processes. Superelasticity occurs when the ambient temperature is greater than the

austenite finish critical temperature. This means that the alloy will be composed entirely of the austenite phase when in equilibrium with the surroundings. By applying mechanical stress, the reverse phase transformation from austenite to martensite occurs due to the relationship between the applied stress and critical transformation temperatures discussed previously. The phase transformation therefore causes a large deformation in the material. However, upon removal of the applied stress, the material returns to the austenite phase and recovers the deformation. While no temperature change has occurred, the material has undergone forward and reverse phase transformation simply through the influence of applied stress upon the critical transformation temperatures.

Therefore, shape memory alloy is capable of recovering deformation through phase transformations which appears similar to the elastic behaviour of conventional materials. However, the amount of recoverable strain due to superelasticity in Nitinol (approximately 4%) is an order of magnitude greater than that expected for aluminum or steel (approximately 0.25%). Figure 6 shows the stress-strain curve that is typically seen during superelastic behaviour of Nitinol. An important characteristic of this behaviour is the presence of a hysteresis effect. As the material is loaded, a large plastic deformation occurs due to phase transformation. However, upon unloading there is an initial elastic portion before the reverse phase transformation occurs. Therefore, energy is absorbed during loading and unloading of the material and superelastic shape memory alloy provides a source of elasticity and damping.

1.3 Applications

The shape memory effect and superelasticity phenomena of shape memory alloys have both been exploited in order to create active and passive devices in a variety of engineering applications, as well as some consumer products. Although the majority of

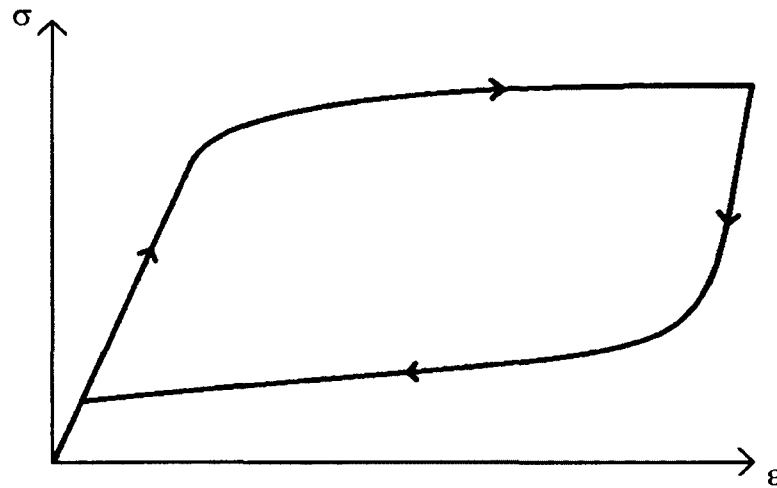


Figure 6: Stress-strain response during superelastic loading and unloading.

applications using shape memory alloys are within the context of scientific research and development, an increasing number of commercial products are becoming available. Two fields of study which show the greatest interest in the application of shape memory alloys are robotics and biomechanical engineering. The use of shape memory alloys as actuators within the field of robotics has increased dramatically due to the low cost of the material and reduction in complexity, size, and mass compared to conventional solutions. Nitinol, as a titanium-based alloy, is also a biocompatible material, making it an appropriate selection for biomedical devices and implants. Many researchers in academia and industry have turned to shape memory alloys to replace or augment conventional devices in other fields of study as well, and the benefits of using the material make it attractive for any application where mass and volume must be minimized.

1.3.1 Commercial & Consumer Products

There are many consumer products available which incorporate shape memory elements and take advantage of either superelasticity or the shape memory effect.

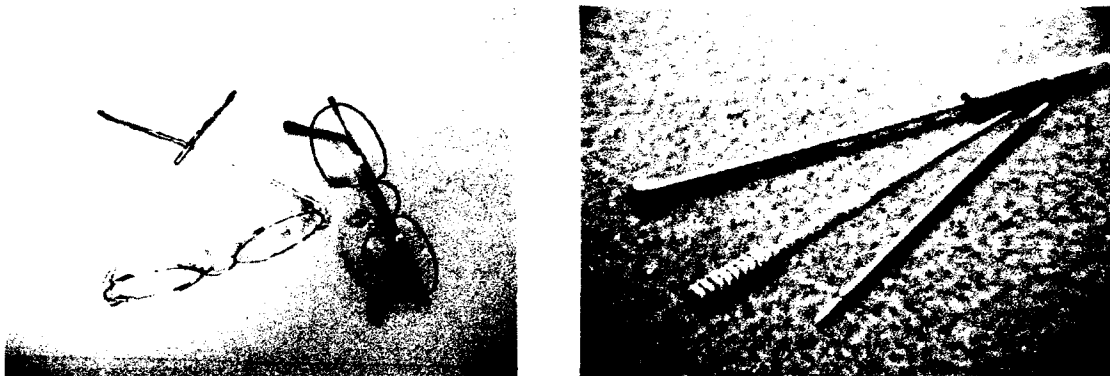


Figure 7: Superelastic Nitinol eyeglass frames (left) and cellphone antennae (right).

Highly flexible shape memory alloy eyeglass frames have been developed by companies Marchon and Eschenbach with Nitinol alloys under the trade names of Flexon and Titanflex, respectively [31], as shown in Figure 7 (left). Due to the superelasticity phenomenon, these eyeglass frames have an unusually high tolerance for bending compared to conventional materials. Women's brassiers have been developed by Wacoal which use shape memory alloy wires for structural support that conform to movement yet return to their original shape [32]. Superelasticity therefore allows greater flexibility (and hence greater comfort) compared to conventional steel wire. Nitinol orthodontic arch wire braces for dental patients have also been developed which reduce discomfort and optimize applied force. This application was conceived by George Andreasen and commercialized by Unitek Corporation, then developed further by Fujio Miura in partnership with TOMY Inc. and Furukawa Electric Co. under the trade name Sentalloy [33]. Shape memory alloy cell phone antennae also take advantage of the superelasticity phenomenon to accommodate large bending deformations without suffering damage [18], as shown in Figure 7 (right).

Miniature valves actuated by shape memory alloy elements have been developed for use in many products. For example, faucets and shower heads are available from TOTO USA which utilize a shape memory alloy valve that acts as an anti-scalding

device by shutting off flow if the water becomes dangerously hot [34]. Some household appliances that use shape memory alloy valves have also been developed, such as a coffee maker which pours water once it has boiled and a rice cooker which releases excess steam. Similar valves have also been applied to air conditioning systems. Several Mercedes-Benz automobile models use shape memory alloy valves to automatically control the flow of oil in order to avoid overheating. The Shinkansen bullet train also uses a shape memory alloy valve to control the level of oil within its gearboxes, resulting in reduced operating temperatures. These devices all take advantage of the shape memory effect in order to activate when the actuating element reaches a critical temperature, without the need for sensors and control inputs [35].

Products using shape memory alloy elements which are actively controlled by electrical input have also been developed. Valves employing shape memory alloy actuator elements have been created by Takasago in partnership with Dolomite [36], as well as by Dynalloy [37]. These valves, unlike those previously discussed, are controlled by electrical input instead of being passively actuated by the temperature of fluid passing through. Pumps activated by shape memory alloy elements have also been developed by Autosplice for use in the Insulet OmniPod insulin pump [38], as well as by TiNi Alloy [39]. Commercially available shape memory alloy actuators have been developed by many companies, including Autosplice [38], Miga Motors [40], TiNi Alloy, and TiNi Aerospace [41]. Fasteners composed of shape memory alloy are also available such as the UniLok heat shrinkable metal ring by IntrinsicDevices [42], which is not activated by electrical input but heated in order to tighten around a wire or bundle of wires. Shape memory alloy release and separation devices are available from TiNi Aerospace in order to replace pyrotechnic devices normally used to deploy spacecraft and their appendages, including the Frangibolt, Pinpuller, and Ejector Release Mechanism [43]. Figure 8 shows the Miga Motors MigaOne actuator (left) and the TiNi Aerospace Frangibolt (right).

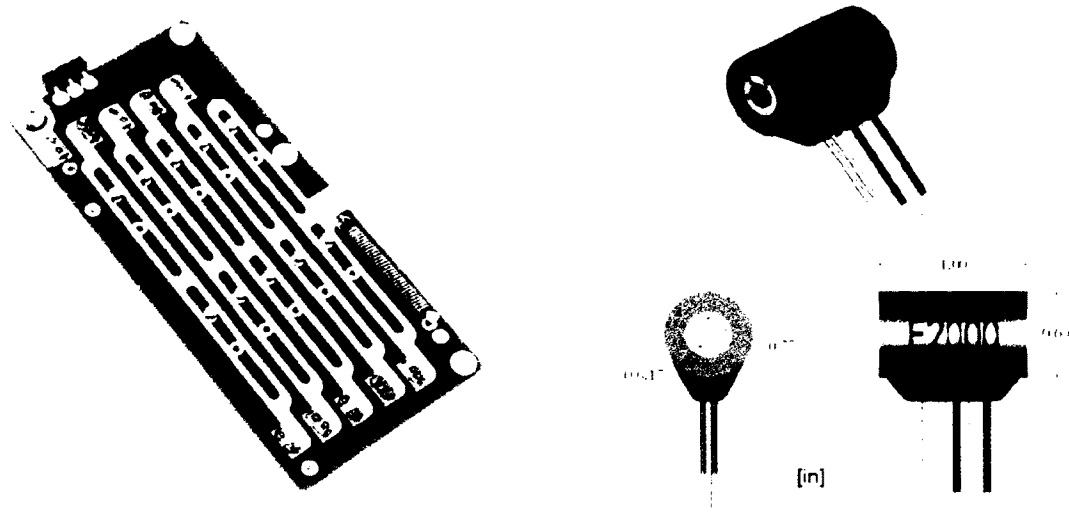


Figure 8: Miga Motors MigaOne actuator (left) [40] and TiNi Aerospace Frangibolt mechanism (right) [43] .

In addition to devices and products which employ shape memory elements, shape memory alloy raw material is also commercially available in many forms. Dynalloy produces a Nitinol alloy under the commercial name Flexinol which is available in wire and strip form [44]. Memry Corp. in partnership with SAES Getters offers Nitinol in wire, tube, sheet, and strip form [45]. A superelastic Nitinol wire under the commercial name Sentalloy is available from GAC International, typically for use in orthodontic applications described previously [33]. Furukawa Electric Company also produces a series of Nitinol alloys in wire form, with transformation properties for applications taking advantage of either superelasticity or the shape memory effect [35].

1.3.2 Biomedical Devices

As previously mentioned, Nitinol is an excellent choice for biomedical applications due to its mechanical properties, biocompatibility and the reduction in size, mass, complexity, and cost when compared to conventional materials and devices [46]. Another advantage of using Nitinol in vivo is the ability to activate the shape memory



Figure 9: Various Nitinol stents.

alloy element with body heat if the material has been manufactured to obtain the appropriate transformation temperatures. Both active and passive devices using Nitinol have been created for use in biomedical applications [47] [48]. Passive devices either take advantage of the superelastic phenomenon to provide exceptional flexibility, or are single use components activated by body heat. Active biomedical devices use shape memory alloy elements as actuators in order to control their movement or configuration.

There are many passive biomedical devices that use or are composed entirely of Nitinol. The most widely used of these is the shape memory alloy self-expandable vascular stent, which is a net-like structure manufactured out of Nitinol [49]. Conventional vascular stents are composed of stainless steel and must be inserted by a catheter into the blood vessel and expanded by a balloon at the desired location. A Nitinol stent requires no balloon for expansion since its transformation temperatures are tailored to cause shape recovery once reaching body temperature. After positioning the stent using a catheter, it is simply released and allowed to expand due to the shape memory effect. This reduces the risk of additional damage due to over-inflation of the balloon [50]. Figure 9 shows examples of various Nitinol stents.

Another successful application of Nitinol in a passive biomedical device is its use as an orthopedic implant. Surgical staples fabricated from Nitinol have been used to



Figure 10: Nitinol surgical staple [51] (left) and proximal humerus connector [54] (right).

fix bone fractures and assist in suturing wounds, as well as correct conditions such as scoliosis [51] [52]. The staple is manufactured in a closed configuration and opened just prior to insertion. Body heat activates the shape memory alloy staple, causing it to close and hold the tissue together. Plates and frames composed of Nitinol have also been used to support fractured bones [53] [54]. After activation due to body heat, the supporting structure provides high strength and flexibility, and may be designed to provide clamping force similar to the Nitinol staple [55] [56]. Figure 10 shows a Nitinol staple design (left) and proximal humerus clamp (right).

Actively controlled biomedical devices using Nitinol have also been designed and studied. Their simplicity and reduced size and mass make Nitinol actuators ideal for actively controlled endoscopes and catheters. Conventional catheters are passive flexible tubes that are inserted into a patient's body in order to perform tasks such as diagnose disease, deliver treatment, or drain fluid. Active catheters have been developed which use shape memory alloy actuators to achieve controlled bending motion in multiple degrees of freedom [57] [58]. Nitinol strip, wire, or spring actuators are arranged around a central hollow tube and separated into multiple segments.

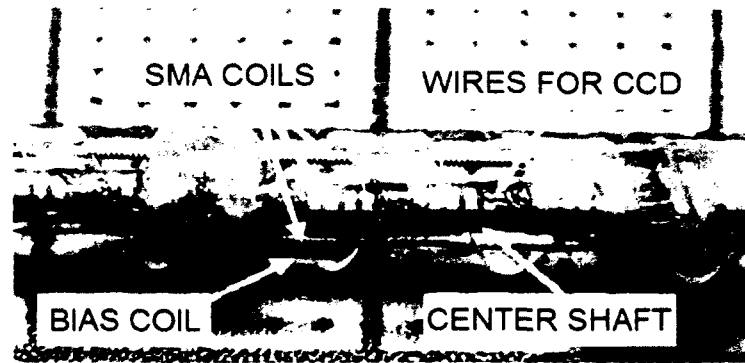


Figure 11: Active endoscope actuated by SMA coil springs [61].

Each segment is activated independently in order to control the overall direction of bending motion. Shape memory alloy actuators have been applied similarly to actively controlled endoscopes as well [59] [60] [61], as shown in Figure 11. These devices are similar in function to the active catheter but with the purpose of observing the patient's interior using a video camera attached to the tip.

Actuators for use in robotic systems for biomedical applications have also been developed using shape memory alloy elements [62] [63]. Many of these actuators are used for minimally invasive surgery devices, such as robotic joints and grippers [64] [65]. Nitinol wire has also been used as a simple actuation method for releasing medication from an implantable drug delivery device [66].

Another biomedical application of shape memory alloys is its use in devices outside of the body. Orthopedic rehabilitation for patients with muscular or joint mobility problems may be accomplished using shape memory alloy driven devices. Healthy regeneration of muscle may be promoted by actively imposing the motion using a shape memory alloy driven brace, such as a glove for hand rehabilitation [47]. Passive shape memory alloy devices may also be used to provide support to weakened muscles or joints, such as a foot arch for reducing impact and improving balance [67]. Furthermore, shape memory alloy actuators have also been studied for use in anthropomorphic prosthetic limbs [68] [69].

1.3.3 Robotics

Shape memory alloys, in particular Nitinol based alloys, have received much attention in many fields of robotics research due to their benefits over conventional approaches, such as low mass and volume, simplicity, high force and stroke output, as well as silent operation and negligible electromagnetic interference [70]. Most robotic applications of shape memory alloys take advantage of their actuating ability in order to generate motion and exert forces [71] [72]. Shape memory alloy elements are often employed as the actuating component within a discrete actuator, but may also be integrated or distributed within the robot body or structure. The reduced size and mass also allow shape memory alloy elements to be used within miniature robotic devices at such a scale where conventional devices are unavailable or fail to meet design requirements [73]. Furthermore, shape memory alloy is considered a good analogue for muscle, and has been studied as an artificial muscle for anthropomorphic and biomimetic robotic applications.

Various types of robotic manipulators actuated by shape memory alloy elements have been designed and studied [74] [75] [76]. Typical robotic manipulators are composed of multiple links interconnected by moving joints which are actuated by electric motors. Each joint motor must be aligned with the joint rotation axis or connected appropriately through a complex transmission system. Locating a motor within an outer link reduces the performance capabilities of the manipulator since the added mass increases the load upon the preceding joint motors, especially in the presence of gravity. Many rotary joints using shape memory alloy actuating elements have been developed for use in robotic manipulators [77] [78]. Replacing the electric joint motors with such actuators improves the manipulator's performance and efficiency, as well as lowers the overall size and mass of the system.

Flexible manipulators employing shape memory alloy actuators have also been

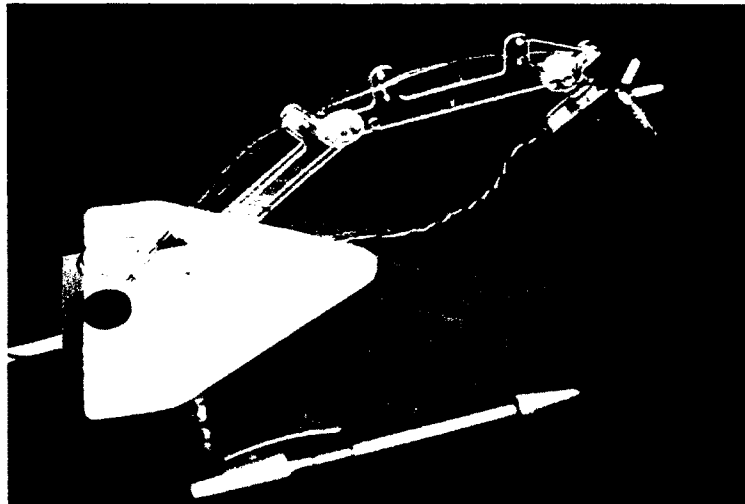


Figure 12: Robotic manipulator actuated by SMA wires [72].

investigated [79] [80] [81]. Instead of a series of rigid links connected by rotating joints, a flexible manipulator is composed of an elastic structure which deforms in order to generate motion. Shape memory alloy elements have been studied as actuators for flexible manipulators in both wire and strip form [82] [83]. The manipulator is divided into segments which each use a set of shape memory alloy actuators in order to generate bending in multiple directions, allowing the overall manipulator to achieve a wide range of configurations. Figure 12 shows a mobile 4-DOF robotic manipulator developed by Mandru et. al. [72].

Biomimetic robots mimic the physiology or behaviour of animals or plants, such as locomotion, sensing, manipulation, or pattern recognition. By taking advantage of processes which have resulted from natural evolution, biomimetic designs present unique and efficient solutions to problems in robotics. Many biomimetic and anthropomorphic robots have been developed which use shape memory alloy actuators. Their silent operation, viscoelastic properties, and ability to generate high force and displacement through contraction make shape memory alloy wires and strips a good

analogue for muscle [84]. Shape memory alloy actuators have been used for underwater robotic systems which mimic the locomotion of aquatic animals such as fish, jellyfish, and manta rays. The actuators are integrated directly into the structure as in the case of the biomimetic jellyfish studied in [85] and manta ray studied in [86], or attached between articulated segments and fins as in the case of the biomimetic tuna robots studied in [87] and [88]. Robots have also been developed which mimic the motion of worms using shape memory alloy actuators. The Omegabot inchworm robot uses flexible segments which are rotated using shape memory alloy coil actuators in order to generate motion similar to an inchworm [89]. Similarly, an earthworm robot studied in [90] uses contraction and elongation actuated by a shape memory alloy spring to generate motion with the help of barbs that grip the surface. Another earthworm robot studied in [91] uses a series of segments composed of polyester braided tubes which contract under the action of shape memory alloy wires to generate a pulsating motion along the body. Some examples of anthropomorphic applications include the use of shape memory alloy wires for actuating artificial fingers [92], hands [93], and eyes [94]. Composite materials using embedded shape memory alloy actuators have also been developed which mimic muscle tissue such as the bio-inspired shape memory alloy composite actuator (BISMAC) [95] and the super-active shape memory alloy composite actuator (SASMAC) [96]. Artificial vasculated flesh has also been developed which allows shape memory alloy wire elements to be embedded in hollow channels within the material and actuated using hot and cold fluid which is pumped through the channels [98]. Figure 13 shows the Jellybot developed by Villaneuva et. al. [85].

Shape memory alloy actuators are also considered an excellent candidate for microelectromechanical systems (MEMS) due to the ability to directly integrate the shape memory alloy elements within the MEMS components [97]. Thin film shape memory alloy actuators are typically used and have been studied widely for MEMS applications

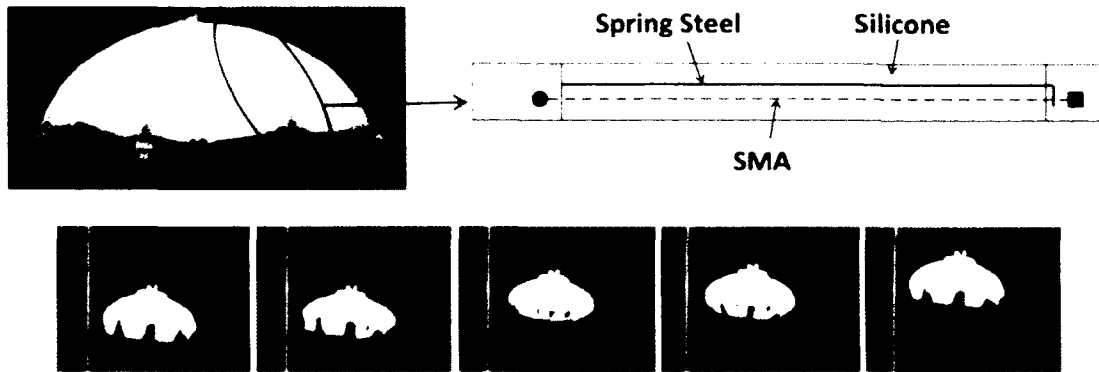


Figure 13: Biomimetic Jellybot design (top) and swimming cycle (bottom) [85]

[98] [99]. Fabrication may be accomplished through sputtering or laser-deposition of the material upon the substrate [100] [101], allowing fine control of the thickness and composition of the material. Some examples of MEMS applications include micro-grippers [102], micro-dampers [103], and micro-pumps [104].

1.3.4 Aerospace

The high energy density of shape memory alloy makes it an excellent choice for applications in aircraft and spacecraft systems, where mass and volume are critical design constraints [105]. Shape memory alloy actuators have been used to actuate systems in both fixed-wing aircraft and rotorcraft, either as a discrete actuator replacing conventional devices such as hydraulic, pneumatic, or electromagnetic actuators, or integrated as part of the structure which is being actuated. Flaps actuated by shape memory alloy wires have been studied for both fixed-wing aircraft [106] and rotorcraft [107], where the actuator wires are applied antagonistically to deflect the hinged flap in both directions. Rotor blades which are capable of varying the twist angle profile of the airfoil have also been studied which use shape memory alloy wires to provide torsional actuation [108] [109]. Shape memory alloy wires

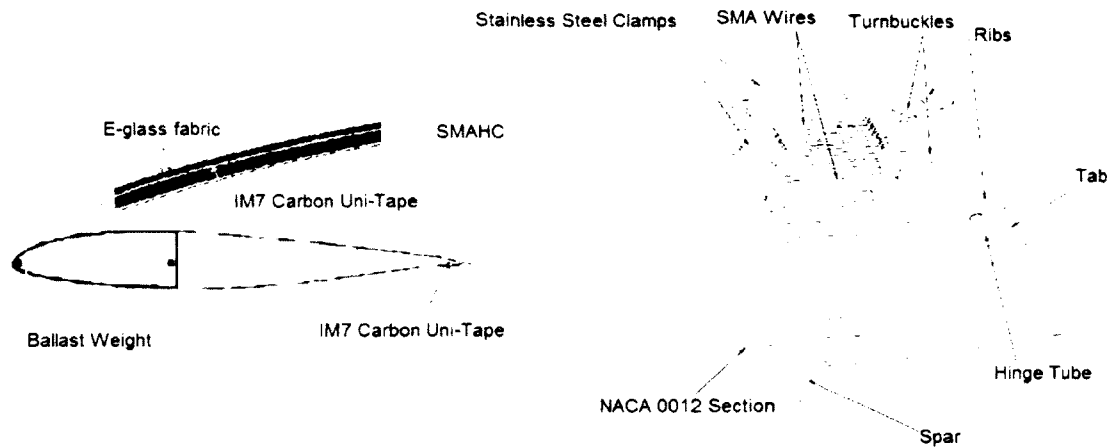


Figure 14: Hybrid SMA composite rotor blade [109] (left) and rotor blade tab actuated by SMA wires [107] (right).

have also been embedded within composite structures in order to provide actuation for variable area exhaust [110] and intake [111] structures. Similar composite structures actuated by shape memory alloy elements have also been studied for use in adaptive wing structures which change shape in order to accommodate varying flight conditions [112] [113]. Furthermore, shape memory alloy has been considered as reinforcement in aluminum structural members to reduce crack propagation [114]. Figure 14 shows an active hybrid SMA composite rotor blade developed by Park et. al. [109] and an active rotor blade tab actuated by SMA wires developed by Singh and Chopra [107].

Spacecraft systems employing shape memory alloy elements have also been investigated, including separation and release devices, actively controlled structures, dampers, and actuators [115]. Typical separation and release devices include pyrotechnic elements which explode in order to sever a connection between spacecraft or their appendages. By using a shape memory alloy element instead of pyrotechnics, the separation device may be operated with much lower shock imparted upon the vehicle, as well as eliminate the risk of shrapnel damage. Separation and release

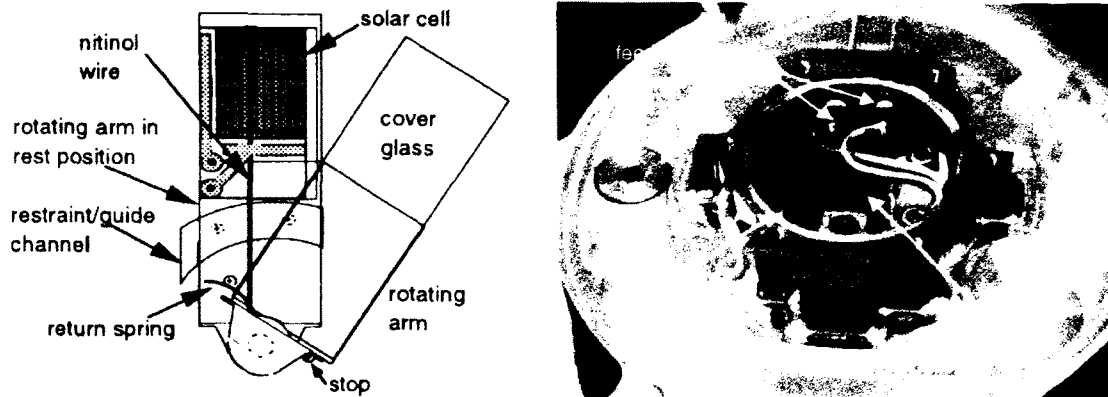


Figure 15: SMA actuators used on the Sojourner rover [124] (left) and Rosetta lander [125] (right).

devices using shape memory alloy elements have been studied and applied extensively [116] [117] [118], including products developed by TiNi Aerospace mentioned previously. Actuators for spacecraft systems have also been developed using shape memory elements instead of conventional electric motors [119] [120]. Appendages such as solar panels [121] [122] may be deployed using shape memory alloy actuators which generate rotational motion, while bending actuators may be used to unfold structures such as antennae or mirrors [123]. Planetary landers and rovers have also used shape memory alloy actuators for systems such as a dust wiper on the Pathfinder mission Sojourner rover [124] and a gas release mechanism on the Rosetta lander [125], both of which are shown in Figure 15.

Furthermore, shape memory alloy actuators have been studied for use in active shape control of structures [126] [127] [128] [129], and vibration damping [130] [131]. Passive shape memory alloy devices have also been used in spacecraft systems such as an automatic radiator panel which opens upon heating above a critical temperature [132]. Another interesting application is a Mars exploration hopper vehicle which uses a shape memory alloy element to contract and store energy within a spring [133]. The spring is then released periodically in order to propel the vehicle into the air and

achieve locomotion through hopping.

1.4 Design Considerations

Although there are many possible applications of shape memory alloy, most of these require similar considerations during design. The following sections briefly describe the major design considerations with focus on the use of Nitinol shape memory alloy in wire form (which is most common) for use as an actuator in a device or structure. Nevertheless, other applications which fall outside of this focus also share many of the same design considerations.

1.4.1 Stroke

Considering the application of shape memory alloy as an actuator, one of the key requirements for design is the amount of desired stroke (actuator displacement). There are two sources of strain within shape memory alloy: mechanical strain and recovery strain. Mechanical strain is due to applied stress and behaves according to Hooke's Law similar to conventional materials. The recovery strain is generated due to the phase transformation process, and is considered negative (compression) for the case where the material has been elongated during initial loading and detwinning of the martensite phase. Typical Nitinol alloys are capable of generating approximately 3-5% recovery strain. Figure 16 demonstrates the relationship between applied stress and available recovery strain as measured experimentally using the apparatus presented in chapter 3. As the applied stress is increased, the recovery strain also increases.

By choosing an appropriate total length of the shape memory alloy wire, the actuator stroke requirements can be met for a known stress or expected range of stress. Often, the wire will be chosen to produce greater stroke than required and

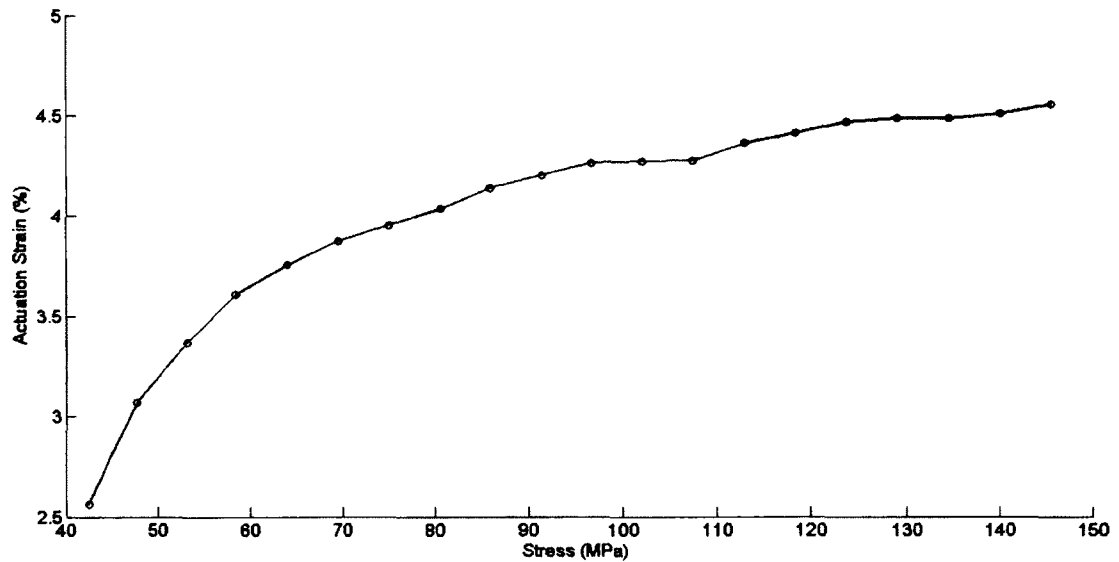


Figure 16: Actuation strain as a function of applied stress.

any additional displacement is constrained through mechanical stops or careful position control. Additionally, many applications of shape memory alloy employ simple machines such as pulleys or levers in order to gain mechanical advantage and produce increased stroke at the cost of increased wire tension (or lower output force).

1.4.2 Load

Nitinol alloys exhibit high strength due to the nickel-titanium composition. A conventional metal obeys Hooke's Law during elastic loading and subsequently undergoes plastic deformation when the applied stress surpasses the yield strength. The stress-strain behaviour of shape memory alloys is much more complex considering the phase transformation processes [134]. Starting in the martensite phase, the material initially undergoes elastic deformation until reaching a critical stress at which the detwinning process begins. This detwinning causes the large amount of apparently plastic strain which is later recovered through the shape memory effect. Further loading of the

detwinned martensite phase results in the typical behaviour of elastic deformation, yield, plastic deformation, and finally ultimate tensile failure.

The stress-strain behaviour of the austenite phase is also similar to a conventional material. However, the influence of applied stress upon the critical phase transformation temperatures must be considered (increasing the applied stress causes the transformation temperatures to increase). Therefore, if the material is kept at a constant temperature then it is possible that the applied stress causes the critical phase transformation temperature, M_s , to rise above the material temperature, inducing a phase transformation from austenite to martensite. When the applied stress is decreased to the point where the critical phase transformation temperature, A_s , is below the material temperature, the phase transformation from martensite to austenite occurs. The phenomenon of superelasticity is driven by this process, as described previously.

In order to ensure that the shape memory behaviour is repeatable and avoid degradation, the applied stress must never exceed the yield stress of the material. Furthermore, there are limitations upon the applied stress during cyclic operation in order to ensure that the impact of fatigue is eliminated or minimized.

Application of shape memory alloys as actuators requires careful consideration of the loading conditions. Since the shape memory effect causes a contraction, applied stress must be used to elongate the wire upon cooling. Most shape memory alloy actuators employ a bias load in order to return the wire to the elongated configuration. The bias load may be generated by a dead weight or spring integrated within the actuator itself, or supplied by external forces depending upon the application environment. The actuator may also use mechanical advantage from pulleys or levers in order to amplify or reduce the actual load on the shape memory alloy element, which also affects the total output stroke of the actuator mechanism.

1.4.3 Activation

Considering an SMA wire actuator under constant stress, activation of the wire will occur when the temperature is raised above the austenite start temperature until reaching the austenite finish temperature. The wire then returns to its original configuration as the temperature falls below the martensite start temperature until reaching the martensite finish temperature. Therefore, heating and cooling of the wire is required in order to activate the actuator.

The most common method for heating the wire is resistive heating using electrical current, with the surrounding air providing passive cooling through conduction and convection. However, it is also possible to provide heating using a separate heating device such as a resistive heating patch, as well as active cooling using a thermoelectric Peltier device. As an example of a more elaborate method, Mascaro and Asada immersed the SMA wire in a fluid which could be exchanged between hot and cold reservoirs in order to provide heating and cooling [135].

Since the actuation speed depends upon the rate of temperature change, faster actuation may be accomplished by applying more heat. However, without active cooling, the actuator will typically return much more slowly, limiting its effective operation frequency. Also, if the actuator is used in a vacuum environment, cooling will only be provided by radiation heat transfer to the surroundings and conduction through the boundary constraints. Therefore, the ambient conditions of the surrounding environment are an important consideration for SMA actuator selection and design.

1.4.4 Boundary Conditions

Integration of an SMA wire actuator within a device is typically much simpler than integration of an electric motor or pneumatic actuator. However, there are some

special considerations that must be made. If electrical resistive heating is used, the SMA wire must be electrically insulated from the device in order to ensure that no short circuit occurs due to undesired contact between the wire and the system. Therefore, clamping of the ends of the wire must provide an electrically conductive connection for heating, but an insulated connection for structural support.

Electrical connections must be provided at both ends of the wire in order to complete the circuit, requiring lead wires that extend from the power supply to both ends of the actuator. However, it is possible to loop the SMA wire through a pulley at the end of the actuator such that both ends of the wire are connected at the same side of the actuator, simplifying the lead wire connections.

In addition to electrical insulation of the connections, it may also be desirable to provide thermal insulation in order to reduce heat transfer from the wire to the device. If the SMA wire is not thermally isolated from the device, the heat loss must be compensated by increasing input power, therefore reducing the efficiency of the actuator.

1.4.5 Fatigue

There are two forms of fatigue experienced by Nitinol: mechanical fatigue and shape memory fatigue. Like other metals, mechanical fatigue is attributed to the formation of dislocations and propagation of cracks through repeated mechanical loading cycles. Shape memory fatigue occurs due to both cyclic mechanical and thermal loading, and results in the degradation of shape memory properties of the alloy. The most prominent effect of shape memory fatigue is the reduction in recoverable strain and accumulation of permanent strain.

The formation of defects during transformation between the martensite and austenite phases of the material is the root cause of shape memory fatigue. Under superelastic conditions, where a constant temperature is maintained and the material

is activated by the cyclic application and removal of stress, shape memory fatigue causes a decrease in the critical transformation stress and accumulation of permanent strain. Due to the dependency between critical transformation temperatures and applied stress, the decrease in the critical transformation stress is actually the result of an increase in the critical martensite start transformation temperature. Similarly, thermal cycling with no applied stress results in shifts in the phase transformation temperatures, which stabilize after many cycles. During thermomechanical cycling of the material under typical actuator conditions (where the material is loaded under constant stress and cyclically activated), fatigue manifests as a decrease in the recoverable strain and the accumulation of permanent strain. Therefore, a shape memory alloy actuator wire subjected to fatigue suffers a loss of actuation stroke due to the decrease in recoverable strain, and retains a small permanent strain after actuation.

Fatigue in Nitinol is an important consideration for applications that demand cyclic actuation of the material, especially if precise position control or repeatability is required. However, the effects of shape memory fatigue must be taken into account regardless of the application due to large initial shifts in the shape memory properties during the first activation cycles after production. In practice, a shape memory alloy element is ‘trained’ by typically activating it through approximately 30 cycles, resulting in stabilization of the shape memory properties. After this training process is complete, the actuator properties are considered stabilized. The subsequent continuation of shape memory fatigue through thermomechanical cycling is then considered separately.

1.5 Electrical Resistance

Research into the electrical properties of Nitinol shape memory alloy has revealed remarkable relationships between the material’s electrical resistivity, temperature, and

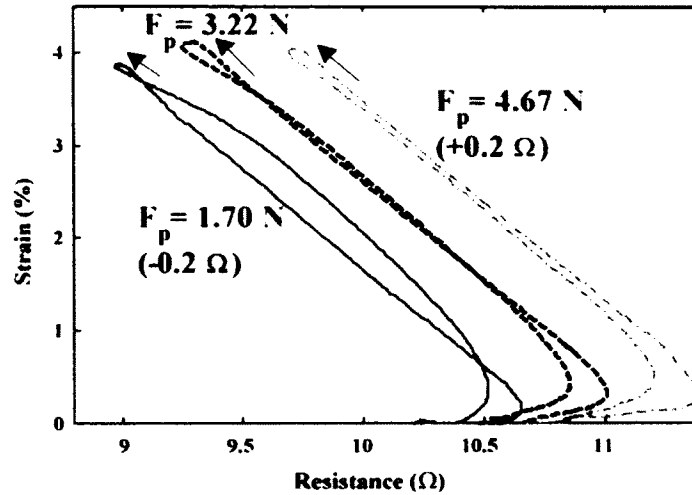


Figure 17: Strain-resistance curves of Nitinol at various stress levels [136].

mechanical stress and strain. Each phase of the shape memory alloy (martensite, austenite, and R-phase) possesses a different electrical resistivity, thus phase transformations induced by changes in temperature or stress cause the overall electrical resistivity of the material to change. The change in electrical resistance may then be measured in order to estimate the temperature or strain of the shape memory alloy element, assuming the applied mechanical stress is known or measured. Therefore, in addition to acting as an actuator, shape memory alloy may also be used as a sensor and has subsequently been labeled a ‘self-sensing’ actuator. Figure 17 shows the relationship between strain and electrical resistance in a Nitinol alloy at various levels of applied stress.

Many applications of electrical resistance feedback in shape memory alloy elements have been studied for estimating strain or temperature. Overheating can occur if the actuator temperature is unnecessarily raised higher than the austenite finish phase transformation temperature, A_f . Reducing the risk of overheating is possible by estimating the actuator displacement through resistance feedback, allowing faster activation speeds and improving the material’s fatigue life. The resistance of an

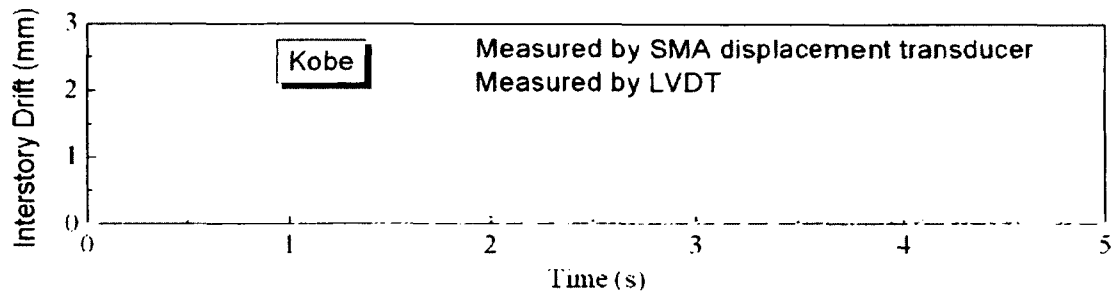


Figure 18: Earthquake monitoring using an SMA transducer [142].

actuator decreases during activation and may be compared to a threshold value to determine if the actuator has contracted to a corresponding position [137] [138] [139]. Continued heating after complete phase transformation causes the electrical resistance to increase, making it possible to infer full contraction based upon the rate of change as well [140]. Similarly, electrical resistance feedback may also be used to maintain the actuator's temperature at the austenite start phase transformation temperature, A_s , in order to prime the actuator for faster response under variable ambient conditions [141]. Electrical resistance feedback has also been used to estimate strain in structures with integrated shape memory alloy elements. Vibrations due to earthquakes may be detected and passively damped using shape memory alloy components within civil structures. The resistance-strain relationship of a shape memory alloy displacement transducer has been modeled using a linear curve in order to measure interstory drift in structures [142], as shown in Figure 18. Furthermore, shape memory alloy wires embedded within composite structures have been used to sense and estimate strain [143] as well as act as self-sensing actuators to mitigate structural damage [144]. The effect of ambient temperature is an important consideration in these passive applications of electrical resistance feedback. Position control of shape memory alloy actuators using electrical resistance feedback has also been investigated and will be discussed in detail in the next chapter.

Modeling of the relationships between electrical resistivity, stress, strain, and temperature has been undertaken using numerous approaches with varying complexity. The established relationships between electrical resistance, resistivity, and temperature are often employed along with a model of the phase transformation and a simple mixture rule. Fractions of the austenite, martensite, and rhombohedral phases may be modeled using phase transformation functions that are dependent upon temperature and stress. The resistivities of the three phases are determined as a function of temperature and then combined using a simple mixture rule to determine the overall resistivity of the material. Strain may be computed as a function of the phase fractions, including both an elastic component from applied stress as well as the actuation component due to phase transformation. The electrical resistance of the material is then determined from the resistivity and strain, where the change in cross-sectional area due to transverse strain may also be considered. This approach to modeling the electrical resistance behaviour of shape memory alloy has been studied with different models of the phase transformation process, such as the Liang & Rogers model [145], Brinson model [146], and numerical or statistical models [139] [147] [148] [149]. Figure 19 shows the results of modeling the electrical resistance using the Liang & Rogers model.

Simple models of the relationship between electrical resistance and strain have also been developed but are often suitable only under certain conditions, such as a particular load, static ambient temperature, or confined range of motion. The application of shape memory alloy as a strain sensor allows the resistance-strain relationship to be modeled linearly without hysteresis since the material remains in a single phase [144] [143] [142]. However, these models must be calibrated according to the applied load or stiffness and do not capture the hysteresis effects which occur during phase transformation. Linear relationships have been studied for use in active control of shape memory alloy actuators, but are only applicable under a

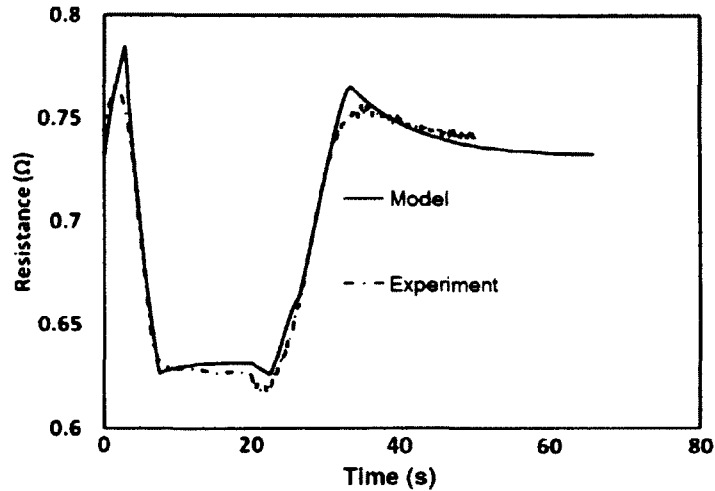


Figure 19: Results of modeling the electrical resistance of Nitinol [145].

particular load and depend upon the absence of R-phase during phase transformation [150] [151] [152] [153]. Hysteresis effects due to the presence of R-phase have been compensated using various techniques, most of which involve the use of two functions representing heating and cooling curves [154] [136] [155] [156]. However, many studies rely upon the absence of R-phase during transformation or the use of Ni-Ti-Cu alloys, which exhibit negligible hysteresis effects compared to Ni-Ti alloys [157] [158]. Artificial neural networks have been used to model the resistance-strain relationship in detail, including hysteresis effects as well as minor loops due to incomplete actuation [159] [160] [161].

1.6 Research Summary

The research presented in this thesis focused on the development of a predictive engineering model of the resistance-stress-strain relationship of Nitinol shape memory alloy for application in actuator position control. Typical position control algorithms depend upon feedback of the actual position using sensors. The addition of sensors

has a significant impact on the mass and volume of the system, especially in robotics and aerospace applications. Conversely, measurement of the electrical resistance of a shape memory actuator is relatively simple since resistive heating is typically used and the voltage and current applied to the actuator may be easily determined. Measurement of the applied stress is possible using load cells or strain gages, which may be integrated within the actuator itself or as part of the parent system. In some cases the applied stress may be known or predicted based on the application conditions or stiffness of the actuated structure, negating the need for a load sensor.

Therefore, the model presented in this research is readily applicable to actuators with varying load conditions. Although temperature is fundamentally the most important parameter when analyzing the behaviour of shape memory alloy, it is not included as a parameter within the model. Electrical resistance acts sufficiently as an indicator of the phase composition which would normally be determined as a function of temperature.

The model which was developed is superior to previous methods since it includes the effects of R-phase, accounts for the influence of applied stress, and is normalized for actuator wire of any length and diameter. Although some previous research has investigated solutions for each of these problems individually, this thesis presents a model which encompasses all three. Therefore, this research is a significant contribution to the study and development of Nitinol shape memory alloy actuators.

Experimental qualitative and quantitative characterization of the resistance-stress-strain behaviour of shape memory alloy actuator wire is described in the first section. This was carried out in order to quantify certain parameters such as the total transformation strain as well as examine and study trends such as the influence of applied stress. The overall resistance-stress-strain behaviour was then captured within the model, which is presented in the second section. Normalization of the model was also carried out in order to accommodate actuator wire of variable length

and diameter. The third section presents a verification of the models applied within a simple position control system using electrical resistance feedback. Position control is successfully demonstrated under varying load conditions with mean errors of approximately 3% of the total actuator stroke.

Characterization, modeling, and control was investigated using two Nitinol alloys: a Ni-Ti alloy commercially named Flexinol and manufactured by Dynalloy and a Ni-Ti-Cu alloy designated NT-H and manufactured by Furukawa Electric. Only the Flexinol alloy exhibited significant hysteresis behaviour due to the presence of R-phase. Therefore, separate models were developed for each of the two alloys. The Furukawa alloy was modeled using a simple polynomial model of the strain-resistance relationship which follows a characteristic curve. The Flexinol alloy required a more complex relationship using a hybrid model with linear asymptotes for heating and cooling, and an exponential function to capture the hysteresis behaviour. The influence of stress was included within the appropriate coefficients of each model using linear and polynomial functions. The performance of the models developed for each alloy demonstrated that they are successful in capturing their respective resistance-stress-strain behaviour in a simple position control application.

Some of the potential applications which may benefit from this research are also discussed, as well as the correlations between the models and current theory, and possible improvements for future consideration.

Chapter 2

Literature Review

Position control of shape memory alloy actuators is a widely studied topic which has received much attention in the past few decades. Similar to other actuation systems, position control is most often achieved using position feedback from sensors such as encoders, but has also been studied using open-loop control and model-based control using feedback of parameters such as temperature. Various control algorithms have been studied for feedback and model-based control, including PID control, adaptive control, and robust control methods. Furthermore, both feedback control and model-based control have been studied in combination, with sensor feedback of position as well as temperature or stress.

Model-based control algorithms typically make use of previously established models of shape memory alloy behaviour in terms of applied stress, strain, and temperature, such as the Liang & Rogers model or Brinson model. However, modeling of the relationship between electrical resistance and strain has also been successfully applied in model-based position control using electrical resistance feedback. The influence of applied stress and the presence of R-phase are the primary challenges in developing comprehensive models for use in shape memory alloy actuators.

The state-of-the-art of position control of shape memory alloy actuators using electrical resistance feedback is presented in this chapter. Control algorithms which

make use of position feedback are reviewed, along with the currently established models of shape memory alloy behaviour.

2.1 Modeling

The behaviour of shape memory alloy has typically been modeled in terms of the applied stress, strain, and temperature. The phase transformations which drive the shape memory phenomenon are modeled by a set of equations which most often predict the fractions of each phase as a function of stress and temperature. Strain due to the shape memory effect is then computed as a function of the phase fractions, and included in an overall constitutive equation. Some models apply a physics-based or energy-based method in order to determine the phase composition. However, the most widely used approaches are based upon the Liang & Rogers model [162] and the Brinson model [163]. Furthermore, typical models assume a one-dimensional approach since most applications use shape memory alloy in wire form.

Both the Liang & Rogers model and Brinson model have similar constitutive equations, which are presented in differential form where the subscript 0 refers to the initial condition. Stress, σ , is a function of the strain, ε , temperature, T , and martensite fraction, ξ . Equation 2.1 is used within the Liang & Rogers model and Brinson model.

$$\sigma - \sigma_0 = E(\xi)(\varepsilon - \varepsilon_0) + \Theta(T - T_0) + \Omega(\xi)(\xi - \xi_0) \quad (2.1)$$

Both models include the typical stress-strain relationship of Hooke's law, as well as the influence of temperature-induced stress-strain through the parameter Θ , which may be considered negligible. The third term adds the strain contribution due to the shape memory effect, ε_L , which is a function of the martensite fraction as shown

in equation 2.2. Simple mixing rules are typically used to determine the overall Young's modulus of elasticity as a function of the moduli of each phase as described by equation 2.3, where the subscripts A and M refer to the austenite and martensite phases respectively.

$$\Omega(\xi) = -E(\xi)\varepsilon_L \quad (2.2)$$

$$E(\xi) = E_M\xi + E_A(1 - \xi) \quad (2.3)$$

While Liang & Rogers consider only a single martensite fraction, Brinson distinguished between the twinned and detwinned components of martensite, ξ_t and ξ_s respectively, in order to capture the stress-strain-temperature behaviour in greater detail. The two components are then summed to determine the total martensite fraction as in equation 2.4.

$$\xi = \xi_t + \xi_s \quad (2.4)$$

Various phase transformation equations have been explored, including exponential relationships proposed by Tanaka, shown in equations 2.5 and 2.6, and cosine relationships used by Liang & Rogers and Brinson, shown in equations 2.7 and 2.8. Each pair of equations represents the phase transformation from martensite-to-austenite and austenite-to-martensite, respectively, as indicated by the subscripts. The parameters a_A , a_M , b_A , and b_M in the Tanaka model are functions of the applied stress.

$$\xi_{M \rightarrow A} = e^{(a_A(T - A_s) + b_A\sigma)} \quad (2.5)$$

$$\xi_{A \rightarrow M} = e^{(a_M(T - M_f) + b_M\sigma)} \quad (2.6)$$

$$\xi_{M \rightarrow A} = \frac{\xi_0}{2} \left(\cos \left(\frac{\pi}{A_f - A_s} \left(T + \frac{\sigma}{C_A} - A_s \right) \right) \right) \quad (2.7)$$

$$\xi_{A \rightarrow M} = \frac{1 - \xi_0}{2} \left(\cos \left(\frac{\pi}{M_s - M_f} \left(T + \frac{\sigma}{C_M} - M_f \right) \right) \right) \quad (2.8)$$

Furthermore, phase transformation occurs only within specific ranges of temperature and applied stress, as described by equations 2.9 and 2.10. Equation 2.9 describes the conditions required for martensite-to-austenite transformation, where A_s and A_f are the stress-free start and finish phase transformation temperatures. Equation 2.10 describes the conditions required for austenite-to-martensite transformation, where M_s and M_f are the start and finish phase transformation temperatures under stress-free conditions.

$$A_s + \frac{\sigma}{C_A} \leq T \leq A_f + \frac{\sigma}{C_A} \quad (2.9)$$

$$M_f + \frac{\sigma}{C_M} \leq T \leq M_s + \frac{\sigma}{C_M} \quad (2.10)$$

The influence of stress may be considered as causing a shift in the phase transformation temperatures, which may be modeled linearly using the coefficients C_A and C_M as seen in the previous equations.

Similar thermodynamic models have also been developed by Ikuta [164], Lagoudas [165], Luo [166], and Elahinia [167]. Numerical modeling of shape memory alloy components has also been studied using these models in finite element analysis [168] [169] [170]. Furthermore, heat transfer analysis is often modeled in order to predict temperature based upon input power as well as account for losses due to convection and conduction.

Modeling of the electrical resistance may be accomplished by considering the conventional relationship between electrical resistance, R , resistivity, ρ , length, L , and cross-sectional area, A , described by equation 2.11 as well as the temperature dependence of resistivity described by equation 2.12. The resistivity is modeled as a linear function of temperature, where ρ_0 is the value at a reference temperature, T_0 , and α is the slope of the resistivity-temperature curve..

$$R = \frac{\rho L}{A} \quad (2.11)$$

$$\rho = \rho_0 (1 + \alpha (T - T_0)) \quad (2.12)$$

In addition, the change in length and area due to strain during phase transformation and elastic loading may also be included within equation 2.11. The contraction in cross-sectional area during elongation of the wire may be considered by assuming either constant volume, as in equation 2.13, or transverse strain due to the Poisson effect, as in equation 2.14. The initial length and area are denoted by the subscript 0, and ν is the Poisson ratio of the material.

$$R = \frac{\rho L_0}{A_0} (1 + 2\varepsilon) \quad (2.13)$$

$$R = \frac{\rho L_0}{A_0} (1 + (1 + 2\nu) \varepsilon) \quad (2.14)$$

Considering the phase composition of the material, the overall resistivity is computed from the individual resistivities of each phase using a simple mixture rule as shown in equation 2.15.

$$\rho = \rho_M \xi + \rho_A (1 - \xi) \quad (2.15)$$

Previously described models of the phase transformation relationships are typically used to determine the martensite fraction and strain given the applied stress and temperature. The electrical resistivity may then be determined from the temperature and martensite fraction using equations 2.12 and 2.15, and the electrical resistance may be determined from the resistivity and strain using equation 2.13 or 2.14. However, this approach requires the use of temperature feedback in order to provide an accurate estimation of the electrical resistance.

Various simplified models have been developed which capture the relationship between strain and electrical resistance for use in shape memory alloy sensors and actuators. Although more detailed descriptions will be given in subsequent sections of this chapter, many models employ a normalized resistance parameter defined by

equation 2.16.

$$\lambda = \frac{R - R_{min}}{R_{max} - R_{min}} \quad (2.16)$$

The measured resistance is compared to the minimum and maximum resistance values, R_{min} and R_{max} , respectively, in order to determine the normalized resistance, λ . The relationship between resistance and strain is then often modeled as a function of λ instead of R . It may even be possible to assume a direct correlation between normalized resistance and martensite fraction, as shown in equation 2.17.

$$\lambda \approx \xi \quad (2.17)$$

However, this correlation is only possible if there is an absence of R-phase during transformation, as seen in Ni-Ti-Cu alloys as well as Ni-Ti alloys under high stress conditions.

2.2 Position-Feedback Control

The application of shape memory alloy as an actuator has been well established, but the development of control algorithms for position control has continued to evolve with increasing complexity and greater use of combined feedback and feed-forward methods. Basic approaches to controlling shape memory alloy actuators involve the use of on-off control and are often restricted to either zero or full contraction of the actuator. Open loop systems have also been investigated, with varying levels of voltage or current used to generate varying steady-state displacement of the actuator. The highly non-linear and hysteretic behaviour of the material makes it difficult to build control algorithms using conventional approaches which are typically developed for linear systems. However, classical PID control algorithms have been applied with

satisfactory results. In order to improve accuracy and response time, more sophisticated control algorithms have also been investigated such as robust control and neural network models.

The control algorithms presented in this section all make use of position feedback instead of electrical resistance feedback. However, the use of electrical resistance feedback in predicting position makes it possible to use these control methods without direct position feedback. Some algorithms employ thermodynamic models which may be redundant when using resistance feedback, but other approaches such as optimal, robust, and PID control may simply replace position feedback with the output of a resistance based position model.

2.2.1 PID Controllers

The majority of position control algorithms for shape memory alloy actuators make use of a PID controller either alone or as part of a more sophisticated control architecture. The PID control law is composed of three terms: proportional control, derivative control, and integral control. Proportional control applies an input signal proportional to the feedback error with gain K_P , derivative control applies an input signal proportional to the derivative of the error with gain K_D , and integral control applies an input signal proportional to the integral of the error with gain K_I . Equation 2.18 defines the total input signal, u , for a PID controller with error signal e . The error signal is defined as the difference between the actual position, x , and desired position, x_d , shown in equation 2.19.

$$u = K_P e + K_D \dot{e} + K_I \int_0^t e dt \quad (2.18)$$

$$e = x - x_d \quad (2.19)$$

The proportional and derivative terms serve to provide the control system with stiffness and damping, respectively, while the integral term allows the system to compensate for steady-state error. Control laws using combinations of P, PD, PI, or PID terms have been studied position control of shape memory alloy actuators. Madill and Wang applied the Ikuta model to a shape memory alloy actuator with constant bias load, then investigated P and PI control laws and showed that the system was stable for all $K_P > 0$ using L2 stability criteria [171]. Barooah and Rey analyzed P, PI, and PID control as well as an adaptive control law developed by Dickinson and Wen, demonstrating successful position control of a variable-area jet engine nozzle as shown in [172]. Shameli et. al. simulated the use of PID control as well as PID-P3 control, in which a control term proportional to the error signal cubed was also included in order to improve performance and efficiency [173]. Singh et. al. applied PID control to the angular position control of a rotor blade trailing edge tab, as well as open loop control using the Brinson model to predict strain [174] as shown in Figure 20. The use of PID control for force control of a shape memory alloy actuator has also been studied by Teh and Featherstone [175]. Furthermore, PID control laws have been used in combination with feed-forward algorithms such as thermodynamic models, neural networks, and linearization methods.

2.2.2 Linearization

Although the behaviour of shape memory alloy actuators is highly non-linear, methods of linearization have been studied in order to improve feedback position control algorithms. Arai et. al. developed a continuous mathematical model of the relationship between strain and temperature including the influence of stress, then applied the model in a feedback linearization approach for position control of a two-link micro-manipulator [176]. Benzaoui et. al. modeled the thermodynamic behaviour of shape

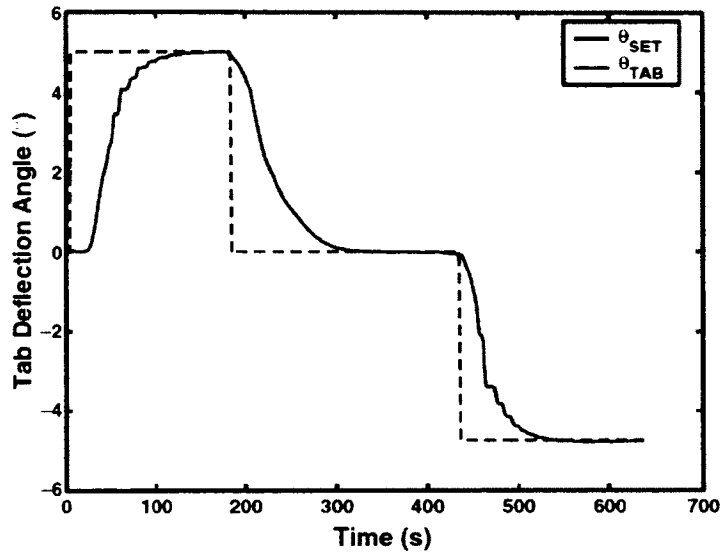


Figure 20: Results of PID control investigated by Singh et. al. [174].

memory alloy using Helmholtz free energy and applied the model to position control using input-output linearization based on Lie algebra [177]. Both position and force control of an actuator were successfully demonstrated using this linearization approach. The use of a linear quadratic regulator and extended Kalman filter has been investigated by Lee and Marvoidis for application in optimal position control of a shape memory alloy actuator [178], as shown in Figure 21. Jayender et. al. also applied a linear quadratic regulator to provide optimal control through gain scheduling of a PI control law [179].

2.2.3 Optimal & Robust Control

Various methods of improving the performance and efficiency of shape memory alloy actuators have been studied for position control using optimal and robust control laws. Variable structure control is a robust control method which consists of different control schemes or gain settings that are chosen depending upon the actuator's position and velocity states. This method has been applied by Grant and Hayward [180]

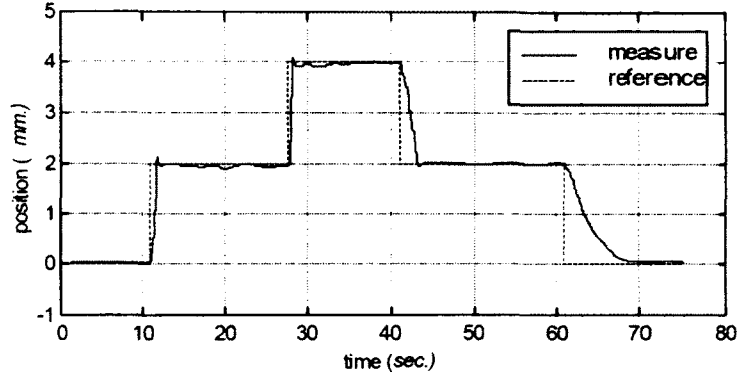


Figure 21: Results of position control using LQR linearized control law investigated by Lee and Marvoidis [178].

as well as Ashrafiuon et. al. [181] in order to maintain stable position control as well as maximize performance while avoiding overshoot. Song investigated the use of sliding mode control in order to provide a feed-forward control term in addition to a PD control law, improving robustness and decreasing overshoot [182]. Lee and Lee employed a non-linear time delay control law within a PID control system in order to minimize the effects of hysteresis such as limit cycle problems and input saturation [183], as shown in Figure 22. The resulting control law is compared to conventional PID control, PID control tuned using the Ziegler-Nichols method, and basic on-off relay control. Both H_2 and H_∞ robust control algorithms have been investigated by Lee and Mavroidis [178] and Jayender et. al. [179], respectively, and show improved performance in the presence of perturbations.

2.2.4 Model-Based Control

Improvements in controller performance have also been achieved using model-based position feedback control. Models of the thermomechanical behaviour of shape memory alloy are typically used to predict the required voltage or current input in order to achieve a desired position. This signal is used as a feed-forward control term and

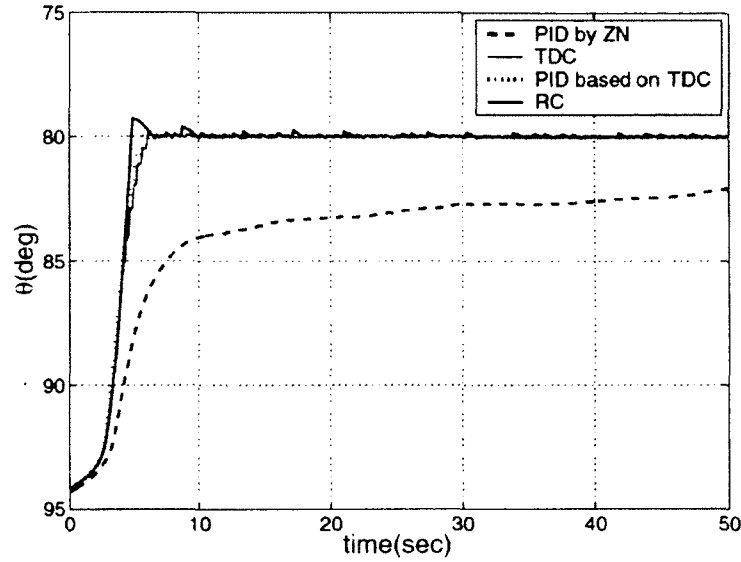


Figure 22: Comparison of position control by Lee and Lee using PID control with Ziegler-Nichols tuning, time delay control, PID control based on time delay control, and relay control [183].

combined with position feedback control. Elahinia et. al. studied the use of the Liang & Rogers model and thermodynamic model in a backstepping feedback control algorithm which computed required voltage input using position feedback [184]. Ashrafiun et. al. also used the Liang & Rogers model within the variable structure control algorithm previously mentioned [181]. Majima et. al. achieved actuator position control using the Brinson constitutive model along with a Preisach hysteresis model to describe the phase transformation process [185], as shown in Figure 23. The Preisach model parameters were identified for the actuator in order to predict the required voltage to reach a desired position, which was superimposed with a PID feedback control law. Wijst et. al. applied a simplified constitutive model including heat transfer to predict required input power, which was used in combination with a PI feedback control law in order to achieve position control of an actuator [186]. Dutta et. al. modeled the phase transformation processes using a Duhem differential hysteresis model, which was then used to provide an inverse compensation term along

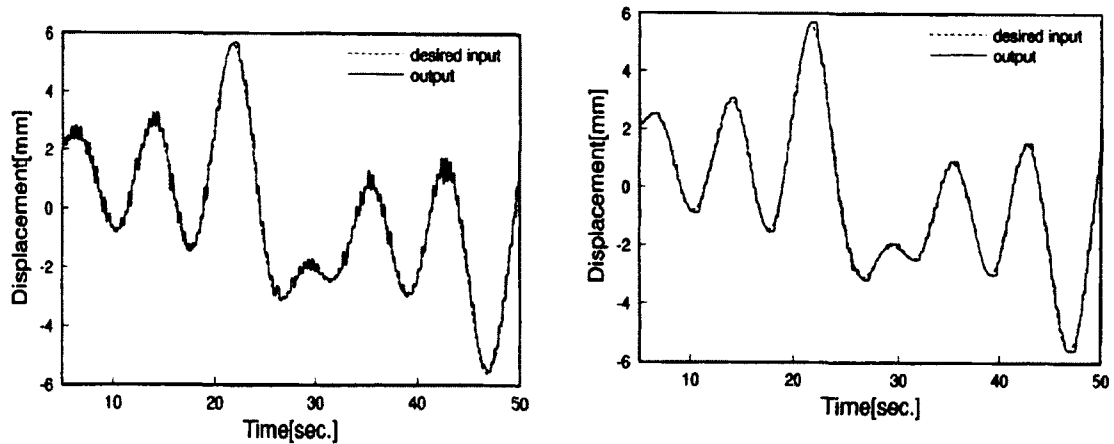


Figure 23: Comparison of PID control (left) and model based control (right) studied by Majima et. al. [185].

with PD feedback control [187]. Ahn and Kha studied the use of a fuzzy Preisach model to capture the hysteresis behaviour and predict the required input current for actuator position control [188]. Both forward and inverse fuzzy Preisach models were structured within an internal model control law which was driven by position feedback. Dnmez et. al. investigated the use of a simple linear model based upon the relationship between applied current and strain. The current-strain model was then inverted in order to predict the required input current, which was combined with a PI feedback control law [189].

2.2.5 Learning-Based Control

Modeling the behaviour of shape memory alloy actuators using learning algorithms has been studied and applied to position control as well. The non-linear and hysteretic behaviour of the material may be captured using methods such as artificial neural networks or fuzzy logic. Models based on these methods are then used to generate feed-forward control terms which may be combined with feedback control to improve actuator performance. Artificial neural networks are the most popular method for

modeling the hysteresis behaviour of shape memory alloy actuators. Song et. al. have investigated both forward and inverse neural network models of the relationship between input voltage and output strain of an actuator [190] as shown in Figure 24. The inverse neural network model was then applied in feed-forward position control with and without PD feedback control [191]. Stevens and Buckner used a similar inverse neural network model of the relationship between input voltage and position to control a 2-DOF miniature surgical robot driven by shape memory alloy actuators [192]. Dönmez modeled the relationship between strain and applied current using a neural network model, which was then used for feed-forward position control of an actuator [189]. Fuzzy logic has also been used to model the hysteresis behaviour of shape memory alloy actuators. Kumagai et. al. developed an actuator control algorithm using fuzzy logic to predict the required input voltage for feed-forward control in combination with PD feedback control [193]. Maffiodo et. al. also studied the use of fuzzy logic for combined feed-forward and PD feedback control [194]. Tchoupo and Leang applied an iterative learning control algorithm to train and stabilize a Preisach model which was used to provide feed-forward control of an actuator along with a proportional feedback control law [195].

2.3 Resistance-Feedback Control

The focus of the research presented in this thesis is position control of shape memory alloy actuators using feedback of electrical resistance and applied stress. As previously mentioned, this approach allows position control to be achieved without the need for position feedback using cumbersome sensors. Position control using resistance feedback has been studied using a variety of models, most of which are based upon linear or polynomial curve fits. The hysteresis effect within the resistance-strain relationship is typically much smaller than within the temperature-strain relationship. However,

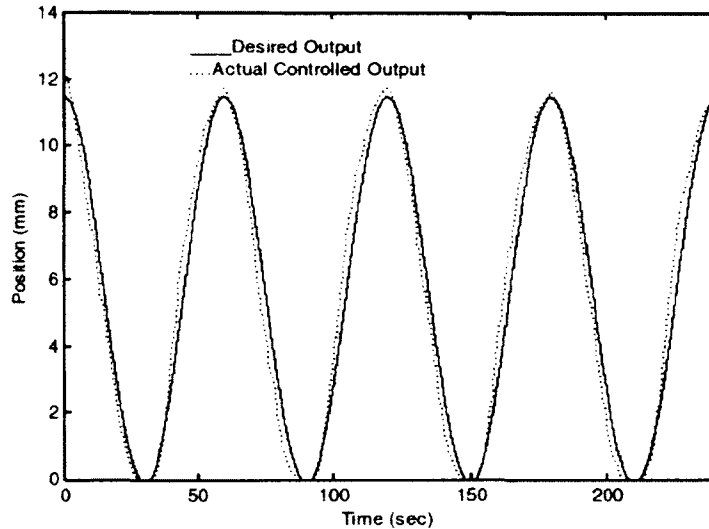


Figure 24: Performance of the neural network based controller developed by Song et. al. [190].

the presence of R-phase during phase transformation causes a significant hysteresis within the resistance-strain relationship, which tends to shrink with increasing applied stress. Therefore, the impact of R-phase is often avoided either by applying a high enough load or using a Ni-Ti-Cu alloy, which does not experience the presence of R-phase during phase transformation [151]. Figure 25 shows the hysteresis gap as a function of the quantity of copper addition. Some models include hysteresis effects by using both heating and cooling paths, or a differential hysteresis model. Furthermore, artificial neural networks have also been used to capture the non-linear hysteresis due to R-phase within the resistance-strain relationship. Most applications of resistance feedback position control employ a position control algorithm such as those previously described, with the majority using a PID control law. Instead of position feedback using a position sensor, the position is predicted using a model based on electrical resistance.

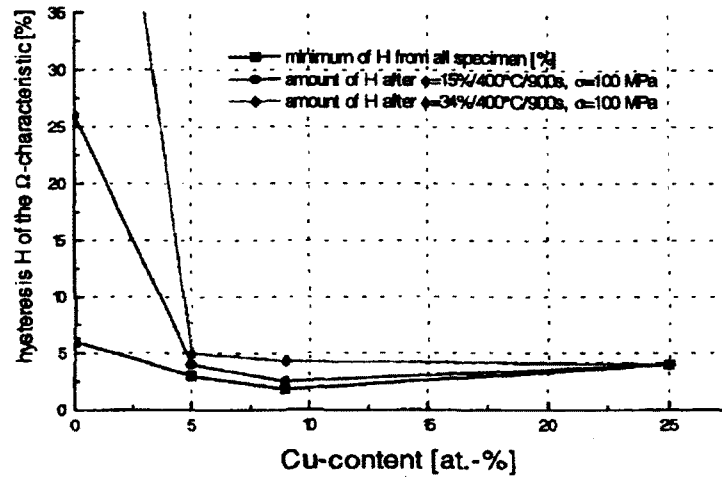


Figure 25: Hysteresis gap as for Ni-Ti alloys with various quantities of copper addition [151].

2.3.1 Linear Models

The relationship between electrical resistance and strain in a shape memory alloy actuator may be approximated using a linear model as described previously. However, linear approximations assume no R-phase is present during phase transformation, and are typically only applicable for a single bias load or spring stiffness. Ikuta et. al. demonstrated antagonistic shape memory alloy actuator control of an active endoscope using electrical resistance feedback. The linear normalized model of electrical resistance was applied using equations 2.16 and 2.17, and the predicted position was used for feedback in a PID control law for each actuator [150]. Yang and Gu used a similar approach for controlling a single shape memory alloy actuator under the same assumptions of a linear model, but controlled the electrical resistance instead of strain through a P control law [152]. Neugebauer et. al. developed a control algorithm with feedback linearization using an energy based thermomechanical model and a linear resistance-strain relationship for position feedback of a Ni-Ti-Cu alloy actuator [157],

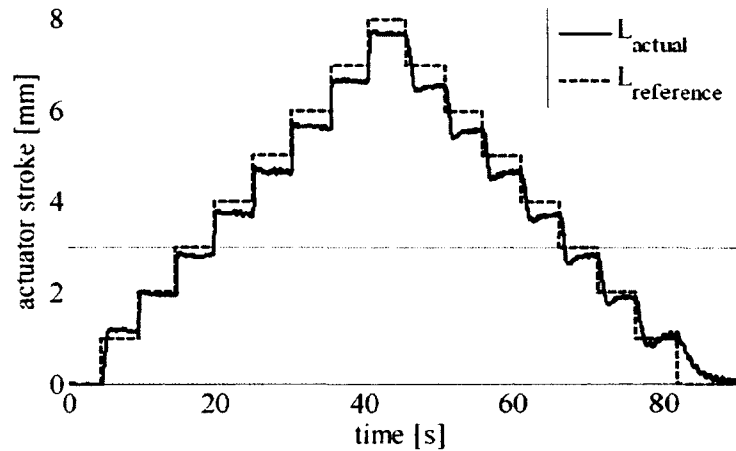


Figure 26: Control performance using the linear model studied by Neugebauer et. al. [157].

as shown in Figure 26. Urata et. al. applied a linear model of the resistance-stress-strain relationship for antagonistic position and force control of shape memory alloy actuators [153]. Hysteresis effects were avoided by restricting the range of motion of the actuators to a region in which the linear model applied.

2.3.2 Polynomial Models

An improvement upon linear models is the use of polynomial functions to model the resistance-strain behaviour of shape memory alloy actuators. Many polynomial models have been used in resistance-feedback control algorithms, but most do not model hysteresis effects and assume no R-phase is present. Arai et. al. used a fourth-order polynomial to model the relationship between electrical resistance and actuator strain [196]. Position control was then accomplished using a PID controller which maintained a desired electrical resistance according to the model. Lan and Fan modeled the resistance-strain relationship of an actuator using sixth-order polynomials for both heating and cooling paths [136], as shown in Figure 27. An appropriate load was chosen to minimize hysteresis so that the heating and cooling paths could be

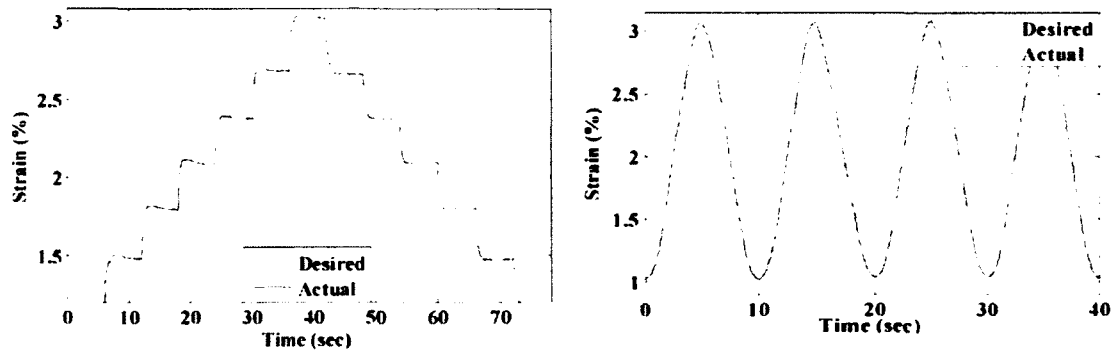


Figure 27: Control performance using the polynomial model studied by Lan and Fan [136].

averaged, resulting in a single polynomial which was used to predict strain in a fuzzy-tuned PID control law [197]. Shi et. al. used fourth-order polynomials to model the resistance-strain relationship during heating and cooling, and studied position control using a PID control law with feedback of the predicted strain [156]. Zhang and Yin developed third-order polynomials of the resistance-length heating and cooling behaviour from constitutive relationships of resistivity, temperature, stress, and strain, as well as thermodynamic and stiffness models [158]. Similar to previous research, the heating and cooling paths were averaged at a high enough load condition to avoid the presence of R-phase, and used to predict strain for a PID feedback control law. Pons et. al. model the resistance-strain relationship of a shape memory alloy actuator using a third-order polynomial and apply the model to a PI feedback control law [198]. Again, the applied load is chosen to minimize the hysteresis effects and allow a single curve to be used.

2.3.3 Hysteresis Compensation

As previously described, most applications of resistance feedback control avoid the effects of hysteresis due to the presence of R-phase either through application of sufficient stress, or selection of an alloy with a copper addition. However, some methods of compensating for hysteresis effects have been developed for resistance feedback control. Meier et. al. developed a control system which models the resistance-strain relationship of an actuator using linear curves for heating and cooling [154]. Position control is achieved using a PID control law which switches between the two curves depending upon whether the actuator is being heated or cooled. Liu et. al. employed a Duhem differential hysteresis model along with a set of second- and third-order polynomials to predict actuator strain for a PID feedback control law [164] [155], as shown in Figure 28. Although the model was developed for a voltage-displacement relationship, the applied voltage is directly related to the electrical resistance and exhibits similar behaviour. The previously mentioned polynomial model developed by Shi et. al. included separate heating and cooling curves, but no details were given regarding the switching method [156]. Another method of handling hysteresis compensation for resistance feedback control is the use of artificial neural networks, which are discussed next.

2.3.4 Neural Network Control

Artificial neural networks have been applied to shape memory alloy actuator position feedback control, as previously discussed, and are also useful for predictive modeling of the resistance-strain relationship. Ma et. al. investigated the use of an artificial neural network model of the resistance-strain relationship of an actuator, but accounting only for the major hysteresis loop behaviour [160], as shown in Figure 29. The predicted strain was then used within a PD feedback control law to achieve position control.

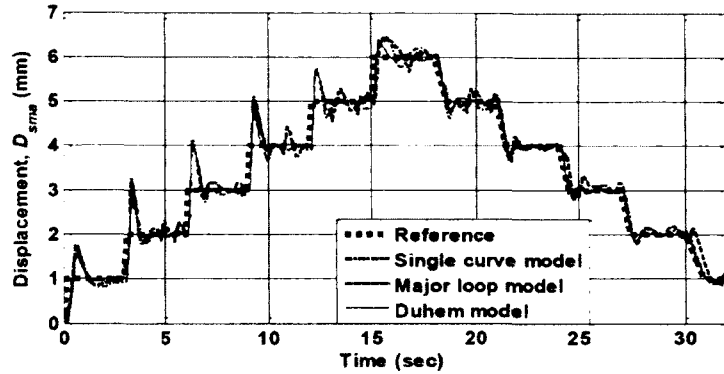


Figure 28: Comparison of control with and without compensation of the hysteresis effects as studied by Liu et. al. [155].

Asua et. al. also applied a neural network model for position control of an actuator, but were able to capture both major and minor hysteresis loop behaviour within the model [161]. Feedback of the predicted strain was used within a PID feedback control law.

2.4 Research Contributions

This thesis presents unique research into the use of electrical resistance feedback for modeling and control of a shape memory alloy actuator including the influence of applied stress. The previously discussed resistance feedback control algorithms suffer from two main drawbacks: the hysteresis effects due to the presence of R-phase during phase transformation, and the impact of applied stress upon the resistance-strain curves. Although each of these issues has been addressed independently, a complete model which accounts for hysteresis as well as varying stress has not been developed for resistance feedback control. Furthermore, many of the resistance-strain models which have been developed are not generalized for different applications. Two separate models of the resistance-stress-strain behaviour were developed for Flexinol Ni-Ti and Furukawa Ni-Ti-Cu alloys. The Flexinol alloy showed significant hysteresis

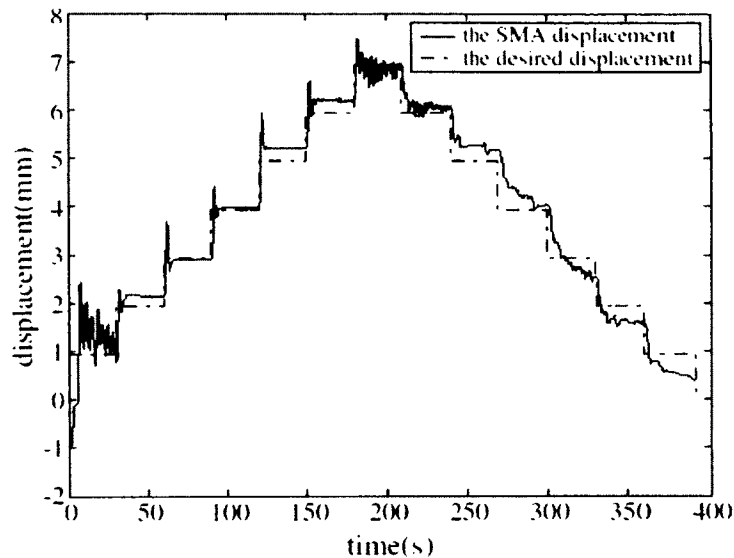


Figure 29: Results of position control using neural network model developed by Ma et. al. [160].

behaviour caused by the occurrence of R-phase, whereas the Furukawa alloy did not.

The Flexinol Ni-Ti alloy that was studied showed significant hysteresis behaviour due to the presence of R-phase during phase transformation. Many investigations of position control using resistance feedback were only applicable when no R-phase was present, which occurs at high levels of applied stress and for certain alloys such as Ni-Ti-Cu. Heating and cooling resistance-strain curves were used to model the hysteresis effects by Meier et. al. [154] and Shi et. al. [156], but only for conditions where these effects were minimized and only under a single applied load. Larger hysteresis effects were modeled using a Duhem differential model by Liu et. al. [155], and using artificial neural networks by Song and Liu [159] and Asua et. al. [161]. However, these models were also only applicable for a single applied load condition.

Modeling of the resistance-strain relationship for Flexinol was accomplished using separate linear functions for the heating and cooling curves of the major hysteresis loop. An exponential curve was used to model the intermediary change in resistance

and strain which connected the heating and cooling curves to complete the hysteresis loop. Minor hysteresis loops were captured by the model using these same exponential curves. Therefore, the model presented in this research for a Ni-Ti alloy captures the hysteresis effects due to R-phase, including both major and minor loops. Negligible hysteresis effects were observed in the behaviour of the Furukawa Ni-Ti-Cu alloy since no R-phase was present during phase transformation. Successful modeling of the resistance-strain behaviour was accomplished using a polynomial function which was averaged from heating and cooling curves. This approach has also been used by Lan and Fan [136], Zhang and Lin [158], and Pons et. al. [198], but for only a single applied load condition in each case.

Both models successfully capture the influence of applied stress upon the resistance-strain relationship. Previous methods of position control using resistance feedback have been restricted to a single load condition from a constant weight or spring. Urata et. al. included the influence of applied load within a model of the resistance-length relationship, however, this model is linear and does not capture the hysteresis effect [153]. Zhang and Yin also included the influence of applied stress within a constitutive model from which a polynomial resistance-stress-length relationship was derived [158]. However, the model depended upon the absence of R-phase and only a single applied load was considered during position control. The models developed for Flexinol and Furukawa alloys each include the influence of applied stress upon the coefficients used to model the resistance-strain behaviour. Position control of an actuator under varying load conditions was also successfully demonstrated using each model.

The models were also normalized with respect to the actuator geometry in order to provide a generalized representation for a specific material. Identification of the model parameters for a given alloy or production run may be performed on a sample of the material and then applied to actuators with different wire sizes. Although

normalized resistance and displacement have been used as parameters in many models developed for position control algorithms [150] [152] [157] [136] [197] [156], they were not generalized in terms of applied stress.

Modeling of the Flexinol Ni-Ti and Furukawa Ni-Ti-Cu alloys in terms of electrical resistance, applied stress, and strain was successfully accomplished and applied to a simple position control algorithm for a shape memory alloy actuator under varying load conditions. The use of electrical resistance feedback greatly reduces the mass, volume, and complexity of the actuator system by eliminating the need for a position sensor. Therefore, the models developed and presented in this thesis are well suited for application in robotic and aerospace systems. For example, the use of shape memory alloys for simple appendages or deployable instruments on spacecraft may benefit from the application of these models in order to provide feedback of the position. Robotic manipulators using shape memory alloy actuators may also employ these models in order to provide position feedback of the joint angles.

Chapter 3

Experimental Setup

A laboratory bench-top setup was used for characterizing the behaviour of both alloys and evaluating the performance of the models developed within a position control algorithm. The experimental setup was provided by the Canadian Space Agency and arranged in the Materials & Thermal Analysis laboratory at the John H. Chapman Space Centre. The purpose of the setup was to provide a frame for vertically suspending a shape memory alloy actuator wire loaded using either a bias mass or spring, and enable measurement of the actuator displacement, applied load, and electrical resistance. Actuator displacement was measured using a linear variable displacement transducer and the applied load was measured using a load cell. The actuator resistance was determined from measurements of the total applied voltage as well as the voltage across a reference resistor. Voltage outputs for the measurements of displacement, applied load, and resistance were captured by a data acquisition system, while applied power input to the actuator wire was provided by a controllable DC power supply. Both the power supply and data acquisition system were monitored and controlled using National Instruments LabView software.

3.1 Test Stand

The supporting test stand was composed of an aluminum structure with a flat plate at the base and a platform at the top from which the actuator wire was hung. Extrusions midway along the test stand provided a channel in which the LVDT position sensor could be mounted and fixed using set screws. The load cell was mounted on the underside of the upper platform and provided the attachment point for the actuator wire, where a universal joint was used to reduce bending. A second platform near the base could be connected in order to allow the installation of a bias spring whose position was adjusted using a threaded rod. Figure 30 shows the test stand with load cell mounting (A), LVDT mounting (B), and bias spring mounting (C).

3.2 Wire Mounting

Actuator wire samples were cut to desired lengths and each end was crimped within a TE Connectivity brass rectangular terminal (#61653-1). One terminal end of the actuator wire was connected by a screw to a rod end mounted at the end of the universal joint hanging from the load cell. The other terminal end of the actuator wire was connected by a screw to another rod end which was mounted to the LVDT probe. Lead wires with ends crimped within the same terminals were also mounted in between each actuator wire terminal and rod end in order to provide power. The rod ends were fabricated from Nylon in order to provide electrical insulation between the actuator wire and test stand. Figure 31 shows the actuator wire mounted between the rod ends on the test stand.

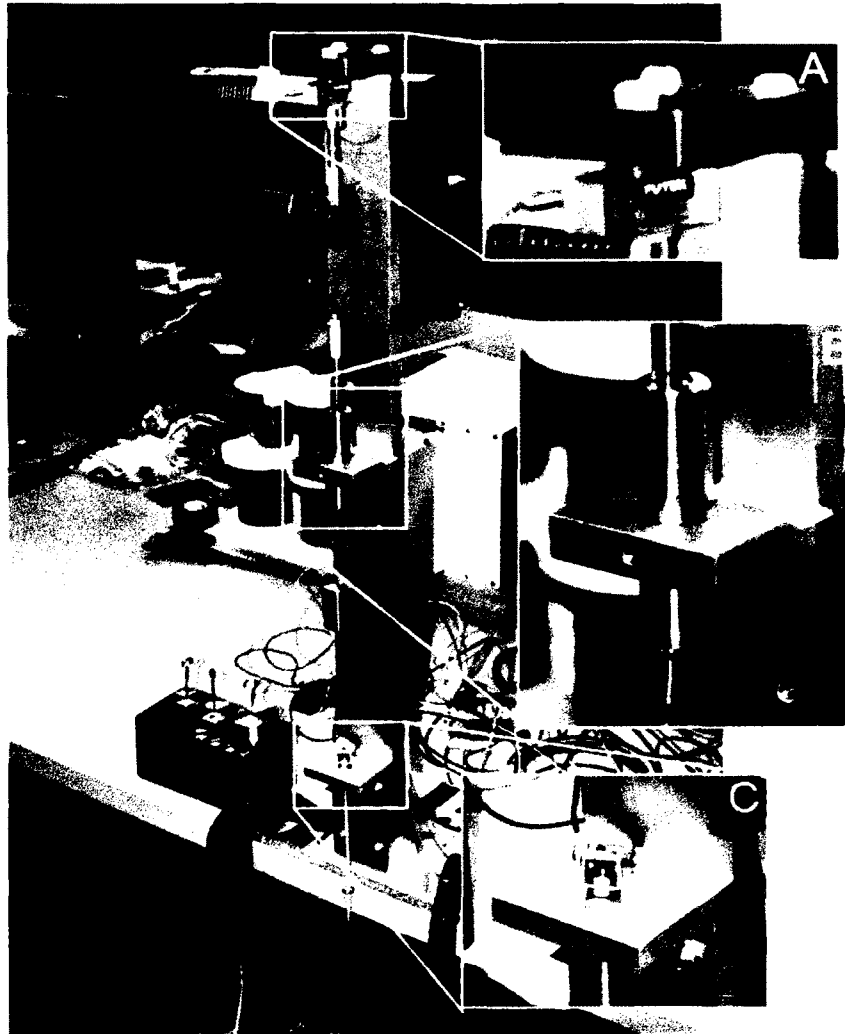


Figure 30: Test stand with load cell mounting (A), LVDT mounting (B), and bias spring mounting (C).



Figure 31: Actuator wire mounting.

3.3 Displacement Transducer

Displacement of the actuator wire was measured using a Solartron Metrology S-Series linear variable displacement transducer. This type of transducer consists of a nickel-iron core which moves along a single direction inside a cylindrical housing. Coils of wire wound around the housing experience induced voltages and produce a net signal that is linearly proportional to the core position within a specified range of motion. The core was attached to a rod and passed freely through the sensor body without touching the interior sides. This probe was then attached to the free end of the shape memory alloy actuator wire in order to provide a measurement of the actuator displacement. The transducer body was mounted within the extrusions on the test stand using set screws as shown in Figure 32, and could be shifted in order to position the sensor for different actuator lengths.

Excitation power was required for the LVDT sensor and provided by a 10 V DC power supply. Both power supply and output signal pass through a single pair of wires, where the output signal was in the form of a varying output current with a

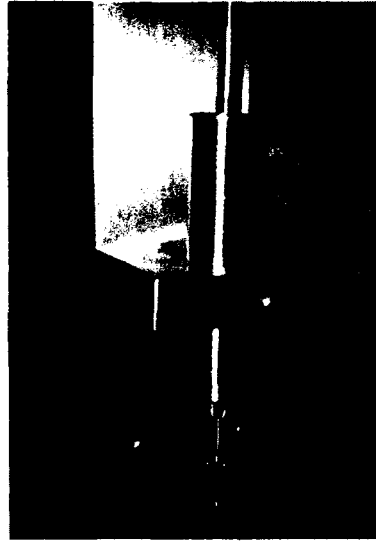


Figure 32: Solartron LVDT displacement transducer mounted on test stand.

range of 4-20 mA. This output current was determined by measuring the voltage across a 10Ω reference resistor placed in series after the transducer. The Solartron S-Series model used in the experimental setup had a measurement travel range of 5 mm and a resolution of approximately $0.1 \mu\text{m}$. Displacement, δ , was therefore determined from the measured current, I , according to equation 3.1.

$$\delta = m_{\delta}I + b_{\delta} \quad (3.1)$$

The expected coefficients m_{δ} and b_{δ} were determined from the expected output current and travel range. However, experimental calibration of the LVDT output was performed in order to ensure accurate measurement of the actuator position. Note that the reference position for the LVDT may be defined according to any desired datum while the slope of the current-position curve remains fixed. The reference position for the core probe was defined as the point at which the core was completely inserted into the body. Calibration was then achieved by hanging the probe at a static position and shifting the sensor body with respect to the frame. A digital micrometer

Coefficient	Expected	Calibrated
m_δ (mm/A)	312.50	315.84
b_δ (mm)	-1.25	-1.26

Table 1: Expected and calibrated coefficients for LVDT position output.

was used to measure the position of the sensor body in order to determine the relative displacement of the core. Table 1 summarizes the expected and experimentally determined coefficients defining the linear current-position relationship.

3.4 Load Cell

The applied load was measured using a Futek LRF300 low profile tension and compression load cell. This model is an in-line rectangular load cell with female threaded connections on opposite ends of the housing. The load cell was placed in between the test stand upper platform and the shape memory alloy actuator as shown in Figure 33, providing a measurement of the tension in the actuator wire. Strain gauges within the aluminum housing are arranged in a Wheatstone bridge configuration and calibrated to output a voltage linearly proportional to the applied load.

The load cell was connected to an Ectron 563H transducer conditioner-amplifier as shown in Figure 34, which reduced noise and amplified the signal as well as provided an excitation voltage of 10 V. The output voltage, V , from the amplifier was measured by the data acquisition system and used to determine the applied load, F , according to equation 3.2.

$$F = m_F V + b_F \quad (3.2)$$

The coefficients m_F and b_F were determined through experimental calibration since the slope and offset of the linear voltage-load relationship depended upon the manually adjusted settings of the amplifier. Calibration was achieved by hanging

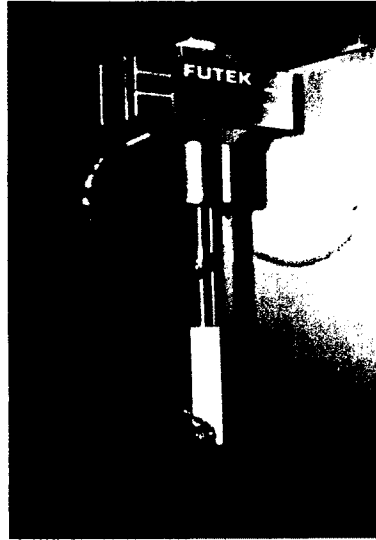


Figure 33: Futek LRF300 load cell mounted on test stand.



Figure 34: Ectron 563H conditioner-amplifier.

a series of known laboratory reference masses from the load cell and recording the output at each load setting. This calibration process was performed before each new experimental session due to drift accumulating within the amplifier signal. In addition to the tension experienced by the actuator wire, the load cell also measured the weight of the parts which connect the wire to the sensor, including the clamping screw and rod end, universal joint, bolt adaptor, and connecting bolts. Furthermore, the weight of the LVDT probe was also included in the applied load on the actuator. However, when performing calibration a different configuration was used to hang the masses from the load cell, including the hook end, universal joint, bolt adaptor, and connecting bolts. The additional weight due these parts was considered during both calibration and application of the load cell.

3.5 Electrical Resistance Feedback

The electrical resistance of the shape memory alloy actuator wire was determined from measurements of the applied voltage and current. The voltage across a 1Ω reference resistor in series with the actuator wire was used to measure the applied current, while the total voltage applied to the circuit was used to measure the applied voltage. From the total applied voltage, V_{net} , and the voltage across the reference resistor, V_{ref} , the resistance of the actuator wire, R_{SMA} , was determined from equation 3.3, where R_{ref} is the resistance of the reference resistor.

$$R_{SMA} = R_{ref} \left(\frac{V_{net} - V_{ref}}{V_{ref}} \right) \quad (3.3)$$

Construction of the circuit also included a series of lead wires, one pair of which connected the circuit input to the DC power supply and another which connected the actuator wire to the circuit. Figure 35 shows the simplified circuit diagram including

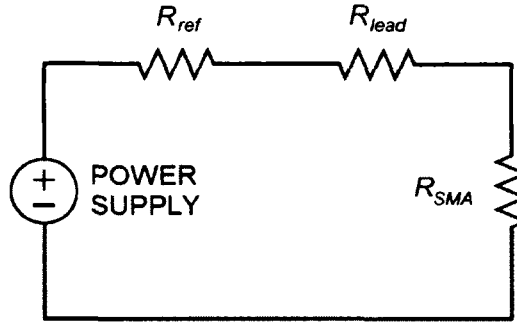


Figure 35: Resistance measurement circuit diagram.

the reference resistor, lead resistance, and actuator wire resistance. Measurement of the total applied voltage was achieved at the circuit, and therefore losses in the lead wires connecting the DC power supply were ignored. However, the losses in the lead wires connecting the actuator wire could not be ignored and were measured by removing the actuator wire and calculating the resistance of the shorted circuit. Therefore, the actual resistance of the actuator wire was determined from equation 3.4, which includes the lead wire resistance, R_{lead} .

$$R_{SMA} = R_{ref} \left(\frac{V_{net} - V_{ref}}{V_{ref}} \right) - R_{lead} \quad (3.4)$$

It should also be noted that the computation of the actuator resistance requires division by the reference resistor voltage, V_{ref} , which was maintained above zero in order to avoid division by zero in equation 3.4. Furthermore, noise within the reference voltage signal was greatly amplified within the measurement of the actuator resistance if the reference voltage was low, which occurred when the total applied voltage was low. Therefore, the total applied voltage was always maintained above a threshold level which was high enough to avoid noise during cooling and low enough to avoid undesired actuation or unsatisfactory cooling response time.

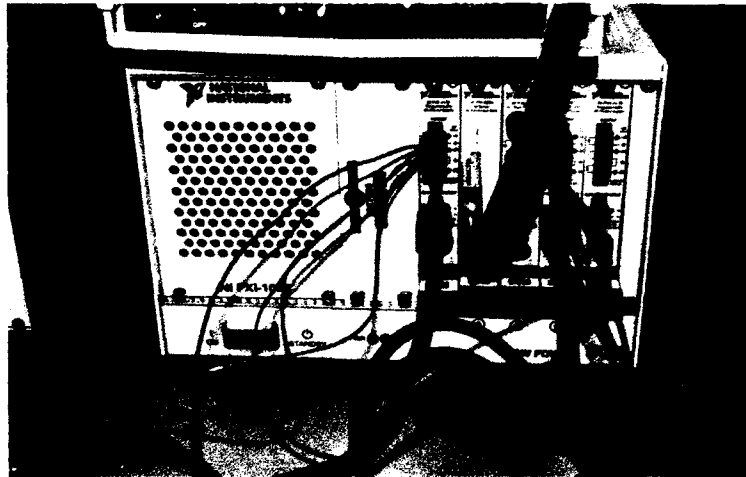


Figure 36: National Instruments PXI-1033 chassis with PXI-4110, PXI-6220, and PXI-4070 modules.

3.6 Data Acquisition

Sensor measurement and power supply control was achieved using a data acquisition system composed of primarily National Instruments (NI) hardware and software. At the centre of the data acquisition system was a NI PXI-1033 chassis which acted as a hub for up to five separate peripheral modules. This main chassis was connected to a Dell Precision 690 computer through a PCIe-8361 data acquisition card which permitted input/output communication for measurement and control. Within the PXI-1033 chassis are three peripheral modules: the NI PXI-4110 Programmable DC Power Supply, an NI PXI-4070 Digital Multimeter, and an NI PXI-6220 Multifunction Data Acquisition Module. Figure 36 shows the PXI-1033 chassis with the peripheral modules installed, including two extra PXI-4110 power supply modules.

The PXI-6220 data acquisition module was connected to an NI SCXI-1000 chassis, which houses up to four peripheral signal acquisition and conditioning modules. Two modules were connected within the SCXI-1000 chassis: an NI SCXI-1102B 32-channel Thermocouple/Voltage Input Module, and an NI SCXI-1122 16-channel Multiplexer Module, as shown in Figure 37. Terminal blocks SCXI-1303 and SCXI-1322 were

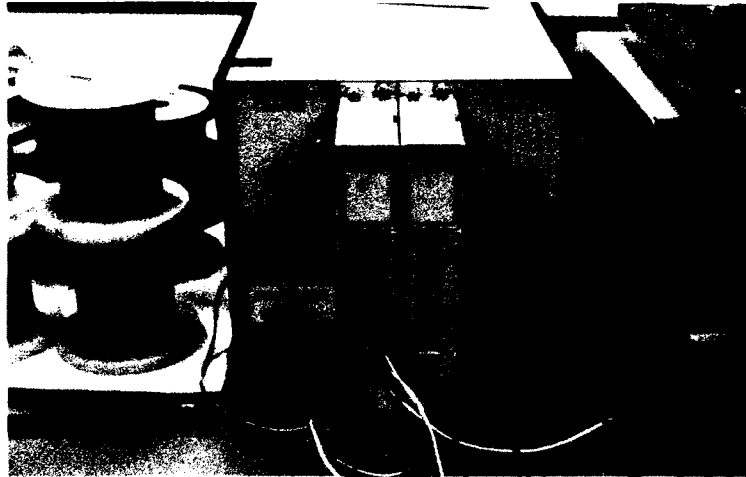


Figure 37: National Instruments SCXI-1000 chassis with SCXI-1102B and SCXI-1122 modules.

mounted to the SCXI-1102B and SCXI-1122 modules, respectively. The SCXI-1122 module was not designed to sample multiple channels simultaneously, therefore the SCXI-1102B module was used to acquire data from the LVDT sensor and load cell, as well as the voltage measurements for resistance feedback. The PXI-4070 multimeter module was not used since the electrical resistance of the actuator wire was determined using the method described previously. Figure 38 shows the complete National Instruments data acquisition and power supply system as well as the Ectron signal conditioner.

The data acquisition system was configured within NI Measurement and Automation Explorer (MAX) in a Windows XP operating environment, where the system architecture was prescribed and input/output channels were tested and pre-defined. Programs were created in NI LabView 7.1 for experimental characterization of the actuator wire, position control using resistance feedback models, and sensor calibration. Sampling of the measured signals was performed at 1000 Hz, while intervals of 50 samples were averaged in order to reduce noise. This resulted in an effective sampling rate of 20 Hz. Data was recorded in tab-delimited ASCII files which are

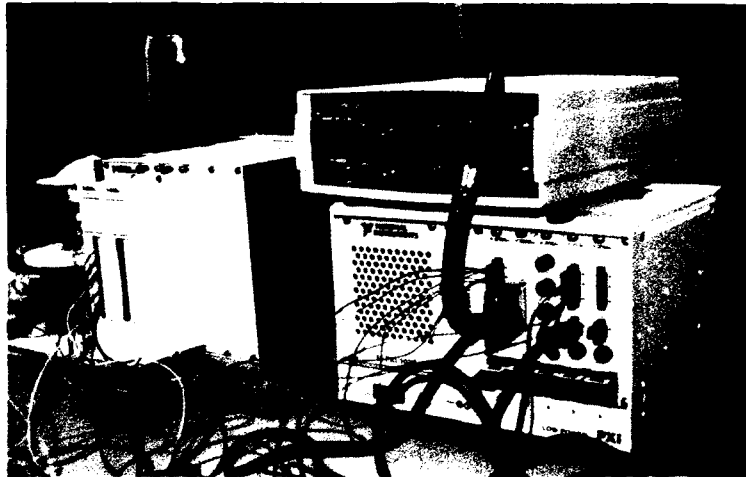


Figure 38: Data acquisition, signal conditioning, and power supply system.

compatible with any text reader, and post-processing of the data was mainly performed in Mathworks MATLAB as well as Microsoft Excel.

3.7 Power Supply

Power was supplied to the shape memory alloy actuator as well as to the LVDT sensor using a National Instruments PXI-4110 Programmable DC Power Supply, which is a modular component integrated within the PXI-1033 chassis described previously. The PXI-4110 power supply has three channels, one of which provides up to 1 A at 6 V and the other two provide up to 1 A at 20 V. Either applied voltage or current could be precisely controlled and monitored within the LabView data acquisition and signal processing software. Voltage and current measurements had resolutions of 0.06 mV and 0.02 mA, respectively, for the 6 V channel, and resolutions of 0.20 mV and 0.02 mA for the 20 V channels. The typical response time was approximately 1 ms, and the control and measurement sampling rate was approximately 300 Hz. Heating of the shape memory alloy actuator was typically performed using a controlled current amplitude while allowing the voltage to change according to the change in actuator

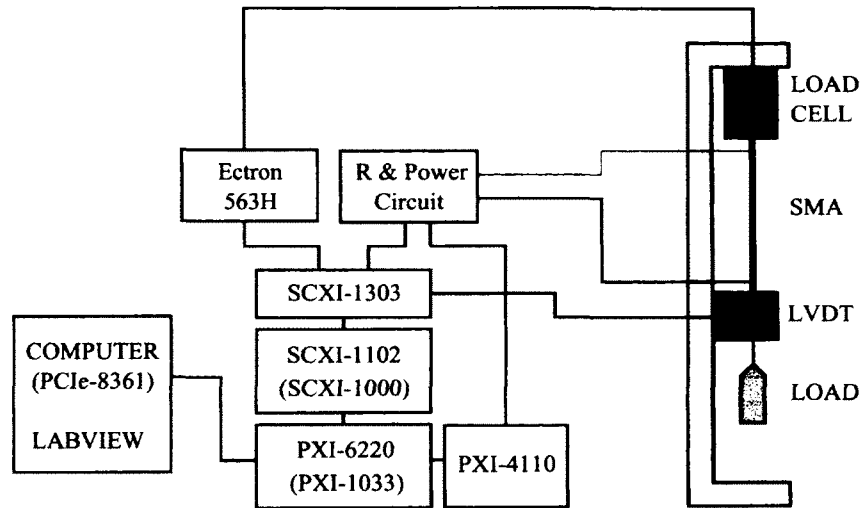


Figure 39: Diagram of the experimental setup.

resistance. The use of current control instead of voltage control was employed in order to more easily accommodate actuators of varying length, and a bias current level of 0.05 A was used in order to mitigate the noise and singularity problem when determining actuator resistance.

A diagram of the experimental setup is shown in Figure 39, where the major components and their connection through the data acquisition and power supply systems are highlighted.

Chapter 4

Material Characterization

Experimental characterization of the Flexinol and Furukawa alloys was performed in order to evaluate the relationships between electrical resistance, applied stress, and strain. These relationships were modeled and used within an actuator position control algorithm, therefore characterization was focused on studying the behaviour of the alloys within the same context. This required that the fundamental relationships between electrical resistance and strain be well understood, as well as the influence of applied stress upon these relationships. The behaviour of the shape memory alloy actuator wire during minor hysteresis loops is also an important feature that must be captured. Minor hysteresis loops occur due to incomplete activation of the material, and must be represented within the model in order to provide smooth actuator position control during incomplete actuation.

The Ni-Ti Flexinol alloy demonstrated significant hysteresis behaviour due to R-phase, and required close examination of the major and minor hysteresis loops. Conversely, the Furukawa alloy showed relatively negligible hysteresis effects during the majority of the activation range and demanded less attention to minor hysteresis loops during incomplete actuation. Characterization of the minor hysteresis loops was therefore more important when studying the behaviour of the Flexinol alloy. The influence of applied stress upon the resistance-strain relationships was studied

by examining the behaviour of the alloys under a set of constant loads as well as under spring constraint loading. Most of the experiments used for characterization consisted of open-loop activation of the actuator wire or the use of a simple on-off control law based on position feedback.

4.1 Flexinol

The Ni-Ti Flexinol alloy is a Nitinol alloy with a composition of approximately 50% nickel and 50% titanium that is developed and manufactured by Dynalloy, and available in both ribbon and wire form of various dimensions. Both low temperature (70 °C) and high temperature (90 °C) Flexinol alloy is available, referring to the temperatures required to cause phase transformation. Only the low temperature wire form of Flexinol shape memory alloy was studied in this research with a diameter of 0.006 inches. This alloy demonstrates significant hysteresis behaviour which indicates the presence of R-phase during phase transformation. Furthermore, there was a significant dependency between the size of the hysteresis effects caused by R-phase and the applied load.

4.1.1 Resistance-Displacement Behaviour

The fundamental resistance-displacement behaviour of Flexinol alloy as an actuator wire was characterized in order to study the major hysteresis loop. Actuator wire samples were mounted and loaded by hanging a weight at the end of the LVDT probe. The resistance-displacement relationship was then observed and recorded by applying a square pulse of electric current, where the amplitude and duration of the pulse were controlled in order to achieve moderate actuation speed and ensure complete actuation. As previously discussed, a bias level of power input was used in order to allow

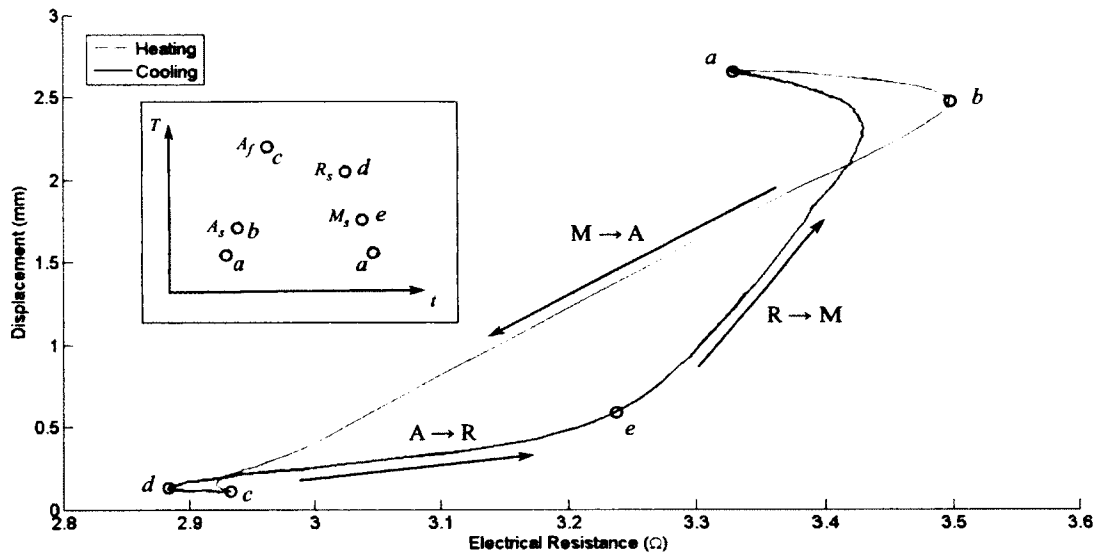


Figure 40: Major hysteresis loop resistance-displacement behaviour of Flexinol actuator wire.

measurement of the electrical resistance even when heating was not required. Cooling occurred passively due to heat loss to the surroundings and resulted in resetting the actuator wire due to the applied load. The resulting measurements of electrical resistance and actuator displacement then demonstrate the fundamental behaviour of the Ni-Ti Flexinol alloy as shown in Figure 40 where a load of approximately 0.96 N was applied.

During heating, the electrical resistance of the Flexinol actuator wire showed an initial increase (from *a* to *b*) and then a decreasing trend as phase transformation from martensite to austenite took place and the actuator contracted (from *b* to *c*). After complete actuation, the electrical resistance again tended to increase until heating stopped. The increase in electrical resistance at the beginning and end of the heating phase was due to the temperature dependence of electrical resistivity described in equation 2.12, while the overall decrease in electrical resistance throughout actuation was due to the strain dependence of electrical resistance described using equation

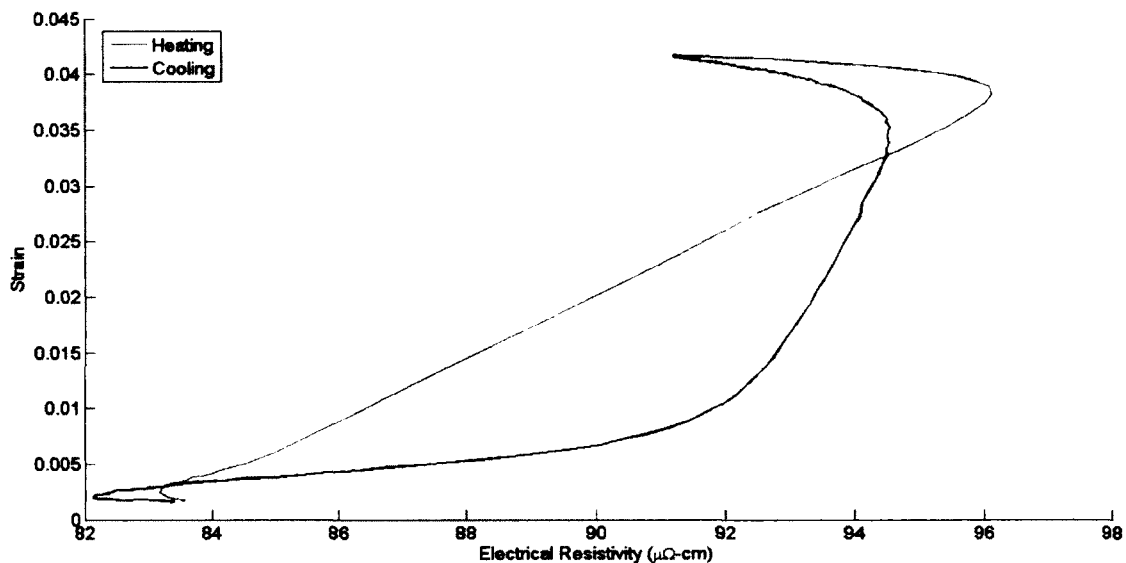


Figure 41: Major hysteresis loop resistivity-strain behaviour of Flexinol actuator wire.

2.13 or 2.14. Although there are highly non-linear and indeterminate regions at the beginning and end of the resistance-strain curve during heating, the overall trend appeared to be linear.

Cooling of the actuator wire caused the electrical resistance to decrease initially due to previous heating past the point of full actuation (from *c* to *d*). Following this initial decrease, the resistance then increased sharply over a small portion of the actuation range (from *d* to *e*) before following another linear trend and increasing throughout the majority of the actuation range. The initial sharp increase in resistance is due to the intermediary phase transformation from austenite to R-phase, while the transformation from R-phase to martensite occurs throughout the remainder of the cooling curve. As the actuator wire experienced reverse phase transformation and approached full extension, another region of decreasing electrical resistance was observed before returning to the initial point.

Figure 41 shows a plot of the actuator strain versus electrical resistivity for the

same case as shown in Figure 40. During heating, not only did the electrical resistance decrease overall as expected for any material in contraction, but the electrical resistivity decreased overall as well. The change in electrical resistivity resulted from the phase transformation during activation and from the influence of temperature upon the resistivities of each phase. Differences in the critical transformation temperatures for forward and reverse martensite-austenite phase transformation also caused a shift in the electrical resistivity between the heating and cooling curves.

The characteristic hysteresis observed in the resistance-displacement response of Ni-Ti shape memory alloy is due to the combined effect of differences between the heating and cooling transformation temperatures and differences in the resistivities of each constituent phase as well as the large strain due to the shape memory effect. These properties cause significant variations in the electrical resistance during forward and reverse phase transformation, which leads to the curves shown in Figures 40 and 41. Figure 42 shows the resistance-displacement response (with actuator length, L , instead of displacement), as well as lines representing constant electrical resistivity for each phase at critical transformation temperatures.

Initially, the actuator is near the martensite finish temperature, M_f , (at point a) and is then heated until reaching the austenite start temperature, A_s , where phase transformation begins (at point b). As the actuator is heated from the austenite start temperature to the austenite finish temperature, A_f , the resistivity of the material shifts from the resistivity of martensite, ρ_M , to the resistivity of austenite, ρ_A , and the wire contracts as it reaches point c . The actuator is then cooled until reaching the R-phase start temperature, R_s , (at point d) where transformation begins as the resistivity shifts from the resistivity of austenite to the resistivity of R-phase. Depending upon the level of applied stress, the actuator reaches the martensite start temperature during transformation from austenite to R-phase (at point e), and begins transformation from R-phase (and any remaining austenite) back to martensite,

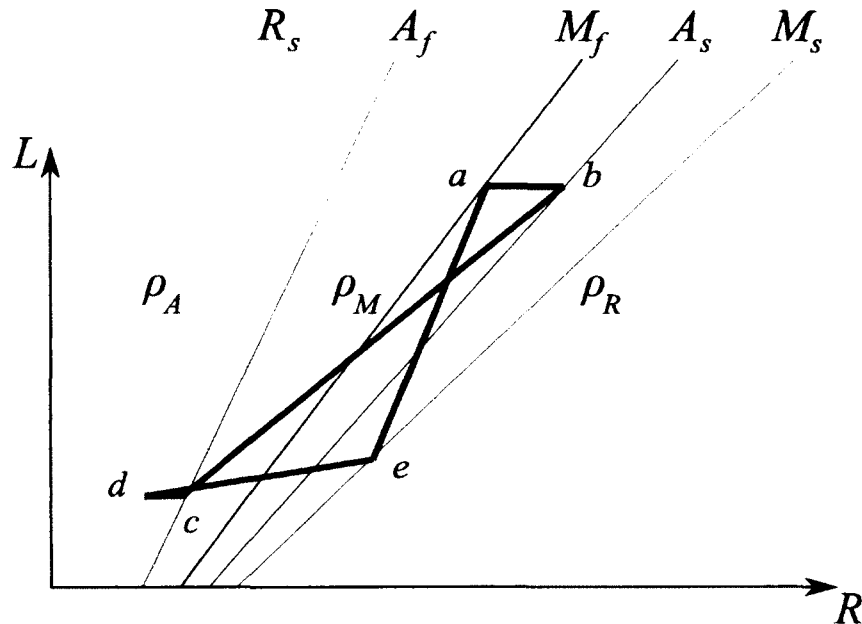


Figure 42: Simplified resistance-displacement response including lines of constant resistivity for martensite at M_f (dark blue), martensite at A_s (light blue), austenite at A_f (red), austenite at R_s (orange), and R-phase at M_s (purple).

extending and returning to point a . Note that the lines of constant resistivity all meet at the origin since the resistance of the actuator wire is linearly dependent upon the length (with no offset).

4.1.2 Influence of Applied Stress

Development of a comprehensive model for resistance feedback control of shape memory alloy actuators requires that the effect of applied stress be captured in order to handle varying load conditions. The influence of applied stress upon the relationship between electrical resistance and actuator displacement was studied by examining the resistance-displacement curves under various load conditions. A set of constant weights which vary from 10 g to 1 kg were used to apply constant loads, while various springs could be used to apply varying load. Selection of the applied weight or spring stiffness was performed with consideration of the stress limits of the shape memory

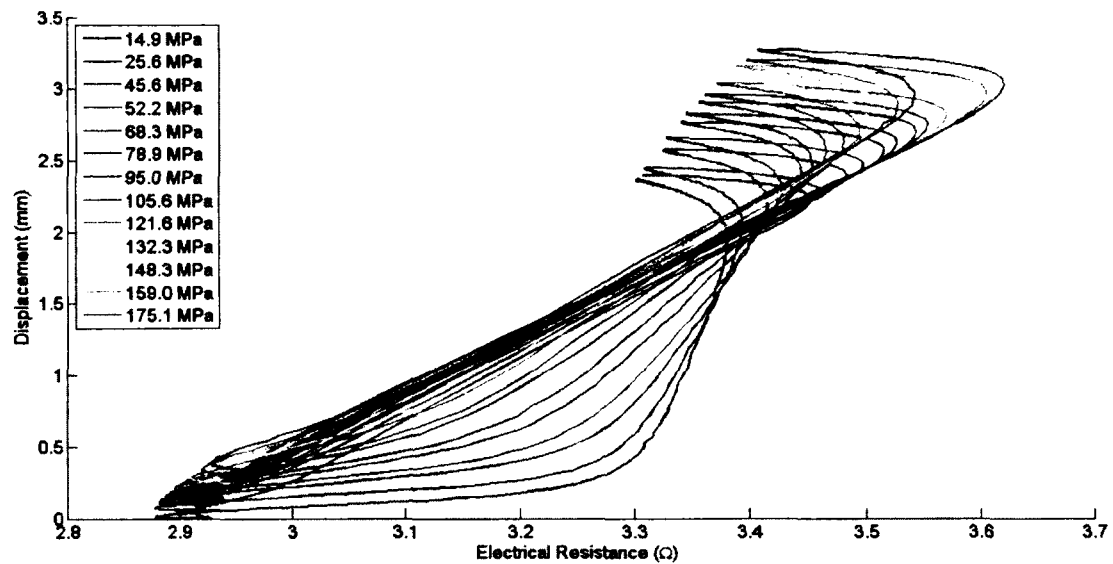


Figure 43: Influence of stress upon the resistance-displacement behaviour of Flexinol actuator wire.

alloy material. Although the yield strength of the Ni-Ti Flexinol alloy is approximately 350 MPa, the applied stress should never exceed approximately 175 MPa in order to ensure actuation is repeatable and the shape memory effect is retained.

The influence of applied stress upon the resistance-strain relationship of Flexinol actuator wire was studied by applying the same open-loop activation pulse described previously. Major hysteresis loops were observed and recorded during activation of the wire under each constant applied load, which varied from 0 to 300 g plus the additional weight of the LVDT probe (28 g). The resulting resistance-displacement behaviour of the actuator wire at various levels of applied stress was then compiled and demonstrated in Figure 43, where the colour of the lines represent the level of stress increasing from blue to red. Figure 44 highlights the separate heating and cooling curves at each level of applied stress.

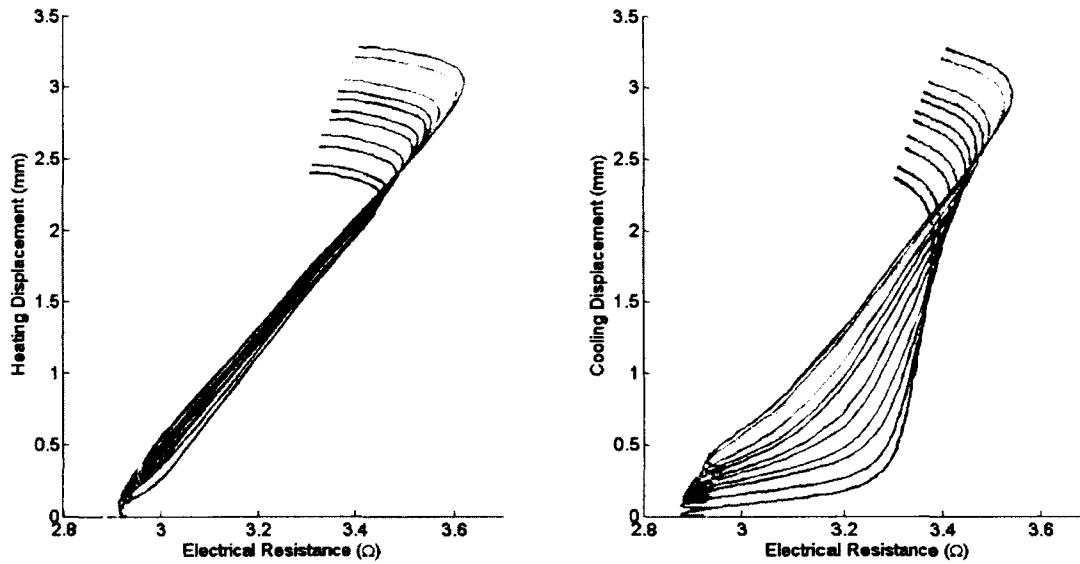


Figure 44: Influence of stress upon the heating and cooling curves of Flexinol actuator wire.

Both the electrical resistance and actuator displacement were affected by the variation of applied stress, which was expected since there is a dependence between applied stress and strain as well as between displacement and electrical resistance. The actuator displacement at zero and full actuation positions increased with increasing applied stress, and the electrical resistance at each limit also increased with increasing applied stress. The increase in actuator displacement is due to the combined effect of elastic mechanical strain, which follows Hooke's law but with non-constant Young's modulus as in equation 2.3, and actuation contraction due to the shape memory effect. The increase in electrical resistance is due to the combined effect of increasing strain and increasing electrical resistivity. Electrical resistivity increased due to the increase in temperature at the beginning and end of phase transformation. This is also expected since the critical start and finish phase transformation temperatures all increase with increasing applied stress according to equations 2.9 and 2.10, therefore requiring higher temperatures for actuation.

The most distinctive and significant effect of varying the applied stress was the change in the shape of the major hysteresis loop. While the resistance-strain curve during heating remained relatively similar with increasing applied stress, the cooling curve tended to shift towards the heating curve. This shift in the cooling curve demonstrates a reduction in R-phase occurrence during phase transformation with increasing applied stress, which has also been reported in previous research. The previously described temperature dependence of electrical resistivity is also a cause of the shift in the heating and cooling curves.

4.1.3 Minor Hysteresis Loops

The overall major hysteresis loop within the resistance-displacement relationship of the Flexinol alloy represents the behaviour during complete actuation. However, position control of a shape memory alloy actuator depends upon the use of partial actuation in order to achieve a specific desired position within the range of motion. The behaviour of the actuator wire during incomplete activation was therefore studied in order to include the minor hysteresis loop effects within the model that was developed. Examination of the minor hysteresis loop behaviour was achieved by actuating the wire under a constant load through a series of position test points, with on-off control applied using position feedback. The test points were uniformly spaced between two positions bounded by the actuator stroke limits, and arranged in a list of set points which was referenced for position control. Partial actuation was then achieved between each possible pair of test points, including both incomplete heating and cooling of the actuator wire. Figure 45 shows the resulting minor hysteresis paths generated by incomplete actuation for a constant applied load of approximately 1.26 N. The minor hysteresis behaviour is further highlighted in Figure 46, where the data is reduced for clarity.

The behaviour of the minor hysteresis paths during cooling is similar to that of the

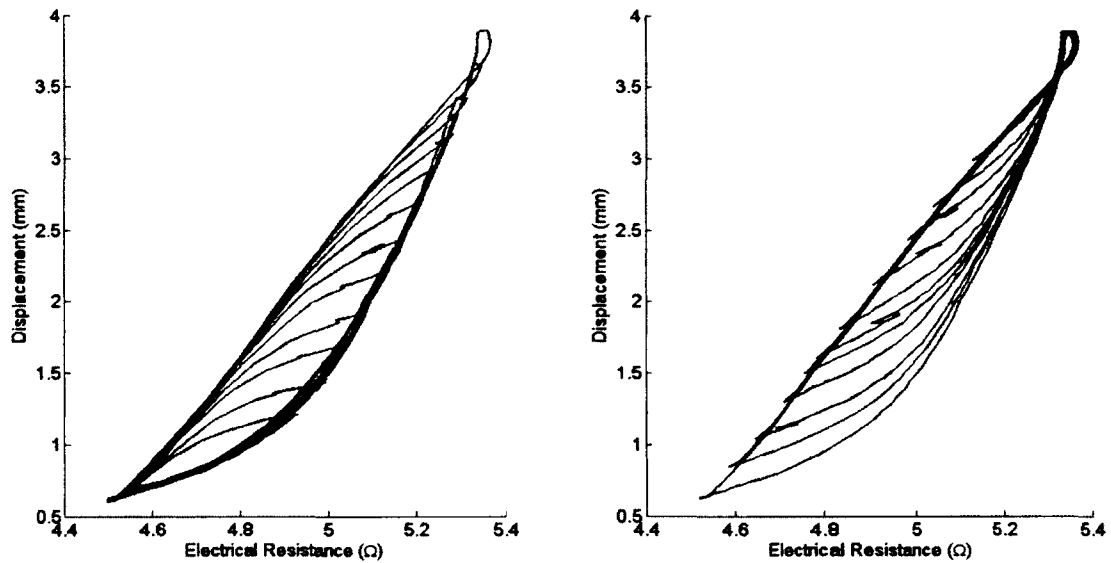


Figure 45: Minor hysteresis loop behaviour of Flexinol actuator wire.

major hysteresis path, with an initial sudden increase in electrical resistance which exponentially approaches the primary cooling path. A similar trend was observed in the minor hysteresis path during heating, where there is a sudden decrease in electrical resistance which exponentially approaches the primary heating path. This effect is primarily due to the presence of R-phase as well as the temperature dependence of electrical resistivity. Furthermore, if the initial strain at the onset of heating is high enough, a non-linear indeterminate region of increasing resistance appears before approaching the primary heating path, similar to the behaviour of the major hysteresis loop.

Minor hysteresis loop behaviour may be considered independent of the applied stress. The heating and cooling curves during incomplete activation tend to exponentially approach the primary heating and cooling curves of the major hysteresis loop, which vary according to the applied stress as previously demonstrated. The minor hysteresis loop behaviour may therefore be described separately from the heating and

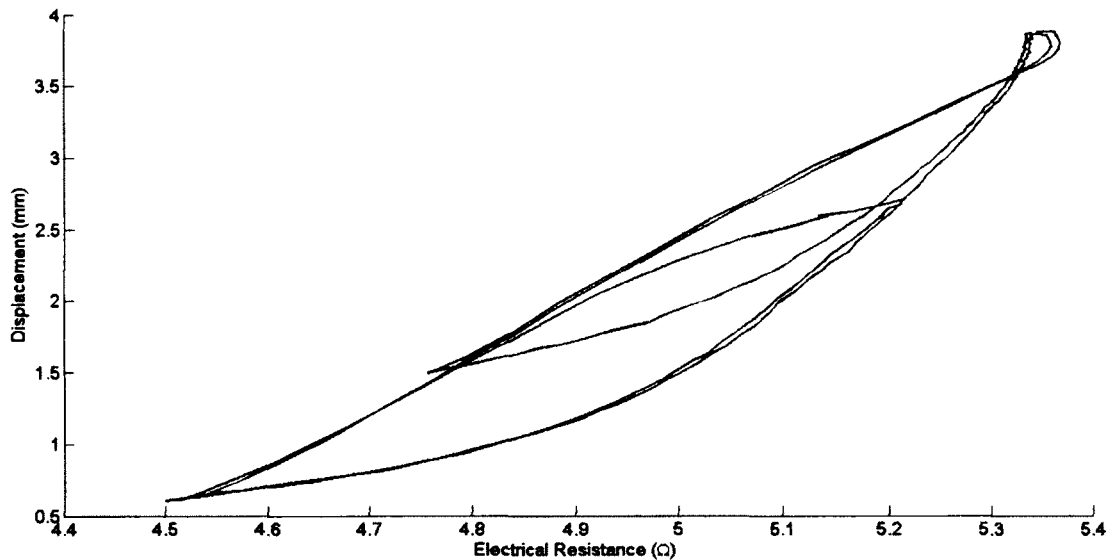


Figure 46: Minor hysteresis loop behaviour of Flexinol actuator wire (reduced).

cooling curves of the major hysteresis loop.

4.1.4 Training & Fatigue

Shape memory alloy actuators which are operated under cyclic loading suffer from moderate fatigue throughout extended use. The accumulation rate of fatigue due to cyclic loading is high for an initial number of cycles, which usually ranges from approximately 30-50 cycles. Additional fatigue accumulates at a slower rate, but nevertheless causes a noticeable degradation in performance due to reduced actuation stroke during phase transformation. The initial high rate of fatigue is referred to as a training period, in which a new actuator wire must be intentionally cycled in order to reach steady-state behaviour. Although fatigue continues to occur during subsequent cyclic loading, the behaviour of the material may be considered steady-state as long as suitable margins are allotted during the design process. The Flexinol actuator wire was cyclically activated using open-loop pulses of current in order to achieve complete

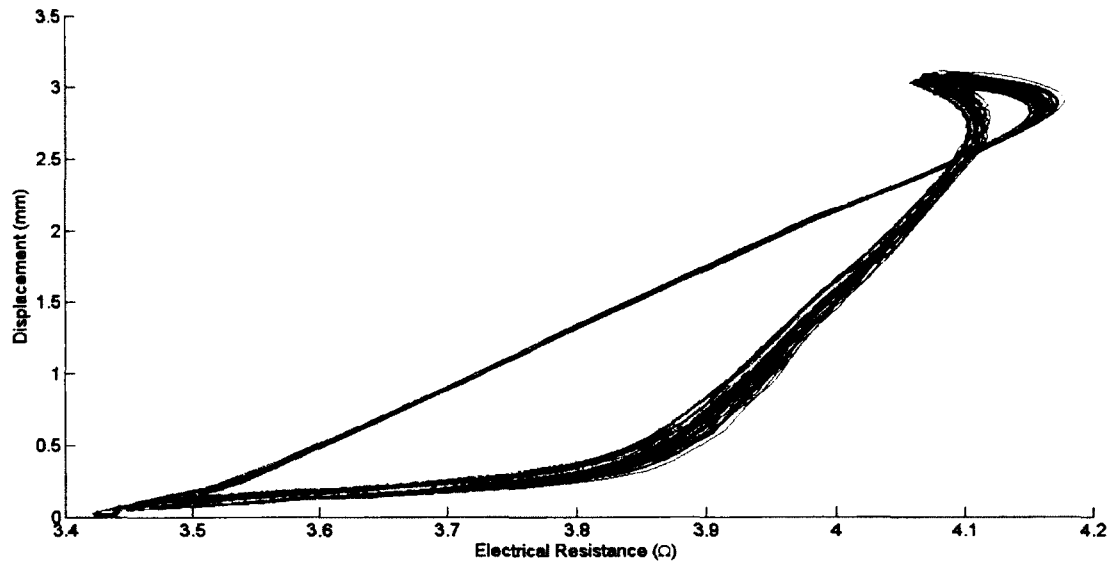


Figure 47: Fatigue behaviour of Flexinol actuator wire.

actuation and return. Figure 47 shows the effect of fatigue on an actuator wire over 100 activation cycles with a constant applied load of approximately 1.26 N, where the color represents the cycle number starting from blue and shifting to red.

The effects of fatigue upon the Ni-Ti Flexinol alloy are apparent in terms of both electrical resistance and actuator displacement. The maximum displacement shows an initially exponential decrease which reaches a constant rate of steady decay, while the minimum displacement does not demonstrate significant fatigue behaviour. The electrical resistance exhibits similar fatigue behaviour as the actuator displacement, with decreasing maximum resistance and unchanging minimum resistance. Minimum and maximum electrical resistance and displacement are fitted as functions of cycle number with a logarithmic curve defined by equation 4.1, where y represents the parameter being fitted, N is the cycle number, and g_1 and g_2 are coefficients determined

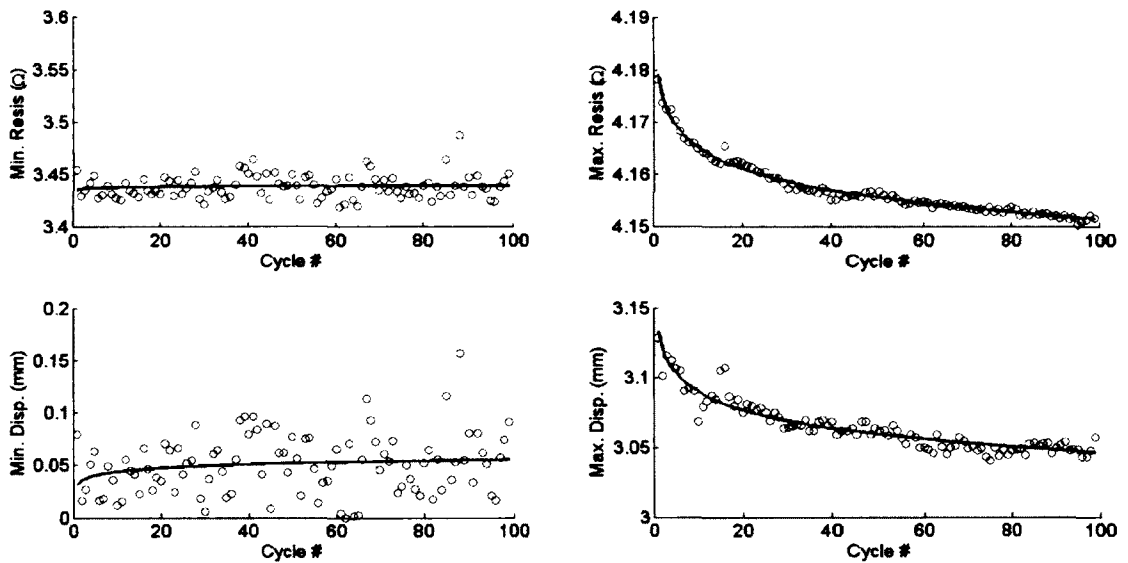


Figure 48: Minimum and maximum resistance and displacement during cycling including logarithmic curve fitting.

through least-squares fitting. Figure 48 shows the results of the logarithmic fitting.

$$y = g_1 \ln N + g_2 \quad (4.1)$$

This logarithmic relationship has been proposed by Meier et. al. and used to model the fatigue degradation of the actuator stroke [154]. Meier et. al. found the coefficients of the fatigue relationship varied significantly according to the applied stress and a look-up table was used for simulation.

The overall resistance-strain behaviour of the Flexinol actuator wire remains unchanged, and the rate of change of the maximum and minimum electrical resistance and displacement are relatively small. However, the application of shape memory alloy actuators in cyclic operation requires consideration of the effects of fatigue within the model or by using appropriate design margins.

4.2 Furukawa

The Ni-Ti-Cu NT-H alloy is a Nitinol alloy with a composition of approximately equiatomic nickel and titanium as well as a copper addition, developed and manufactured by Furukawa Electric Company. Although no literature is available regarding the exact composition of the Furukawa alloy, Nitinol alloys with copper additions typically contain 5-10% copper. The Ni-Ti-Cu Furukawa alloy is available in various dimensions of both wire and ribbon form as well as helical springs, but only the wire form of Furukawa NT-H alloy with a diameter of 0.20 mm was used for this study. There are three main advantages of using a Ni-Ti-Cu alloy compared with a Ni-Ti alloy: the phase transformation process shows smaller temperature-strain hysteresis, no R-phase occurs during phase transformation, and the alloy is more resistant to fatigue. The smaller temperature-strain hysteresis translates into a smaller resistance-displacement hysteresis due to martensite-austenite phase transformation. Furthermore, the absence of R-phase eliminates the large hysteresis behaviour observed in the resistance-displacement relationships of the Ni-Ti Flexinol alloy.

4.2.1 Resistance-Displacement Behaviour

Similar to the Ni-Ti Flexinol alloy, the principal relationship between electrical resistance and actuator strain in the Ni-Ti-Cu Furukawa alloy was studied. No significant hysteresis effects were expected within the resistance-displacement behaviour of the Furukawa alloy due to the copper addition. The process of observing and recording the open-loop actuation behaviour of the Furukawa alloy was the same as was used for investigation of the Flexinol alloy. Square pulses of current were applied to the actuator in order to achieve complete actuation and recovery. Figure 49 demonstrates the relationship between electrical resistance and displacement for a Furukawa alloy actuator wire with an applied load of 0.47 N.

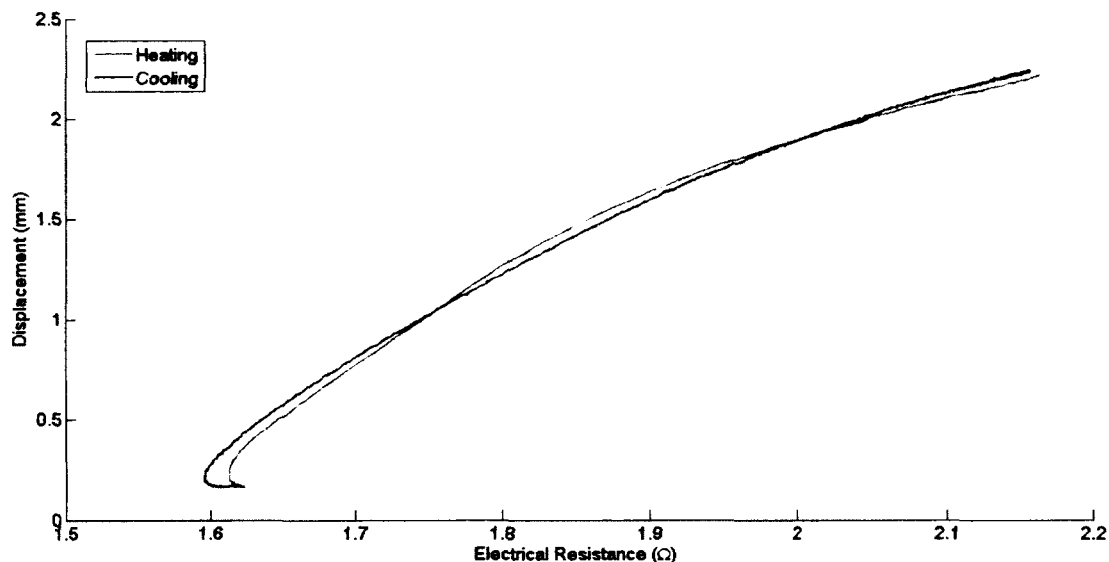


Figure 49: Overall resistance-displacement behaviour of Furukawa actuator wire.

While there does appear to be some hysteresis effect due to different heating and cooling curves, the overall resistance-displacement relationship of the Ni-Ti-Cu Furukawa alloy showed almost negligible hysteresis compared with the Ni-Ti Flexinol alloy. Due to the smaller temperature hysteresis during phase transformation and the lack of R-phase, the change in electrical resistance during heating and cooling is due to the dependence upon strain and temperature as described by equations 2.12, 2.13, and 2.14. The resistance-displacement curve during heating shows a similar trend as the Flexinol alloy during heating, with small increases in electrical resistance before and after phase transformation occurs. During cooling, the electrical resistance initially decreased along with temperature until phase transformation caused an overall increase which followed a non-linear path close to the heating curve. Although both heating and cooling resistance-displacement curves of the Furukawa alloy are non-linear and demonstrate an indeterminate region at full actuation, the overall behaviour is much simpler than that of the Flexinol alloy.

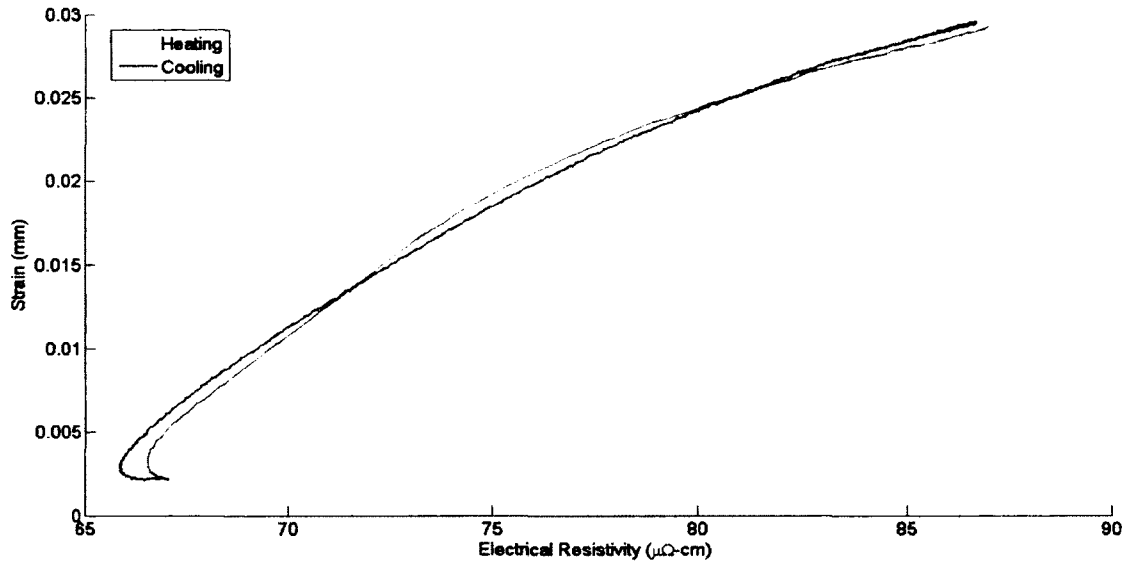


Figure 50: Overall resistivity-displacement behaviour of Furukawa actuator wire.

The relationship between electrical resistivity and strain follows almost exactly the same trends as the relationship between electrical resistance and displacement, as demonstrated by Figure 50. This change in electrical resistivity throughout phase transformation is the cause of the non-linear behaviour as well as the slight hysteresis gap between heating and cooling curves. Although the temperature hysteresis is smaller, there is a difference in the phase transformation temperatures during forward and reverse transformation which causes a shift in the electrical resistivity between heating and cooling curves.

4.2.2 Influence of Applied Stress

The effect of applied stress upon the relationship between electrical resistance and displacement was also investigated for the Furukawa alloy in order to support the development of a comprehensive model for position control. Again, open-loop activation of the actuator wire was used to ensure complete actuation for a series of constant

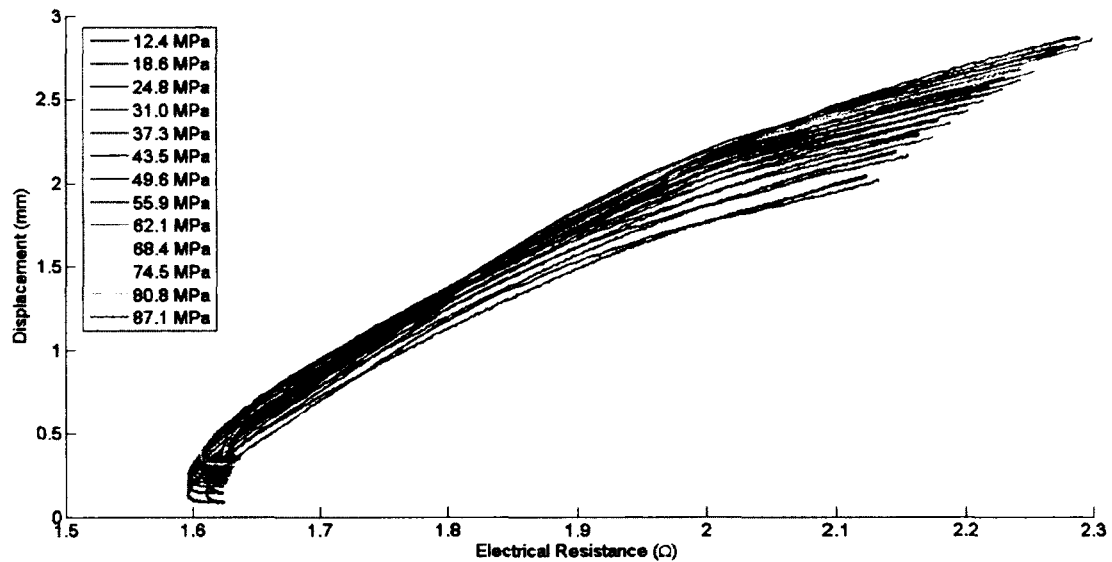


Figure 51: Influence of stress upon the resistance-displacement behaviour of Furukawa actuator wire.

applied loads provided by the brass weights described previously. Although the yield strength of the alloy was unavailable, similar loading conditions that were used to study the Flexinol alloy were also applied to the Furukawa alloy. The resistance-displacement relationship was examined for constant loads ranging from 0.1 N to 2.45 N plus the weight of the LVDT probe. Figure 51 shows the compiled set of resistance-displacement curves for the various levels of stress applied to the wire.

Unlike the Flexinol Ni-Ti alloy, the overall trends of the resistance-displacement behaviour of the Furukawa alloy are not dependent upon the applied stress conditions. However, both the electrical resistance and actuator displacement are influenced by the variation of applied stress. Maximum electrical resistance at the initial position in the martensite phase increases with increasing applied stress, while the minimum electrical resistance at the fully actuated position in the austenite phase shows negligible dependence upon the level of applied stress. The actuator displacement at both the

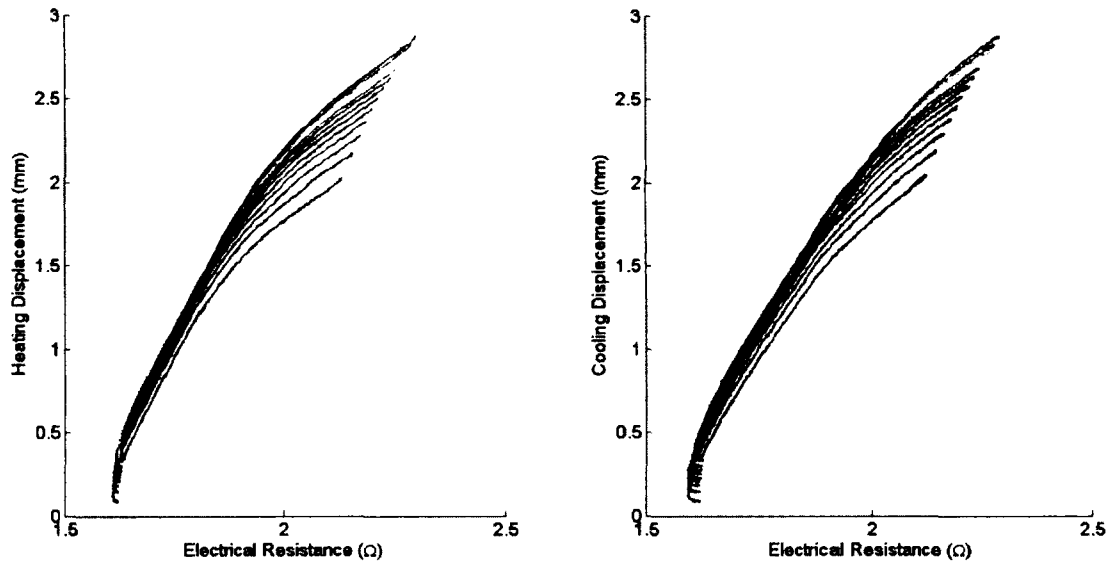


Figure 52: Influence of stress upon heating and cooling curves of the Furukawa actuator wire.

initial and fully contracted positions increases with increasing applied stress. Therefore, the trend of the resistance-displacement relationship remains similar but the boundaries of both resistance and displacement stretch depending upon the level of applied stress.

Total actuation displacement of the Furukawa wire increases with increasing applied stress, similar to the behaviour of the Flexinol alloy and also driven by both the variation of Young's modulus as well as the phase transformation process. The dependence between the phase transformation temperatures and applied stress, described in equations 2.9 and 2.10, causes a shift in the electrical resistivity throughout the heating and cooling curves. Figure 52 shows the difference between the heating and cooling curves at various stress levels.

Although the limits of the resistance-displacement curves for the Furukawa alloy depend upon the level of applied stress, the overall trend of the relationship remains similar. The heating and cooling curves both maintain the same relative hysteresis

gap, with no dependence upon stress as is caused by R-phase in the Flexinol alloy.

4.2.3 Minor Hysteresis Loops

Incomplete activation of the Furukawa actuator wire was studied to develop a complete model of the resistance-displacement behaviour for position control. The wide hysteresis gap observed in the resistance-displacement relationships of the Flexinol alloy caused the appearance of minor hysteresis loops during incomplete activation of the wire. However, the Furukawa alloy demonstrated a much smaller hysteresis gap within the resistance-displacement relationship and therefore the appearance of minor hysteresis effects was expected to be much more subtle and ineffectual in comparison. Investigation of the minor hysteresis loops within the resistance-displacement relationship of the Furukawa alloy was performed using the same procedure described for the Flexinol alloy. The actuator wire was partially activated to reach a series of test points using on-off control with position feedback. The test points were again arranged in order to achieve motion between each possible pair of initial and final positions. Incomplete actuation of the Furukawa actuator wire is demonstrated in the resulting resistance-displacement curves shown in Figures 53 through 55.

Heating and cooling of the Furukawa actuator wire through partial activation tends to follow the trends of the heating and cooling curves for full actuation. Transition between the two curves occurs during incomplete activation and results in the appearance of minor hysteresis loops. Since the heating and cooling resistance-displacement curves are close in proximity, the transition from one to the other is small and difficult to discern compared with the overall behaviour. The transition between the heating and cooling curves is smooth and gradual, and occurs due to the difference between phase transformation temperatures for the forward and reverse transformation processes. Overall, incomplete actuation of the Furukawa alloy shows negligible minor hysteresis effects compared with the Flexinol alloy.

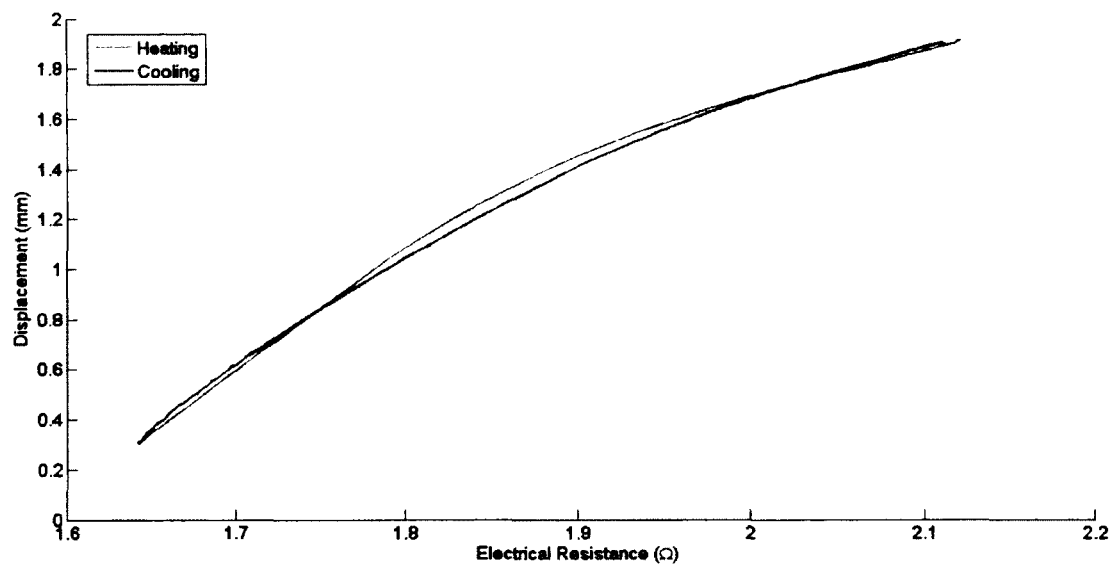


Figure 53: Minor hysteresis loop behaviour of Furukawa actuator wire (incomplete heating).

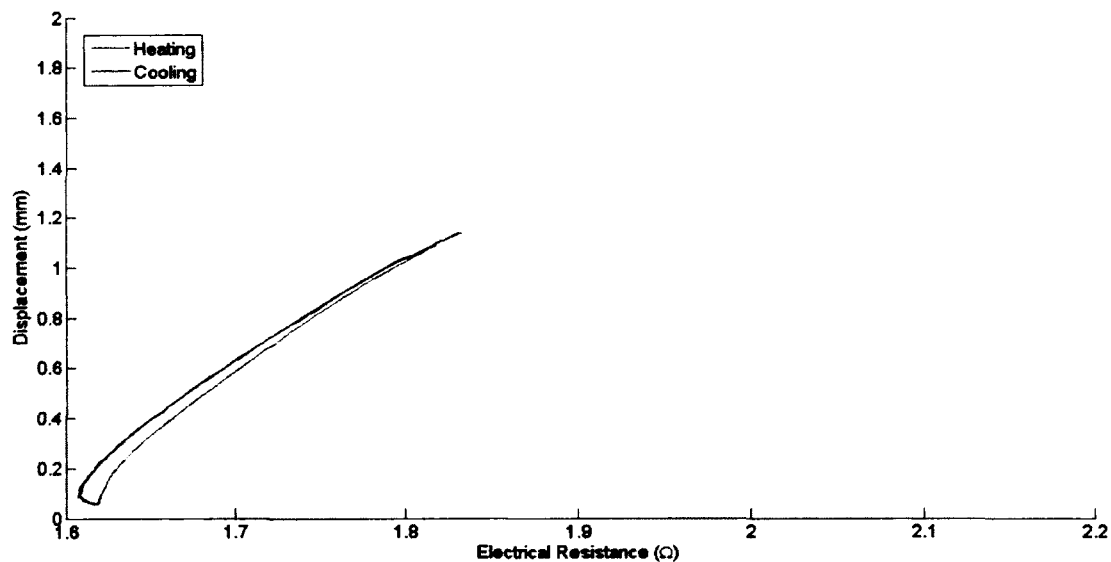


Figure 54: Minor hysteresis loop behaviour of Furukawa actuator wire (incomplete cooling).

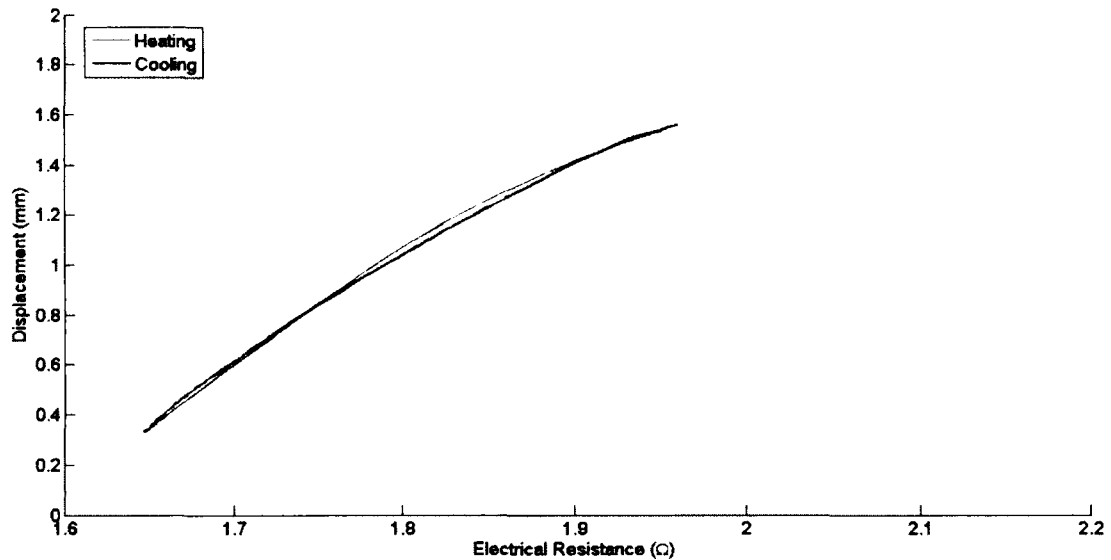


Figure 55: Minor hysteresis loop behaviour of Furukawa actuator wire (incomplete heating and cooling).

4.2.4 Training & Fatigue

As described previously, Nitinol shape memory alloy actuators suffer from fatigue over extended cyclic operation. The use of a copper addition in the Furukawa alloy has the benefit of greatly improving the fatigue life, which is an important consideration when applied as an actuator wire. Examination of the fatigue behaviour of the Furukawa alloy was accomplished using the same process described for the Flexinol alloy. Open-loop activation of the wire was performed using pulses of electrical current with amplitude and duration chosen to achieve full actuation and recovery under a constant applied load. Figure 56 demonstrates the fatigue behaviour for the Furukawa alloy actuator wire over 100 actuation cycles under an applied load of 1.26 N, where the color represents the cycle number starting from blue and shifting to red.

The effects of fatigue are less prominent in the cyclic response of the Furukawa alloy when compared to that of the Flexinol alloy. Both electrical resistance and

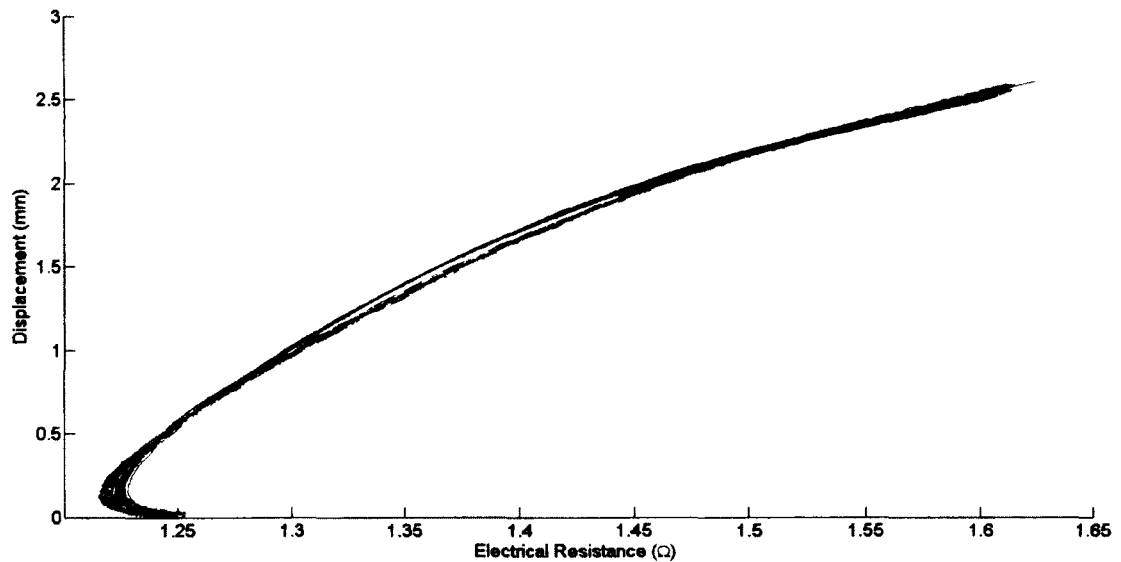


Figure 56: Fatigue behaviour of Furukawa actuator wire.

actuator displacement in the Furukawa alloy are affected by fatigue, but the relative amount of degradation is smaller. Minimum electrical resistance decreases as the actuator is cycled, but maximum electrical resistance appears to remain constant. Minimum and maximum actuator displacement both decrease over numerous loading cycles, with initially high rate of degradation associated with the training process discussed previously. The initial reduction in actuator displacement and the rate of actuator displacement degradation over subsequent cycles are much smaller compared to the fatigue behaviour of the Flexinol alloy.

The logarithmic fitting function proposed by Meier et. al. is also used to model the minimum and maximum values of electrical resistance and actuator displacement in terms of cycle number. Figure 57 shows the maximum and minimum values as well as the fitted curves.

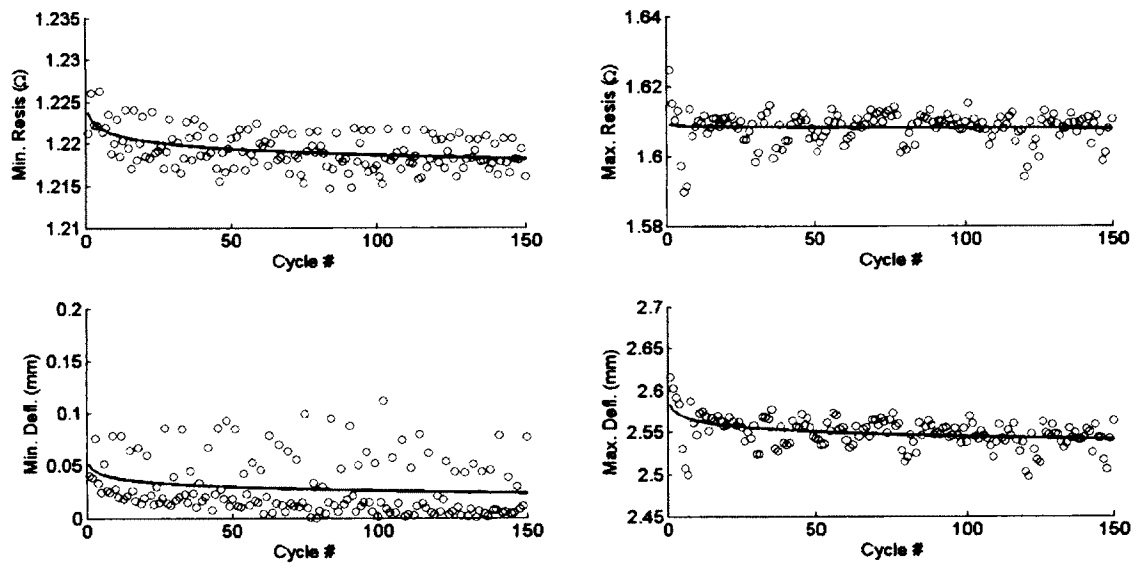


Figure 57: Minimum and maximum resistance and displacement during cycling including logarithmic curve fitting.

Chapter 5

Modeling

The relationships between electrical resistance, applied stress, and strain for shape memory alloy wire were modeled for the purpose of actuator position control using resistance feedback. The models were developed to predict actuator strain based on electrical resistance and applied stress, where the resistance is measured and the applied stress may be either measured or estimated depending upon the loading conditions. Development of the models was focused on capturing three important features of the material behaviour: the overall resistance-displacement relationships consisting of heating and cooling curves, the minor hysteresis effects due to incomplete actuation, and the influence of applied stress. These features are considered important in order to develop a comprehensive model for position control of shape memory alloy actuators under varying load conditions. Although the applied stress was included as an input parameter for the models, measurement of the load is not required if it is known or predictable. For example, an actuator which lifts a known mass allows the assumption of a constant load, while an actuator embedded within a composite structure allows the load to be predicted based on the structural stiffness.

Separate models were developed for the Ni-Ti Flexinol alloy and Ni-Ti-Cu Furukawa alloy due to the differences in overall resistance-displacement behaviour. The

resistance-displacement curves during forward and reverse phase transformation processes were represented by heating and cooling curves. Hysteresis effects which occur during the transition between these curves was considered in order to capture the effects of complete and partial actuation. Only the Flexinol alloy demonstrated significant hysteresis effects due to larger differences in the transformation temperatures and the presence of R-phase during phase transformation. Therefore, the major and minor hysteresis loops were modeled in detail for the Flexinol alloy, while the model for the Furukawa alloy was simplified to a single actuation curve. Both models account for the effect of varying applied stress upon the resistance-displacement relationship by defining the appropriate coefficients as functions of applied stress. Furthermore, the models were normalized for general application of either Ni-Ti or Ni-Ti-Cu shape memory alloy actuator wire of any length and diameter.

Previous modeling of the relationships between electrical resistance, applied stress, and strain for shape memory alloy actuator wires has either failed to cover all aspects of the behaviour or includes the use of temperature as a parameter. As discussed previously, models of the resistance-strain behaviour have been successfully applied to position control but were limited to a single load condition or reduced range of motion. More detailed modeling of the phase transformation process and constitutive relationship has required the use of temperature in order to predict the fractions of martensite and austenite. The actuator strain is then determined from the combined effect of applied stress and phase transformation. Temperature measurement is often difficult and the use of temperature sensors counteracts the benefit that was initially gained by eliminating the need for a position sensor using resistance feedback. Modeling the thermodynamics and heat transfer of the actuator system provides a method of predicting the temperature. However, the environmental conditions and system parameters must be known in order to accurately model heat losses, and errors in the

prediction of temperature would have a large effect upon the position control performance of the actuator. Additionally, if the actuator temperature and applied stress are both known, then the strain may be predicted from models which have already been established without considering electrical resistance.

Examination of the resistance-displacement curves which were observed and recorded during characterization of each alloy showed that the behaviour is non-linear and hysteretic. The option of rearranging previously established models in order to predict temperature and phase fraction based upon electrical resistance was not pursued since this approach would be needlessly complex. However, without the use of temperature as a parameter, it is difficult to develop a model which predicts phase transformation and strain based upon the currently established constitutive relationships. Instead, a curve fitting approach was used to approximate the relationships between electrical resistance, applied stress, and strain. Artificial neural networks and fuzzy logic may be used to capture the hysteresis and non-linear effects of the actuator behaviour, but these methods were ignored due to the unintuitive and enigmatic nature of the models that would be produced. Based upon initial inspection of the relationships between electrical resistance and displacement, curve fitting using linear, polynomial, and exponential functions was adopted for development of each model.

5.1 Flexinol

Modeling of the relationships between electrical resistance, applied stress, and strain for the Flexinol alloy required detailed consideration of the major and minor hysteresis loops. The hysteresis effects were exhibited in separate resistance-displacement curves during heating and cooling, as forward and reverse phase transformations occurred over different temperature ranges. Phase transformation during cooling also

caused the presence of R-phase, which had a significant effect upon the electrical resistance and widened the hysteresis loop. These heating and cooling curves are followed during both full and partial actuation, and both curves are approximately linear for the majority of the actuation range. Therefore, linear functions were used to model the primary heating and cooling curves within the resistance-displacement relationship. Transition between the heating and cooling curves was modeled using an exponential function where the slope of the transition curve approaches the slope of the appropriate heating or cooling curve.

The resulting behaviour of the model consists of the actuator resistance-displacement position asymptotically approaching and following the respective curve during heating and cooling. The heating and cooling curves are therefore referred to as asymptotes. Furthermore, the exponential transition curves are considered differentially in order to model minor hysteresis loops due to incomplete actuation or recovery. Applied stress had a significant effect upon the resistance-displacement relationship, causing the heating and cooling asymptotes to shift dramatically. The coefficients of the heating and cooling asymptotes were simply modeled as polynomial functions of the applied stress, while the exponential transition curves were assumed to be independent of applied stress. Therefore, the overall resistance-stress-strain model of Flexinol actuator wire consists of a hybrid model composed of linear heating and cooling asymptote curves with coefficients that are polynomial functions of stress as well as an exponential function for transition between each asymptote.

5.1.1 Heating & Cooling Curves

The resistance-displacement curves during heating and cooling are followed throughout both complete and partial actuation and form the basis for the development of the Flexinol model. Both curves are linear throughout the majority of the actuation range, with small non-linear and indeterminate regions at the beginning and

end of each curve. These extreme regions were ignored and therefore the working actuation range is reduced for an actuator applying this model for measurement or control. Analysis of the results from characterization of the Flexinol actuator wire yielded slope and intercept coefficients for heating and cooling asymptotes that fit the respective linear regions. Equations 5.1 and 5.2 are used to model the linear relationships of actuator displacement, δ , as a function of electrical resistance, R . The coefficients a and b represent the slope and intercept, respectively, and are denoted by the subscript H and C for the heating and cooling asymptotes.

$$\delta_H = a_H R + b_H \quad (5.1)$$

$$\delta_C = a_C R + b_C \quad (5.2)$$

Figure 58 shows the resistance-displacement major hysteresis loop of a Flexinol actuator wire subjected to a constant applied load of 0.47 N with the corresponding heating and cooling asymptotes.

Modeling the heating and cooling curves using linear functions resulted in a good approximation of the resistance-displacement behaviour over the majority of the actuation range. The non-linear and indeterminate regions were not well represented since the assumption of a linear relationship cannot accommodate those features. However, the region near full actuation does not deviate from the linear approximation greatly during heating and may be considered part of the transition curve during cooling. The region near full recovery shows a much larger section of non-linear and indeterminate behaviour and must therefore be ignored during application. The linear region of the heating curve is larger than that of the cooling curve, thus the accuracy of the model during cooling was expected to be lower than during heating. Nevertheless, the use of linear asymptote functions during actuation and recovery is suitable for representing the heating and cooling curves.

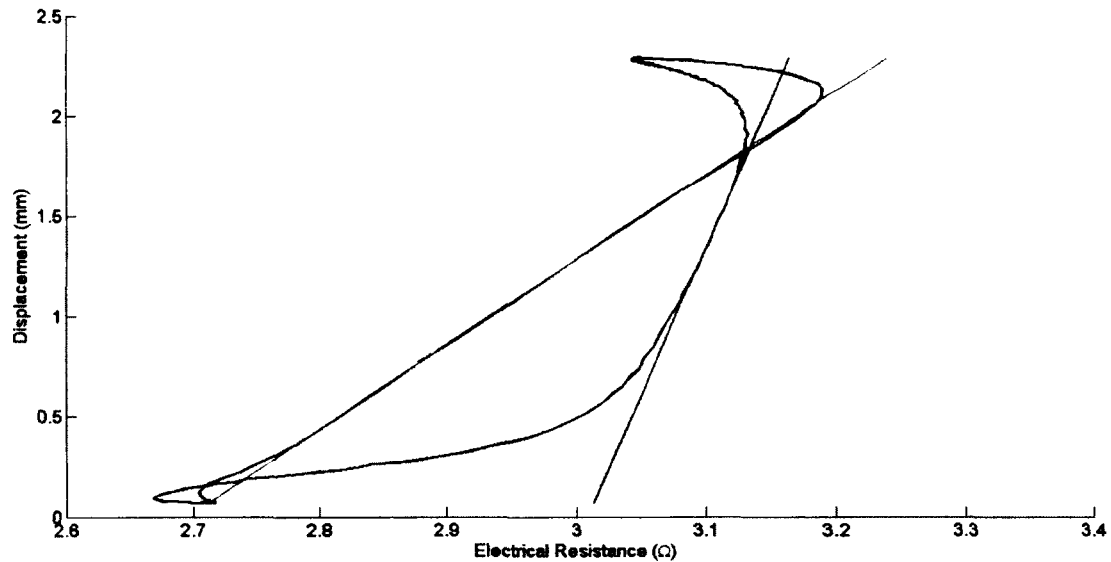


Figure 58: Heating and cooling asymptotes for major hysteresis loop of Flexinol wire.

The assumption of a linear model without any consideration of the hysteresis effect during transition results in errors of up to 300% of the actuator stroke. Characterization of the resistance-displacement relationship at various constant loads also revealed a dependency between applied stress and the shape of the heating and cooling curves. Therefore, consideration of the influence of applied stress and the hysteresis effects was required and will be discussed in subsequent sub-chapters.

5.1.2 Influence of Applied Stress

The influence of applied stress upon the resistance-displacement relationship of Flexinol has been studied during the experimental characterization of the material. Minimum and maximum electrical resistance and displacement as well as the shape of the resistance-displacement curve were all found to vary depending upon the level of applied stress. Although the shape of the overall major hysteresis loop changed

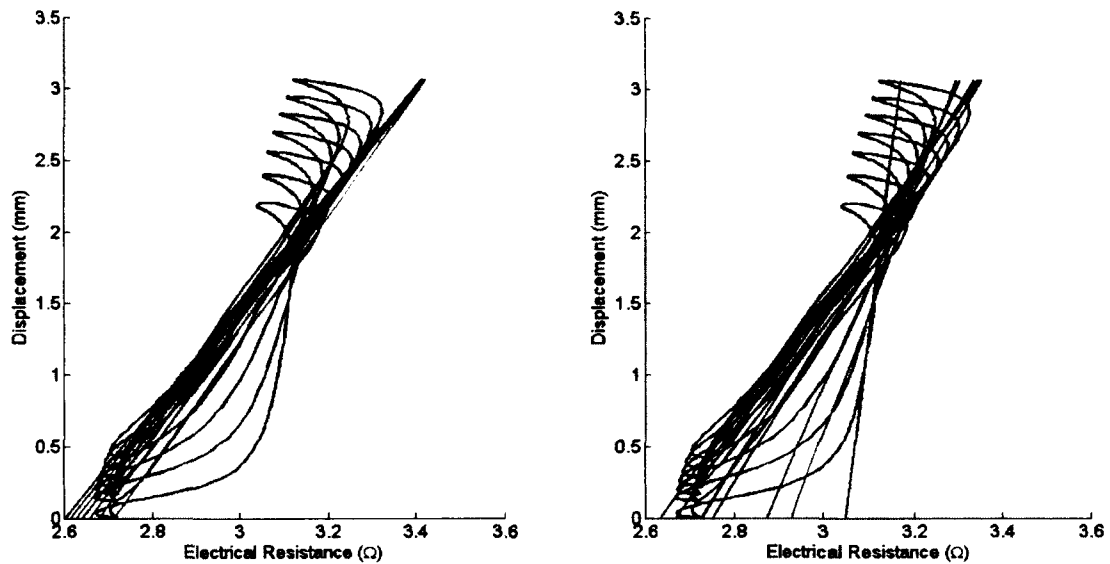


Figure 59: Families of heating and cooling asymptotes for Flexinol wire.

according to applied stress, the heating and cooling curves remained linear for the majority of the actuation range. Analyzing the heating and cooling asymptotes for each constant applied load resulted in a family of linear functions. This family of curves for the heating and cooling asymptotes was described by the variation in slope and intercept coefficients as a function of applied stress. Figure 59 shows the family of heating and cooling asymptotes while Figure 60 shows the relationships between slope and intercept coefficients and applied stress.

The family of heating asymptote functions shows only slight variations in the slope and intercept coefficients with increasing applied stress. Much larger variations are seen in the slope and intercept coefficients for the family of cooling asymptote functions. The slope coefficients of both heating and cooling asymptotes follow a decreasing trend with increasing applied stress, while the intercept coefficients of both asymptotes follow an increasing trend. Examination of Figure 60 showed that these trends are all non-linear, but appeared to be smooth and predictable monotonic

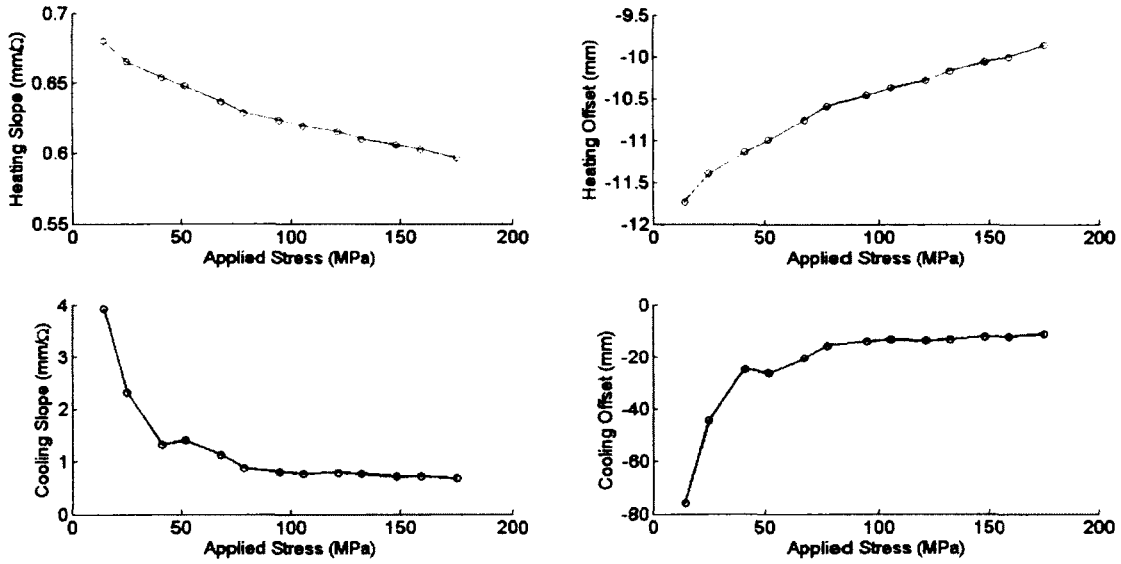


Figure 60: Slope and intercept coefficients of heating and cooling asymptotes for Flexinol wire.

curves. The heating slope and intercept coefficients experience continuous gradual change with respect to applied stress while the cooling coefficients show an exponential dependency. Second-order polynomial functions were chosen to model the slope and intercept coefficients as functions of applied stress. Equations 5.3 through 5.6 show the relationships used where the coefficients, β , are denoted with subscripts a and b for the slope and intercept, H and C for heating and cooling, and numbered indices according to the polynomial order.

$$a_H(\sigma) = \beta_{aH_2}\sigma^2 + \beta_{aH_1}\sigma + \beta_{aH_0} \quad (5.3)$$

$$b_H(\sigma) = \beta_{bH_2}\sigma^2 + \beta_{bH_1}\sigma + \beta_{bH_0} \quad (5.4)$$

$$a_C(\sigma) = \beta_{aC_2}\sigma^2 + \beta_{aC_1}\sigma + \beta_{aC_0} \quad (5.5)$$

$$b_C(\sigma) = \beta_{bC_2}\sigma^2 + \beta_{bC_1}\sigma + \beta_{bC_0} \quad (5.6)$$

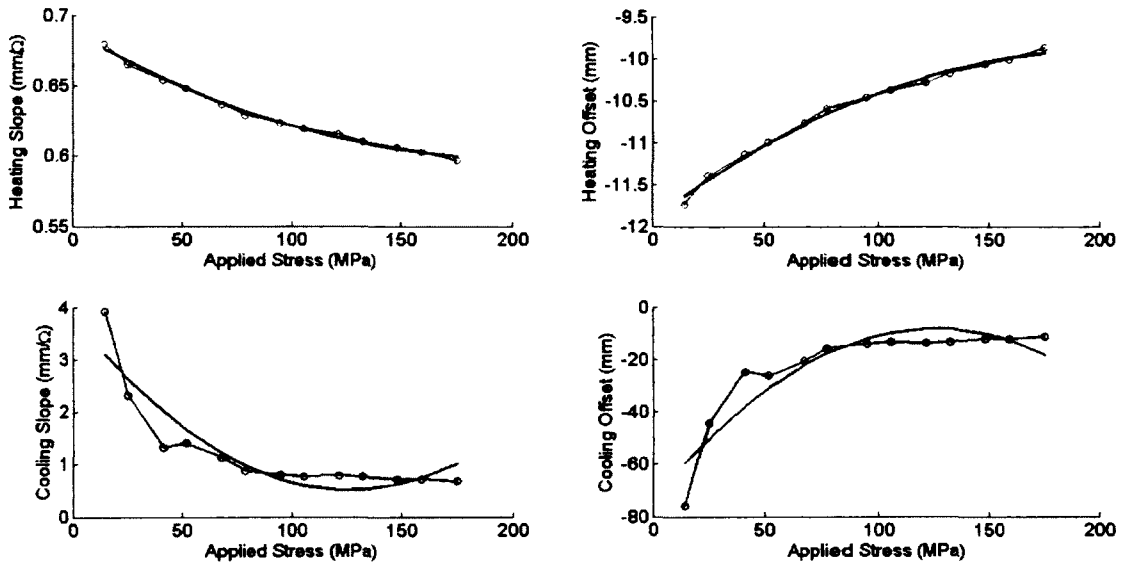


Figure 61: Polynomial fitting of relationships between applied stress and asymptote coefficients.

The stress coefficients, β , were determined from least-squares fitting of the estimated asymptote slope and intercept coefficients. The resulting curves fit the relationships of the slope and intercept coefficients as shown in Figure 61, which demonstrates the validity of using polynomial functions to model the influence of applied stress upon the asymptote functions.

In practice, the applied stress must be continuously used to update the slope and intercept coefficients of the heating and cooling asymptotes. If the applied stress is constant then the slope and intercept coefficients may be computed and treated as constants. In the case of bias spring loading, the applied load will be related to the actuator displacement and the stress terms within equations 5.3 through 5.6 may be replaced by the respective stiffness functions. More complicated loading conditions may be modeled separately in order to provide stress input to the shape memory alloy model.

The use of second-order polynomials is preferred in order to make application of

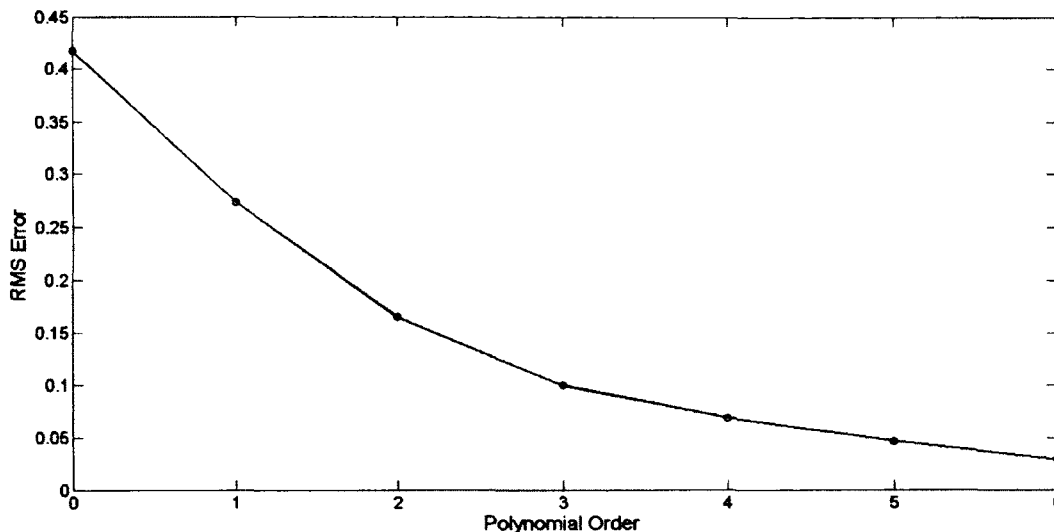


Figure 62: RMS error of model coefficients as a function of polynomial order.

the model easier within the LabView environment since the precision of the polynomial coefficients when exporting and importing from MATLAB using delimited text files may cause errors to occur. However, the RMS error of the slope and offset coefficients for the heating and cooling curves was investigated for polynomials of increasing orders (up to sixth-order). Figure 62 shows the decrease in error as the polynomial order is increased. Although higher order polynomials could be used to improve the performance of the model, the use of second-order polynomials is satisfactory for the scope of this research.

5.1.3 Hysteresis Loops

The overall resistance-displacement behaviour of the Flexinol shape memory alloy actuator wire was represented by the heating and cooling asymptotes. Although the influence of applied stress was investigated and modeled, the major and minor hysteresis loops were also modeled in order to account for transition between the heating

and cooling asymptotes. The resistance-displacement transition curves have previously been examined during experimental characterization of hysteresis effects within the Flexinol alloy. Both major and minor hysteresis loops follow a similar trend, where the resistance-displacement position of the actuator exponentially approaches the respective asymptote during heating or cooling. In order to include the hysteresis effects within the resistance-displacement model, the transition curves were modeled using an exponential function. The non-linear resistance-displacement curve during transition between heating and cooling curves represents phase transformation driven by thermodynamic processes, whose differential equations have exponential-based solutions. Therefore, the use of an exponential function to represent the transition curve is suitable. Many previous models of the phase transformation process have been based upon exponential functions, such as the model developed by Ikuta et. al. [164] and applied by Madill and Wang [171], as well as other constitutive relationships used by Shu et. al. [199], Shameli et. al. [173], and Jayender et. al. [179]. Furthermore, most artificial neural networks use activation functions which are based on exponential terms in order to capture non-linear and hysteretic behaviour.

Modeling of the transition curves between the heating and cooling asymptotes was accomplished using a differential approach in which the resistance-displacement gradient was modeled and integrated with respect to the change in resistance. This approach allows the same transition curve relationship to be applied at any location within the resistance-displacement actuation space, which is bounded between the heating and cooling asymptotes. Therefore, the effects of both major and minor hysteresis loops were captured and the actuator displacement could be modeled during full or partial activation. The slope of the resistance-displacement transition curve is modeled using an exponential function described by equation 5.7.

$$a = (a_F - a_0)e^{-\tau z} + a_0 \quad (5.7)$$

Where a is the slope of the resistance-displacement curve, a_F and a_0 are the initial and final slope values, τ is the transition parameter, and z is the difference between the electrical resistance on the heating or cooling asymptote and the resistance of the actuator. The transition curve was modeled using equation 5.7 for both heating and cooling processes, but the final slope value, a_F , and resistance difference, z , are different for each case. Equations 5.8 through 5.11 define the resistance difference, z , for both heating and cooling as denoted by the subscripts H and C . Equations 5.12 and 5.13 then describe the functions for transition from cooling to heating and vice versa.

$$z_H = R - R_H \quad (5.8)$$

$$z_C = R_C - R \quad (5.9)$$

$$R_H = \frac{\delta - b_H}{a_H} \quad (5.10)$$

$$R_C = \frac{\delta - b_C}{a_C} \quad (5.11)$$

$$a = (a_H - a_0)e^{-\tau z_H} + a_0 \quad (5.12)$$

$$a = (a_C - a_0)e^{-\tau z_C} + a_0 \quad (5.13)$$

When the actuator is initially departing either asymptote, the resistance difference between the actuator and the other asymptote is large. Therefore the exponential term within the transition curve function becomes small, and the slope of the transition curve is approximately the initial value, a_0 . As the actuator resistance changes, the transition curve begins to approach the relevant asymptote, hence reducing the resistance difference, z . As the resistance difference diminishes, the slope of the transition curve exponentially approaches the slope of the asymptote curve. Similar to a simple first-order control law, the resistance difference ensures that the transition curve approaches and follows the appropriate asymptote.

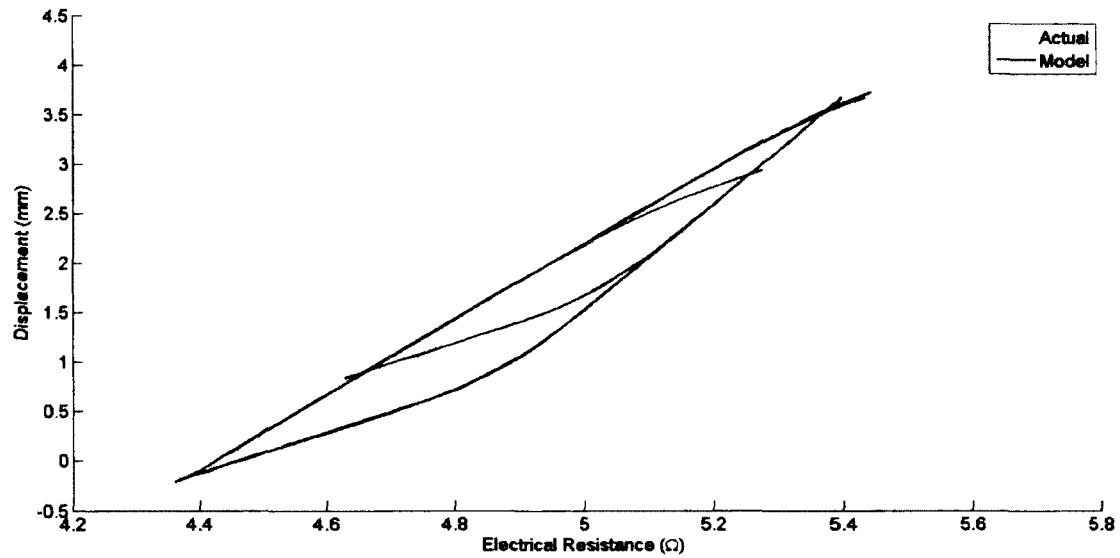


Figure 63: Exponential transition curves for Flexinol wire.

After analyzing data from the material characterization of the minor hysteresis loops, the values for τ and a_0 were determined through trial and error in order to match the measured transition curves. Application of the exponential transition functions to the experimental resistance data resulted in the comparison of experimental and modeled transition curves shown in Figure 63.

The overlap between experimental data and the model shows that the exponential relationships defined by equation 5.12 and 5.13 successfully capture the behaviour during transition between heating and cooling asymptotes. Some error occurs due to a slight shift in the cooling asymptote and the use of constant values for the initial slope and transition parameter. Given the linear heating and cooling asymptotes, the influence of stress upon the asymptote coefficients, and the exponential curves during transition between asymptotes, the comprehensive model is ready for application in resistance feedback position control of Flexinol shape memory actuator wire.

5.1.4 Simulation

Numerical simulation of the Flexinol model was used to validate the overall performance based on experimental data obtained during characterization of the material. The performance of the model was evaluated by simulating the response under various load conditions and through both complete and partial actuation cycles. While the model was developed from experimental curves of electrical resistance and strain at constant applied loads, the response under varying applied load was also examined. Application of the model within a numerical simulation required that appropriate conditions be applied and the system of equations discretized. After recasting the relationships for discrete numerical modeling, the set of equations for the Flexinol model of resistance-stress-strain behaviour is summarized in equations 5.14 to 5.23.

Most parameters must be computed at each time step with the exception of the established model coefficients. Therefore, the subscript k is used on each parameter to represent the discrete time step index. The first step in the simulation process is to compute the values of the heating and cooling asymptote slope and intercept coefficients from the current measurement or predicted applied stress. Equations 5.14 to 5.17 are used to determine the asymptote coefficients at time step k .

$$a_{H,k} = \beta_{aH_2}\sigma_k^2 + \beta_{aH_1}\sigma_k + \beta_{aH_0} \quad (5.14)$$

$$b_{H,k} = \beta_{bH_2}\sigma_k^2 + \beta_{bH_1}\sigma_k + \beta_{bH_0} \quad (5.15)$$

$$a_{C,k} = \beta_{aC_2}\sigma_k^2 + \beta_{aC_1}\sigma_k + \beta_{aC_0} \quad (5.16)$$

$$b_{C,k} = \beta_{bC_2}\sigma_k^2 + \beta_{bC_1}\sigma_k + \beta_{bC_0} \quad (5.17)$$

Given the slope and intercept coefficients of the heating and cooling asymptotes, the respective values of electrical resistance may be computed for each asymptote

at the current displacement. Since the model is discretized and the current strain position is unknown, the previous displacement was used to determine the heating and cooling asymptote resistance values. Equations 5.18 and 5.19 are used to compute the respective resistance values of the heating and cooling asymptotes.

$$R_{H,k} = \frac{\delta_{k-1} - b_{H,k}}{a_{H,k}} \quad (5.18)$$

$$R_{C,k} = \frac{\delta_{k-1} - b_{C,k}}{a_{C,k}} \quad (5.19)$$

The differences between the electrical resistance of the actuator and each asymptote are then determined from equations 5.20 and 5.21.

$$z_{H,k} = R_k - R_{H,k} \quad (5.20)$$

$$z_{C,k} = R_{C,k} - R_k \quad (5.21)$$

The slope of the actuator resistance-displacement curve was then determined from the appropriate asymptote slope and electrical resistance difference, depending upon whether heating or cooling was occurring. Although temperature was not measured and the heat transfer was not modeled, heating and cooling of the actuator may be differentiated based upon the applied power settings. This choice is simple for on-off control algorithms since the actuator may be assumed to experience heating while the controller is on and cooling when the controller is off. For more complex algorithms such as PID control the applied power input may be compared to a threshold level in order to estimate whether the actuator is heating or cooling. Furthermore, the rate of change of electrical resistance may also provide an indication of the heating or cooling condition assuming the actuator is performing within the determinate region of the resistance-displacement space.

Equations 5.22 and 5.23 are used to determine the slope of the actuator resistance-displacement curve, where equation 5.22 is applied during heating and equation 5.23 is applied during cooling.

$$a_k = (a_{H,k} - a_0)e^{-\tau z_{H,k}} + a_0 \quad (5.22)$$

$$a_k = (a_{C,k} - a_0)e^{-\tau z_{C,k}} + a_0 \quad (5.23)$$

After selecting the appropriate slope function, the actuator displacement was then determined using equation 5.24, which is simply discrete forward integration of the displacement based upon the change in electrical resistance and modeled resistance-displacement slope. The actuator displacement is related to the strain, ε_k , and initial actuator length, L_0 , using equation 5.25.

$$\delta_k = a_k(R_k - R_{k-1}) + \delta_{k-1} \quad (5.24)$$

$$\delta_k = \varepsilon_k L_0 \quad (5.25)$$

In discrete numerical simulation, it is possible for the actuator wire resistance-displacement position to cross either the heating or cooling asymptote as it is approached. The exponential relationship of the transition curves then causes the actuator displacement to diverge and the model collapses. In order to avoid this numerical problem, the resistance differences may be monitored and saturated in order to ensure the values are always positive.

Simulation of the resistance-stress-strain model for Flexinol was performed in Mathworks MATLAB based on coefficients determined from material characterization. The described process of discrete simulation was used in order to predict the actuator displacement given the electrical resistance and applied stress measurements. Actual actuator displacement was provided by the position feedback of the LVDT

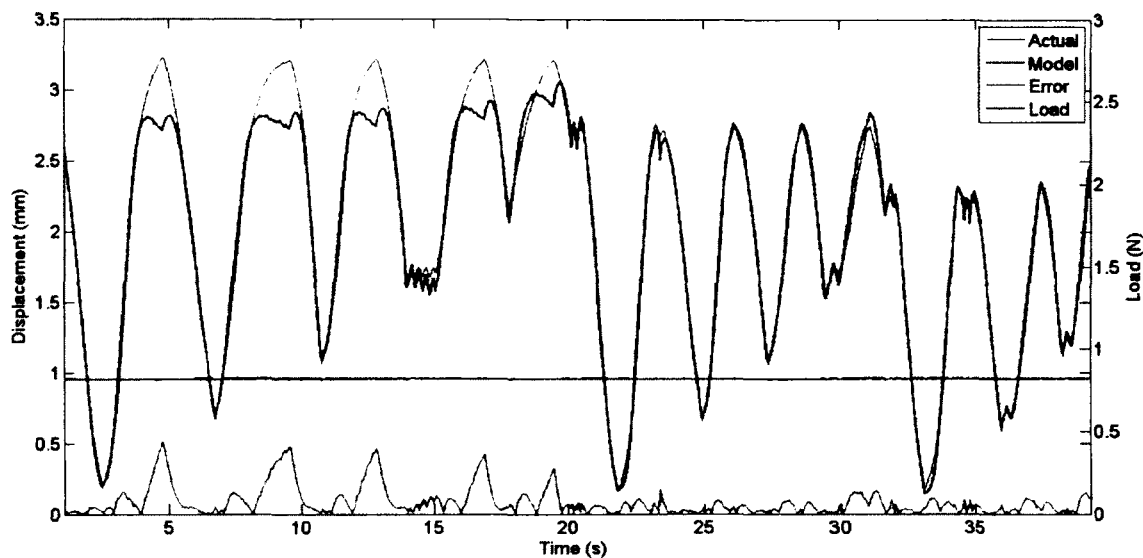


Figure 64: Simulation results for the Flexinol model under constant load of 0.49 N.

sensor, and was compared to the model output in order to assess the accuracy and performance of the model. The model was simulated under various conditions of constant applied stress and activated through full and partial actuation. Loading of the actuator using a spring fixed to the test stand was also simulated in order to test the performance of the model under varying stress conditions.

Results of the simulation of the Flexinol model are shown in Figures 64 through 73, including the displacement profile over the duration of each experiment as well as the resistance-displacement curves. Figures 64 through 69 show the results of simulation under constant applied load conditions, while Figures 70 through 73 show the results of simulation under the spring constraint loading condition. The displacement profiles show actual actuator displacement and model prediction, along with the applied load and absolute error between the actual and model displacements. The impact of assuming a constant applied load under varying load conditions was also investigated, where the results are shown in Figures 72 and 73.

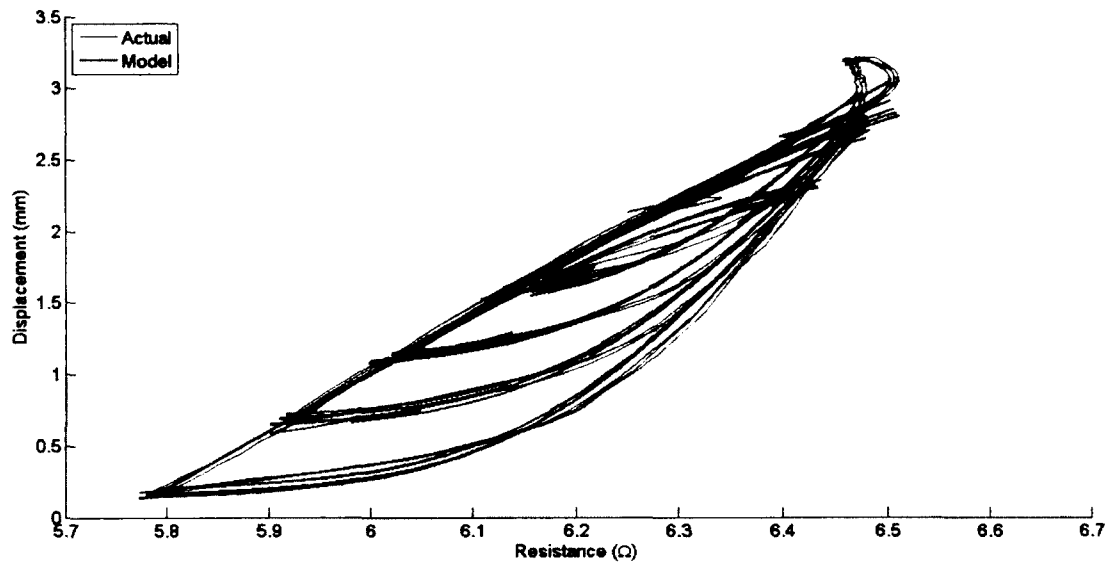


Figure 65: Simulated resistance-displacement curves for the Flexinol model (0.49 N).

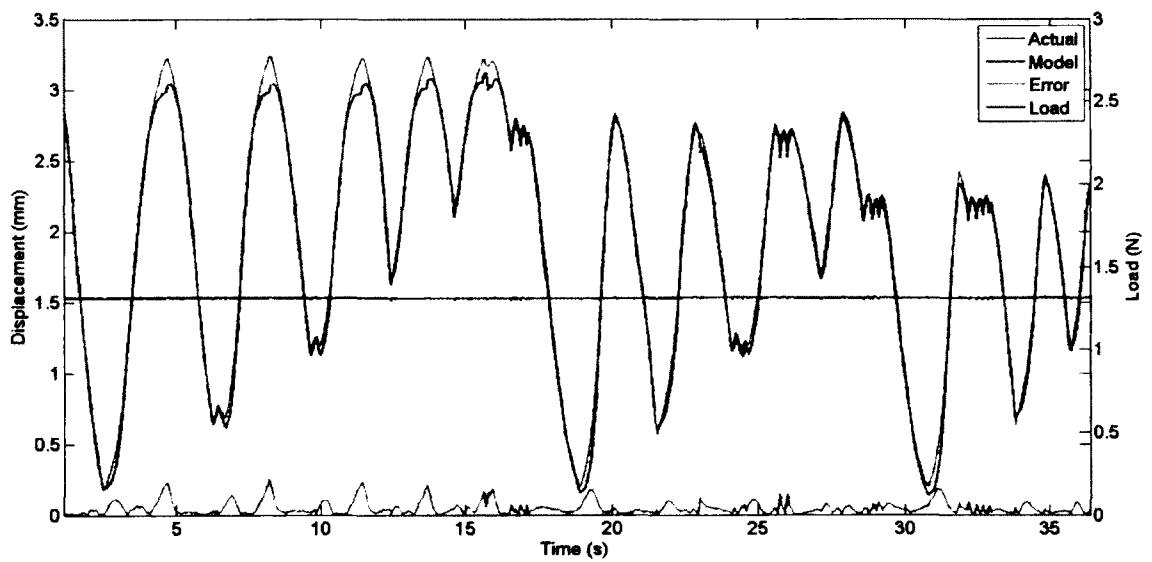


Figure 66: Simulation results for the Flexinol model under constant load of 0.98 N.

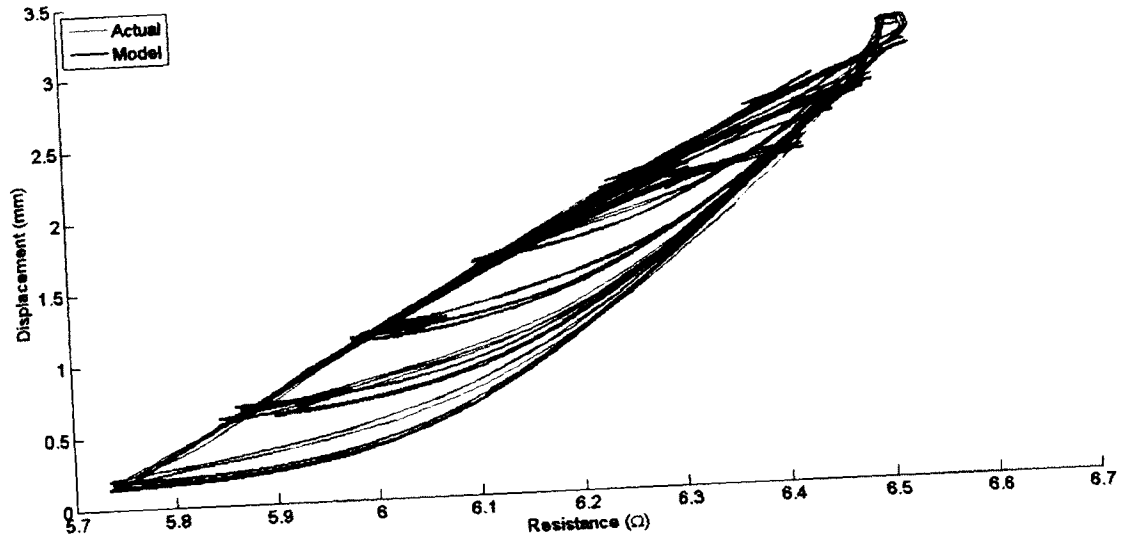


Figure 67: Simulated resistance-displacement curves for the Flexinol model (0.98 N).

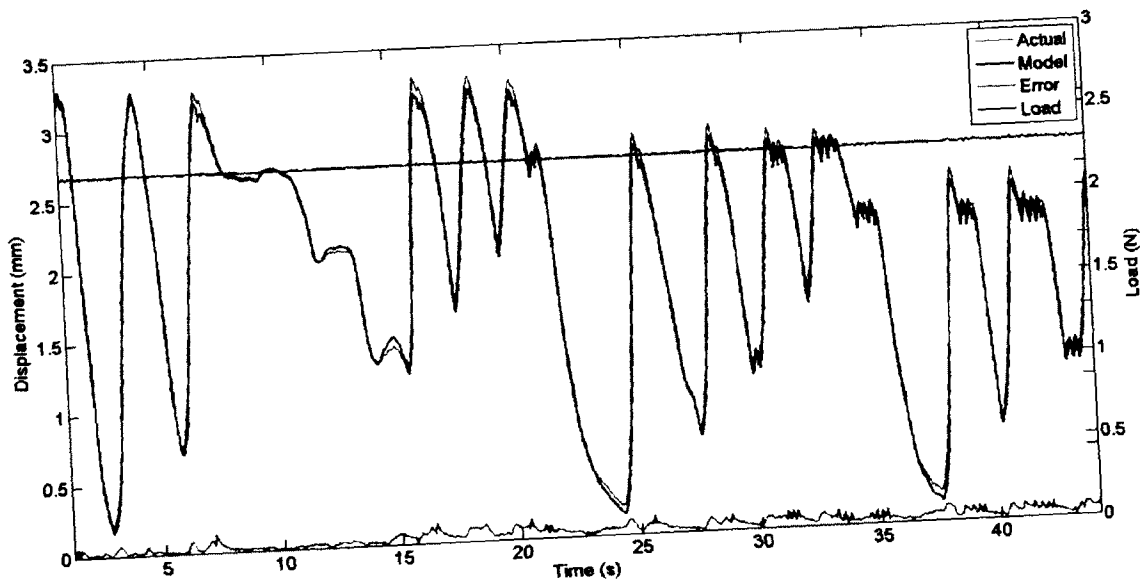


Figure 68: Simulation results for the Flexinol model under constant load of 1.96 N.

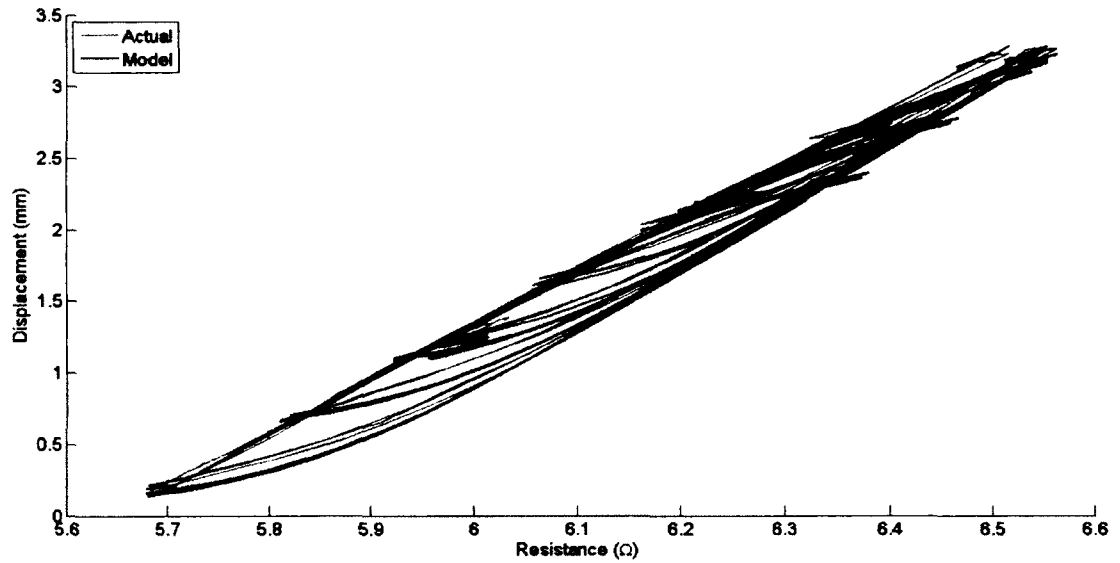


Figure 69: Simulated resistance-displacement curves for the Flexinol model (1.96 N).

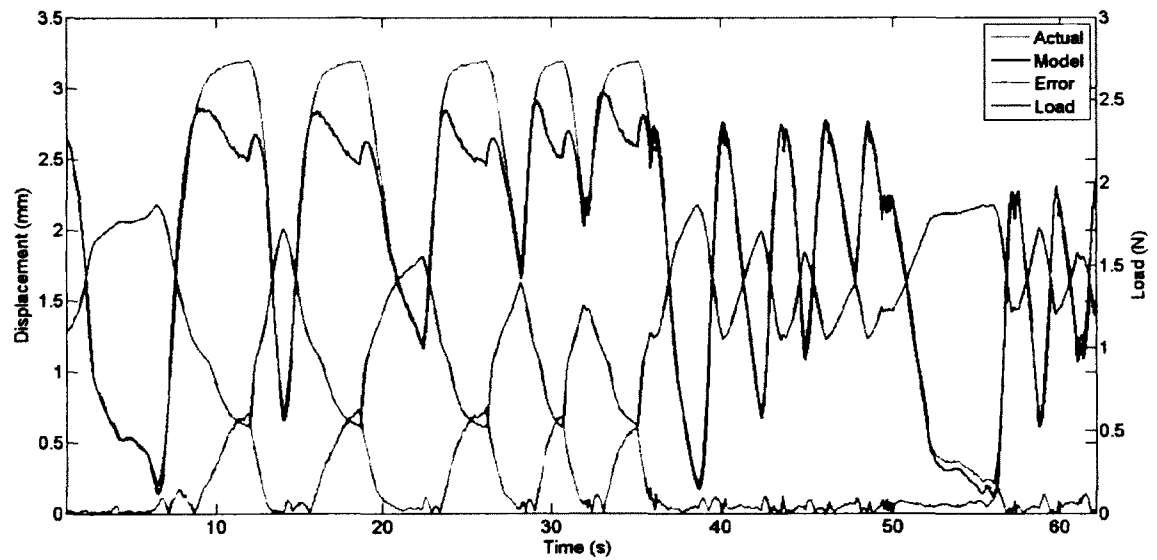


Figure 70: Simulation results for the Flexinol model under spring constraint loading.

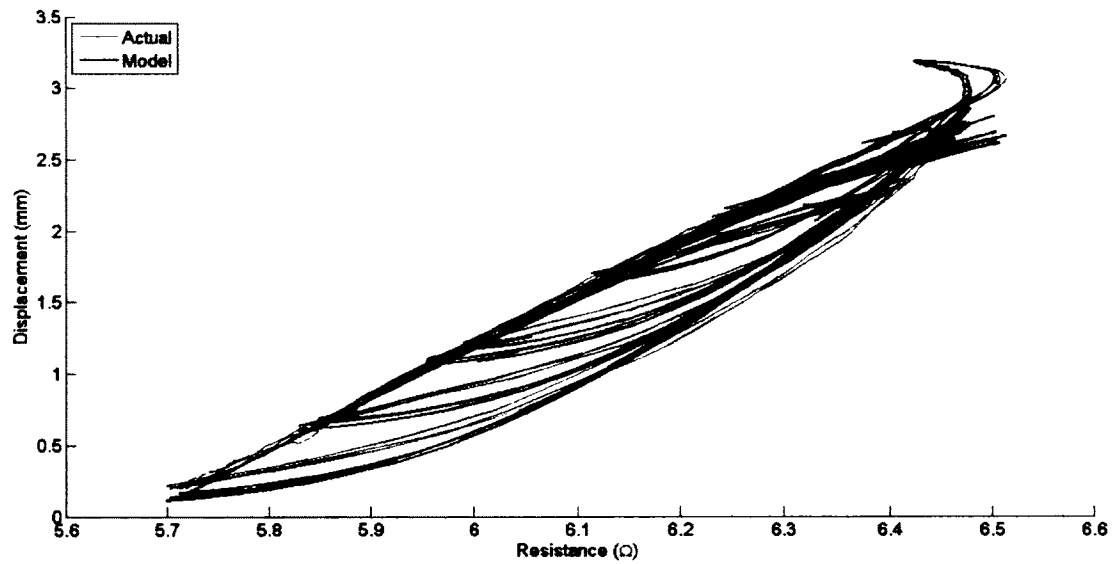


Figure 71: Simulated resistance-displacement curves for the Flexinol model (spring constraint).

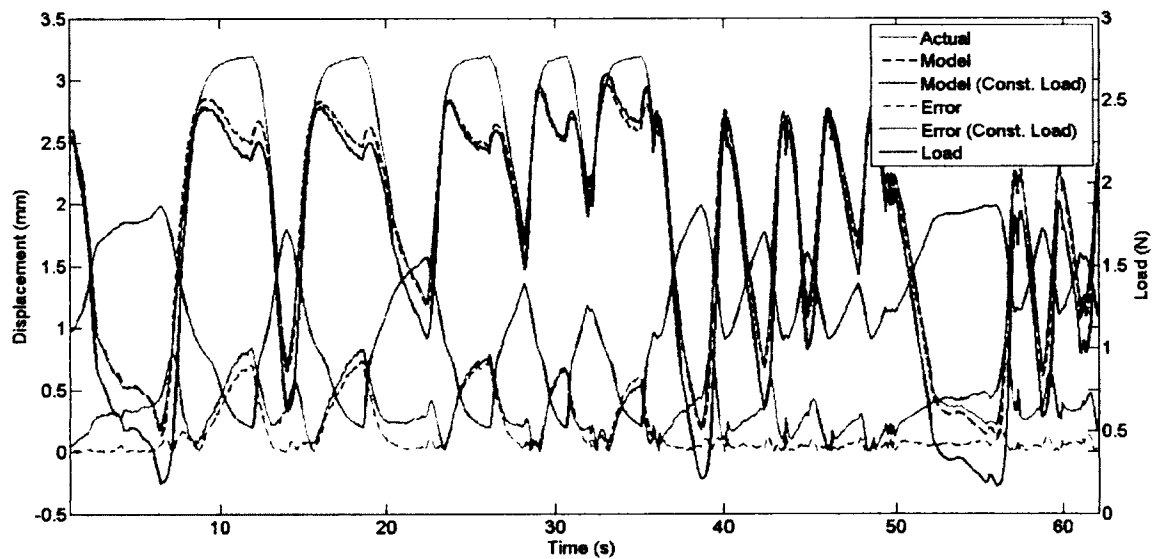


Figure 72: Simulation results for the Flexinol model under spring constraint loading while assuming constant applied load.

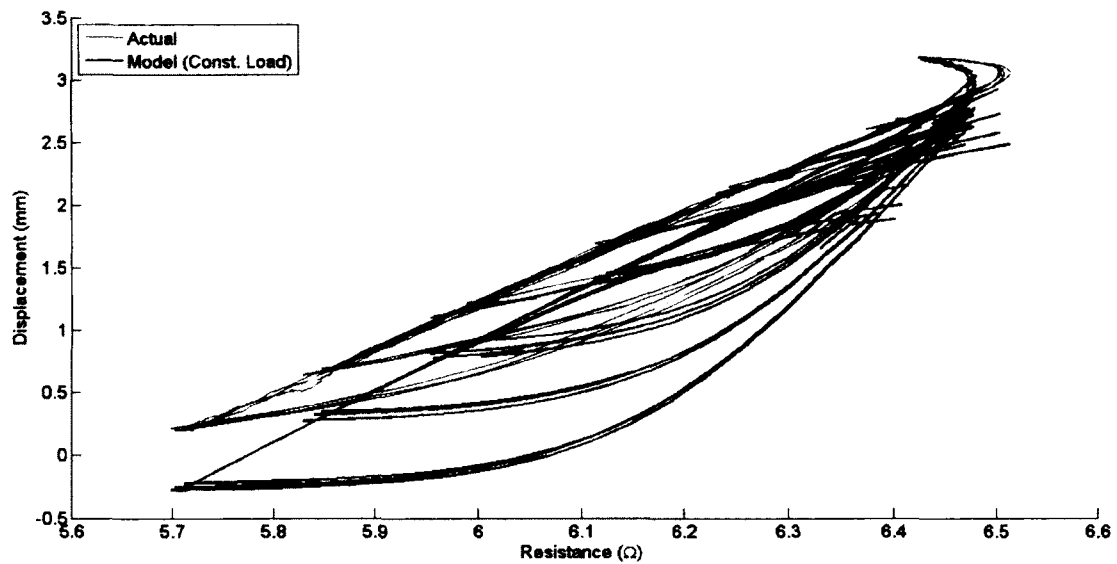


Figure 73: Simulated resistance-displacement curves for the Flexinol model (spring constraint with assumption of constant applied load).

The results of the simulation demonstrate successful prediction of the actuator displacement under both constant load conditions and varying load conditions. Although the highly non-linear indeterminate region at the upper limit of the stroke range results in large errors, the Flexinol model captured the overall behaviour with a mean error of approximately 2.03% of the total typical actuator stroke of 4% strain. Plots of the resistance-displacement hystereses in Figures 67, 69, and 71 emphasize the ability of the model to capture the primary heating and cooling curves as well as the intermediary transition curves.

Table 2 summarizes the mean error for each experiment, where the model was simulated both with and without the inclusion of stress influence effects. The assumption of a constant load during the application of spring constraint conditions resulted in larger errors, as seen in Figures 72 and 73, with a mean value of 7.76% of the total stroke.

Load Condition	Mean Error (% Stroke)	
	Stress Influence	Constant Load
Constant (0.49 N)	1.99	2.26
Constant (0.98 N)	1.36	6.48
Constant (1.96 N)	1.26	13.15
Spring Condition	3.52	9.15

Table 2: Mean absolute error for simulations under each load condition with stress influence effects included as well as assuming a constant load condition.

5.1.5 Normalization

Modeling of the resistance-stress-strain behaviour of Flexinol alloy actuator wire has been successfully demonstrated through simulation. The model has been developed using relationships which may be easily characterized for various actuator wires of different length or material properties. However, further analysis of the model coefficients for a set of actuators of varying length showed that the resistance-stress-strain behaviour may be normalized with respect to the original actuator dimensions. Normalization of the Flexinol model was therefore performed in order to present a model of the resistance-stress-strain behaviour which may be applied in position control algorithms for actuators of various dimensions. Figure 74 shows the resistance-length response curves of a set of five different Flexinol actuator wires of different lengths.

The model was altered in order to capture the resistivity-stress-strain behaviour, where the resistance was normalized with respect to an initial reference point. Equation 5.26 shows the normalized electrical resistance, λ , as a function of the actuator resistance, R , and initial resistance, R_0 .

$$\lambda = \frac{R}{R_0} \quad (5.26)$$

The initial resistance at zero applied load is used for R_0 , corresponding to a point

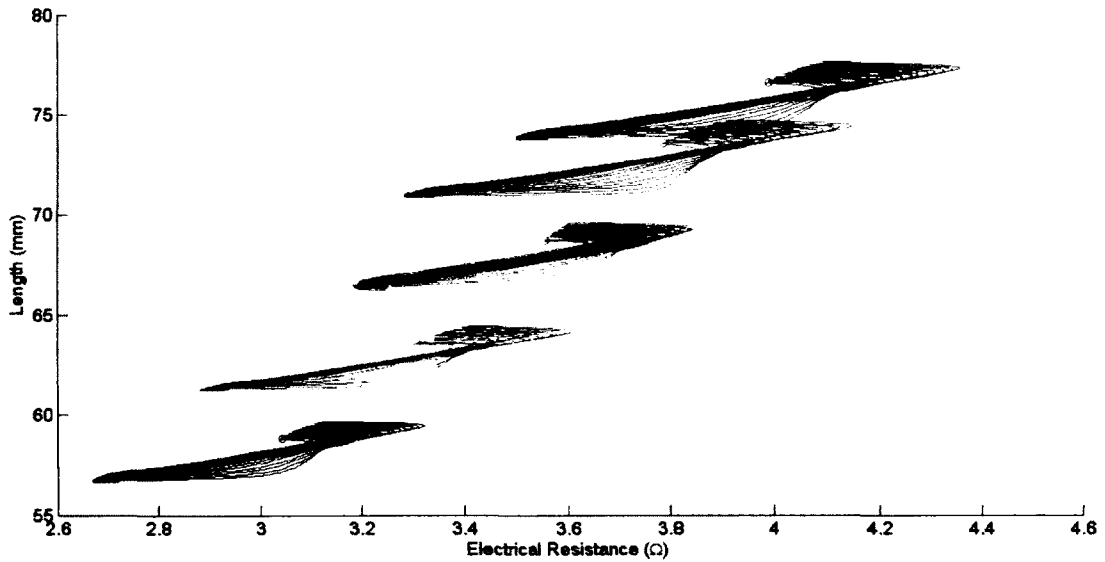


Figure 74: Resistance-strain responses of Flexinol actuator wires with various lengths.

at which the actuator is composed entirely of martensite, while equation 5.27 is used to describe the initial resistance in terms of actuator geometry. The initial resistance is determined from the resistivity of martensite, ρ_M , and initial length, L_0 , and cross-section area, A_0 , of the actuator wire.

$$R_0 = \frac{\rho_M L_0}{A_0} \quad (5.27)$$

Figure 5.17 shows the initial resistance for the various wire lengths previously presented in Figure 5.16. As predicted, the initial resistance is linearly proportional to the wire length, and least-squares fitting of the data resulted in a linear function which passes through the origin. The slope of the linear fitting curve was also used to determine the resistivity of martensite for application in the normalized model.

The normalized electrical resistance must also be accounted for within the slope and intercept coefficients of the heating and cooling asymptotes. Equations 5.1 and

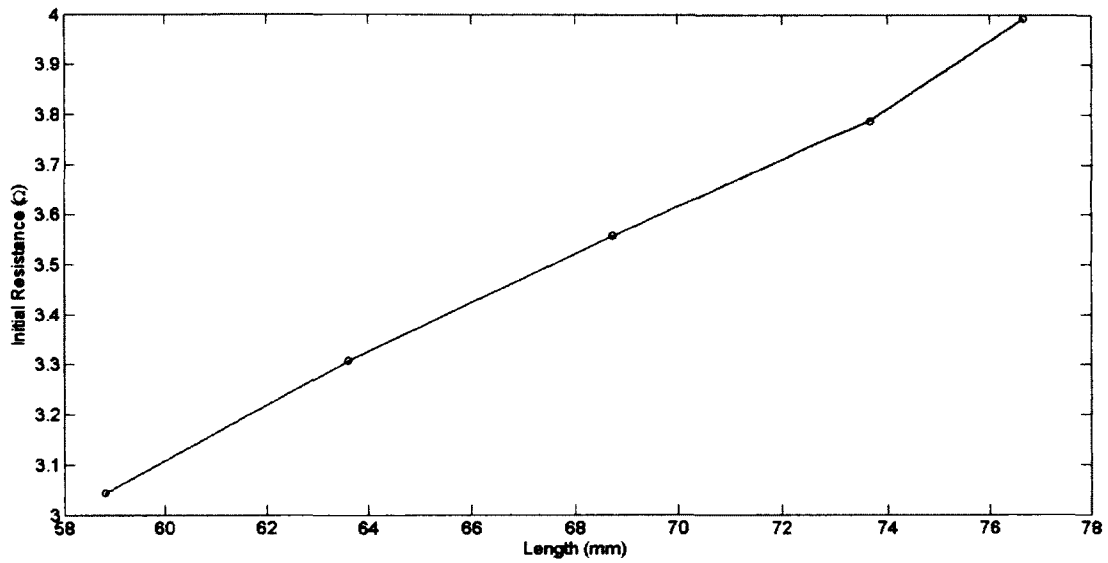


Figure 75: Initial resistance of Flexinol actuator wires with various lengths.

5.2 were therefore modified to be functions of normalized resistance, λ , described by equations 5.28 and 5.29. The slope and intercept coefficients were also modified according to equations 5.30 through 5.33.

$$\varepsilon_H = \tilde{a}_H \lambda + \tilde{b}_H \quad (5.28)$$

$$\varepsilon_C = \tilde{a}_C \lambda + \tilde{b}_C \quad (5.29)$$

$$\tilde{a}_H = a_H R_0 \quad (5.30)$$

$$\tilde{a}_C = a_C R_0 \quad (5.31)$$

$$\tilde{b}_H = \frac{b_H}{L_0} \quad (5.32)$$

$$\tilde{b}_C = \frac{b_C}{L_0} \quad (5.33)$$

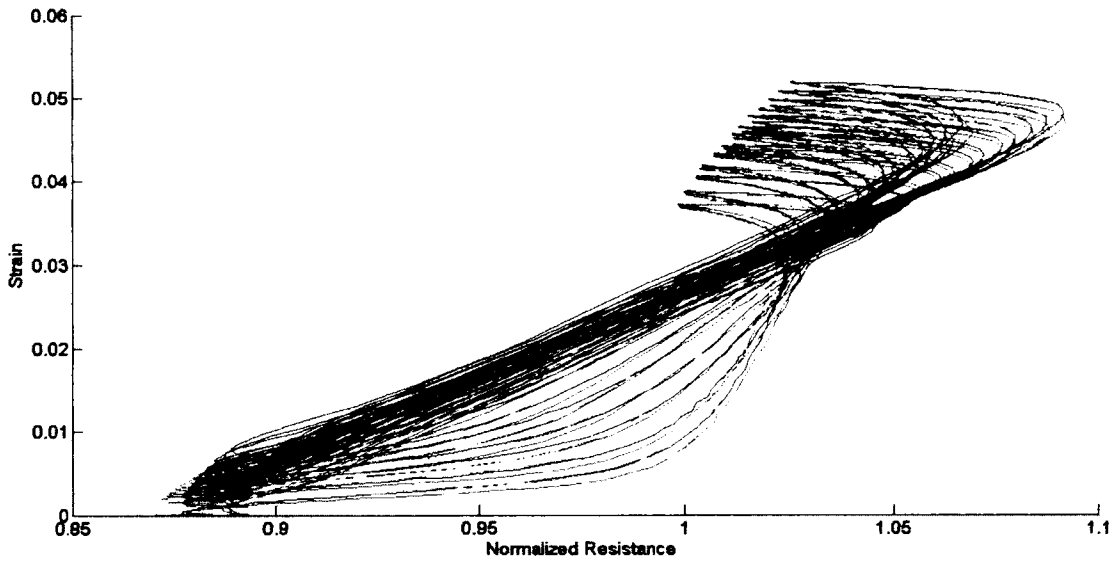


Figure 76: Normalized actuation curves of Flexinol actuator wires with various lengths.

The resulting β stress coefficients described in equations 5.3 to 5.6 were determined from analysis of a set of asymptotes determined under various load conditions. However, normalization of the electrical resistance modifies the relationship for the stress coefficients of a_H and a_C similar to the functions described in equations 5.30 through 5.33. The relationships between the normalized electrical resistance and asymptote coefficients are independent of the applied stress, as shown in Figure 76, which demonstrates the normalized curves for the various lengths of actuator wire.

The exponential transition curves were also normalized, and equations 5.8 through 5.13 were all modified to be functions of normalized electrical resistance. Equations 5.34 through 5.39 show the modified functions for the transition curves.

$$\tilde{z}_H = \lambda - \lambda_H \quad (5.34)$$

$$\tilde{z}_C = \lambda_C - \lambda \quad (5.35)$$

$$\lambda_H = \frac{\varepsilon - \tilde{b}_H}{\tilde{a}_H} \quad (5.36)$$

$$\lambda_C = \frac{\varepsilon - \tilde{b}_C}{\tilde{a}_C} \quad (5.37)$$

$$\tilde{a} = (\tilde{a}_H - \tilde{a}_0)e^{-\tau \tilde{z}_H} + \tilde{a}_0 \quad (5.38)$$

$$\tilde{a} = (\tilde{a}_C - \tilde{a}_0)e^{-\tau \tilde{z}_C} + \tilde{a}_0 \quad (5.39)$$

During discrete simulation and control, the actuator strain was determined from equation 5.40, which is the normalization of the forward integration function presented in equation 5.24.

$$\varepsilon_k = \tilde{a}_k(\lambda_k - \lambda_{k-1}) + \varepsilon_{k-1} \quad (5.40)$$

The resulting normalized model was characterized from experimental data in order to determine the polynomial stress influence coefficients, β , initial martensite resistivity, ρ_M , and transition curve parameters \tilde{a}_0 and τ .

5.1.6 Model Correlations

The research presented in this thesis focuses on the development of predictive strain models based upon measurement of the electrical resistance and applied stress as inputs. The actuator temperature is not included within the model since the phase transformation processes are instead indicated by the electrical resistance. Although the exclusion of temperature simplifies the practical application of the model, it is still the driving parameter within the phase transformation processes. Consequently, the established relationships described previously cannot be used within the model if the actuator temperature is unknown.

Recent research by Brammajyosula et. al. has demonstrated the extension of the Liang & Rogers model to include R-phase transformation in order to predict the electrical resistance and strain based upon input of the temperature and applied

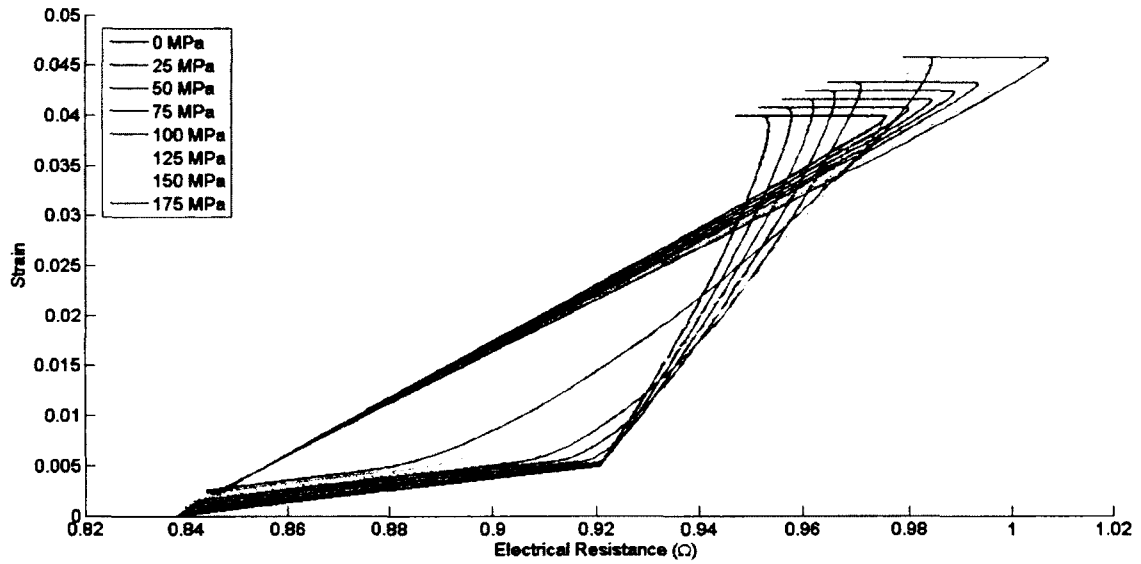


Figure 77: Simulated actuation curves of Ni-Ti actuator wire using the extended model by Brammajyosula under various constant applied loads.

stress [145]. Therefore, this extended model may be used for comparison in order to investigate correlations between the previously established relationships and the Flexinol models developed in this thesis. The extended model developed by Brammajyosula is based upon the Liang & Rogers model described previously but includes an R-phase fraction parameter along with the appropriate phase transformation equations, mixing rule, and constitutive equation.

Simulation of the extended model was performed in MATLAB, where the actuator temperature and applied stress were prescribed as inputs. The actuator temperature was linearly increased from just below the martensite finish phase transformation temperature to just above the austenite finish temperature, and then decreased linearly back to the initial point. This resulted in a complete actuation and recovery of the actuator wire, and was simulated at various levels of constant applied stress. The resulting family of hysteresis curves, shown in Figure 77, closely resembles the experimental results.

The results of the Brammajyosula model simulations reveal similar trends as observed in the experimental response of the Flexinol alloy. The linear asymptotes during heating and cooling are apparent in the extended model, as well as the significant dependence upon applied stress. Most importantly, analysis of the phase transformation temperatures provides an explanation for the large stress-dependent hysteresis caused by the presence of R-phase. Figure 78 shows the relationship between austenite, martensite, and R-phase transformation temperatures and the applied stress. During heating, the transformation process from martensite to austenite occurs as the temperature increases from A_s to A_f . As the actuator cools, the alloy transforms from austenite to R-phase and then from R-phase to martensite. However, at higher levels of applied stress, the transformation from R-phase to martensite starts before the transformation from austenite to R-phase has completed. Since the resistivity of R-phase is much greater than that of austenite and martensite, significant hysteresis is caused by the intermediary transformation from austenite to R-phase during cooling. As the level of applied stress is increased, the amount of R-phase present during cooling is decreased and the size of the hysteresis is reduced.

Considering the established relationships between resistivity, temperature, length, and strain, the Liang & Rogers constitutive and phase transformation equations, as well as the simple mixing rule for material properties, analytical expressions were determined for the Flexinol model coefficients (slope and offset parameters a_H , b_H , a_C , and b_C). The heating asymptote was assumed to connect the point at which the actuator is at the austenite start temperature, A_s , composed of martensite, and fully elongated, to the point at which the actuator is at the austenite finish temperature, A_f , composed of austenite, and fully contracted. Therefore, equations 5.41 to 5.44 describe the resistance and displacement of the start and finish points of the heating asymptote, which are found through substitution of the appropriate temperature and strain values within equations 2.12, 2.13, and 2.14. The temperature varies from

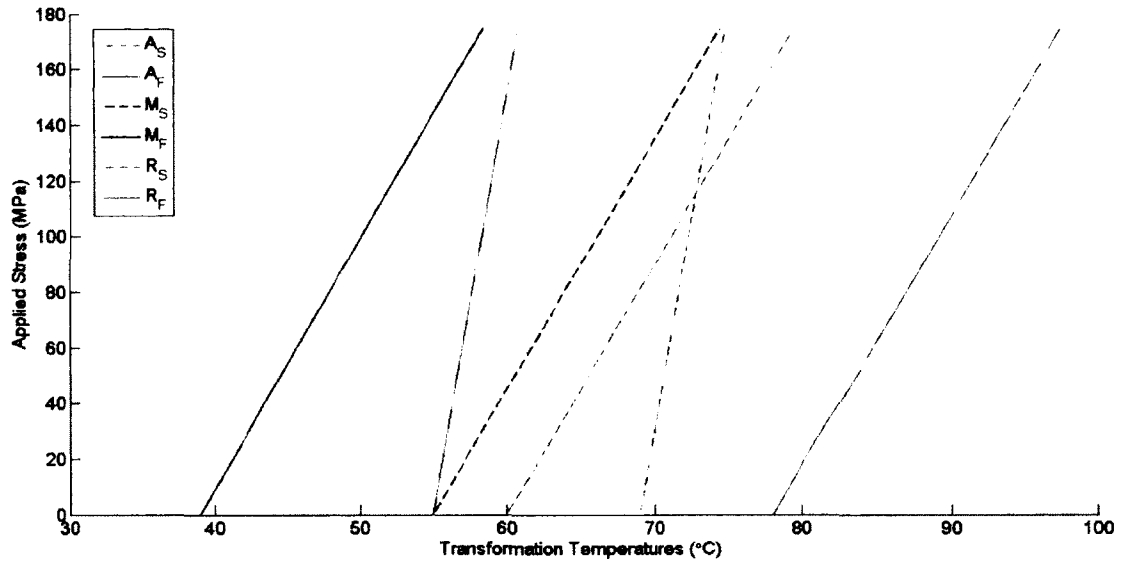


Figure 78: Relationship between phase transformation temperatures and applied stress.

$T = A_s + \frac{\sigma}{C_A}$ to $T = A_f + \frac{\sigma}{C_A}$ as a function of the applied stress, while the material is composed of martensite at the start of the transformation and austenite at the end. The strain is a combination of applied mechanical strain, which is determined from Hooke's law using the Young's modulus of the appropriate phase, as well as the transformation strain, which is maximum (ϵ_{LM}) at the start of transformation and zero at the end.

$$R_{Hs} = \frac{\rho_M L_0}{A_0} \left(1 + \alpha_M \left(A_s + \frac{\sigma}{C_A} - T_0 \right) \right) \left(1 + 2 \left(\epsilon_{LM} + \frac{\sigma}{E_M} \right) \right) \quad (5.41)$$

$$R_{Hf} = \frac{\rho_A L_0}{A_0} \left(1 + \alpha_A \left(A_f + \frac{\sigma}{C_A} - T_0 \right) \right) \left(1 + 2 \frac{\sigma}{E_A} \right) \quad (5.42)$$

$$\delta_{Hs} = L_0 \left(\epsilon_{LM} + \frac{\sigma}{E_M} \right) \quad (5.43)$$

$$\delta_{Hf} = L_0 \frac{\sigma}{E_A} \quad (5.44)$$

The slope and offset coefficients for the heating asymptote are then described using equations 5.45 and 5.46.

$$a_H = \frac{\delta_{Hs} - \delta_{Hf}}{R_{Hs} - R_{Hf}} \quad (5.45)$$

$$b_H = \frac{\delta_{Hf} R_{Hs} - \delta_{Hs} R_{Hf}}{R_{Hs} - R_{Hf}} \quad (5.46)$$

Analysis of the cooling asymptote coefficients was slightly more complicated since the influence of applied stress upon the amount of R-phase present must be considered. Assuming the material is fully austenite at the onset of cooling, equation 5.47 determines the fraction of R-phase present at the start of phase transformation from R-phase to martensite and equation 5.48 determines the resistivity of the material. The Liang & Rogers model of phase transformation using a cosine relationship is employed for the R-phase transformation by Brammajyosula, as shown in 5.47.

$$\xi_R = \frac{1}{2} \left(\cos \left(\frac{\pi}{R_s - R_f} \left(M_s + \frac{\sigma}{C_M} - R_f - \frac{\sigma}{C_R} \right) \right) + 1 \right) \quad (5.47)$$

$$\rho_{Cs} = \xi_R \rho_R \left(1 + \alpha_R \left(M_s + \frac{\sigma}{C_M} - T_0 \right) \right) + (1 - \xi_R) \rho_A \left(1 + \alpha_A \left(M_s + \frac{\sigma}{C_M} - T_0 \right) \right) \quad (5.48)$$

The resistance and displacement at the start and finish points of the cooling asymptote are then given by equations 5.49 to 5.52. Equations 2.12, 2.13 and 2.15 are used to determine the resistance of the material at the start and end of phase transformation during cooling. The resistivity at the start of transformation is a mixture of the resistivities of austenite and R-phase, while the resistivity at the end

of the transformation is that of the martensite phase.

$$R_{Cs} = \frac{\rho_{Cs}L_0}{A_0} \left(1 + 2 \left(\varepsilon_{LR} + \frac{\sigma}{\xi_R E_R + (1 - \xi_R) E_A} \right) \right) \quad (5.49)$$

$$R_{Cf} = \frac{\rho_M L_0}{A_0} \left(1 + \alpha_M \left(M_f + \frac{\sigma}{C_M} - T_0 \right) \right) \left(1 + 2 \left(\varepsilon_{LM} + \frac{\sigma}{E_M} \right) \right) \quad (5.50)$$

$$\delta_{Cs} = L_0 \left(\varepsilon_{LR} + \frac{\sigma}{\xi_R E_R + (1 - \xi_R) E_A} \right) \quad (5.51)$$

$$\delta_{Cf} = L_0 \left(\varepsilon_{LM} + \frac{\sigma}{E_M} \right) \quad (5.52)$$

The slope and offset coefficients for the cooling asymptote are then described using equations 5.53 and 5.54.

$$a_C = \frac{\delta_{Hf} - \delta_{Hs}}{R_{Hf} - R_{Hs}} \quad (5.53)$$

$$b_C = \frac{\delta_{Hs} R_{Hf} - \delta_{Hf} R_{Hs}}{R_{Hf} - R_{Hs}} \quad (5.54)$$

The coefficients for both the heating and cooling asymptotes were evaluated over a range of stress values and compared to experimental data in Figure 79. The overall trends are similar for each of the coefficients, and the values are relatively close considering the use of material properties for a different Ni-Ti alloy during analysis. Therefore, characterization of the appropriate material properties for Flexinol could possibly be used to determine the model coefficients through analysis instead of experimental calibration. The phase transformation temperatures, stress influence coefficients, moduli of elasticity and resistivity parameters for each phase, as well as the stroke parameters would all have to be determined through experimental characterization of the stress-strain-resistance-temperature behaviour.

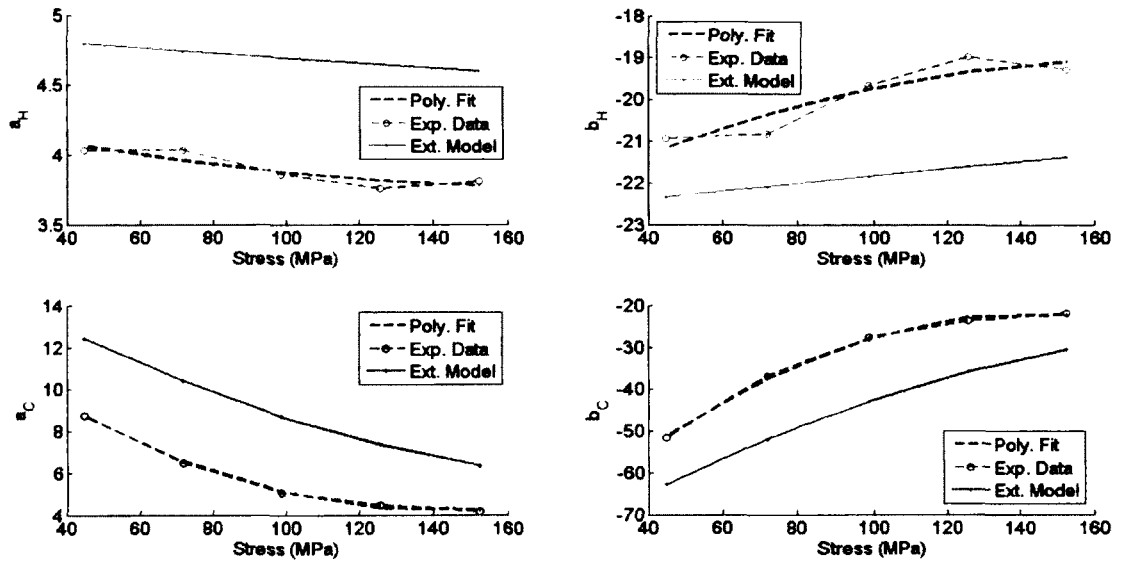


Figure 79: Comparison of slope and offset coefficients determined experimentally and fitted for Flexinol wire as well as determined analytically for the Ni-Ti alloy model by Brammajyosula.

5.2 Furukawa

A separate model was developed for the Ni-Ti-Cu Furukawa alloy since it demonstrated significantly smaller hysteresis effects within the relationships between electrical resistance and displacement compared to the Ni-Ti Flexinol alloy. Forward and reverse transformation between martensite and austenite phases takes place over different temperature ranges in both alloys. However, the gap between the sets of critical transformation temperatures for the Furukawa alloy is much smaller than that for the Flexinol alloy and the presence of R-phase was not observed during transformation of the Furukawa alloy. Therefore, the hysteresis of the resistance-displacement relationship is greatly reduced by the absence of R-phase effects, and the heating and cooling resistance-displacement curves are much closer due to the smaller gap in transformation temperatures. Apart from a small non-linear and indeterminate region near the fully actuated position, the resistance-displacement relationship for

Furukawa is relatively simple and therefore requires a less complex model compared to the Flexinol alloy.

The resistance-displacement curves during heating and cooling were first analyzed and modeled separately using results obtained during material characterization. Each curve was represented by a second-order polynomial equation which predicts the actuator displacement as a function of electrical resistance. Similar to the model for Flexinol, the coefficients of the polynomial resistance-displacement curve were also found to be dependent upon the level of applied stress. Therefore, another series of second-order polynomial functions was used in order to model the coefficients of the resistance-displacement curve in terms of applied stress. Considering the smaller hysteresis gap, both heating and cooling resistance-displacement curves were then averaged in order to produce a single activation curve. The resulting family of polynomial functions represents the resistance-stress-displacement behaviour of the Furukawa alloy during both heating and cooling. Normalization of the model allows a further simplification in which the activation curve may be considered independent of applied stress.

5.2.1 Heating & Cooling Curves

Although the hysteresis effects are small, the resistance-displacement curves are different during heating and cooling of the Furukawa alloy. The primary heating and cooling resistance-displacement curves are followed during full and partial activation and form the basis of the resistance-stress-displacement model. Each curve is composed of a smooth monotonic non-linear region which extends the majority of the actuation range, along with a small highly non-linear and indeterminate region near the point of complete actuation. This indeterminate region was ignored when developing the model since it covers only a small portion of the actuation range. After reducing the data accordingly, the heating and cooling curves were each modeled using

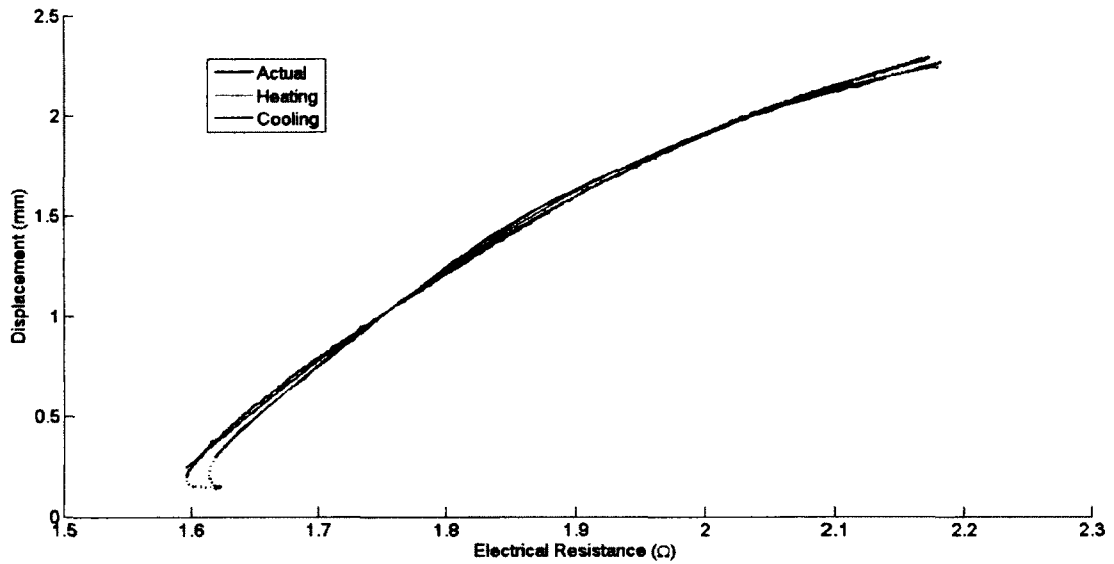


Figure 80: Heating and cooling resistance-displacement curves of Furukawa alloy with polynomial fitting functions.

second-order polynomial functions. Equations 5.55 and 5.56 describe the polynomial functions of electrical resistance, R , for modeling the displacement, δ , during heating and cooling, respectively. The polynomial coefficients G are denoted by subscripts H and C for heating and cooling and numbered indices referring to the polynomial order.

$$\delta_H = G_{H_2}R^2 + G_{H_1}R + G_{H_0} \quad (5.55)$$

$$\delta_C = G_{C_2}R^2 + G_{C_1}R + G_{C_0} \quad (5.56)$$

The coefficients of the heating and cooling polynomial functions were determined through least-squares fitting of the reduced resistance-displacement data. Figure 80 shows the open-loop resistance-displacement response of a Furukawa actuator wire under a constant load of 1.26 N. The reduced heating and cooling curves are highlighted and the polynomial functions are included for comparison.

Ignoring the indeterminate region at full actuation allows the polynomial functions to be fitted closely to the heating and cooling resistance-displacement curves. Since the curves show relatively simple smooth trends, the second-order polynomial functions capture the resistance-displacement behaviour accurately within the reduced actuation region. Errors at the region near full actuation are larger since the resistance-displacement relationship becomes indeterminate and departs from the trend observed in the majority of the curve. However, the indeterminate region is small enough to be ignored without significantly reducing the actuator capabilities.

The use of higher order polynomials improves the accuracy of the heating and cooling functions, but may cause numerical problems in practice due to the high sensitivity of the higher order terms. Furthermore, the influence of stress is more accurately modeled using lower order polynomial functions, as will be discussed in the next sub-chapter. Therefore, second-order polynomial functions were used for modeling the heating and cooling curves in order to maintain simplicity but higher order polynomials may also be chosen without changing the model structure.

5.2.2 Influence of Applied Stress

Characterization of the Furukawa alloy revealed a change in the resistance-displacement relationship under various constant applied loads. However, the absence of R-phase during phase transformations results in heating and cooling resistance-displacement curves which do not change shape significantly as a function of stress. The hysteresis gap between the heating and cooling curves remains constant along with the shapes, while the upper and lower limits of resistance and displacement varies according to the applied stress. Modeling of the heating and cooling curves using the polynomial functions in equations 5.55 and 5.56 was performed for the set of resistance-displacement curves with various constant applied loads. This resulted

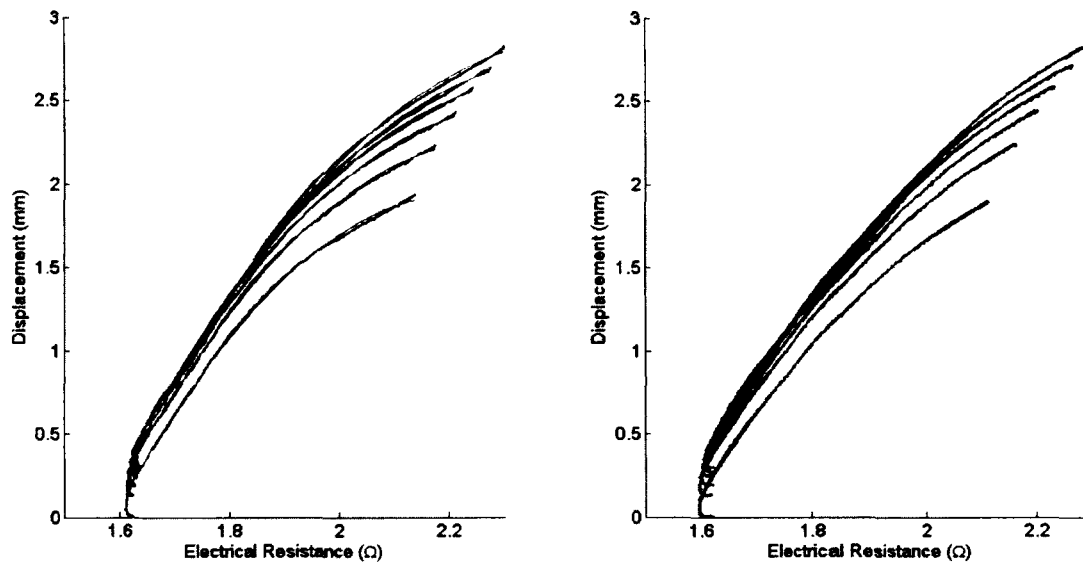


Figure 81: Heating and cooling asymptote families for Flexinol wire.

in families of polynomial functions for representing heating and cooling resistance-displacement curves of the Furukawa alloy. Figure 81 shows the families of heating and cooling polynomial functions, while Figure 82 shows the relationships between the polynomial coefficients and applied stress.

Both families of heating and cooling polynomial functions do not show significant change in the shape of the curves, but the polynomial coefficients are clearly dependent upon applied stress. The relationships between the coefficients and applied stress follow trends which show an increase in both the overall displacement and the mean slope of the resistance-displacement curves. Each of the coefficients was modeled as a function of applied stress based upon analysis of the trends shown in Figure 82. These trends are smooth and monotonic, and may be modeled using the same approach applied to the Flexinol model coefficients. Second-order polynomials were again chosen to capture the influence of stress upon the coefficients of the heating and cooling resistance-displacement curves. Equations 5.57 and 5.58 show the polynomial

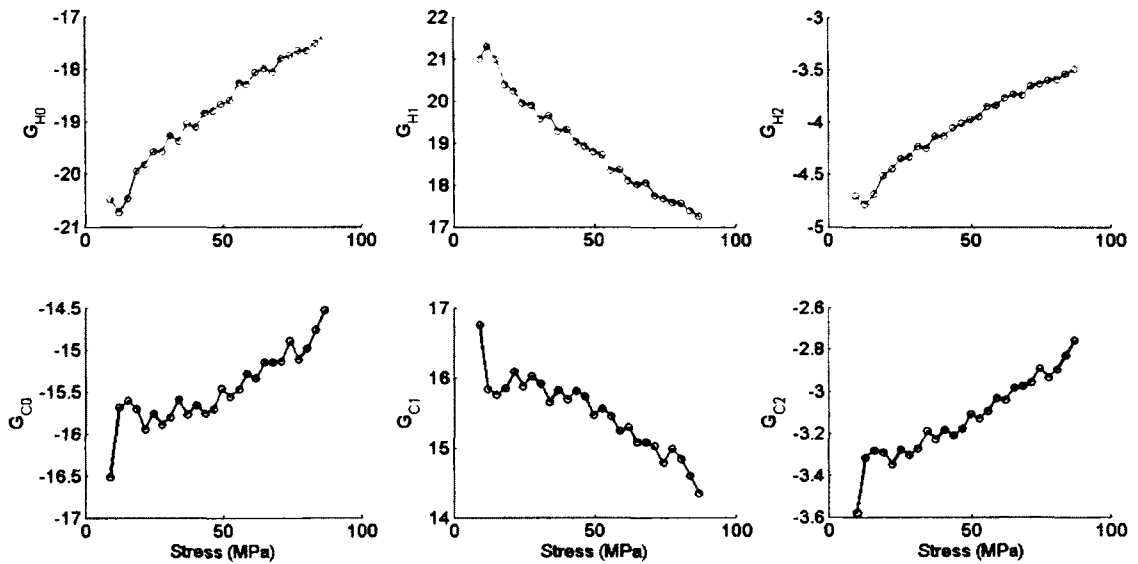


Figure 82: Slope and intercept coefficients of heating and cooling asymptotes for Furukawa wire.

functions which approximate the heating and cooling curve coefficients, G_H and G_C , in terms of applied stress. The subscript i refers to the coefficient, γ , for the i^{th} -order term of the heating and cooling resistance-strain polynomial functions.

$$G_{H_i}(\sigma) = \gamma_{H_{i2}}\sigma^2 + \gamma_{H_{i1}}\sigma + \gamma_{H_{i0}} \quad (5.57)$$

$$G_{C_i}(\sigma) = \gamma_{C_{i2}}\sigma^2 + \gamma_{C_{i1}}\sigma + \gamma_{C_{i0}} \quad (5.58)$$

Least-squares fitting of each of the G_H and G_C coefficients was used to determine the appropriate γ coefficients. The resulting polynomial approximations of the relationships between each coefficient and the applied stress are shown in Figure 83. Second-order polynomial functions appear to effectively capture the influence of applied stress upon the resistance-displacement relationships during heating and cooling.

The effect of increasing the polynomial order of the fitting functions upon the

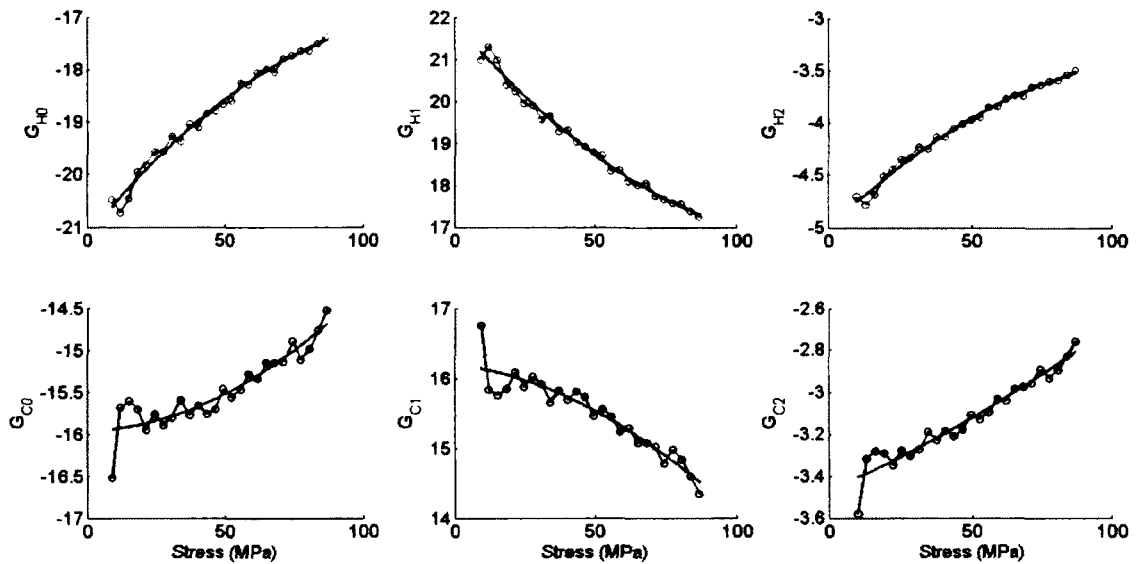


Figure 83: Polynomial fitting of the heating and cooling curve coefficients.

model error is shown in Figure 84. Although increasing the polynomial order may result in lower errors, the use of second-order polynomials is satisfactory. Similar to the application of the Flexinol model, the precision of the polynomial coefficients must be considered when being stored and read from the appropriate data file.

As described for the Flexinol model, the applied stress must be input into the Furukawa model but may also be predicted using a known value or load model if sensor measurement is unavailable or impractical.

5.2.3 Hysteresis Loops

Separate curves were used for modeling of both heating and cooling resistance-displacement relationships of the Furukawa alloy, therefore a function for transition between the curves was necessary. Although the hysteresis effects in the Furukawa alloy are much smaller than those in the Flexinol alloy, the small hysteresis gap between the heating and cooling curves leads to major and minor hysteresis loops in the

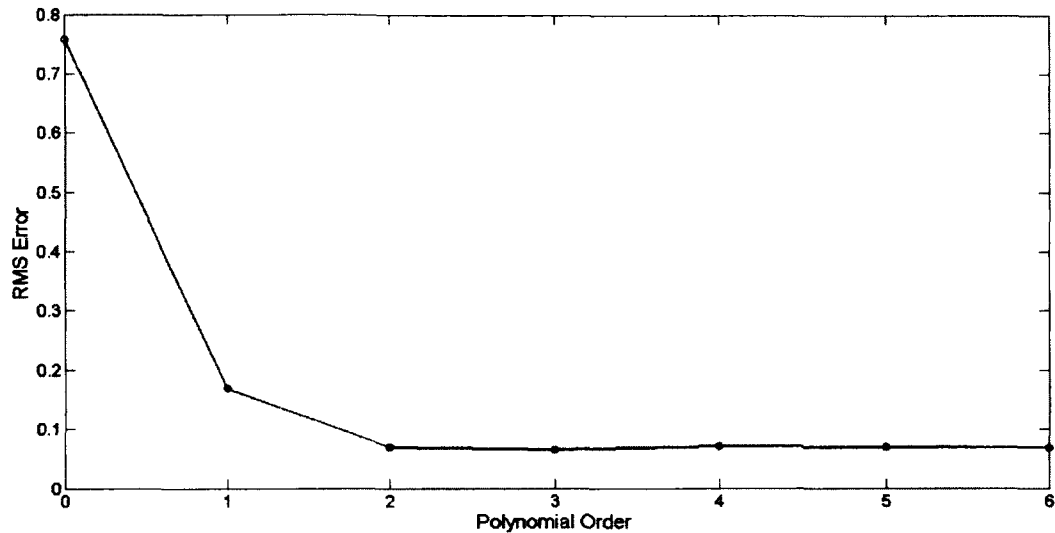


Figure 84: Error of the Furukawa model as a function of polynomial order.

resistance-displacement behaviour. Investigation of the minor hysteresis loops during material characterization demonstrated the transition between the heating and cooling curves during incomplete actuation. This transition was found to be smooth and caused the resistance-displacement position of the actuator to approach the appropriate heating or cooling curve, similar to the hysteresis behaviour in the Flexinol alloy. Therefore, an exponential function was developed to model the resistance-displacement transition behaviour in Furukawa alloy considering again the thermodynamic nature of the phase transformation process.

Transition curves for the Furukawa alloy tend to approach the appropriate heating or cooling curve starting from an initial resistance-displacement position on the previous curve. Therefore, hysteresis effects were considered by combining the heating and cooling curves in a simple mixture rule where the proportions of each curve are controlled by an exponential function. The relative hysteresis position, h , is used to represent the amount of intermediary transformation between the heating and cooling curves, where $h = 0$ refers to a position on the cooling curve and $h = 1$ refers to a

position on the heating curve.

The evolution of the relative hysteresis position, h , was modeled using the exponential functions described by equations 5.59 and 5.60 for transition from heating to cooling and cooling to heating, respectively, with a decay coefficient of η . Initial conditions of the electrical resistance and hysteresis position, R_S and h_S , are updated whenever there is a switch from heating to cooling of the actuator (or vice versa).

$$h = (h_S - 1)e^{\eta(R-R_S)} + 1 \quad (5.59)$$

$$h = h_S e^{(-\eta(R-R_S))} \quad (5.60)$$

The simple mixing rule in equation 5.61 was then used to determine the position of the actuator, δ , based on the relative hysteresis position, where δ_H and δ_C are the heating and cooling curves described by equations 5.55 and 5.56.

$$\delta = \delta_H h + \delta_C (1 - h) \quad (5.61)$$

Application of the exponential transition equations in modeling the response of Flexinol wire during incomplete actuation resulted in the plot shown in Figure 85. The model was simulated with and without the transition curves included, where direct switching between the heating and cooling curves was used for the latter simulation.

The use of the exponential functions in modeling the transition between heating and cooling curves improved the model performance compared with direct switching, but not as significantly as expected. The model including the transition curves experienced higher maximum error near the point of full actuation due to the indeterminate region of the response. After ignoring the indeterminate region, the improvement over direct switching was more obvious. However, considering the combination of error sources such as sensor measurement, material characterization, and

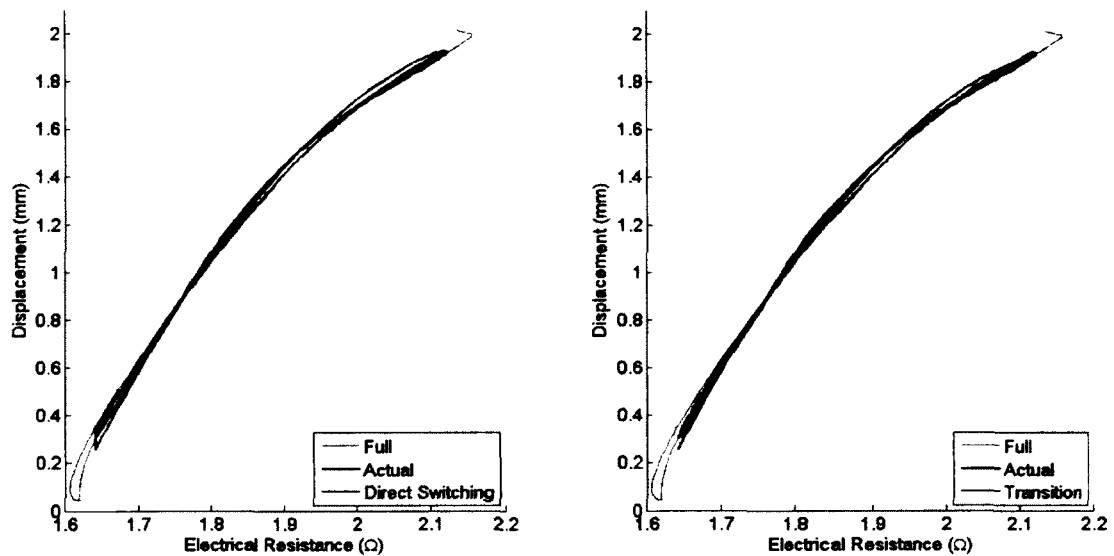


Figure 85: Comparison of transition curves and direct switching in the Furukawa model.

curve fitting, the overall benefit of applying the exponential function may only be marginal. Direct switching allows either the heating or cooling curve to be computed and selected based upon activation conditions. This greatly reduces the complexity of the model algorithm, which is beneficial in practice since the control algorithm is less computationally expensive.

Using the direct switching method caused the model to experience discontinuities during switching between the heating and cooling curves. Although the error due to the sudden change in modeled displacement was not significantly large, the presence of a discontinuity may be undesirable in some control or simulation systems. Therefore, the use of another simplified model was studied where the heating and cooling resistance-displacement curves were averaged to produce a single polynomial activation curve. Figure 86 shows the results of applying the averaged model in comparison with the direct switching model.

The use of an averaged activation curve to describe the resistance-displacement

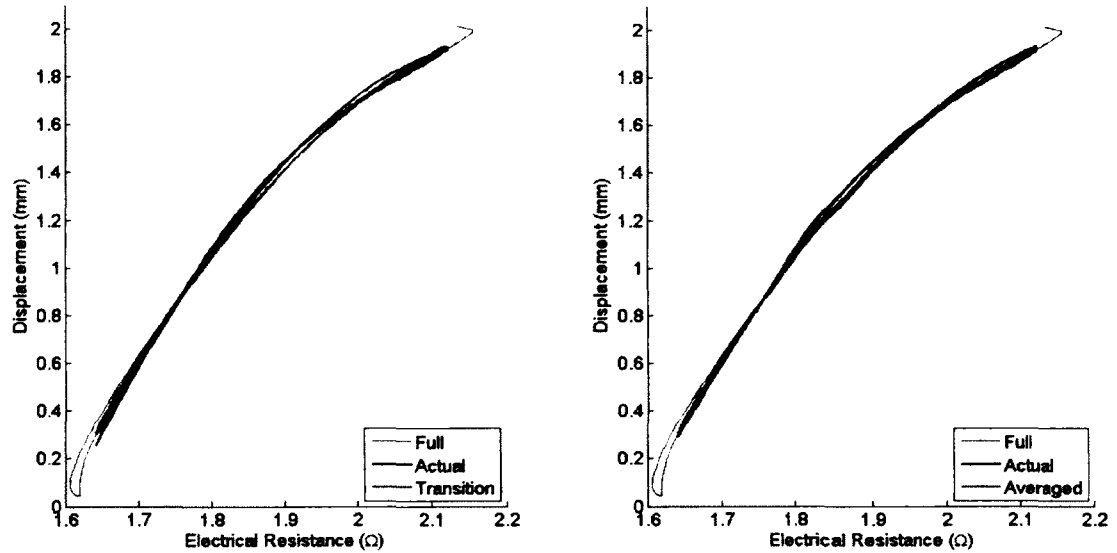


Figure 86: Comparison of transition curves and averaged activation curve in the Furukawa model.

relationship during both heating and cooling resulted in a small increase in error compared with the use of the models based on direct switching and exponential transition curves. While the mean error was larger for the averaged model, the benefit of using a single activation curve makes the approach favourable since actuator displacement may be directly computed from electrical resistance and applied stress without consideration of hysteresis or heating conditions. The average activation polynomial function has coefficients, G , that are the mean values of the heating and cooling coefficients, G_H and G_C . Furthermore, the stress influence coefficients, γ_H and γ_C , were averaged to obtain a single set of coefficients, γ , that describe the activation curve. Equation 5.62 describes the averaged activation function from equations 5.55 and 5.56, and equation 5.63 describes the averaged stress influence function from equations 5.57 and 5.58.

$$\delta = G_2 R^2 + G_1 R + G_0 \quad (5.62)$$

$$G_i(\sigma) = \gamma_{i_2}\sigma^2 + \gamma_{i_1}\sigma + \gamma_{i_0} \quad (5.63)$$

The Furukawa model is therefore composed of heating and cooling curves which are fitted and averaged in order to produce a single family of activation curves that depend upon applied stress. Coefficients for the resistance-displacement activation curve were computed as a function of applied stress and the actuator displacement was then determined from the electrical resistance.

5.2.4 Simulation

Validation of the Furukawa resistance-stress-displacement model was performed in Mathworks MATLAB using the same simulation approach as was used for the Flexinol model. Both constant applied loads as well as varying load conditions were simulated, along with full and partial activation of the actuator wire. The model was compared to data obtained during material characterization by computing the predicted displacement based on the measured electrical resistance and applied load. Discretization of the model algorithm is required in order to be applied in numerical simulation and control. Using the simplified average activation curves, the discrete simulation process is given by equations 5.64 to 5.66.

Similar to the Flexinol model, the model coefficients, y , are constant properties of the actuator which are known and characterized experimentally. The discrete model is again presented with the subscript k referring to the time step index. From measurement or prediction of the applied stress, the activation polynomial coefficients, G , are computed from the set of stress influence polynomial functions in equation 5.64.

$$G_{ik}(\sigma_k) = \gamma_{i_2}\sigma_k^2 + \gamma_{i_1}\sigma_k + \gamma_{i_0} \quad (5.64)$$

The actuator displacement is computed from the electrical resistance measurement

using equation 5.65, where the averaged activation polynomial function coefficients are determined from equation 5.64. Displacement of the actuator may be related to actuator displacement using equation 5.66, where L_0 is the actuator length.

$$\delta_k = G_{2k}R_k^2 + G_{1k}R_k + G_{0k} \quad (5.65)$$

$$\delta_k = \varepsilon_k L_0 \quad (5.66)$$

If both heating and cooling curves are left separate and the transition behaviour is modeled, then the activation and stress influence polynomial functions for heating and cooling must both be evaluated. Equations 5.67 and 5.68 show the discretized functions for computing the heating and cooling curve coefficients, while equations 5.69 and 5.70 show the discretized functions for computing the heating and cooling curves.

$$G_{H_{ik}} = \gamma_{H_{i2}}\sigma_k^2 + \gamma_{H_{i1}}\sigma_k + \gamma_{H_{i0}} \quad (5.67)$$

$$G_{C_{ik}} = \gamma_{C_{i2}}\sigma_k^2 + \gamma_{C_{i1}}\sigma_k + \gamma_{C_{i0}} \quad (5.68)$$

$$\delta_{H_k} = G_{H_{k1}}R_k^2 + G_{H_{k2}}R_k + G_{H_{k0}} \quad (5.69)$$

$$\delta_{C_k} = G_{C_{k1}}R_k^2 + G_{C_{k2}}R_k + G_{C_{k0}} \quad (5.70)$$

For the direct switching method, the model displacement is computed using either equations 5.69 or 5.70 depending upon whether the actuator is being heated or cooled. Equation 5.71 summarizes the selection and defines the displacement output of the model using direct switching.

$$\delta_k = \begin{cases} \delta_{H_k} & \text{heating} \\ \delta_{C_k} & \text{cooling} \end{cases} \quad (5.71)$$

The exponential transition curve method may also be discretized and applied for simulation and control. Equations 5.72 through 5.74 are the discretized exponential transition functions which determine the relative hysteresis position. Both heating and cooling curves are computed using equations 5.69 through 5.70 and used within the simple mixture rule of equation 5.74 to determine the actuator displacement.

$$h_k = (h_{Sk} - 1)e^{\eta(R_k - R_{Sk})} + 1 \quad (5.72)$$

$$h_k = h_{Sk}e^{-\eta(R_k - R_{Sk})} + 1 \quad (5.73)$$

$$\delta_k = \delta_{H_k}h_k + \delta_{C_k}(1 - h_k) \quad (5.74)$$

Equation 5.72 is used during heating transition while equation 5.73 is used during cooling transition. The initial conditions h_{Sk} and R_{Sk} are constant throughout transition and updated if the heating condition changes. Although the model was not applied differentially and there is no implicit coupling between the transition curves and displacement output, the relative hysteresis position, h_k , is saturated between 0 and 1 to ensure the model remains within the appropriate bounds.

The simulation results for the Furukawa models are shown in Figures 87 through 98, including both displacement profiles and resistance-displacement curves. Simulation of the averaged model under constant applied loading is shown in Figures 87 through 92, while the results of simulation under spring constraint loading are shown in Figures 93 and 94. The displacement profiles show actual actuator displacement and model prediction, along with the applied load and absolute error between the actual and model displacements. Figures 95 and 96 show the results of simulation under varying load conditions while assuming a constant applied load. Furthermore, a comparison of the Furukawa models using averaged curves, the direct switching method, and intermediary transition curves is presented in Figures 97 and 98.

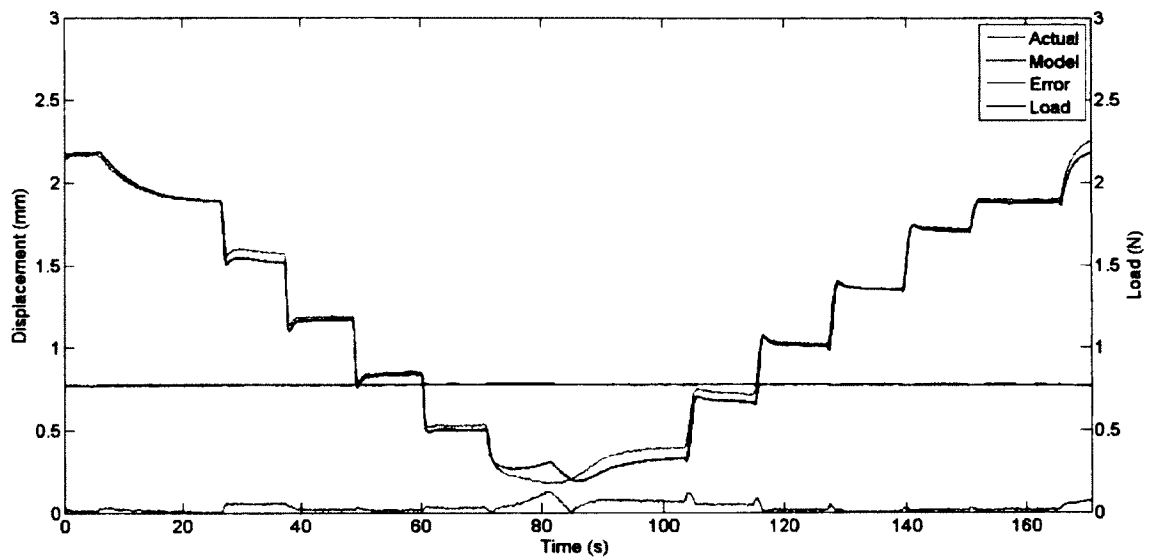


Figure 87: Simulation results for the averaged Furukawa model under constant load of 0.49 N.

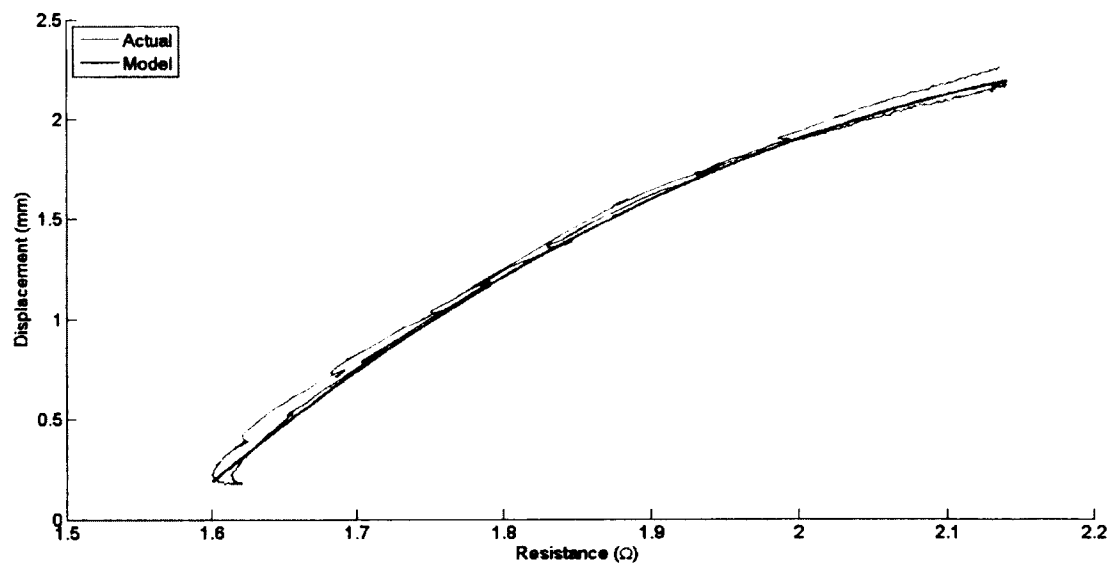


Figure 88: Simulated resistance-displacement curves for the averaged Furukawa model (0.49 N).

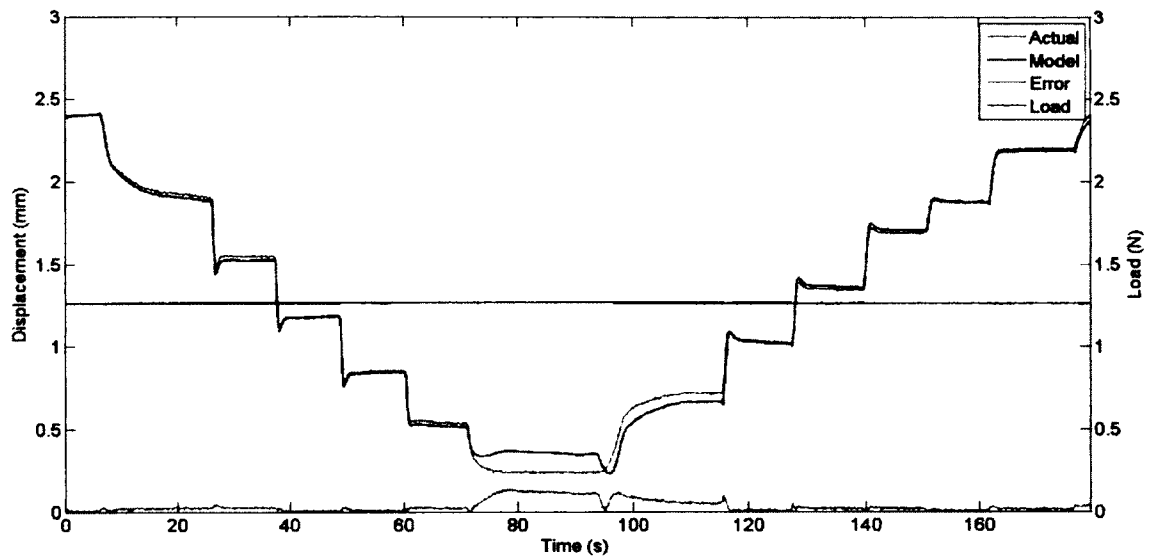


Figure 89: Simulation results for the averaged Furukawa model under constant load of 0.98 N.

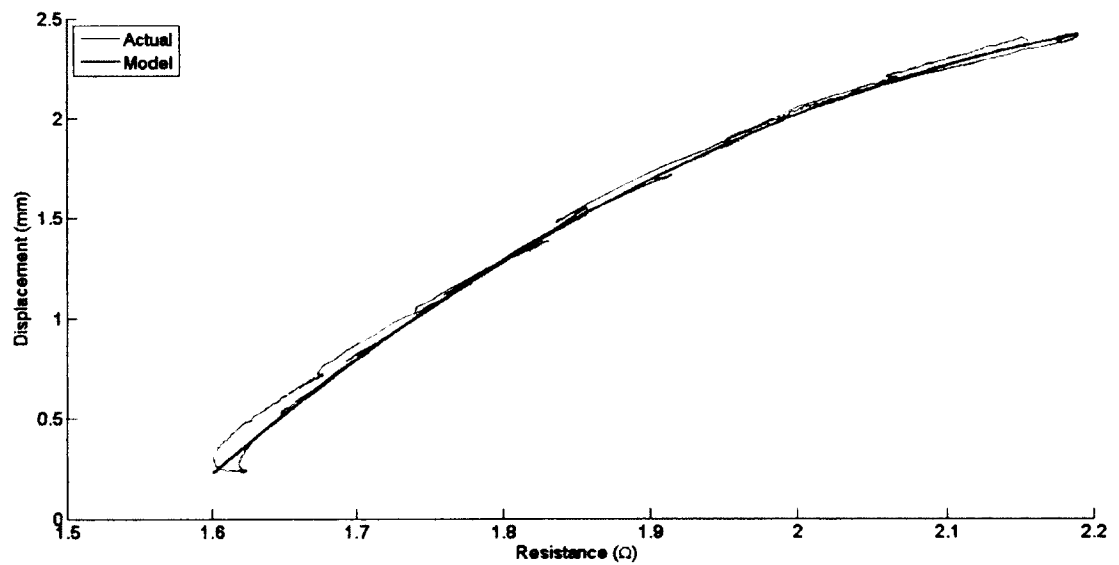


Figure 90: Simulated resistance-displacement curves for the averaged Furukawa model (0.98 N).

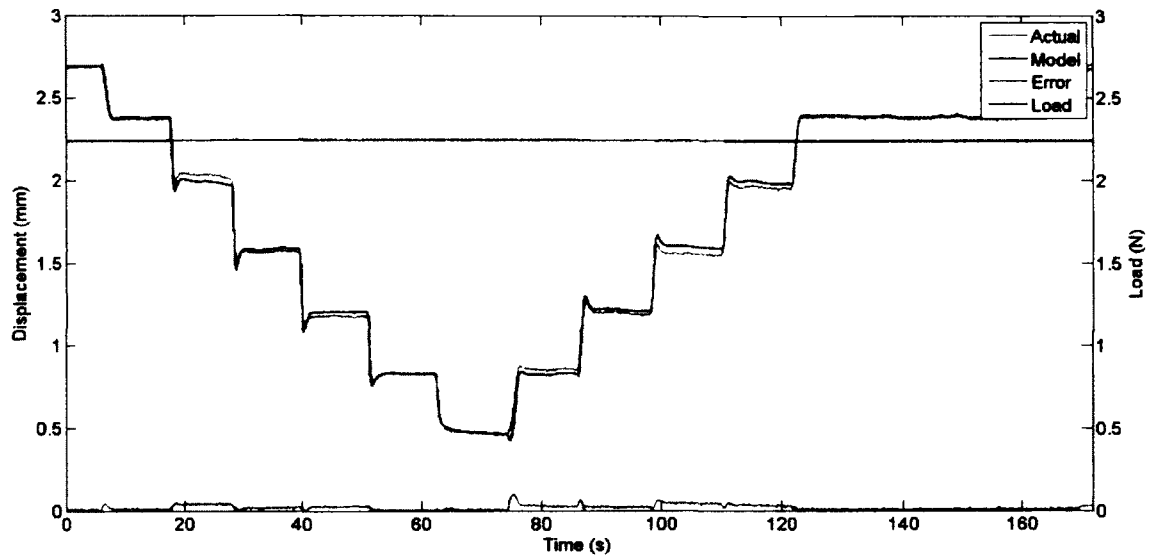


Figure 91: Simulation results for the averaged Furukawa model under constant load of 1.96 N.

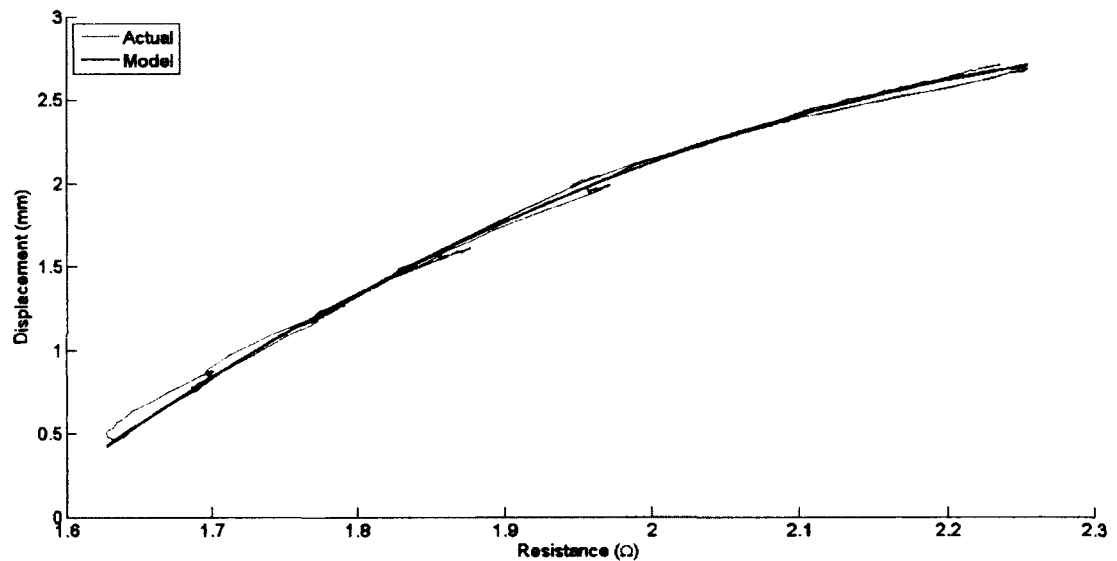


Figure 92: Simulated resistance-displacement curves for the averaged Furukawa model (1.96 N).

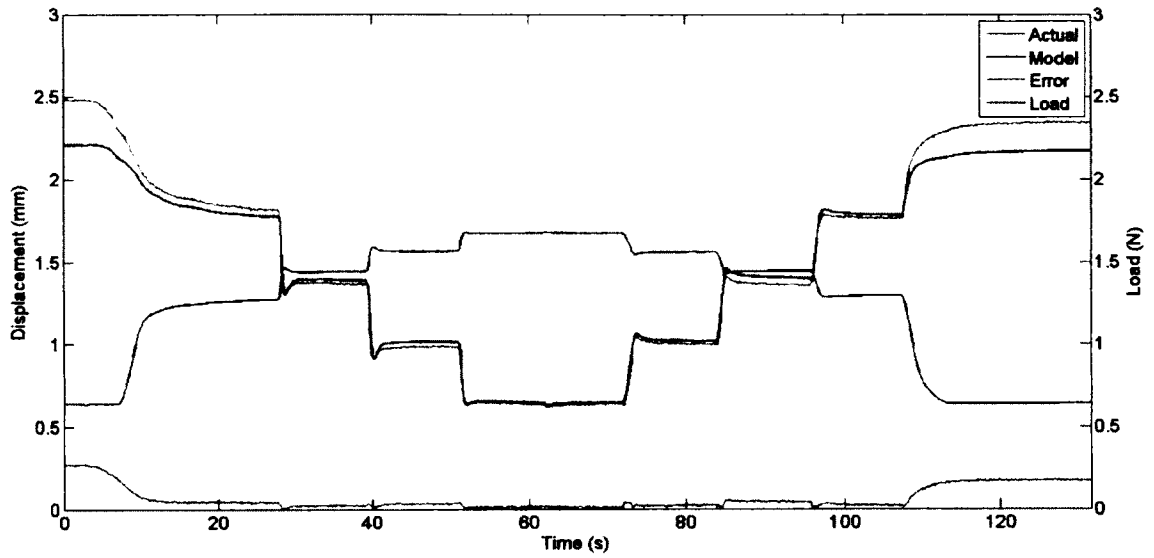


Figure 93: Simulation results for the averaged Furukawa model under spring constraint loading.

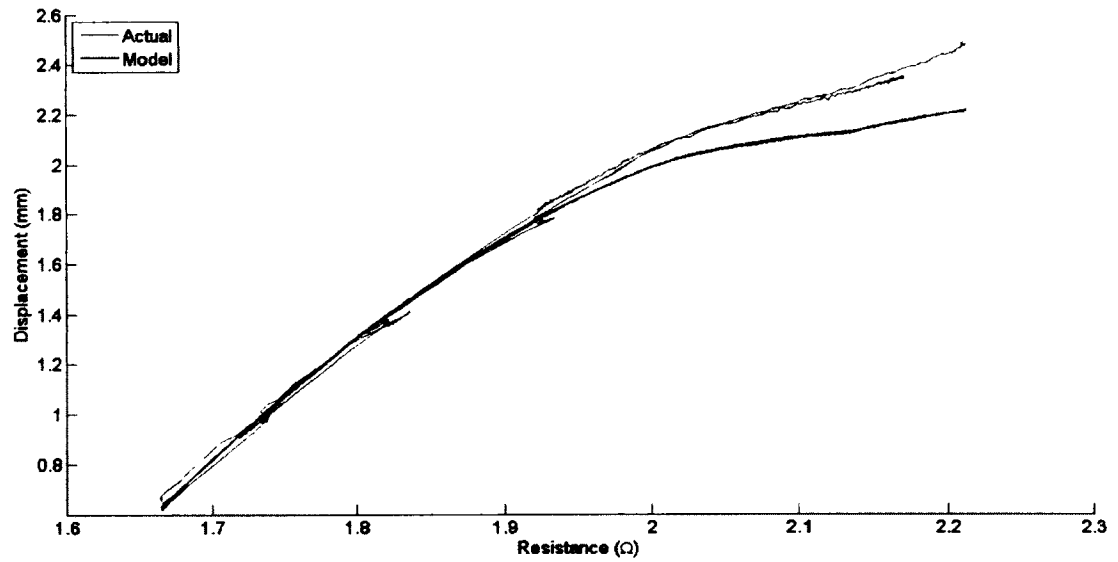


Figure 94: Simulated resistance-displacement curves for the averaged Furukawa model (spring constraint).

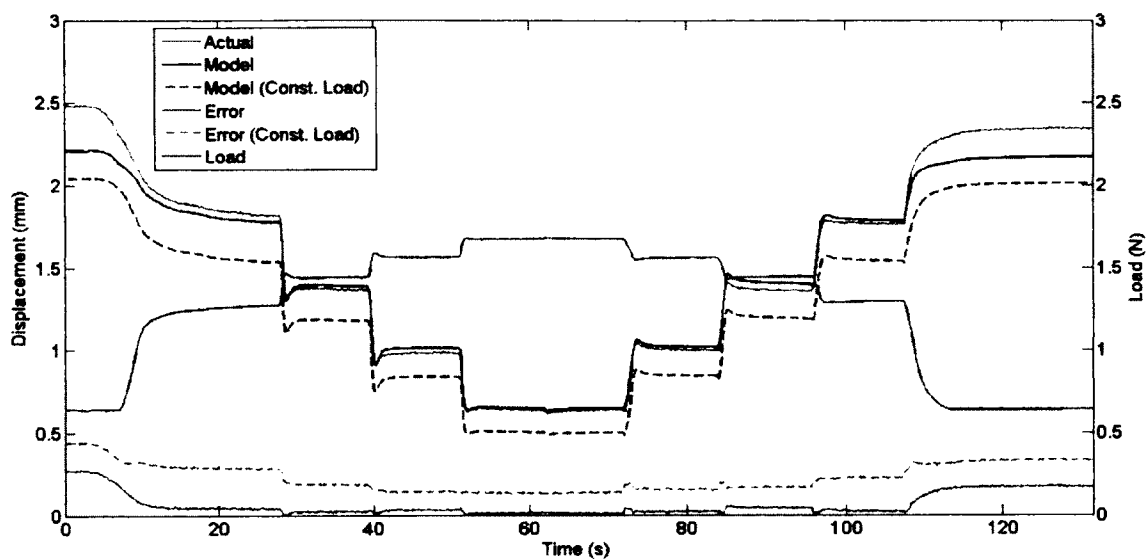


Figure 95: Simulation results for the averaged Furukawa model under spring constraint loading while assuming constant applied load.

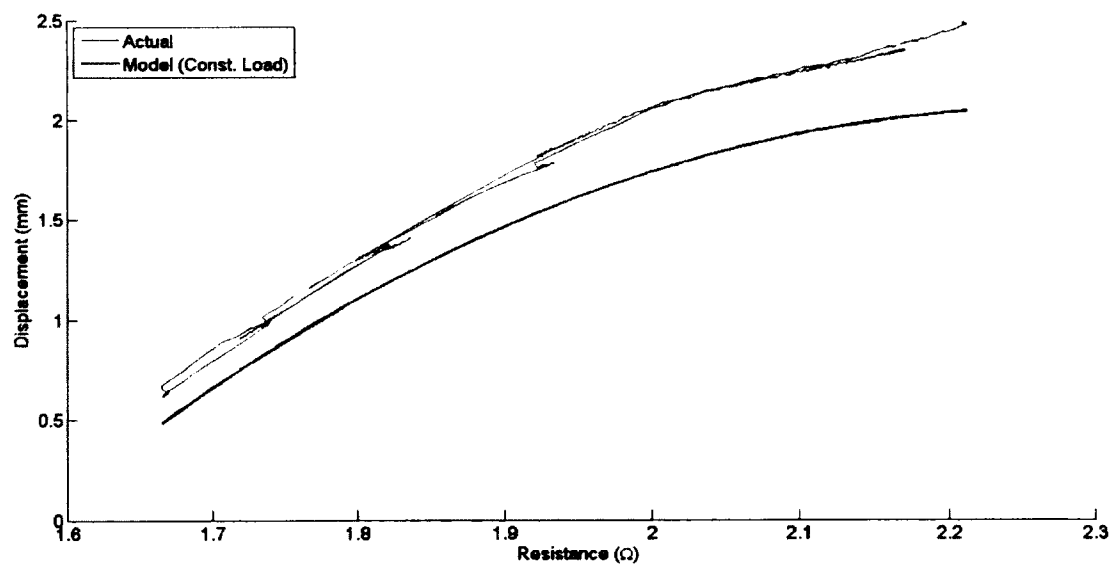


Figure 96: Simulated resistance-displacement curves for the averaged Furukawa model under spring constraint loading while assuming constant applied load.

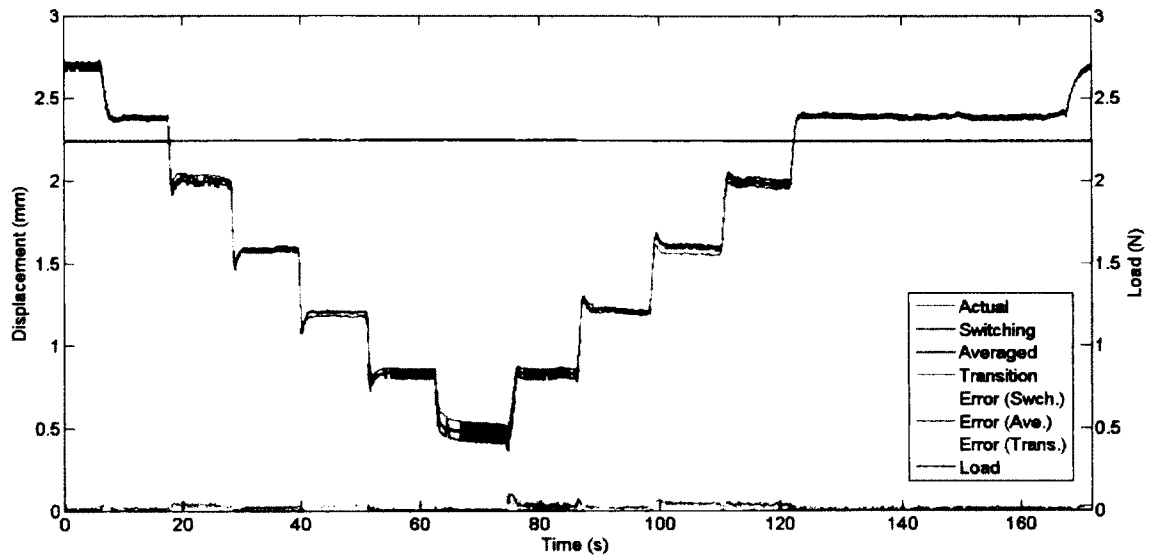


Figure 97: Comparison of simulation results using the direct switching, smooth transition curves, and averaged Furukawa models.

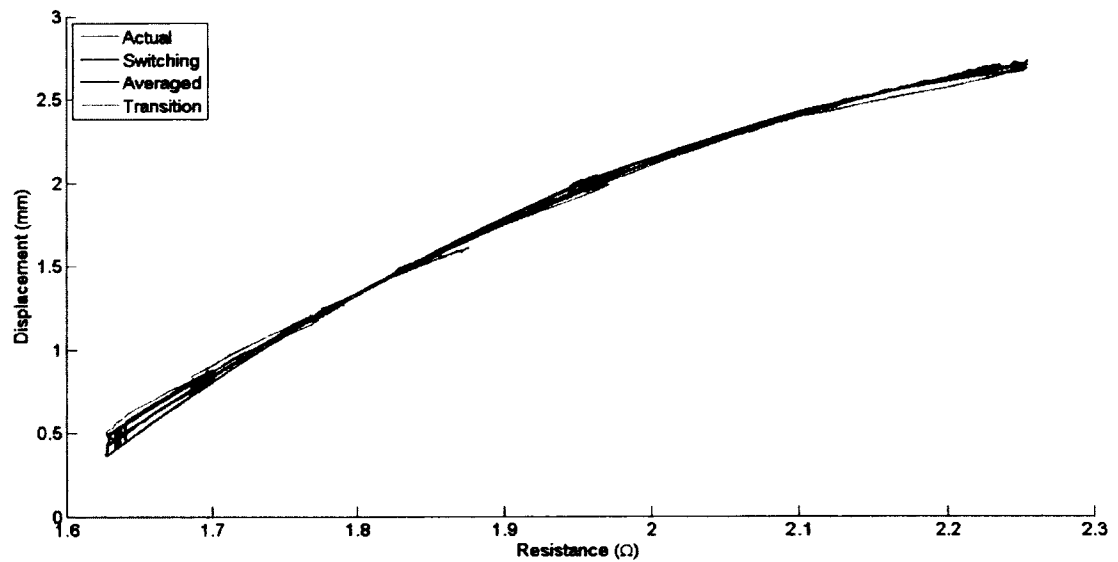


Figure 98: Comparison of simulated resistance-displacement curves using the direct switching, smooth transition curves, and averaged Furukawa models.

Load Condition	Mean Error (% Stroke)			
	Average	Direct Switching	Transition	Constant Load (Average)
Constant (0.49 N)	1.01	1.11	1.28	4.33
Constant (0.98 N)	1.08	1.16	1.08	6.47
Constant (1.96 N)	0.61	0.85	0.73	10.95
Spring Condition	2.15	2.27	2.13	7.55

Table 3: Mean absolute error for simulations under each load condition using the averaged model, direct switching model, transition curve model, and average model without stress influence.

Successful prediction of the actuator displacement was achieved within simulation of the Furukawa models under constant and varying load conditions. Larger errors were observed at the limits of actuation due to the highly non-linear and indeterminate region at full contraction and numerical fitting errors within the model. However, the mean error of the average Furukawa model was approximately 1.21% of the total actuator stroke of 4% strain. The comparison of the average model, direct switching model, and transition curve model is shown in Figures 98 and 98. No significant improvement was observed when using separate heating and cooling curves with either direct switching or transition curves, suggesting the average model is sufficient. Simulation of the model under spring constraint loading conditions with an assumed constant load resulted in a mean error of 7.32%.

The mean absolute error for the simulation cases investigated using the Furukawa models are summarized in Table 3. Each applied load condition was simulated using the averaged model, as well as using separate heating and cooling curves with both direct switching and transition curve methods. The results of the simulations assuming a fixed constant load are also included to demonstrate the significant increase in error when the influence of applied stress was excluded.

5.2.5 Normalization

The model developed for the Furukawa actuator wire has been successfully characterized using experimental data and tested through simulation. General application of the model for a Ni-Ti-Cu wire of any length and diameter is possible after proper characterization of the model coefficients. However, analysis of the resistance-stress-strain relationships for a series of actuator wires of various lengths revealed trends which allow further simplifications of the model. The resulting simplified relationships used for modeling the resistance-stress-strain behaviour are therefore normalized for general application. Two processes were used to normalize the model of the Furukawa alloy, including the generalization of the resistance-strain activation curves in terms of applied stress and the normalization of the functions in terms of actuator geometry.

The activation curves are represented by a family of polynomial functions described by equations 5.62 and 5.63. However, considering each curve normalized by the ranges of electrical resistance and actuation displacement, the family of activation curves are found to follow a single characteristic trend which is independent of applied stress. Figure 99 shows the overlapping resistance-displacement curves after normalization, where the normalized electrical resistance, λ , is determined using equation 5.75 and the normalized actuator displacement, ξ , is determined using equation 5.76. The subscripts *min* and *max* refer to the maximum and minimum values of the resistance, R , and displacement, δ .

$$\lambda = \frac{R - R_{min}}{R_{max} - R_{min}} \quad (5.75)$$

$$\xi = \frac{\delta - \delta_{min}}{\delta_{max} - \delta_{min}} \quad (5.76)$$

The activation curve was then modeled using the normalized polynomial function

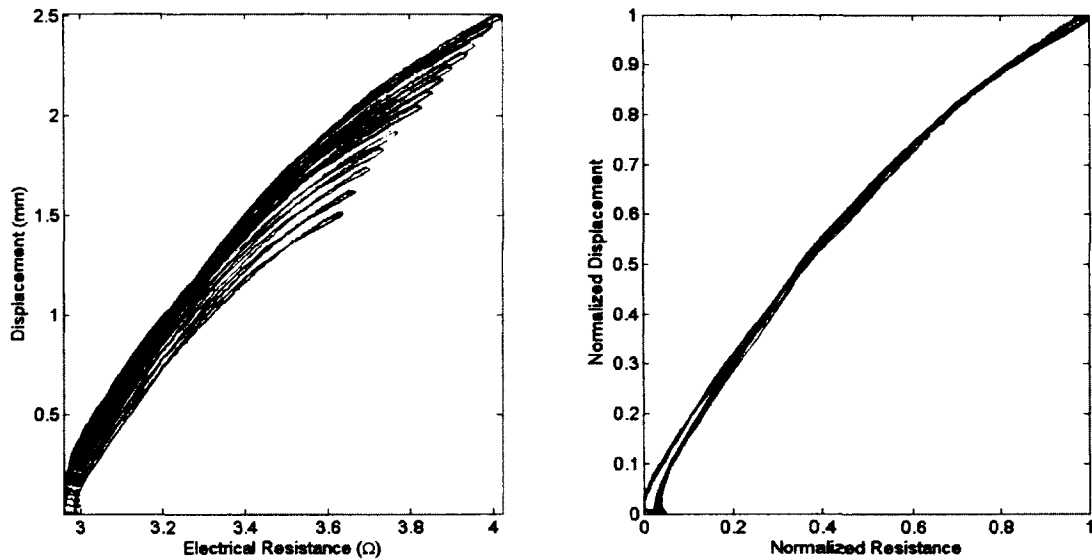


Figure 99: Normalized resistance-displacement activation curves for the Furukawa alloy.

described in equation 5.77 with coefficients C , and shown in Figure 100.

$$\xi = C_2\lambda^2 + C_1\lambda + C_0 \quad (5.77)$$

The upper and lower bounds of the activation curve vary according to the applied stress and were modeled in order to incorporate the influence of stress within the normalized model. The minimum displacement is considered a mechanical component due to elasticity, while the maximum displacement represents the actuator stroke. Therefore, the minimum displacement and actuation stroke are used as parameters for the model. Both mechanical and actuation components of displacement are simple and smooth non-linear functions of the applied stress, while only the maximum electrical resistance shows a dependency upon the applied load. The minimum electrical resistance is found to vary only slightly with applied stress and was therefore assumed to be constant. Figure 101 shows the maximum and minimum values of

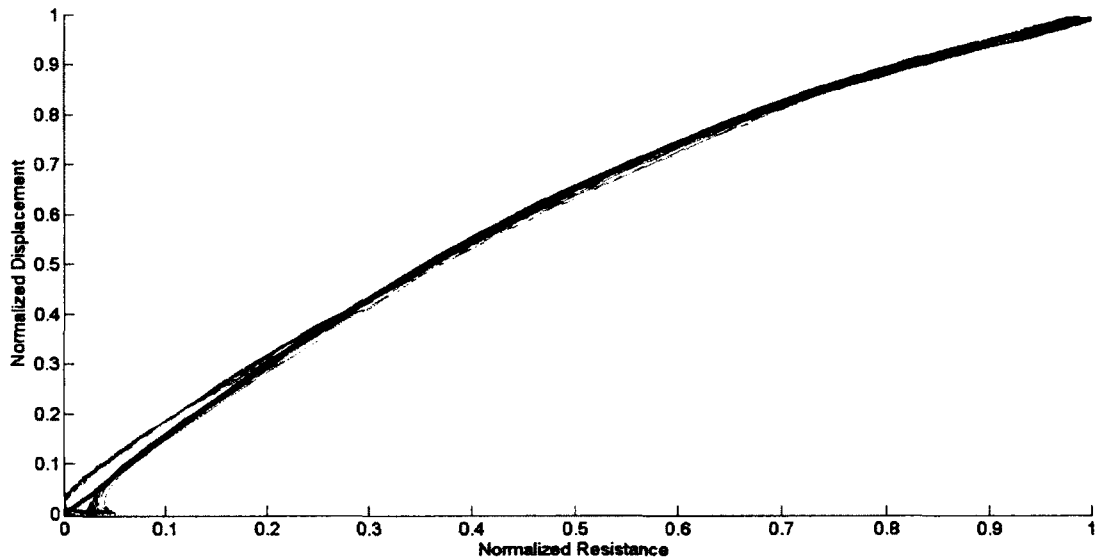


Figure 100: Normalized resistance-displacement activation curves for the Furukawa alloy with polynomial fit.

electrical resistance and displacement as functions of applied stress.

Each of the electrical resistance and displacement parameters were modeled as functions of the applied stress, with the exception of the minimum resistance, which was assumed to be constant. Polynomial functions were chosen to model the relationships for each parameter and fitted using a least-squares method. Equations 5.78 through 5.80 describe the functions used for modeling the mechanical displacement, δ_M , actuation stroke, δ_L , and maximum resistance, R_{max} , with coefficients S_M , S_L , and w . The actuator displacement, δ , defined by equation 5.81, is then computed from the sum of the mechanical and actuation displacements, where the actuation displacement is the normalized displacement, ξ , multiplied by the actuation stroke, $L_0 \in L$. The polynomial functions fitted to the mechanical displacement, actuation stroke, and maximum resistance are shown in Figure 102.

$$\delta_M = S_{M2}\sigma^2 + S_{M1}\sigma + S_{M0} \quad (5.78)$$

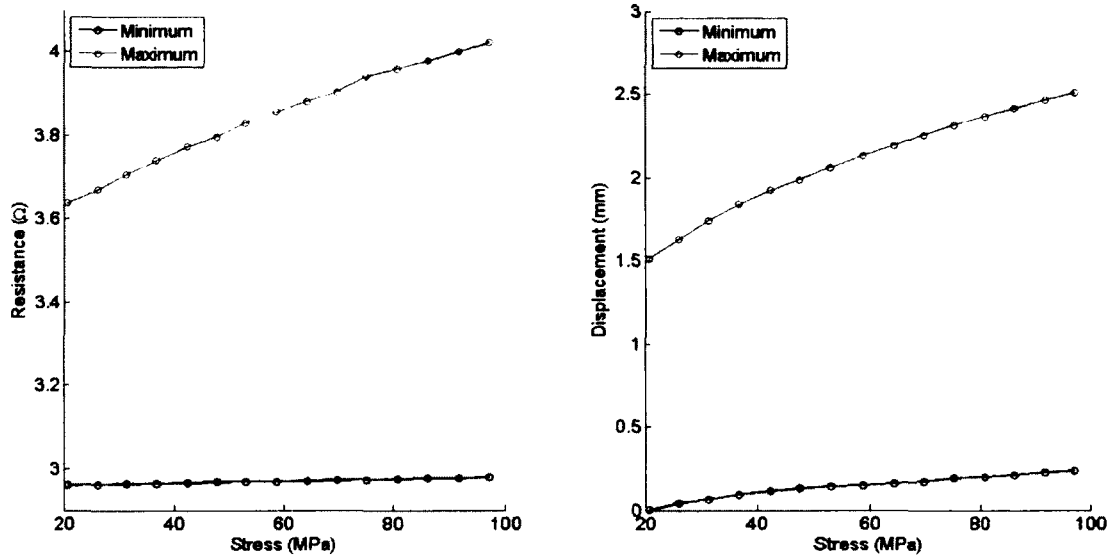


Figure 101: Upper and lower limits of resistance and displacement for normalized activation curves.

$$\delta_L = S_{L_2}\sigma^2 + S_{L_1}\sigma + S_{L_0} \quad (5.79)$$

$$R_{max} = w_2\sigma^2 + w_1\sigma + w_0 \quad (5.80)$$

$$\delta = \delta_M + \delta_L\xi \quad (5.81)$$

The second normalization process involves the analysis and comparison of the resistance-stress-strain relationships for Furukawa actuator wires of various lengths. Sets of the resistance-length curves under various constant applied loads are plotted in Figure 103 for the actuator wires of different lengths. Each set of data was experimentally recorded using the open-loop actuation process described previously.

The overall dependency between the resistance-stress-strain relationships and the length of the actuator is linear as expected due to the fact that the behaviour of the wire is driven by changes in the electrical resistance, which is linearly dependent upon length. Further analysis of the minimum and maximum resistance values confirm the

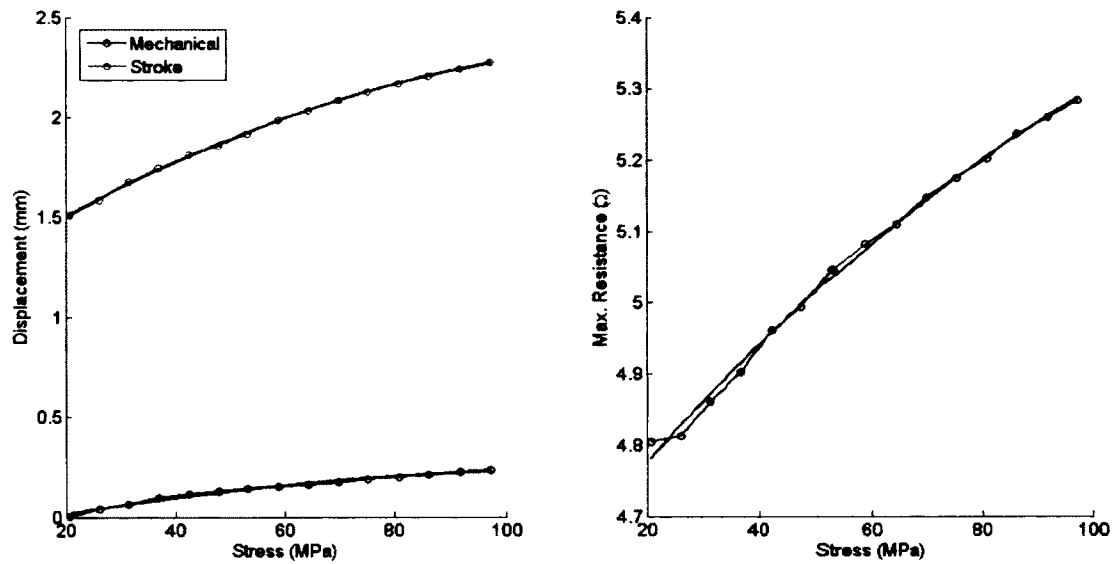


Figure 102: Polynomial curves approximating mechanical displacement, actuation stroke, and maximum resistance.

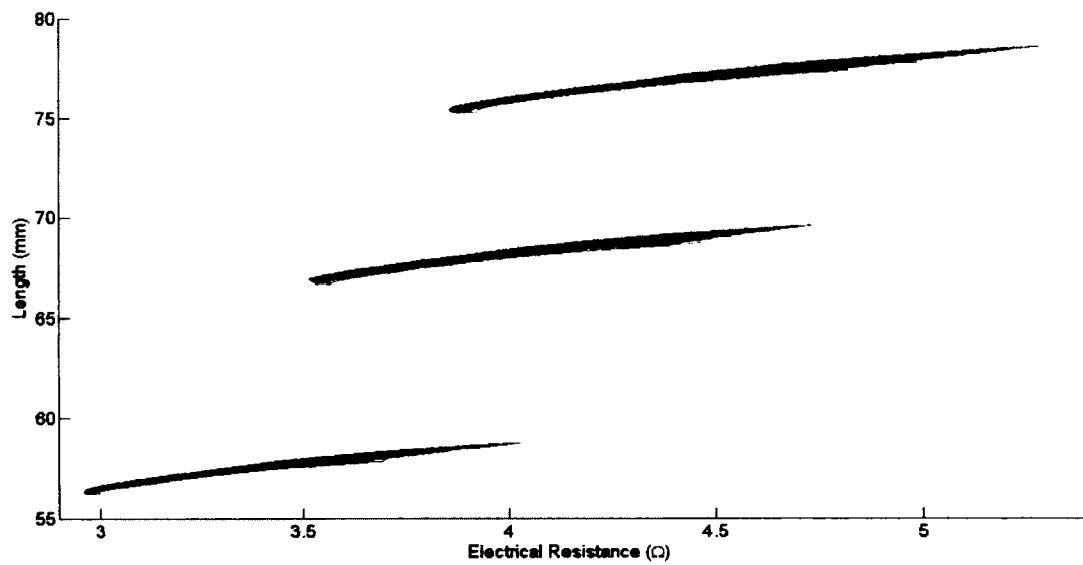


Figure 103: Resistance-length relationships for Furukawa actuator wires of various lengths.

linear relationships in terms of actuator length.

As previously described, the minimum resistance, R_{min} , is independent of applied stress while the maximum resistance, R_{max} , is modeled as a second-order polynomial function of stress. Accounting for the relationship between resistance, resistivity, and actuator length and area (L_0 and A_0), equations 5.82 and 5.83 describe the minimum and maximum resistance, respectively. The minimum resistivity is the resistivity of the austenite phase at the austenite finish temperature, ρ_A , while the maximum resistivity is the resistivity of the martensite phase at the martensite start temperature, ρ_M . The resistivity of the martensite phase is defined by equation 5.84 using the normalized relationship between maximum resistance and applied stress in equation 5.80 with coefficients ϕ_M .

$$R_{min} = \frac{\rho_A L_0}{A_0} \quad (5.82)$$

$$R_{max} = \frac{\rho_M L_0}{A_0} \quad (5.83)$$

$$\rho_M = \phi_{M_2} \sigma^2 + \phi_{M_1} \sigma + \phi_{M_0} \quad (5.84)$$

Normalized mechanical displacement and actuation stroke are defined as the mechanical strain, ε_M , and actuation strain, ε_L , respectively, which are defined by second-order polynomials with coefficients ψ_M and ψ_L as shown in equations 5.85 and 5.86. The total actuator strain, ε , is then determined using equation 5.87, from which the actuator displacement may be determined based on the initial length.

$$\varepsilon_M = \psi_{M_2} \sigma^2 + \psi_{M_1} \sigma + \psi_{M_0} \quad (5.85)$$

$$\varepsilon_L = \psi_{L_2} \sigma^2 + \psi_{L_1} \sigma + \psi_{L_0} \quad (5.86)$$

$$\varepsilon = \varepsilon_M + \varepsilon_L \xi \quad (5.87)$$

The normalized model was then characterized from experimental data to determine the austenite phase resistivity, ρ_A , as well as polynomial coefficients for the normalized activation curve, C , martensite phase resistivity, ϕ_M , mechanical strain, ψ_M , and actuation strain, ψ_L .

5.2.6 Model Correlations

Similar to the Flexinol model, no consideration of the actuator temperature is made within the model of the resistance-stress-strain behaviour of the Furukawa alloy. However, modeling of the resistance-stress-strain behaviour using the previously established relationships was investigated for comparison. The unaltered Liang & Rogers model was directly applied for modeling the phase transformation processes, and the electrical resistance was determined using the conventional relationship as a function of temperature and strain. The material properties of a similar Ni-Ti-Cu alloy were used in order to simulate the resistance-stress-strain behaviour for examination. Figure 104 shows the results of the simulated Liang & Rogers model using material properties of an alloy investigated by Wu et. al. [200]. Note that the stress influence coefficients were assumed to be the same as for a typical Ni-Ti alloy.

The simulated relationship between electrical resistance and actuator displacement is relatively similar but also significantly different than what is observed from experimental characterization of the Furukawa alloy. Although there is indeed a much smaller hysteresis effect, which is due to a smaller gap between the forward and reverse phase transformation temperatures, the influence of applied stress does not appear to be captured correctly. Furthermore, the overall activation curve appears to be linear in comparison to the non-linear curve observed experimentally.

The influence of applied stress was expected to be incorrectly represented since the Liang & Rogers model assumes a constant actuation stroke, meanwhile experimental characterization reveals a dependency between the actuation stroke and applied stress.

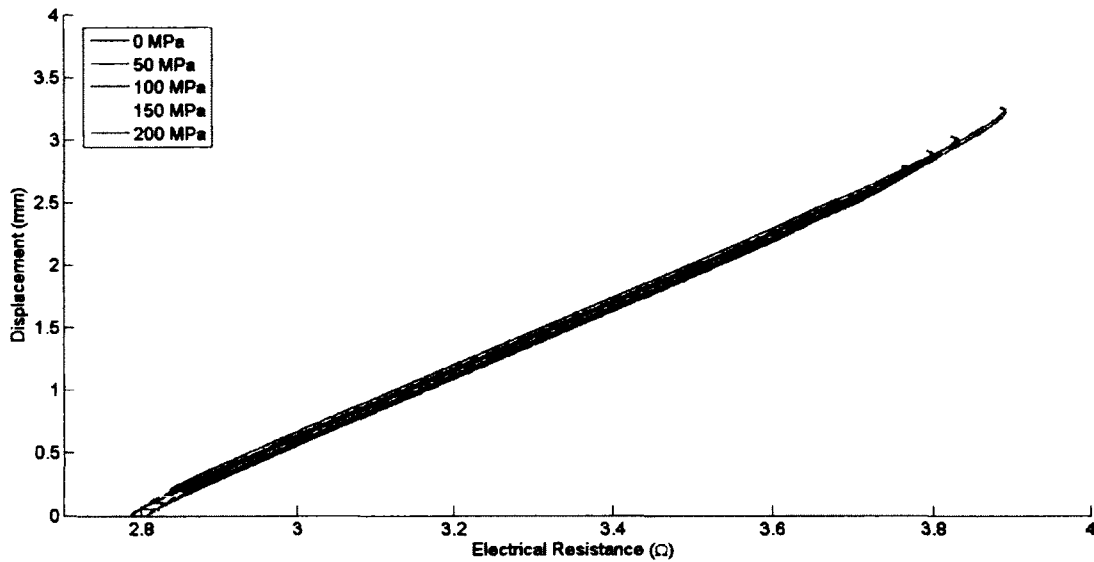


Figure 104: Simulated actuation curves of Ni-Ti-Cu actuator wire using the Liang & Rogers model.

The assumption of a cosine function dictating the phase transformation processes may be the cause of a mismatch between the overall shape of the activation curve. Also, further complexity in the phase transformation process may be incurred due to the influence of the copper addition. By modifying the Liang & Rogers model to include actuation stroke as a linear function of applied stress, the simulated analytical model results were much improved in comparison to the experimental characterization of the Furukawa alloy. Figure 105 shows the results of the modified Liang & Rogers model.

The model coefficients were not compared to analytical results since there is a significantly greater difference between the experimental and analytical results when compared to the Flexinol model. However, a more detailed investigation of the complete thermo-electro-mechanical behaviour may provide the necessary characterization parameters for improving the analytical model and estimating the Furukawa model coefficients.

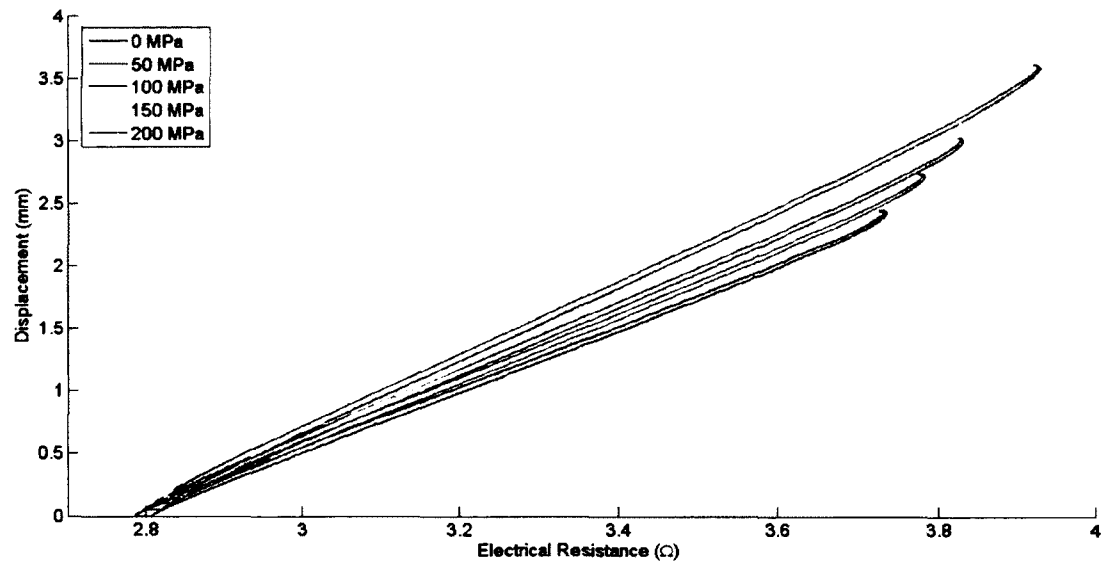


Figure 105: Simulated actuation curves of Ni-Ti-Cu actuator wire including stress-dependent actuator stroke.

Chapter 6

Control

Both models were developed for the purpose of position control for shape memory alloy actuators using feedback of the electrical resistance and applied load. The performance of the Flexinol and Furukawa models in simulation suggest they are suitable for capturing the hysteresis effects, incomplete actuation behaviour, and influence of applied load. These capabilities are important when considering the operational behaviour of actuation systems, where the actuator is commanded to reach intermediary positions within its range of motion and the applied load conditions are most often variable. Therefore, the Flexinol and Furukawa models were applied in a simple position control algorithm to verify the performance of each model in responding to various desired position responses and load conditions.

Application of the models in position control of the Flexinol and Furukawa shape memory alloy actuators focused on the use of a simple PID feedback control law. Feedback of the actuator position using sensor measurements was replaced with prediction of the actuator position using the appropriate model based on electrical resistance feedback. Similar control systems may be studied using a different feedback control law, or applying the predictive models for feed-forward control in combination with feedback control. However, the use of a PID control law is sufficient for verifying the performance of each model in effectively predicting position for feedback control.

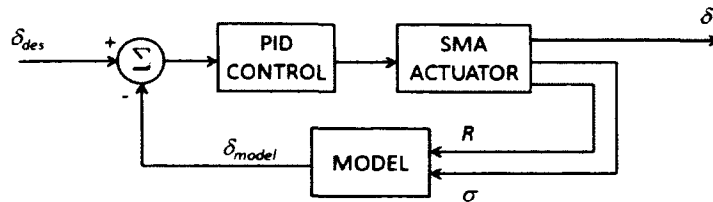


Figure 106: Block diagram of PID position control algorithm based on model feedback.

Based upon the input of the position error, velocity error, and integrated position error, the PID control law generates a desired input current signal for the power supply. The desired input current is then saturated to fall within limits, with maximum current chosen to avoid overheating and minimum current maintained to allow resistance measurement. Figure 106 shows the control algorithm used for position control of both Flexinol and Furukawa alloy actuator wires.

Position control of the actuator is investigated with the purpose of verifying the performance of the models as applied within a control loop instead of position feedback. Gains for the PID control law are coarsely tuned by trial and error in order to provide a reasonable control response which is underdamped and settles quickly, although it is possible that improvements in the control algorithm may cause the model to perform more accurately. Application of the model for actuator position control is used to validate the performance of the models under expected operational conditions without considering the performance of the control algorithm.

The control law is independent of the model, but in practice the error which drives the controller is based upon the predicted actuator position. Therefore, the performance of the control system is not only indicative of the model fidelity but also the quality of the control algorithm. The system performance is evaluated by analyzing the errors between the desired position, measured position, and predicted position. The output error is defined as the difference between the desired position

and measured position, and represents the performance of both the control system and model combined. The control error is defined as the difference between the desired position and predicted position, and represents the performance of the control law. The model error is defined as the difference between the measured position and predicted position, and represents the performance of the model. Output error is considered the most important measure of the actuator control system performance in terms of the end user point of view. However, the model error is considered the most significant measure within the overall context of this research since it represents the quality of the model.

Position control of the Flexinol and Furukawa alloy actuator wire was investigated for both step-wise and continuous desired position responses using constant applied loads and spring constraints. The step-wise desired position response consisted of varying the desired position in discrete steps between the limits of the actuator stroke, where each position was held for a period of time before moving to the next. The continuous desired position consisted of a wave function with a sufficiently long period to accommodate cooling, as well as amplitude and offset which also fit within the actuator stroke limits.

6.1 Flexinol

The discrete algorithm for the Flexinol model described previously was applied within a LabView program in order to estimate the position from feedback of electrical resistance and applied load, and determine desired input current using the PID control law. Position control was investigated using the exclusive model developed for a particular actuator wire as well as the normalized model developed for actuator wires of any geometry. Model coefficients were determined for a particular actuator wire sample and applied within the discrete algorithm to test the performance of the exclusive

Model Type	Mean Model Error	Mean Control Error	Mean Output Error
Exclusive	2.53%	2.95%	3.80%
Normalized	3.74%	1.83%	4.39%

Table 4: Summary of Flexinol model, control, and output errors in terms of total actuator stroke.

model. The normalized model was similarly tested using coefficients determined from a set of actuator wires of various lengths and applied to a selected wire.

Successful position control was achieved using both the exclusive and normalized Flexinol models. Each model was tested under combinations of constant load and spring constraint conditions, demonstrating the ability to adapt to varying applied loads. Step-wise desired position tracking was shown using both exclusive and normalized models, and continuous tracking was shown using the normalized model. The mean values of the model error, control error, and output error are summarized in Table 4, and expressed as a percentage of the typical Nitinol actuator stroke of 4% strain.

Lower model errors are expected for the exclusive model since it is fitted directly to the actuator being used for testing, whereas the normalized model is fitted to a series of data points and interpolated for the applied actuator. However, the overall performance of both the exclusive and normalized Flexinol models was similar and resulted in mean position errors of approximately 3.21% of the total stroke.

6.1.1 Exclusive Model

Position control of a Flexinol actuator wire was investigated using an exclusive model with coefficients that are calibrated for the particular wire being controlled. The stress influence coefficients, β , were determined from the open-loop actuation results of a series of constant applied loads, as described previously, and input into the LabView

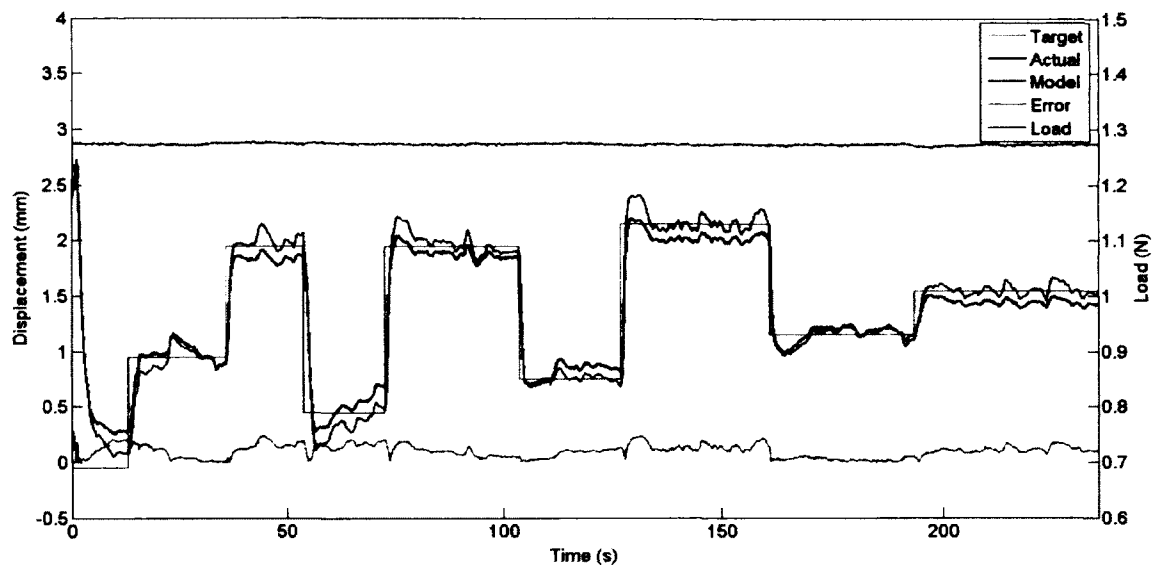


Figure 107: Step-wise tracking response of the control system under a constant applied load using the exclusive Flexinol model.

control program. The control system was then commanded to drive the actuator to random positions within the stroke limits of the wire, and maintain each position for a short period of time. Both constant applied loads and spring constraint loading conditions were investigated using the exclusive model.

Figures 107 through 109 show the response of the exclusive model control algorithm for Flexinol, including the desired displacement, measured displacement, model displacement, model error, and applied load. Figure 107 and Figure 108 demonstrate the results of position control under constant load conditions and spring constraint conditions, respectively. Position control under varying load conditions is demonstrated in Figure 109, where the load condition is changed during active control.

The response of the control algorithm demonstrates that the exclusive Flexinol model is suitable for resistance feedback position control of the actuator wire. Although the behaviour of the alloy is non-linear and hysteretic, the PID control law performed adequately in terms of overshoot and response time. Perturbations due

Experiment #	Mean Model Error	Mean Control Error	Mean Output Error
1	3.40%	4.44%	5.33%
2	2.20%	2.50%	3.39%
3	1.99%	1.91%	2.69%

Table 5: Summary of mean model, control, and output errors using the exclusive Flexinol model.

to heat losses from the wire to the surrounding air are a source of control error, and are seen more prominently in the results of Figure 107 and Figure 109. Model inaccuracies result in some steady-state error seen over the duration of hold time at each set point, but remain within reasonable limits. Sudden changes in the applied load also caused large errors as seen in Figure 109, however, subsequent activation of the wire tends to drive the model error down. The mean model, control, and output errors for the position control experiments shown in Figures 107 through 109 are summarized in Table 5. The overall mean error using the exclusive Flexinol model was approximately 3.09% of the total actuator stroke.

6.1.2 Normalized Model

The normalized Flexinol model was tested within the same position control algorithm as the exclusive model, with coefficients determined from a series of wires. Analysis of the experimental data for wires of various lengths yielded the polynomial stress influence coefficients, β , initial martensite resistivity, ρ_M , and transition curve parameters \tilde{a}_0 and τ . The length and diameter of a selected wire were then input to the normalized model applied within a LabView control program. Step-wise desired position tracking was investigated, where the actuator was commanded to move to a series of positions within the stroke range of the wire and maintain each position for a given duration. Continuous desired position tracking was also investigated, where

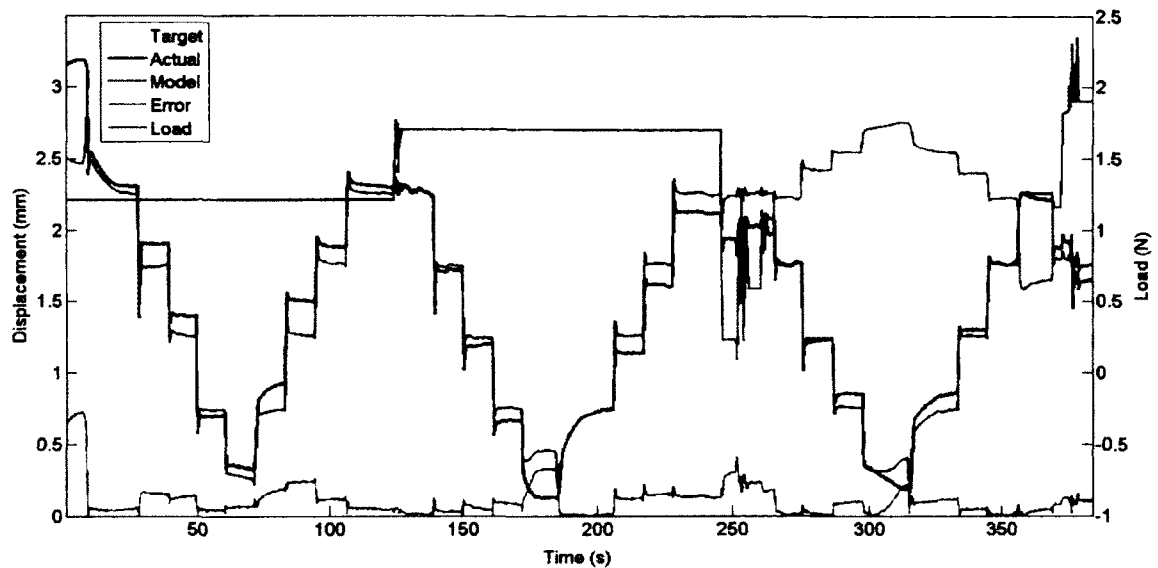


Figure 110: Step-wise tracking response of the control system under varying applied load using the normalized Flexinol model.

the actuator was commanded to track a sine wave position signal. The applied load in each case was varied between constant loads and spring constraints in order to test the performance of the model-based control system under varying load conditions.

Figures 110 and 111 show the response of the normalized model control algorithm for Flexinol, including the desired displacement, measured displacement, model displacement, model error, and applied load. Figure 110 shows the results of step-wise position tracking and Figure 111 shows the results of continuous position tracking for the normalized Flexinol model, with varying applied load conditions during both experiments.

Position control using the normalized Flexinol model was successfully demonstrated for both step-wise and continuous position tracking. Larger errors are expected when compared with the exclusive model since the normalized model was not characterized for the individual wire being used. As seen in the performance of the exclusive model, sudden changes in the applied load caused large errors which are

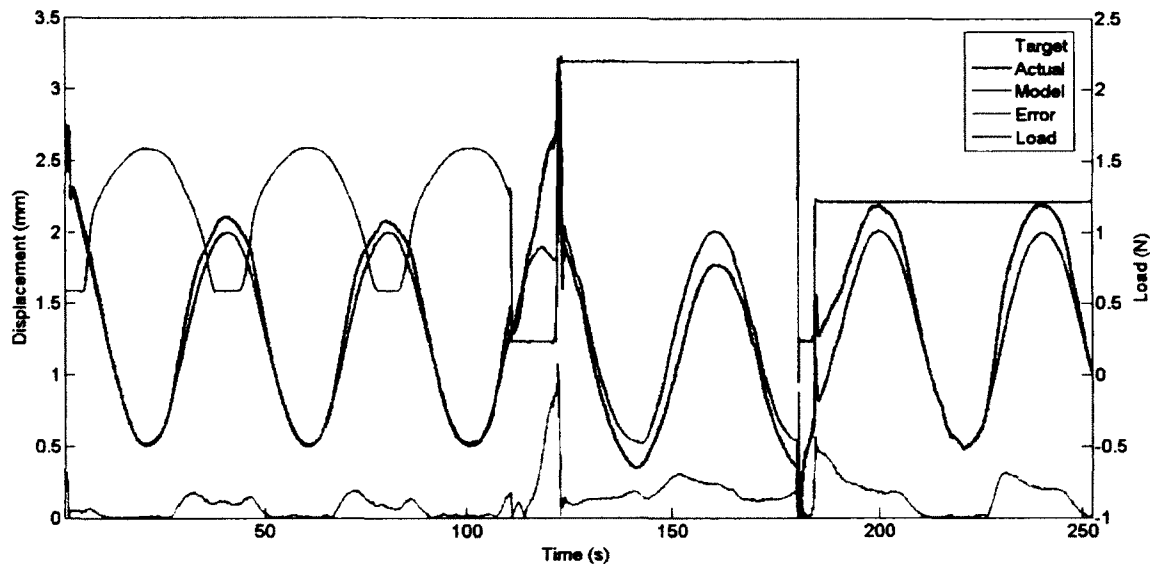


Figure 111: Sine tracking response of the control system under varying applied load using the normalized Flexinol model.

Experiment #	Mean Model Error	Mean Control Error	Mean Output Error
1	3.43%	1.79%	4.15%
2	4.04%	1.88%	4.62%

Table 6: Summary of mean model, control, and output errors using the normalized Flexinol model.

reduced through subsequent actuation. The results of position control using the normalized model demonstrate the capability to adapt to varying load conditions and track intermediary positions with an overall mean error of 3.32% of the total actuator stroke. Table 6 summarizes the mean model, control, and output errors for the position control experiments shown in Figures 110 and 111.

Model Type	Mean Model Error	Mean Control Error	Mean Output Error
Exclusive	1.90%	1.85%	2.59%
Normalized	1.79%	2.92%	3.79%

Table 7: Summary of Furukawa model, control, and output errors in terms of actuator stroke.

6.2 Furukawa

The discrete model of the Furukawa alloy was similarly tested within the simple PID control system using feedback of the electrical resistance and applied load. Both exclusive and normalized Furukawa models were applied within LabView control programs. Although the averaged transformation curve was ultimately chosen for the Furukawa model, the use of separate heating and cooling curves with direct switching was also investigated using the exclusive model. Coefficients for the exclusive model were determined for a particular actuator wire and applied within position control of the same wire. Normalized model coefficients were determined from a set of actuator wires of various lengths and applied to a selected wire.

Position control was successfully demonstrated using the exclusive and normalized Furukawa models. The performance of the models under varying applied load conditions was tested using constant loads, changing constant loads, and spring constraints. Step-wise desired position tracking was shown using both exclusive and normalized models, and continuous wave tracking was shown using the normalized model. The mean values of the model error, control error, and output error are summarized in Table 7, and expressed as a percentage of the typical Nitinol actuator stroke of 4% strain.

Although model errors are expected to be smaller for the exclusive model since the coefficients are determined for the particular wire being tested, the simple fundamental transformation relationship results in better numerical fitting compared with

the Flexinol model. The model errors are therefore similar for the exclusive and normalized Furukawa models, and are smaller than those for the Flexinol models due to smaller hysteresis effects and less dependence upon applied load. Position control using the Furukawa models resulted in mean errors of approximately 2.47% of the total stroke.

6.2.1 Exclusive Model

The exclusive Furukawa model was used for position control of a particular actuator wire for which the model coefficients are specifically calibrated. Heating and cooling curve coefficients, G_H and G_C , and averaged transformation curve coefficients, G , were determined from the experimental results of open-loop actuation at various constant applied loads. The appropriate coefficients were applied to the model algorithm within LabView control programs using both the averaged model and direct switching model. The actuator wire was then commanded to move to a series of positions stepping up and down through the actuator stroke limits, and hold each position for a short period of time. Varying applied load conditions were investigated using constant applied loads and spring constraint loads.

Figures 112 through 115 demonstrate the results of position control using the exclusive Furukawa model within a PID control law, including the desired displacement, measured displacement, model displacement, model error, and applied load. Figure 112 shows the results of position control using separate heating and cooling curves with the direct switching method under constant load conditions. Figures 113 and 114 demonstrate the results using the averaged transformation curve under constant load conditions and spring constraint conditions, respectively. Figure 115 shows the results of position control using the averaged model under varying load conditions.

The Furukawa actuator wire successfully tracked the desired position using position feedback based upon the exclusive model. As can be seen in Figure 112, the

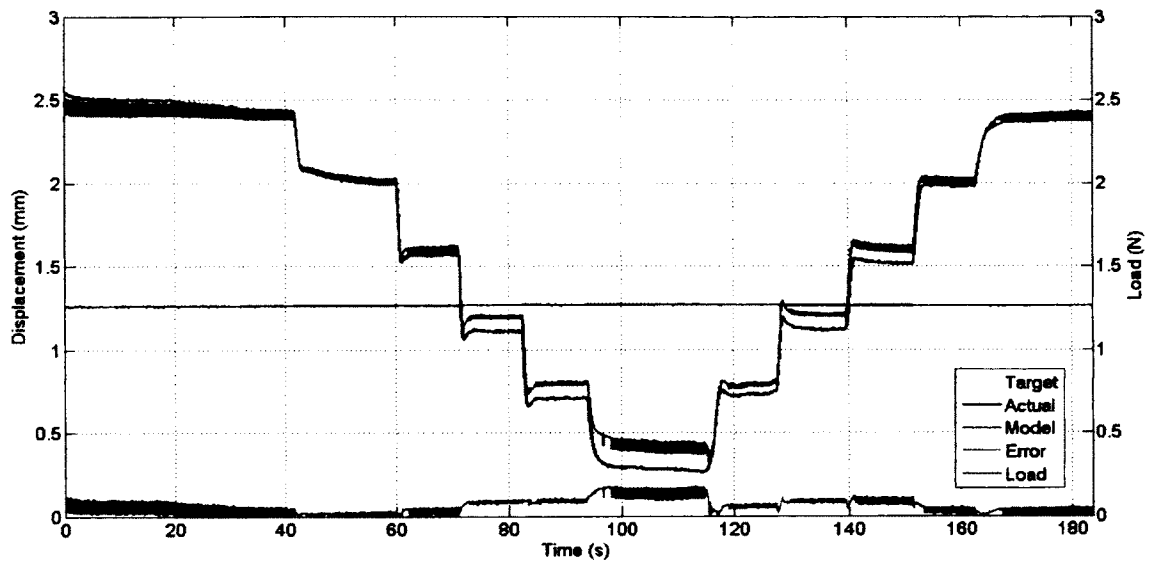


Figure 112: Step tracking response of the control system under constant applied load using the exclusive Furukawa model with direct switching between heating and cooling curves.

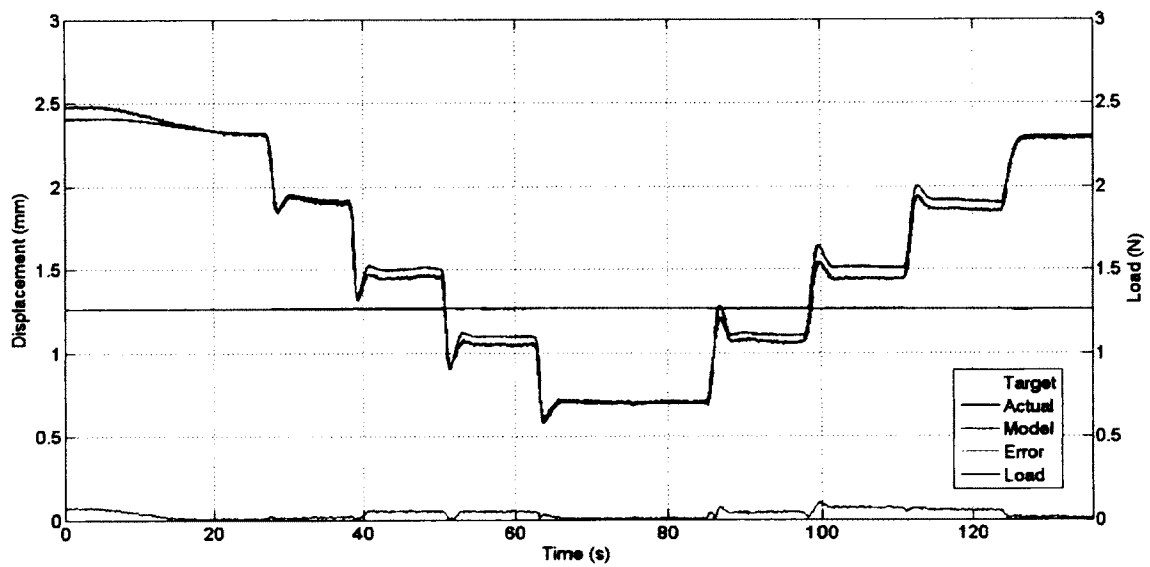


Figure 113: Step tracking response of the control system under constant applied load using the averaged exclusive Furukawa model.

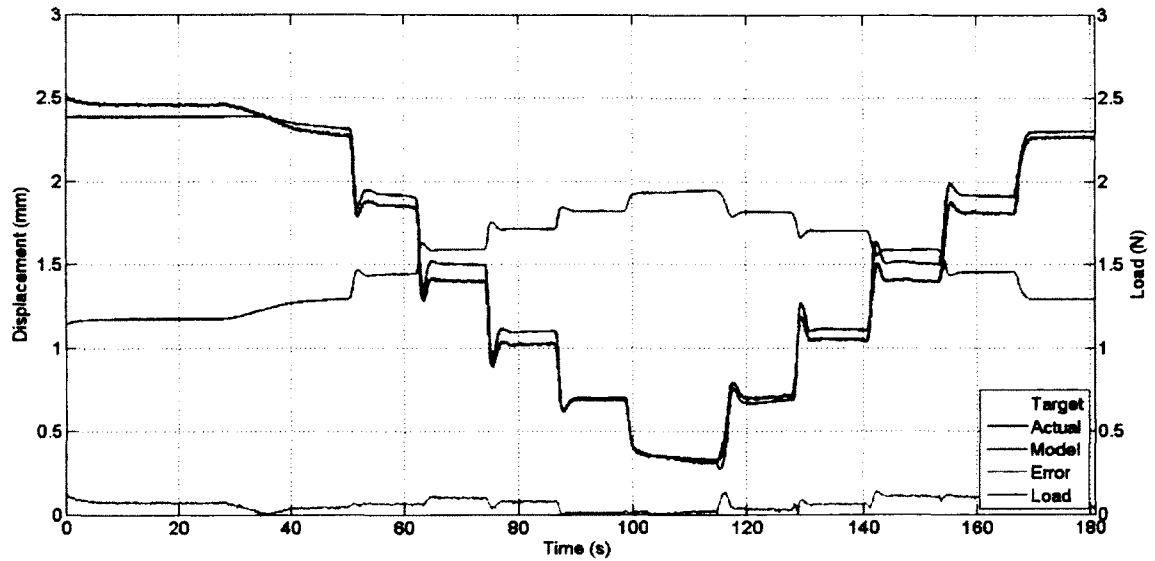


Figure 114: Step tracking response of the control system under spring constraint loading using the averaged exclusive Furukawa model.

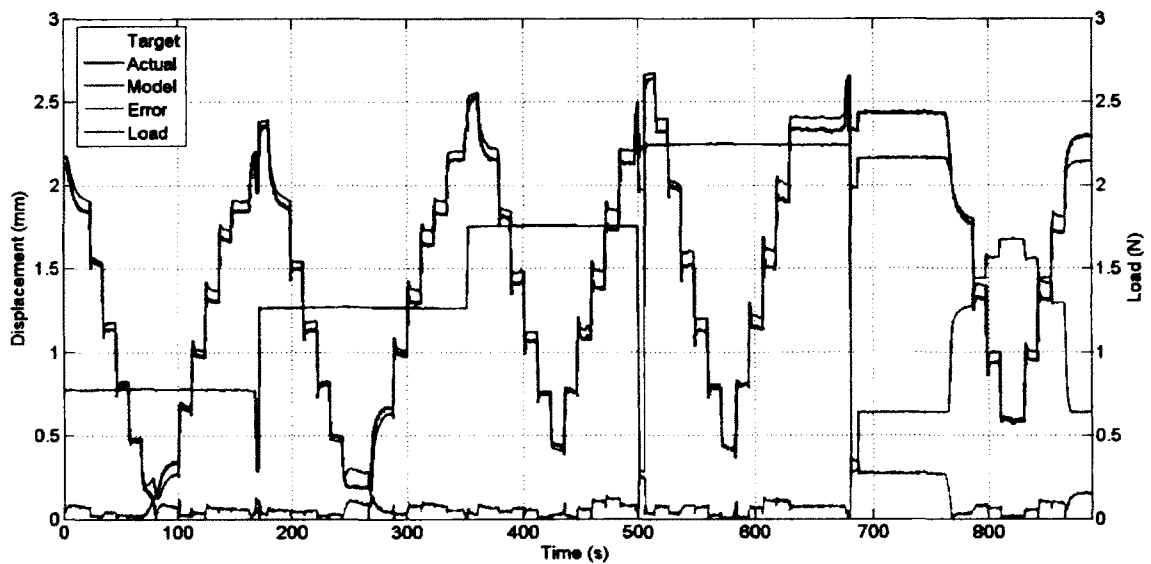


Figure 115: Step tracking response of the control system under varying applied load using the averaged exclusive Furukawa model.

Experiment #	Mean Model Error	Mean Control Error	Mean Output Error
1	1.97%	1.46%	2.65%
2	1.11%	1.47%	2.06%
3	1.92%	1.90%	2.64%
4	2.62%	2.58%	3.00%

Table 8: Summary of mean model, control, and output errors using the exclusive Furukawa model.

use of heating and cooling curves along with direct switching resulted in chatter as the controller attempted to hold each position. Although the proposed transition function for the Furukawa model may be included to provide smooth transition, the resulting reduction in model error was relatively small compared with the model error due to numerical fitting. Additionally, model errors during the experiments using the averaged model were close to those during the experiment using the heating and cooling curves with direct switching. Therefore, the averaged model is preferred in order to provide a simpler model algorithm. Figures 113 and 114 demonstrate successful position control under both constant applied load and spring constraint loading, with some steady-state error at each hold position due to model error. The response of the control algorithm in Figure 115 also demonstrates successful position control under varying load conditions. Table 8 summarizes the mean model, control, and output errors for the position control experiments using the exclusive Furukawa model, where the overall mean error was approximately 2.11% of the total actuator stroke.

6.2.2 Normalized Model

Position control of a Furukawa alloy actuator wire was also investigated using the normalized model within the PID control algorithm. The polynomial coefficients for the normalized activation curve, C , martensite phase resistivity, ϕ_M , mechanical strain, ψ_M , and actuation stroke, ψ_L , as well as the austenite phase resistivity, ρ_A ,

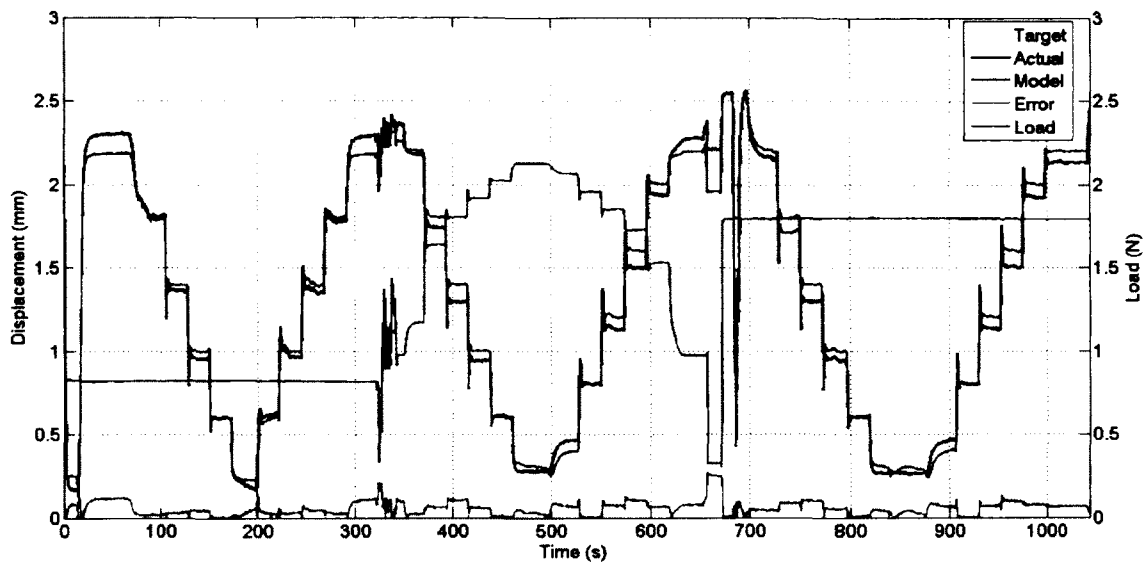


Figure 116: Step-wise tracking response of the control system under varying applied load using the normalized Furukawa model.

were determined from a series of wires of various lengths. The discrete normalized Furukawa model was then implemented along with the PID control algorithm within LabView. Step-wise position control was tested, with the actuator stepping up and down within the stroke range and holding each position briefly. Continuous position control was also tested, with the actuator tracking a triangle wave function. The load condition was again varied between constant applied loading and spring constraint loading.

Figures 116 and 117 demonstrate the results of position control using the normalized Furukawa model within a PID control law, including the desired displacement, measured displacement, model displacement, model error, and applied load. Step-wise position control under varying applied load is shown in Figure 116, while continuous position control under constant applied load is shown in Figure 117.

Position control using the normalized Furukawa model was successfully achieved for both step-wise and continuous desired position tracking. Model errors were similar

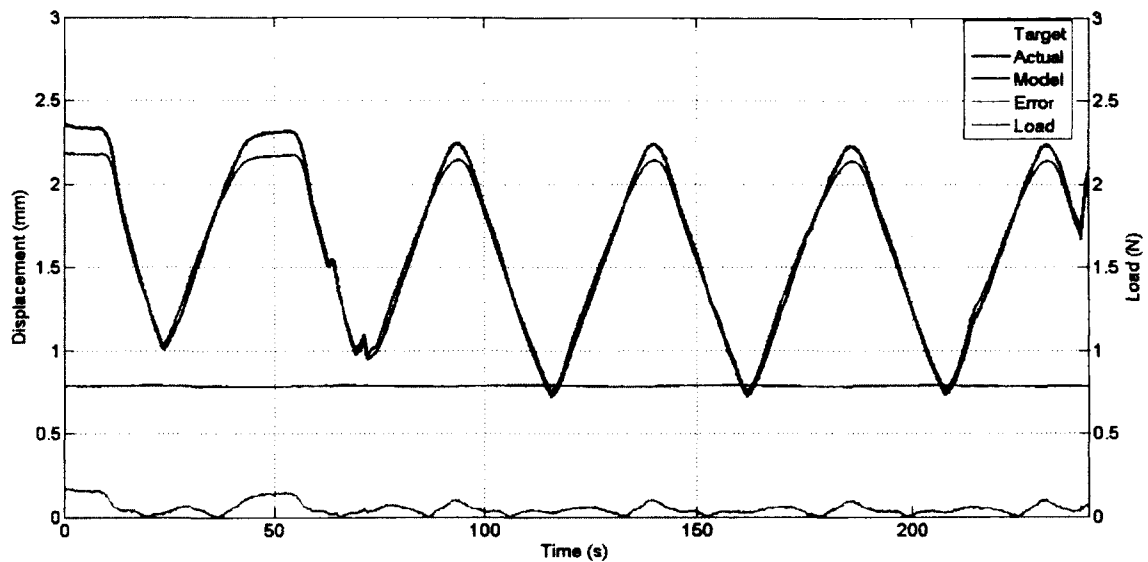


Figure 117: Triangle wave tracking response of the control system under constant load using the normalized Furukawa model.

Experiment #	Mean Model Error	Mean Control Error	Mean Output Error
1	1.89%	3.25%	4.32%
2	1.69%	2.59%	3.26%

Table 9: Summary of mean model, control, and output errors using the normalized Furukawa model.

to those of the exclusive model, with some steady-state error during step-wise position control as seen in Figure 116. Higher model error was also seen at the upper limit of the actuator stroke in both Figures 116 and 117, resulting from numerical fitting of the polynomial functions. The overall mean error during position control using the normalized Furukawa model was approximately 2.83%. Mean model, control, and output errors for the experiments shown in Figures 116 and 117 are summarized in Table 9.

Chapter 7

Conclusions

This thesis presents a significant contribution to the field of Nitinol shape memory alloy actuator modeling and position control. Measurement of the electrical resistance and applied load was successfully used to predict the actuator position based upon the developed models. The performance of each model was validated through simulation as well as a simple control application, demonstrating the ability to capture the hysteresis behaviour, the influence of varying applied load, and the effects of incomplete actuation. Characterization, modeling, and control was accomplished for both the Dynalloy Flexinol Ni-Ti alloy and the Furukawa Electric NT-H Ni-Ti-Cu alloy. Significant hysteresis behaviour was observed in the Flexinol alloy due to the presence of R-phase, whereas the Furukawa alloy exhibited negligible hysteresis effects. Furthermore, the relationships between electrical resistance and actuator strain for both alloys displayed a considerable dependency upon the applied stress.

Previous research has addressed position control of shape memory alloy actuators using feedback of electrical resistance. However, the approaches which have been studied are typically only applicable to a single applied load condition and wire geometry, and often do not fully capture the hysteresis effects. The research in this thesis presents models for both Ni-Ti and Ni-Ti-Cu alloys, with the hysteresis effects due to the occurrence of R-phase included in the model of Ni-Ti. Each model was

also normalized in terms of wire length and diameter, allowing the algorithms to be applied to any actuator wire from a given alloy. Additionally, the influence of applied stress upon the relationships between electrical resistance and actuator strain was also included within the models. Therefore, this research contributes algorithms for predicting the strain of an actuator wire of any length and diameter, under varying load conditions, and with or without the presence of R-phase.

Modeling of the Flexinol alloy was performed using a family of linear curves for heating and cooling paths, along with an exponential relationship during transition between the two paths. The influence of stress was included through the use of polynomial functions for describing the slope and offset parameters of the linear heating and cooling paths. Normalization of the model was also performed in order to be applicable to actuator wires of any length and diameter. The Furukawa alloy was modeled using relatively simpler relationships, with a single polynomial activation function describing the relationship between electrical resistance and actuator displacement. Each coefficient of the primary activation function was modeled as a function of applied stress using polynomial functions, resulting in a set of coefficients describing the family of curves. The Furukawa model was also normalized in terms of actuator wire diameter and length.

Position control of Flexinol and Furukawa alloy actuator wires was accomplished using a simple PID control algorithm with position feedback replaced with predicted model position based upon feedback of the electrical resistance and applied load. Successful tracking of step-wise and continuous desired position signals was demonstrated for both alloys, using exclusive models developed for a single actuator wire as well as the normalized models. Applied load conditions were changed during position control experiments in order to verify the models' ability to adapt to varying applied stress. Although model errors occurred due to the numerical fitting of the model functions, the overall mean error during control experiments was approximately 2.85% of the

typical total actuator stroke of 4% strain.

Position control using the simple PID control algorithm successfully demonstrated the ability of the models to predict the actuator position to replace sensor feedback. However, more sophisticated and robust control algorithms may also be used with model feedback in order to improve the performance of the control system. Feed-forward control terms may also be included based upon the model prediction. Although the applied stress is a necessary input, measurement of the actuator load may be replaced with a model based upon environmental conditions or known boundary conditions.

The configuration of the models also provides flexibility in terms of the fitting functions since higher order polynomials or more elaborate functions may be used for increased accuracy. For example, an artificial neural network model of the heating and cooling functions may be able to capture the non-linear and indeterminate regions in order to replace the simple linear asymptotes. The exponential transition function of the Flexinol model need not be altered in this case since a differential approach is used for the model algorithm. While an averaged activation curve is recommended for the Furukawa model, transition curve functions are also proposed which may increase model accuracy at the cost of higher complexity.

Some other improvements could also be addressed in future research using the proposed models. For example, the model coefficients may be related to material properties after an extensive characterization of the behaviour in terms of applied stress, strain, electrical resistance, and temperature. By assuming a given set of transformation functions, it may also be possible to estimate the actuator temperature based upon the measured electrical resistance. Furthermore, the influence of actuator cycling and fatigue may also be included with logarithmic functions for the appropriate strain and resistance parameters.

Appendix A

Load Cell Calibration

Calibration of the load cell is performed using a set of known laboratory calibration weights whose masses are verified using a precision scale. The test stand is configured with a hook attached to the load cell through a universal joint, and the output voltage of the Ectron 563H amplifier and signal conditioner is measured for a series of masses between 10 g and 1000 g. The output voltage for each test point is averaged over a recorded duration of 10 seconds. A linear curve is then fitted to the experimental data in order to determine the slope, m_F , and offset, b_F , of the load cell force-voltage relationship as defined by equation 3.2. Note that the masses of the components which are used to hang the calibration weights from the load cell must also be included in the analysis, and are measured using a precision scale. Equation A.1 shows the linear fitting function with the appropriate slope and offset values, where the input is the measured voltage signal, V , in volts and the output is the load, F , in Newtons. The linear correlation coefficient is approximately 0.9999985.

$$F = 12.7297V - 0.0598 \quad (\text{A.1})$$

Figure 118 shows the resulting experimental data and linear fitting function.

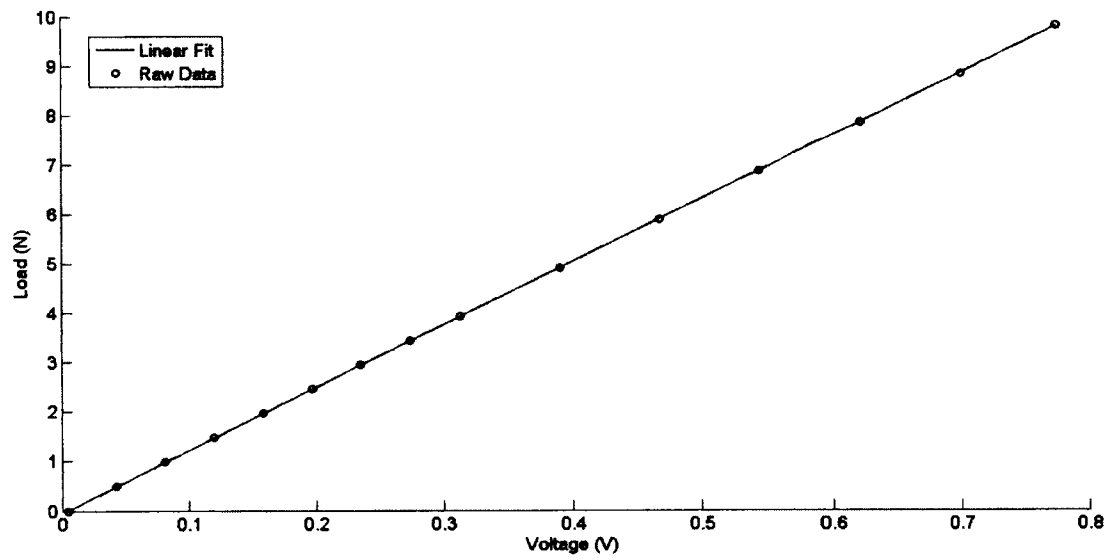


Figure 118: Linear fit of experimental data for load cell calibration.

Appendix B

LVDT Calibration

The LVDT sensor is calibrated by hanging the probe from the test stand and moving the transducer housing relative to the test stand mounting position. Measurement of the true displacement is accomplished using a digital micrometer, where the displacement of the probe is considered relative to the upper edge of the LVDT housing. Similar to the load cell calibration process, the sensor output is recorded for a duration of approximately 10 seconds and averaged for each data point. A linear curve is then fitted to the experimental data in order to determine the slope, m_δ , and offset, b_δ , of the current-displacement relationship defined by equation 3.1. Equation B.1 shows the linear fitting function with the appropriate slope and offset values, where the input is the measured current signal, I , in amperes and the output is the probe displacement, δ , in millimetres. The linear correlation coefficient is approximately 0.9997455.

$$\delta = 315.842I - 1.2195 \quad (\text{B.1})$$

Figure 119 shows the resulting experimental data and linear fitting function.

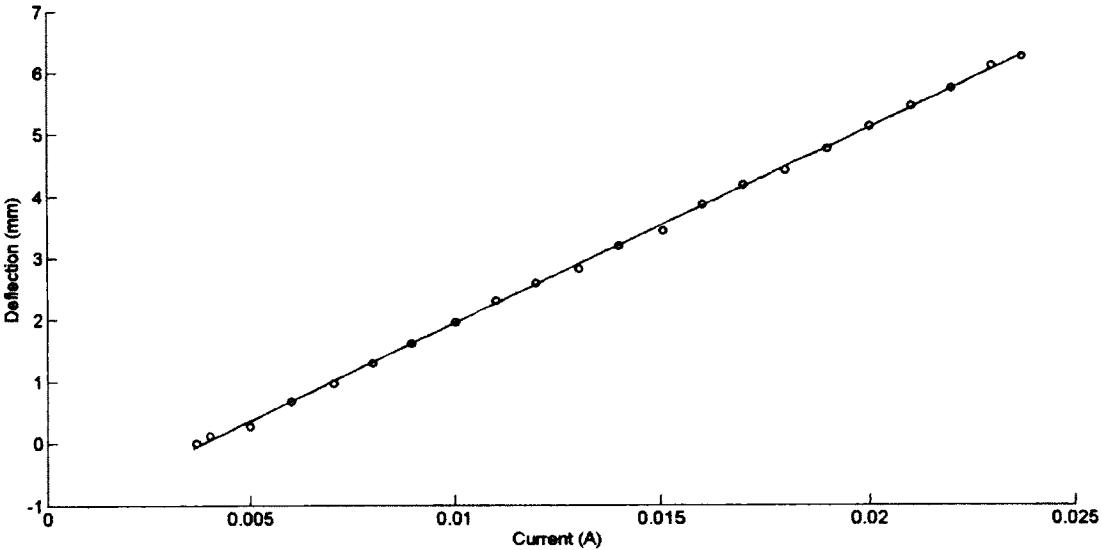


Figure 119: Linear fit of experimental data for LVDT calibration.

Appendix C

Flexinol Model Asymptote Slope & Offset Determination

The slope and offset of the heating and cooling asymptotes for the Flexinol alloy model are determined using the following algorithm implemented in MATLAB. Note that the wire is actuated using an open-loop square wave current signal over 3 cycles and the results averaged to reduce noise, with this process repeated for each constant load condition.

1. Split the overall hysteresis loop into the heating and cooling portions using the applied current as a reference for the heating/cooling condition.
2. For the heating curve:
 - (a) Compute the piece-wise linear least-squares fitting functions for each data point in the heating curve from $i - w_H$ to $i + w_H$, where i is the index of the data point and w_H defines the size of the piece-wise window.
 - (b) Determine the linear coefficient of correlation, r at each data point.
 - (c) Find the region of the heating curve where the coefficient of correlation is above some tolerance, $r_{tol,H}$.

- (d) Compute the linear least-squares fitting function for the region of the curve which meets the tolerance condition.
 - (e) Set the slope and offset of the heating asymptote to be the respective coefficients of this linear fitting function.
3. For the cooling curve:
- (a) Perform the same piece-wise linear least-squares fitting process as described for the heating curve, with a window size of w_C .
 - (b) Determine the linear coefficient of correlation, r at each data point.
 - (c) Discard any data points whose linear fitting function has a negative slope (since a positive slope is expected for all load conditions).
 - (d) Determine the first and second derivatives of r with respect to the data index, $\frac{\partial r}{\partial i}$ and $\frac{\partial^2 r}{\partial i^2}$.
 - (e) Retain only data points where r is greater than some tolerance, $r_{tol,C}$.
 - (f) Find the regions where the absolute value of $\frac{\partial r}{\partial i}$ is below a tolerance, $r'_{tol,C}$ (this narrows the data to regions where the change in linearity is below the tolerance).
 - (g) Depending upon the level of applied stress, there will be either one or two regions which meet the above criteria: one corresponding to the intermediate cooling pathway during transformation from austenite to R-phase, and a second corresponding to the cooling asymptote during transformation from R-phase and austenite to martensite. Therefore, if there are two regions, ignore the first one.
 - (h) Find the data point where $\frac{\partial r}{\partial i}$ is minimum.
 - (i) Compute the linear least-squares fitting function for the three data points centred upon the previously determined data point.

- (j) Set the slope and offset of the cooling asymptote to be the respective coefficients of this linear fitting function.

The following parameters are used during analysis of the Flexinol alloy:

$$w_H = 4$$

$$w_C = 10$$

$$r_{tol,H} = 0.999$$

$$r_{tol,C} = 0.995$$

$$r'_{tol,C} = 0.001$$

List of References

- [1] R. Lane and B. Craig. “Materials that sense and respond, an introduction to smart materials.” *The AMPTIAC Quarterly* **7-2**, 9–14 (2003).
- [2] R. E. Newnham. “Piezoelectric sensors and actuators: Smart materials.” *IEEE Frequency Control Symposium* pages 513–524 (1992).
- [3] K. Otsuka and C. Wayman. *Shape Memory Materials*. Cambridge University Press (1998).
- [4] W. S. Jr., J. Sirkis, and P. Gardiner. “Smart materials and structures: What are they?” *Smart Materials and Structures* **5**, 247–254 (1996).
- [5] H. Hongsheng, W. Juan, C. Liang, W. Jiong, and J. Xuezheng. “Design, control and test of a magnetorheological fluid fan clutch.” *Proceedings of the IEEE International Conference on Automation and Logistics* pages 1248–1253 (2009).
- [6] S. Guo, X. Dong, G. Wang, F. Lu, H. Kang, and Y. Wang. “Properties evaluation of piezoelectric materials in application of cochlear implant.” *Ferroelectrics* pages 272–278 (2011).
- [7] M. J. Konak, I. G. Powlesland, S. P. van der Velden, and S. C. Galea. “Analysis of a self-powered piezoelectric vibration damper.” *Smart Structures and Devices* pages 328–339 (2001).
- [8] K. Kuribayashi. “Micro sma actuator and motion control.” *2000 International Symposium on Micromechatronics and Human Science* pages 35–42 (2000).
- [9] F. Zhong, Y. Mei, S. Dongya, and L. Weiyi. “Research of piezoelectric sensor array in structural health.” *Seventh International Symposium on Instrumentation and Control Technology: Sensors and Instruments* (2008).
- [10] J. Rocha, L. Goncalves, P. Rocha, M. Silva, and S. Lanceros-Mndez. “Energy harvesting from piezoelectric materials fully integrated in footwear.” *IEEE Transactions on Industrial Electronics* **57-3**, 813–819 (2010).

- [11] J. Aboudi. "The response of shape memory alloy composites." *Smart Materials and Structures* **6**, 1–9 (1997).
- [12] M. Ray and A. Pradhan. "On the use of vertically reinforced 1-3 piezoelectric composites for hybrid damping of laminated composite plates." *Mechanics of Advanced Materials and Structures* **14**, 245–261 (2007).
- [13] F. K. Strauby and D. J. Merkleyz. "Design of a smart material actuator for rotor control." *Smart Materials and Structures* **6**, 223–234 (1997).
- [14] C. Mavroidis, C. Pfeiffer, and M. Mosley. "Conventional actuators, shape memory alloys, and electrorheological fluids." *Invited Chapter in Automation, Miniature Robotics and Sensors for Non-Destructive Testing and Evaluation* (1999).
- [15] C. Mavroidis. "Development of advanced actuators using shape memory alloys and electrorheological fluids." *Research in Nondestructive Evaluation* **14**, 1–32 (2002).
- [16] M. A. Rahman. "Patents on superelastic shape memory alloy." *Recent Patents on Mechanical Engineering* **1**, 65–67 (2008).
- [17] F. Gil and J. Planell. "Shape memory alloys for medical applications." *Proceedings of the Institution of Mechanical Engineers, Part H: Journal of Engineering in Medicine* **212**, 473–489 (1998).
- [18] M. H. Wu and L. M. Schetky. "Industrial applications for shape memory alloys." *Proceedings of the International Conference on Shape Memory and Superelastic Technologies* pages 171–182 (2000).
- [19] M. H. Wu and L. M. Schetky. "Industrial applications for shape memory alloys." *Proceedings of the International Conference on Shape Memory and Superelastic Technologies* pages 171–182 (2000).
- [20] M. Es-Souni, M. Es-Souni, and H. F. Brandies. "On the transformation behaviour, mechanical properties and biocompatibility of two niti-based shape memory alloys: Niti42 and niti42cu7." *Biomaterials* **22**, 2153–2161 (2001).
- [21] C. Xie, L. Zhao, and T. Lei. "Effect of precipitates on the electrical resistivity-temperature curves in an aged ti-51.8 at% ni shape memory alloy." *Scripta Metallurgica* **23**, 2131–2136 (1989).

- [22] I. Mihalcz. “Fundamental characteristics and design method for nickel-titanium shape memory alloy.” *Periodica Polytechnica Ser. Mech. Eng.* **45-1**, 77–86 (2001).
- [23] R. Santamarta, J. Pons, and E. Cesari. “Thermo-mechanical behaviour of a ni-ti-cu melt spun alloy.” *Journal de Physique IV* **11**, 351–356 (2001).
- [24] J. Frenzel, J. Pfetzing, K. Neuking, and G. Eggeler. “On the influence of thermomechanical treatments on the microstructure and phase transformation behavior of nitife shape memory alloys.” *Materials Science and Engineering* **481**, 635–638 (2007).
- [25] X. Huang, G. J. Ackland, and K. M. Rabe. “Crystal structures and shape-memory behaviour of niti.” *Nature Materials* **2**, 307–311 (2003).
- [26] K. Otsuka and X. Ren. “Recent developments in the research of shape memory alloys.” *Intermetallics* **7**, 511–528 (1999).
- [27] Y. Liu and P. McCormick. “Criteria of transformation sequences in niti shape memory alloys.” *Materials Transactions, JIM* **37**, 691–696 (1996).
- [28] Z. Lekston and E. Lagiewka. “X-ray diffraction studies of niti shape memory alloys.” *Archives of Materials Science and Engineering, Polish Academy of Sciences* **28-11**, 665–672 (2007).
- [29] K. Ng and Q. Sun. “Stress-induced phase transformation and detwinning in niti polycrystalline shape memory alloy tubes.” *Mechanics of Materials* **38**, 41–56 (2006).
- [30] T. W. Choon, A. S. Salleh, S. Jamian, , and M. I. Ghazali. “Phase transformation temperatures for shape memory alloy wire.” *Proceedings of World Academy of Science, Engineering and Technology* **21**, 304–307 (2007).
- [31] B. Donohue. “Developing a good memory: Nitinol shape memory alloy.” *Today's Machining World* pages 43–48 (2009).
- [32] Y. Stoeckel. “Superelastic niti wire.” *Wire Journal International* pages 45–50 (1991).
- [33] A. Teramoto. “Sentalloy: the Story of Superelasticity.” (2010).
- [34] TOTO USA. “Kiwami Renesse Thermostatic Mixing Valve.”
- [35] Furukawa Electric Company. “Furukawa NT Alloys.” Product datasheet.

- [36] The Dolomite Centre. “Micro Shape Memory Alloy Valve.” Product datasheet.
- [37] Dynalloy, Inc. “Electrostem II Valve.”
- [38] AutosplICE. “Shape Memory Actuation.”
- [39] A. Johnson, V. Gupta, V. Martynov, and L. Menchaca. “Silicon oxide diaphragm valves and pumps with thin film actuation.” *Proceedings of the International Conference on Shape Memory and Superelastic Technologies 2003* pages 605–612 (2004).
- [40] Miga Motor Company. “Application Notes: MigaOne On Board Actuators.” (2007).
- [41] A. Johnson. “State-of-the-art of shape memory actuators.” TiNi Alloy Company.
- [42] T. Borden. “Shape-memory alloys: Forming a tight fit.” *Mechanical Engineering* **113-10**, 67–73 (1991).
- [43] TiNi Aerospace, Inc. “Frangibolt Actuator.”
- [44] Dynalloy, Inc. “Technical Characteristics of Flexinol Actuator Wires.”
- [45] SAES Getters. “SmartFlex Wire.”
- [46] F. Gil, J. Manero, and J. Planell. “Relevant aspects in the clinical applications of nitinol shape memory alloys.” *Journal of Materials Science: Materials in Medicine* **7**, 403–406 (1996).
- [47] L. Petrini and FrancescoMigliavacca. “Biomedical applications of shape memory alloys.” *Journal of Metallurgy* pages 1–15 (2011).
- [48] C. Song. “History and current situation of shape memory alloy devices for minimally invasive surgery.” *The Open Medical Devices Journal* **2**, 24–31 (2010).
- [49] F. Migliavacca, L. Petrini, P. Massarotti, S. Schievano, F. Auricchio, and G. Dubini. “Stainless and shape memory alloy coronary stents: a computational study on the interaction with the vascular wall.” *Biomechanics and Modeling in Mechanobiology* **2**, 205–217 (2004).
- [50] K. Kuribayashi, K. Tsuchiya, Z. You, D. Tomus, M. Umemoto, T. Ito, and M. Sasaki. “Self-deployable origami stent grafts as a biomedical application of ni-rich nitinol shape memory alloy foil.” *Materials Science and Engineering A* **419**, 131–137 (2006).

- [51] S. M. Russell. "Design considerations for nitinol bone staples." *Journal of Materials Engineering and Performance* **18**, 831–835 (2009).
- [52] M. Shillington, R. Labrom, G. Askin, and C. Adam. "A biomechanical investigation of vertebral staples for fusionless scoliosis correction." *Clinical Biomechanics* **26**, 445–451 (2011).
- [53] D. Tarnita, D. N. Tarnita, R. Tarnita, C. Berceanu, and F. Cismaru. "Modular adaptive bone plate connected by nitinol staple." *Materialwissenschaft und Werkstofftechnik* **41-12**, 83–93 (2010).
- [54] S.-G. Xu and C.-C. Zhang. "Design and clinical application of proximal humerus memory connector." *Journal of Materials Engineering and Performance* **20-1**, 143–146 (2011).
- [55] Q. Fu, X. Liu, S. Xu, M. Li, and C. Zhang. "Stress-shielding effect of nitinol swan-like memory compressive connector on fracture healing of upper limb." *Journal of Materials Engineering and Performance* **2009**, 797–804 (2009).
- [56] G. Olender, R. Pfeifer, C. W. Muller, T. Gosling, S. Barcikowski, and C. Hurschler. "A preliminary study of bending stiffness alteration in shape changing nitinol plates for fracture fixation." *Annals of Biomedical Engineering* **39-5**, 1546–1554 (2011).
- [57] M.-S. Kim, S.-K. Lee, and S.-H. Lee. "Shape memory alloy bending actuator for catheter with movable link and guide wires." *1997 International Symposium on Micromechatronics and Human Science* pages 219–224 (1997).
- [58] T. Mineta, T. Mitsui, Y. Watanabe, S. Kobayashi, Y. Haga, and M. Esashi. "Batch fabricated flat winding shape memory alloy actuator for active catheter." *Proceedings of the IEEE Thirteenth Annual International Conference on Micro-Electro-Mechanical Systems* pages 375–380 (2000).
- [59] S. Maeda, K. Abe, K. Yamamoto, O. Tohyama, and H. Ito. "Active endoscope with sma (shape memory alloy) coil springs." *Proceedings. IEEE, The Ninth Annual International Workshop on Micro Electro Mechanical Systems. An Investigation of Micro Structures, Sensors, Actuators, Machines and Systems* pages 290–295 (1996).
- [60] B. applications of Ti50Ni41Cu9 shape memory films for wireless capsule endoscope. "H.j. du and y.q. fu and s. zhang and j.k. luo and a.j. flewitt and w.i. milne." *Smart Materials III* **5648**, 184–193 (2005).

- [61] W. Makishi, T. Matunaga, Y. Haga, and M. Esashi. "Active bending electric endoscope using shape memory alloy coil actuators." *Transactions of the Institute of Electrical Engineers of Japan Part E* **127E**, 75–81 (2007).
- [62] T. Sugawara, K. ichi Hirota, M. Watanabe, T. Mineta, E. Makinob, S. Toh, and T. Shibata. "Shape memory thin film actuator for holding a fine blood vessel." *Sensors and Actuators A* **130-131**, 461–467 (2006).
- [63] Y. Kanazawa, K. Kato, T. Yabuhara, T. Uzuka, H. Takahashi, and Y. Fujii. "Improvement of needle type applicator made of shape memory alloy." *30th Annual International IEEE EMBS Conference* pages 4372–4375 (2008).
- [64] M. Ho and J. P. Desai. "Characterization of sma actuator for applications in robotic neurosurgery." *31st Annual International Conference of the IEEE EMBS* pages 6856–6859 (2009).
- [65] Z. Shi, D. Liu, C. Ma, and D. Zhao. "Accurate controlled shape memory alloy actuator for minimally invasive surgery." *Proceedings of the 2011 IEEE International Conference on Mechatronics and Automation* pages 817–822 (2011).
- [66] D. Reynaerts, J. Peirs, and H. V. Brussel. "Design of a shape memory alloy actuated implantable drug delivery system." *Euroensors X* pages 1185–1188 (1996).
- [67] Y. Shimizu and M. Kobayashi. "The development of foot orthotics using shape memory alloy for preventing falls." *2011 11th IEEE International Conference on Bioinformatics and Bioengineering* pages 117–120 (2011).
- [68] C. M. L. dos Santos, F. L. da Cunha, and V. I. Dynnikov. "The application of shape memory actuators in anthropomorphic upper limb prostheses." *Artificial Organs* **27-5**, 473–477 (2003).
- [69] E. Henderson and A. Buis. "Nitinol for prosthetic and orthotic applications." *Journal of Materials Engineering and Performance* **20-4**, 663–665 (2011).
- [70] T. Raparelli, P. B. Zobel, and F. Durante. "A robot actuated by shape memory alloy wires." *Proceedings of the 2002 IEEE International Symposium on Industrial Electronics* pages 420–423 (2002).
- [71] G. Roznowski. "Underwater robot actuated by shape memory alloy wires." *MEMSTECH 2006* pages 149–150 (2006).

- [72] D. Mandru, I. Lungu, S. Noveanu, and O. Tatar. "Shape memory alloy wires as actuators for a minirobot." *2010 IEEE International Conference on Automation, Quality and Testing, Robotics* pages 4–7 (2010).
- [73] K. Kuribayashi. "Millimeter size joint actuator using shape memory alloy." *Proceedings: IEEE Micro Electro Mechanical Systems. An Investigation of Micro Structures, Sensors, Actuators, Machines and Robots* pages 139–144 (1989).
- [74] F. Arai, D. Azuma, K. Narumi, Y. Yamanishi, and Y.-C. Lin. "Design and fabrication of a shape memory alloy actuated exoskeletal microarm." *2007 18th International Symposium on Micro-NanoMechatronics and Human Science* pages 148–152 (2007).
- [75] S. M. Rahman and K. K. Ahn. "The study of tracking control of a robotic manipulator actuated by shape memory alloy." *Proceedings of 11th International Conference on Computer and Information Technology* pages 282–287 (2008).
- [76] F. Garcia-Cordova, J. Lopez-Coronado, and A. Guerrero-Gonzalez. "Design of an anthropomorphic finger using shape memory alloy springs." *1999 IEEE International Conference on Systems, Man, and Cybernetics* pages 794–799 (1999).
- [77] M. Wen, G. Tu, Q. Zong, and C. Xie. "A study of niti shape memory alloy springs and its application in a new robotic actuator." *Proceedings of the IEEE International Conference on Industrial Technology* pages 215–219 (1994).
- [78] A. Price, A. Jnifene, and H. Naguib. "Design and control of a shape memory alloy based dexterous robot hand." *Smart Materials and Structures* **16**, 1401–1414 (2007).
- [79] K. Yang and C. Gu. "Research on planar and spacial bending embedded shape memory alloy actuators." *Proceedings of the Eighth International Conference on Electrical Machines and Systems* pages 2418–2421 (2005).
- [80] J.-H. Wang, C.-H. Fan, and C.-C. Lan. "A two-way flexural rotation manipulator using opposing shape memory alloy wires." *2009 IEEE/ASME International Conference on Advanced Intelligent Mechatronics* pages 6–11 (2009).
- [81] S. S. Ge, K. P. Tee, I. E. Vahhi, and F. E. Tay. "Tracking and vibration control of flexible robots using shape memory alloys." *IEEE/ASME Transactions On Mechatronics* **11-6**, 690–698 (2006).

- [82] S. Aramaki, S. Kaneko, K. Arai, Y. Takahashi, H. Adachi, and K. Yanagisawa. "Tube type micro manipulator using shape memory alloy (sma)." *Sixth International Symposium on Micro Machine and Human Science* pages 115–120 (1995).
- [83] E. Lanteigne and A. Jnifene. "Design of a linkless hyper-redundant manipulator and composite shape memory alloy actuator." *Canadian Journal of Electrical and Computer Engineering* **31-4**, 191–194 (2006).
- [84] A. Price, A. Edgerton, C. Cocaud, H. Naguib, and A. Jnifene. "A study on the thermomechanical properties of shape memory alloys-based actuators used in artificial muscles." *Journal Of Intelligent Material Systems And Structures* **18**, 11–18 (2007).
- [85] A. Villanueva, C. Smith, and S. Priya. "A biomimetic robotic jellyfish (robogel) actuated by shape memory alloy composite actuators." *Bioinspiration & Biomimetics* **6**, 1–16 (2011).
- [86] Z. Wang, Y. Wang, J. Li, and G. Hang. "A micro biomimetic manta ray robot fish actuated by sma." *Proceedings of the 2009 IEEE International Conference on Robotics and Biomimetics* pages 1809–1813 (2009).
- [87] J. Finkbeiner, J. Ahmad, W. Santosa, G. Y. Xu, and J. Xiao. "Biomimetic fish actuated by shape memory alloy." *6th IEEE Conference on Industrial Electronics and Applications* pages 2139–2144 (2011).
- [88] A. Suleman and C. Crawford. "Design and testing of a biomimetic tuna using shape memory alloy induced propulsion." *Computers and Structures* **86**, 491–499 (2008).
- [89] T. Saito, T. Kagiwada, and H. Harada. "Development of an earthworm robot with a shape memory alloy and braided tube." *Advanced Robotics* **23**, 1743–1760 (2009).
- [90] Y. P. Lee, B. Kim, M. G. Lee, and J.-O. Park. "Locomotive mechanism design and fabrication of biomimetic micro robot using shape memory alloy." *Proceedings of the 2004 IEEE International Conference on Robotics & Automation* pages 5007–5012 (2004).
- [91] J.-S. Koh and K.-J. Cho. "Omegabot : Biomimetic inchworm robot using sma coil actuator and smart composite microstructures (scm)." *Proceedings of the*

- 2009 IEEE International Conference on Robotics and Biomimetics* pages 1154–1159 (2009).
- [92] J. Ko, M. B. Jun, G. Gilardi, E. Haslam, and E. J. Park. “Fuzzy pwm-pid control of cocontracting antagonistic shape memory alloy muscle pairs in an artificial finger.” *Mechatronics* **21**, 1190–1202 (2011).
- [93] K. Andrianesis and A. Tzes. “Design of an anthropomorphic prosthetic hand driven by shape memory alloy actuators.” *Proceedings of the 2nd Biennial IEEE/RAS-EMBS International Conference on Biomedical Robotics and Biomechatronics* pages 517–522 (2008).
- [94] W.-C. Kim, J.-H. Kim, M. Lee, J.-K. Shin, and H. Yonezu. “Biologically motivated active vision system using artificial retina chip and shape memory alloy actuator.” *Proceedings of the 9th International Conference on Neural Information Processing* pages 1305–1309 (2002).
- [95] A. Villanueva, K. Joshi, J. Blottman, and S. Priya. “A bio-inspired shape memory alloy composite (bismac) actuator.” *Smart Materials and Structures* **19**, 1–17 (2010).
- [96] R. Barrett and R. S. Gross. “Super-active shape-memory alloy composites.” *Smart Materials and Structures* **5**, 255–260 (1996).
- [97] H. Kahny, M. Huffz, and A. Heuery. “The tini shape-memory alloy and its applications for mems.” *Journal of Micromechanics and Microengineering* **8**, 213–221 (1998).
- [98] K. Ikuta, H. Fujita, M. Ikeda, and S. Yamashita. “Crystallographic analysis of tini shape memory alloy thin film for micro actuator.” *Proceedings. IEEE Micro Electro Mechanical Systems-An Investigation of Micro Structures, Sensors, Actuators, Machines* pages 38–39 (1990).
- [99] P. Krulevitch, A. P. Lee, P. B. Ramsey, J. C. Trevino, J. Hamilton, and M. A. Northrup. “Thin film shape memory alloy microactuators.” *Journal of Microelectromechanical Systems* **5-4**, 270–282 (1996).
- [100] C.-L. Shih, B.-K. Lai, H. Kahn, S. M. Phillips, and A. H. Heuer. “A robust co-sputtering fabrication procedure for tini shape memory alloys for mems.” *IEEE Journal Of Microelectromechanical Systems* **10-1**, 69–79 (2001).

- [101] A. Camposeo, N. Puccini, F. Fuso, M. Allegrini, E. Arimondo, and A. Tuissi. "Laser deposition of shape-memory alloy for mems applications." *Applied Surface Science* **208**, 518–521 (2003).
- [102] I. Roch, P. Bidaud, D. Collard, and L. Buchaillot. "Fabrication and characterization of an su-8 gripper actuated by a shape memory alloy thin film." *Journal of Micromechanics and Microengineering* **13**, 330–336 (2003).
- [103] Q. Pan and C. Cho. "The investigation of a shape memory alloy micro-damper for mems applications." *Sensors* **7**, 1887–1900 (2007).
- [104] W. L. Benard, H. Kahn, A. H. Heuer, and M. A. Huff. "Thin-film shape-memory alloy actuated micropumps." *Journal of Microelectromechanical Systems* **7-2**, 245–251 (1998).
- [105] D. Hartl and D. Lagoudas. "Aerospace applications of shape memory alloys." *Proceedings of the Institution of Mechanical Engineers, Part G: Journal of Aerospace Engineering* **221**, 535–553 (2007).
- [106] M. Brennison, R. Barrett, and L. Kerth. "Development & flight test of a shape memory alloy actuator flight control system." *Active and Passive Smart Structures and Integrated Systems 2010* **7643**, 1–14 (2010).
- [107] K. Singh and I. Chopra. "Design of an improved shape memory alloy actuator for rotor blade tracking." *Smart Structures and Materials 2002: Smart Structures and Integrated Systems* **4701**, 244–266 (2002).
- [108] H. Prahlad and I. Chopra. "Design of a variable twist tiltrotor blade using shape memory alloy (sma) actuators." *Smart Structures and Materials 2001: Smart Structures and Integrated Systems* **4327**, 46–59 (2001).
- [109] J.-S. Park, S.-H. Kim, S. N. Jung, and M.-K. Lee. "Design and analysis of variable-twist tiltrotor blades using shape memory alloy hybrid composites." *Smart Materials and Structures* **20-1**, 1–10 (2011).
- [110] G. Song, N. Ma, H.-J. Lee, and S. Arnold. "Design and control of a proof-of-concept variable area exhaust nozzle using shape-memory alloy actuators." *Smart Structures and Materials 2004: Industrial and Commercial Applications of Smart Structures Technologies* **5388**, 78–86 (2004).
- [111] B.-S. Jung, M.-S. Kim, J.-S. Kim, Y.-M. Kim, W.-Y. Lee, and S.-H. Ahn. "Fabrication of a smart air intake structure using shape memory alloy wire embedded composite." *Physica Scripta* **T139**, 1–6 (2010).

- [112] U. Icardi and L. Ferrero. "Preliminary study of an adaptive wing with shape memory alloy torsion actuators." *Materials and Design* **30**, 4200–4210 (2009).
- [113] E. Abdullah, C. Bil, and S. Watkins. "Adaptive airfoil control system using shape memory alloy actuator for unmanned aerial vehicle." *Incorporating Sustainable Practice in Mechanics of Structures and Materials* pages 141–146 (2011).
- [114] Y.-C. Park, Y.-J. Jo, S.-H. Baek, and Y. Furuya. "Fatigue design curve of a titanium/aluminum shape memory alloy composite for aircraft stringer design." *Smart Materials and Structures* **18**, 1–9 (2009).
- [115] L. M. Schetky. "Shape memory alloy applications in space systems." *Materials & Design* **12-1**, 29–32 (1991).
- [116] A. Peffer, K. Denoyer, E. Fosness, and D. Sciulli. "Development and transition of low-shock spacecraft release devices." *IEEE Aerospace Conference Proceedings* **4**, 277–284 (2000).
- [117] M.-S. L. abd Jae-Uk Jo, W.-J. Tak, and B. Kim. "Shape memory alloy (sma) based non-explosive separation actuator (nea) with a redundant function." *International Journal of Precision Engineering and Manufacturing* **12-3**, 569–572 (2011).
- [118] P. Rossoni. "Structural bus and release mechanisms on the st5 satellites summary and status." *2007 IEEE Aerospace Conference* pages 1–14 (2007).
- [119] W. Huang, S. Pellegrino, and D. Bashford. "Shape memory alloy actuators for deployable structures." *Proceedings of the Conference on Spacecraft Structures, Materials & Mechanical Testing* pages 53–62 (1996).
- [120] P. Hull, S. Canfield, and C. Carrington. "A radiant energy-powered shape memory alloy actuator." *Mechatronics* **14**, 757–775 (2004).
- [121] T. Iwata, Y. Fujiwara, A. Ogawa, H. Murakami, and Y. Toda. "Solar paddle actuator for small satellites using shape memory alloy." *European Space Agency, (Special Publication) ESA SP* pages 249–253 (2001).
- [122] T. Iwata, Y. Komoda, A. Ogawa, and H. Murakami. "Solar paddle actuator for small satellites using shape memory alloy (ii)." *10th European Space Mechanisms and Tribology Symposium* pages 409–412 (2003).

- [123] E. L. Pollard and C. H. Jenkins. "Shape memory alloy deployment of membrane mirrors for spaceborne telescopes." *Journal of Spacecraft and Rockets* **44-1**, 109–120 (2007).
- [124] P. P. Jenkins and G. A. Landis. "A rotating arm using shape-memory alloy." *The 29th Aerospace Mechanisms Symposium* pages 167–171 (1995).
- [125] R. Edesona, M. Whalleya, B. Kenta, S. Canferb, and E. Sawyera. "Smagag release mechanism for the rosetta landers ptolemy instrument." *Acta Astronautica* **58**, 576–582 (2006).
- [126] E.-J. Yoo, J.-H. Roh, and J.-H. Han. "Wrinkling control of inflatable booms using shape memory alloy wires." *Smart Materials and Structures* **16**, 340–348 (2007).
- [127] F. Peng, X.-X. Jiang, Y.-R. Hu, and A. Ng. "Application of shape memory alloy actuators in active shape control of inflatable space structures." *2005 IEEE Aerospace Conference* pages 2769–2778 (2005).
- [128] F. Peng, Y.-R. Hu, , and A. Ng. "Testing of membrane space structure shape control using genetic algorithm." *Journal of Spacecraft and Rockets* **43-4**, 788–793 (2006).
- [129] X. Wang, W. Zheng, and Y.-R. Hu. "Active flatness control of membrane structures using adaptive genetic algorithm." *Industrial and Commercial Applications of Smart Structures Technologies 2007* **6527-04**, 1–10 (2007).
- [130] B. Maclean, G. Patterson, and M. Misra. "Modeling of a shape memory integrated actuator for vibration control of large space structures." *Journal of Intelligent Materials Systems and Structures* **2**, 72–94 (1991).
- [131] M. E. Regelbrugge, A. Carrier, and W. C. Dickson. "Performance of a smart vibration isolator for precision spacecraft instruments." *Journal of Intelligent Materials Systems and Structures* **7**, 211–215 (1996).
- [132] H. Nagano, A. Ohnishi, and Y. Nagasaka. "Development of a lightweight deployable/stowable radiator for interplanetary exploration." *Applied Thermal Engineering* **31**, 3322–3331 (2011).
- [133] S. Montminy, E. Dupuis, and H. Champiaud. "Mechanical design of a hopper robot for planetary exploration using sma as a unique source of power." *Acta Astronautica* **62**, 438–452 (2008).

- [134] D. A. Miller and D. C. Lagoudas. “Thermomechanical characterization of niticu and niti sma actuators: influence of plastic strains.” *Smart Materials and Structures* **9**, 640–652 (2000).
- [135] S. A. Mascaro and H. H. Asada. “Wet shape memory alloy actuators for active vasculated robotic flesh.” *Proceedings of the 2003 IEEE International Conference on Robotics & Automation* pages 282–287 (2003).
- [136] C.-C. Lan and C.-H. Fan. “An accurate self-sensing method for the control of shape memory alloy actuated flexures.” *Sensors and Actuators A* **163**, 323–332 (2010).
- [137] R. Featherstone and Y. H. Teh. “Improving the speed of shape memory alloy actuators by faster electrical heating.” *Proceedings of the International Symposium of Experimental Robotics* pages 18–21 (2004).
- [138] A. Villanueva and S. Priya. “Bismac control using sma resistance feedback.” *Proceedings of Electroactive Polymer Actuators and Devices (EAPAD) 2010* **7642**, 1–12 (2010).
- [139] H. Meier, A. Czechowicz, C. Haberland, and S. Langbein. “Smart control systems for smart materials.” *Journal of Materials Engineering and Performance* **20-4**, 559–563 (2011).
- [140] F. Schiedeck and S. Mojrzisch. “Design of a robust control strategy for the heating power of shape memory alloy actuators at full contraction based on electric resistance feedback.” *Smart Materials and Structures* **20-4**, 1–11 (2011).
- [141] M. E. Dib, R. Gorbet, E. Kubica, X. Gao, A. Browne, and N. Johnson. “Adaptive sma actuator priming using resistance feedback.” *Smart Materials and Struct* **20**, 1–14 (2011).
- [142] C. Mao, H. Li, and J. Ou. “Experimental study on shape memory alloy displacement transducer.” *Earth and Space Conference 2008: Proceedings of the 11th Aerospace Division International Conference on Engineering, Science, Construction, and Operations in Challenging Environments* **323**, 1–8 (2008).
- [143] G. Triantafyllou and G. Psarras. “Probing the reverse martensitic transformation in constrained shape memory alloys via electrical.” *Journal of Intelligent Material Systems and Structures* **21**, 975–982 (2010).
- [144] H. Nagai and R. Oishi. “Shape memory alloys as strain sensors in composites.” *Smart Materials and Structures* **15**, 493–498 (2006).

- [145] R. Brammajyosula, V. Buravalla, and A. Khandelwal. "Model for resistance evolution in shape memory alloys including r-phase." *Smart Materials and Structures* **20**, 1–11 (2011).
- [146] D. Cui, G. Song, and H. Li. "Modeling of the electrical resistance of shape memory alloy wires." *Smart Materials and Structures* **9-5**, 1–9 (2010).
- [147] H. Song, E. Kubica, and R. Gorbet. "Resistance modelling of sma wire actuators." *Proceedings of the Smart Materials, Structures and NDT in Aerospace Conference 2011* pages 1–10 (2011).
- [148] V. Novak, P. Sittner, G. Dayananda, F. Braz-Fernandes, and K. Mahesh. "Electric resistance variation of niti shape memory alloy wires in thermomechanical tests: Experiments and simulation." *Materials Science and Engineering A* **481-482**, 127–133 (2008).
- [149] S. J. Furst and S. Seelecke. "Modeling and experimental characterization of the stress, strain, and resistance of shape memory alloy actuator wires with controlled power input." *Journal of Intelligent Material Systems and Structures* **23-11**, 1233–1247 (2012).
- [150] K. Ikuta, M. Tsukumoto, and S. Hirose. "Shape memory alloy servo actuator system with electric resistance feedback and application for active endoscope." *Proceedings of the 1988 IEEE International Conference on Robotics and Automation* **1**, 427–430 (1988).
- [151] M. Mertmann and E. Hornbogen. "Grippers for the micro assembly containing shape memory actuators and sensors." *Journal de Physique IV* **7-C5**, 621–626 (1997).
- [152] K. Yang and C. Gu. "A novel robot hand with embedded shape memory alloy actuators." *Proceedings of the Institution of Mechanical Engineers* **216**, 737–746 (2002).
- [153] J. Urata, T. Yoshikai, I. Mizuuchi, and M. Inaba. "Design of high d.o.f. mobile micro robot using electrical resistance control of shape memory alloy." *Proceedings of the 2007 IEEE/RSJ International Conference on Intelligent Robots and Systems* pages 3828–3833 (2007).
- [154] H. Meier, A. Czechowicza, and C. Haberland. "Control loops with detection of inner electrical resistance and fatigue-behaviour by activation of niti -shape

- memory alloys.” *Proceedings of the 2009 European Symposium on Martensitic Transformations* **05006**, 1–8 (2009).
- [155] S.-H. Liu, T.-S. Huang, and J.-Y. Yen. “Tracking control of shape-memory-alloy actuators based on self-sensing feedback and inverse hysteresis compensation.” *Sensors* **10**, 112–127 (2010).
- [156] Z. Shi, D. Liu, C. Ma, and D. Zhao. “Accurate controlled shape memory alloy actuator for minimally invasive surgery.” *Proceedings of the 2011 IEEE International Conference on Mechatronics and Automation* pages 817–822 (2011).
- [157] R. Neugebauer, A. Bucht, K. Pagel, and J. Jung. “Numerical simulation of the activation behavior of thermal shape memory alloys.” *Proceedings of Industrial and Commercial Applications of Smart Structures Technologies 2010* **7645**, 1–12 (2010).
- [158] J. Zhang and Y. Yin. “Sma-based bionic integration of self-sensor-actuator for artificial skeletal muscle.” *Sensors and Actuators A* **181**, 94–102 (2012).
- [159] N. Ma, G. Song, and H. Lee. “Position control of sma actuators with internal electrical resistance feedback.” *Proceedings of Smart Structures and Materials 2003: Modeling, Signal Processing, and Control* **5049**, 46–55 (2003).
- [160] N. Ma, G. Song, and H. Lee. “Position control of shape memory alloy actuators with internal electrical resistance feedback using neural networks.” *Smart Materials and Structures* **13**, 777–783 (2004).
- [161] E. Asua, J. Feutchwanger, A. Garcia-Arribas, and V. Etxebarria. “Sensorless control of sma-based actuators using neural networks.” *Journal of Intelligent Material Systems and Structures* **21**, 1809–1818 (2010).
- [162] C. Liang and C. Rogers. “One-dimensional thermomechanical constitutive relations for shape memory materials.” *Journal of Intelligent Material Systems and Structures* **1**, 207–235 (1990).
- [163] L. Brinson and M. Huang. “Simplifications and comparisons of shape memory alloy constitutive models.” *Journal of Intelligent Material Systems and Structures* **7**, 108–114 (1996).
- [164] K. Ikuta, M. Tsukamoto, and S. Hirose. “Mathematical model and experimental verification of shape memory alloy for designing micro actuator.” *Proceedings. IEEE Micro Electro Mechanical Systems. An Investigation of Micro Structures, Sensors, Actuators, Machines and Robots* pages 103–108 (1991).

- [165] J. Boyd and D. Lagoudas. "A thermodynamical constitutive model for shape memory materials, part i. the monolithic shape memory alloy." *International Journal of Plasticity* **12-6**, 805–842 (1996).
- [166] Y. Luo, T. Okuyama, and T. Takagi. "One-dimensional constitutive model of stress-induced transitions between ms and mf in shape memory alloys." *Smart Structures and Materials 2002: Active Materials: Behavior and Mechanics* **4699**, 335–342 (2002).
- [167] M. H. Elahinia and M. Ahmadian. "An enhanced sma phenomenological model: I. the shortcomings of the existing models." *Smart Materials and Structures* **14**, 1297–1308 (2005).
- [168] J. Amalraj, A. Bhattacharyya, and M. Faulkner. "Finite-element modeling of phase transformation in shape memory alloy wires with variable material properties." *Smart Materials and Structures* **9**, 622–631 (2000).
- [169] M. Ghomshei, A. Khajepour, N. Tabandeh, and K. Behdinan. "Finite element modeling of shape memory alloy composite actuators: Theory and experiment." *Journal of Intelligent Material Systems and Structures* **12**, 761–774 (2001).
- [170] G. Dumont and C. Kuhl. "Finite element simulation for design optimisation of shape memory alloy spring actuators." *Engineering Computations: International Journal for Computer-Aided Engineering and Software* **22-7**, 835–848 (2004).
- [171] D. R. Madill and D. Wang. "Modeling and l2-stability of a shape memory alloy position control system." *IEEE Transactions on Control Systems Technology* **6-4**, 473–481 (1998).
- [172] P. Barooah and N. Rey. "Closed loop control of a shape memory alloy actuation system for variable area fan nozzle." *Smart Structures and Materials 2002: Modeling, Signal Processing, and Control* **4693**, 384–395 (2002).
- [173] E. Shameli, A. Alasty, and H. Salaarieh. "Stability analysis and nonlinear control of a miniature shape memory alloy actuator for precise applications." *Mechatronics* **15**, 471–486 (2005).
- [174] K. Singh, J. Sirohi, and I. Chopra. "An improved shape memory alloy actuator for rotor blade tracking." *Journal Of Intelligent Material Systems and Structures* **14**, 767–787 (2003).

- [175] Y. H. Teh and R. Featherstone. “Accurate force control and motion disturbance rejection for shape memory alloy actuators.” *Proceedings of the 2007 IEEE International Conference on Robotics and Automation* pages 4454–4459 (2007).
- [176] K. Arai, S. Ararnaki, and K. Yanagisawa. “Feedback linearization for sma (shape memory alloy).” *Proceedings of the 34th SICE Annual Conference. International Session Papers* pages 1383–1386 (1995).
- [177] H. Benzaoui, N. Chaillet, C. LExcellent, and A. Bourjault. “Non linear motion and force control of shape memory alloys actuators.” *Proceedings of the SPIE Conference on Mathematics and Control in Smart Structures* **3667**, 337–348 (1999).
- [178] C. J. Lee and C. Mavroidis. “Analytical dynamic model and experimental robust and optimal control of shape-memory-alloy bundle actuators.” *Proceedings of the 2002 ASME International Mechanical Engineering Congress and Exposition* pages 491–498 (2002).
- [179] J. Jayender, R. V. Patel, S. Nikumb, and M. Ostojic. “Modeling and control of shape memory alloy actuators.” *IEEE Transactions on Control Systems Technology* **16-2**, 279–287 (2008).
- [180] D. Grant and V. Hayward. “Variable structure control of shape memory alloy actuators.” *IEEE Control Systems Magazine* **17-3**, 80–88 (1997).
- [181] H. Ashrafiun, M. Eshraghi, and M. H. Elahinia. “Position control of a three-link shape memory alloy actuated robot.” *Journal Of Intelligent Material Systems and Structures* **17**, 381–393 (2006).
- [182] G. Song. “Robust position regulation of a rotary servo actuated by a shape memory alloy wire.” *2001 IEEE International Symposium on Industrial Electronics Proceedings* **3**, 1923–1928 (2001).
- [183] H. J. Lee and J. J. Lee. “Time delay control of a shape memory alloy actuator.” *Smart Materials and Structures* **13**, 227–239 (2004).
- [184] M. Elahinia, J. Koo, M. Ahmadian, and C. Woolsey. “Backstepping control of a shape memory alloy actuated robotic arm.” *Journal of Vibration and Control* **11**, 407–429 (2005).
- [185] S. Majima, K. Kodama, and T. Hasegawa. “Modeling of shape memory alloy actuator and tracking control system with the model.” *IEEE Transactions on Control Systems Technology* **9-1**, 54–59 (2001).

- [186] M. van der Wijst, P. Schreurs, and F. Veldpaus. "Application of computed phase transformation power to control shape memory alloy actuators." *Smart Materials and Structure* **6**, 190–198 (1997).
- [187] S. M. Dutta, F. H. Ghorbel, and J. B. Dabney. "Modeling and control of a shape memory alloy actuator." *Proceedings of the 2005 IEEE International Symposium on Intelligent Control* pages 1007–1012 (2005).
- [188] K. K. Ahn and N. B. Kha. "Internal model control for shape memory alloy actuators using fuzzy based preisach model." *Sensors and Actuators A* **13**, 730–741 (2006).
- [189] B. Donmez, B. Ozkan, and S. Kadioglu. "Precise position control using shape memory alloy wires." *Turkish Journal of Electrical Engineering and Computer Science* **18-5**, 899–912 (2010).
- [190] G. Song, V. Chaudhry, and C. Batur. "A neural network inverse model for a shape memory alloy wire actuator." *Journal Of Intelligent Material Systems and Structures* **14**, 371–378 (2003).
- [191] G. Song, V. Chaudhry, and C. Batur. "Precision tracking control of shape memory alloy actuators using neural networks and a sliding-mode based robust controller." *Smart Materials and Structures* **12**, 223–231 (2003).
- [192] J. M. Stevens and G. D. Buckner. "Intelligent control of a micro-manipulator actuated with shape memory alloy tendons." *Smart Structures and Materials 2003: Modeling, Signal Processing, and Control* **5049**, 56–64 (2003).
- [193] A. Kumagai, P. Hozian, and M. Kirkland. "Neuro-fuzzy model based feedback controller for shape memory alloy actuators." *Proceedings of SPIE - The International Society for Optical Engineering, Smart Structures and Materials 2000: Mathematics and Control in Smart Structures*, **3984**, 291–299 (2000).
- [194] D. Maffiodo, T. Raparelli, and G. Belforte. "Fuzzy logic position control of a shape memory alloy wire." *Ventil* **16-2**, 136–145 (2010).
- [195] G. Tchoupo and K. K. Leang. "Hysteresis compensation for high-precision positioning of a shape memory alloy actuator using integrated iterative-feedforward and feedback inputs." *Proceedings of the 2007 American Control Conference* pages 4246–4253 (2007).

- [196] F. Arai, D. Azuma, K. Narumi, Y. Yamanishi, and Y.-C. Lin. "Design and fabrication of a shape memory alloy actuated exoskeletal microarm." *Proceedings of the 2007 18th International Symposium on Micro-NanoMechatronics and Human Science* pages 148–152 (2007).
- [197] C.-C. Lan and C.-H. Fan. "Investigation on pretensioned shape memory alloy actuators for force and displacement self-sensing." *Proceedings of the 2010 IEEE/RSJ International Conference on Intelligent Robots and Systems* pages 3043–3048 (2010).
- [198] J. Pons, D. Reynaerts, J. Peirs, R. Ceres, and H. V. Brusse. "Comparison of different control approaches to drive sma actuators." *Proceedings of the 1997 8th International Conference on Advanced Robotics* pages 819–824 (1997).
- [199] S. G. Shu, D. C. Lagoudas, D. Hughes, and J. T. Wen. "Modeling of a flexible beam actuated by shape memory alloy wires." *Smart Materials Structure* **6**, 265–277 (1997).
- [200] S. Wu, H. Lin, and T. Lin. "Electrical resistivity of ternary binary and ternary ($x = \text{Fe, Cu}$) ternary shape memory alloys." *Materials Science and Engineering* **438**, 536–539 (2006).